Titre: Title:	Modeling the Tribomechanical Properties of Multifunctional Thin Film Coatings
Auteur: Author:	Michael Laberge
Date:	2019
Type:	Mémoire ou thèse / Dissertation or Thesis
Référence: Citation:	Laberge, M. (2019). Modeling the Tribomechanical Properties of Multifunctional Thin Film Coatings [Thèse de doctorat, Polytechnique Montréal]. PolyPublie. https://publications.polymtl.ca/4045/

POLYTECHNIQUE MONTRÉAL

affiliée à l'Université de Montréal

Modeling the tribomechanical properties of multifunctional thin film coatings

MICHAEL LABERGE

Département de génie physique

Thèse présentée en vue de l'obtention du diplôme de *Philosophiæ Doctor*

Génie physique

Août 2019

POLYTECHNIQUE MONTRÉAL

affiliée à l'Université de Montréal

Cette thèse intitulée :

Modeling the tribomechanical properties of multifunctional thin film coatings

présentée par **Michael LABERGE**

en vue de l'obtention du diplôme de *Philosophiæ Doctor*

a été dûment acceptée par le jury d'examen constitué de :

Yves-Alain PETER, président
Ludvik MARTINU, membre et directeur de recherche
Jolanta-Ewa SAPIEHA, membre et codirectrice de recherche
Martin LÉVESQUE, membre
André MCDONALD, membre externe

DEDICATION

I keep the white-belt mentality that I can learn from anyone, anywhere, anytime

Georges St-Pierre

ACKNOWLEDGEMENTS

J’aimerais remercier profondément mes directeurs de thèse, Ludvík et Jolanta, pour m’avoir donné l’opportunité et la confiance de mener à terme mon doctorat. Puisqu’il m’est pratiquement impossible de mentionner tout le monde sans en oublier, j’aimerais remercier tous les gens sans exception que j’ai côtoyée dans notre groupe de recherche pendant toutes ces années. J’ai tellement appris de chacun de vous dans plein de domaines lors des discussions de bureau, autour d’un café ou même dans le fameux couloir devant le CMS-18. Merci également à toutes les partenaires industrielles avec qui j’ai eu la chance de travailler. Chacun de vous m’avez appuyé et encouragé à poursuivre et persévérer et vous avez fait une différence importante. Finalement, merci à la vie de m’avoir permis d’avoir cette chance et le désir de continuellement apprendre et partager.

RÉSUMÉ

L'adoption des traitements de surface par dépôt de revêtements à couche mince s'est rapidement propagée dans divers champs industriels et technologiques tels que les outils d'usinage, les revêtements protecteurs, les revêtements décoratifs, les surfaces hautement réfractaires, les filtres optiques, les composantes optoélectroniques, les dispositifs magnétiques et sensoriels, les prothèses biomédicales et la microélectronique. Avec l'augmentation des requis de performance, les revêtements utilisés pour ces dispositifs doivent être adaptés et conçus pour survivre aux conditions tribomécaniques d'opérations, et ce pour la durée de vie attendue. Pour atteindre cette cible, le concept du design par revêtements multifonctionnels a largement été embrassé par la communauté. Cette approche consiste à déposer une multicouche dans laquelle chacune des couches joue un rôle spécifique dans le fonctionnement global du dispositif. En revanche, avec l'augmentation de la complexité et des subtilités impliquées dans le design de couches multifonctionnelles, un besoin important de développer des outils et modèles prédictifs se manifeste. Par conséquent, l'objectif principal de cette thèse est de développer des modèles numériques reproduisant les conditions tribomécaniques à l'échelle des revêtements; premièrement pour élucider les mécanismes fondamentaux responsables de la dégradation des surfaces revêtues et dans un deuxième temps assister le design de l'architecture des revêtements pour augmenter leur résilience structurale. Lors de l'accomplissement de cette thèse, trois principaux sujets ont été approfondis. La première étude concerne la réponse mécanique d'un revêtement bicouche déposé sur acier, en particulier l'influence d'une inter-couche à haute capacité de charge sur la formation d'empreintes résiduelles ainsi que sur la défaillance du revêtement de surface. En exploitant un modèle de mécanique des milieux continus quasi statique, nous avons caractérisé et prédit les conditions critiques qui mènent à ce type d'endommagement. La deuxième étude porte sur la formation d'un réseau de fissure à la surface d'un revêtement optique déposé sur un substrat de polymère. À l'aide d'essais de traction in situ et d'un modèle à éléments finis en contraintes planes correspondant, nous avons étudié la fracturation et la ténacité de différentes configurations multicouches. En commençant par la caractérisation des propriétés de rupture de monocouches, nous avons clarifié le chemin de fracturation à travers le revêtement et ainsi identifié les paramètres critiques responsables de la défaillance catastrophique du film. Finalement, dans la troisième étude, nous avons sondé la possibilité d'utiliser un revêtement bio-inspiré à gradient de propriétés pour

améliorer la résistance à l'usure par érosion. Nous avons étudié l'influence du profil mécanique de la couche sur la répartition de la charge ainsi que sur l'intensité des contraintes en pointes de fissures. Nous avons démontré qu'un profil mécanique particulier basé sur celui présent dans les dents de mammifères a un haut potentiel d'augmenter de façon significative la résistance à la propagation de fissures.

ABSTRACT

The adoption of thin film coating technologies has been quickly spreading to numerous major industrial and technological fields including machining tools, protective coatings, decorative films, high temperature resistant surfaces, optics, optoelectronic, magnetic and sensorics devices, biomedical prosthetic and microelectronics. As the requirements for high performance continuously increase, the coating of thee components must be adapted and tailored to withstand the tribomechanical solicitations to which they are subjected during the expected lifetime under their typical operation conditions. To meet this objective and associated challenges the multifunctional coating design concept has been widely adopted by the community. In this approach, a layered material is deposited on a supporting substrate in which each layer serves a specific role to the overall device functionality. However, as the complexity and intricacies involved in the design of such multifunctional coatings increase, so is the need for predictive modeling tools to assist in this task. Accordingly, the main objective of this thesis is to develop coating-scale tribomechanical numerical models, first to uncover the underlying mechanisms responsible for the degradation of the coated surfaces, and secondly to guide the coating architectural design to further improve the surface resilience. This thesis presents several case studies which are divided into three principal investigations. In the first study, we investigated the tribomechanical response of a duplex coated steel substrate, most notably the influence of a load-carrying underlayer on the formation of permanent indents and failure of the top coating. Using a quasi-static continuum mechanics indentation model, we were able to characterize and predict the critical conditions which lead to the apparition of the related surface damage. The second case study was related to the formation of crack patterns at the surface of an optical film deposited on a polymer substrate. Using an in situ tensile experiment and a corresponding plane strain finite element model, we investigated the fracturability and toughness of different stack configurations. By first characterizing the fracture properties of the single layers individually, we were able to uncover the fracture pathway in a multilayer coating and identify the most critical parameters responsible for the catastrophic failure of the stack. Finally, we probed the potential application of bio-inspired functionally graded coatings for enhanced protection against erosive wear. The influence of the mechanical depth profile on the load spreading and crack driving forces were investigated. We have shown that an intrinsic toughening mechanism resulting from a peculiar

profile based on mammal teeth has the potential to significantly increase the crack growth resistance.

TABLE OF CONTENTS

LIST OF TABLES

LIST OF FIGURES

LIST OF SYMBOLS AND ABBREVIATIONS

Abbreviations

COS	Crack onset strain
CSP	Concentrated solar power
DIC	Digital image correlation
DOF	Degrees of freedom
ERR	Energy release rate
FEA	Finite element analysis
FE	Finite element
FEM	Finite element modeling
IAD	Ion assisted deposition
PP	Photovoltaic panel
SEM	Scanning electron microscopy
SM	Solar mirror
SPE	Solid particle erosion
SSBV	Severe-service ball valves

Symbols

E	Young's modulus
E_t	Tangent modulus
$\bar{E}$	Plane strain modulus
F_n	Normal force
G	Energy release rate
H	Hardness

$\oint J$	J-integral
k_c	Contact stiffness
K	Stress intensity factor
K_{IC}	Mode I fracture toughness
L_y	Normal load to initiate plastic deformation
L_f	Critical normal load for ring crack formation
T	Traction force
W	Strain energy density
δ_p	Contact interpenetration distance
ρ	Density
ε	Strain
σ_{ij}	Cauchy stress tensor
σ_y	Yield stress
σ_r	Residual stress
υ	Poisson's ratio

LIST OF APPENDICES

CHAPTER 1 INTRODUCTION

1.1 General introduction to the field of thin film coating technology

Let's imagine ourselves in a typical living room, taking a look around us at the different appliances, technological devices, and gadgets that we use every day. Even though they may not be visible to the naked eye, we have become surrounded with engineered components with surfaces covered via thin film coating deposition processes. The advancement in the field of thin film deposition techniques in the last decades, leading to the rise and miniaturization of modern microelectronics, may be the most well-known exploitation of this technology [1]. Less obvious examples of thin films and coatings used in common household objects are those present in low emissivity windows [2], food packaging [3], oleophobic/antireflective [4] coatings on phones/tablets surfaces and camera lenses, optical filters for security devices on bank notes and cards [5], thin-film solar panels [6], and numerous others. Hard protective coatings can also be found for example on tools such as drill bits to increase both their cutting performances and lifetime [7]. Maybe a few of us even own items such as specialized sportswear or kitchen equipment covered with an hydrophobic coating to grant them liquid repellant properties [8]. In all these applications, different film materials are used such that they perform a specific function to contribute to the holistic requirements of the device. To give a visual representation of a multi-functional coating, we present in figure 1.1 an example of a typical multilayer anti-reflective coating deposited on a glass or polymer supporting material. To enhance the durability and performances, functional layers such as an anti-fouling/self-cleaning top coating and a scratch resistant protective layer are added to the design [9, p. 14].

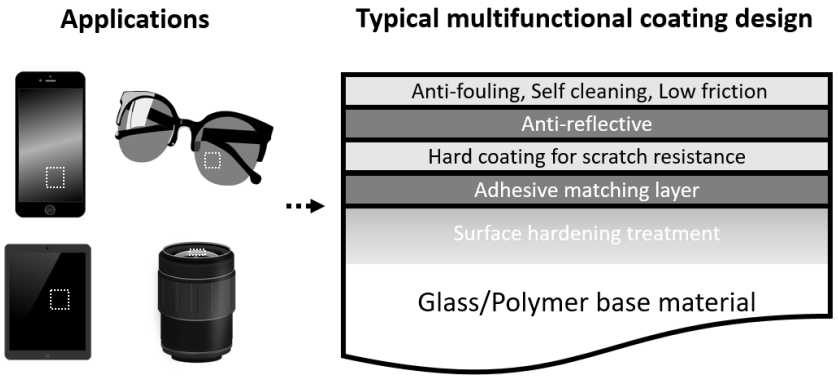

Figure 1.1 Typical multifunctional anti-reflective coating design used to protect glass or polymer-based optical components during its normal utilization.

The omnipresence of thin film coatings in everyday items is already becoming a reality; nonetheless with the introduction of flexible electronics to the consumer market it is envisioned that their presence will grow at an even faster rate in the near future [10].

One of the major drawbacks to coatings is that they can be damaged, and once they are removed from the base-material, the surface functionalities of the worn area is directly compromised. To mitigate those risks, surface engineers are taking different research paths including the development of new surface treatments and deposition processes, exploration of new materials with enhanced properties, and optimization of the coating architectural design that are adapted to the operational conditions and environment of the device. To test and compare the new coating solutions, well controlled tribological tests recreating the mechanical solicitations are employed and the final design is selected when it reaches all the requirements of the application.

Figure 1.2 presents the important progress illustrated by the number of publications related to tribological testing applied to coatings in the past ten years. Also shown in this figure, is the great discrepancy between empirical studies and studies that include predictive modeling of the tribological conditions. In spite of this fruitful industry, there is still a lack of predictive modeling tools for engineers and researchers exploiting thin film coatings technologies. The design phase still faces significant challenges concerning the tribomechanical and environmental stabilities of thin film coatings since they must meet both the functional properties of the coating and the mechanical reliability in the operational conditions and environment.

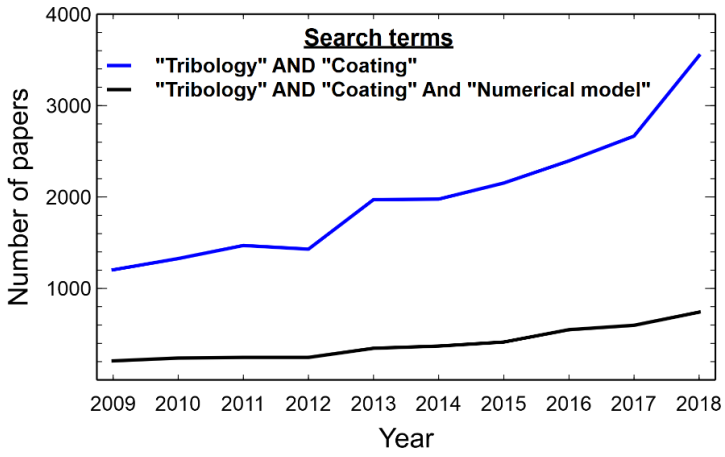

Figure 1.2 Number of published papers in the past decade. Data retrieved on Microsoft Academic website.

The durability of coatings has been a major cause of concern in our society even long before the apparition of thin film technologies. To give an easily relatable example, it can be seen in another type of coating very common in modern houses: interior painting on the walls and finishing plaster used for drywall joints. Over time, these materials are subjected to temperature cycles and mechanical solicitations that can lead to failures such as peeling and cracking along the most stressed zones. The wall surfaces are also subject to be worn by sliding contact and impact from a door knob, for example, which in both cases can gradually remove the paint layer and also leads to cracks and delamination failures. Very comparable phenomena apply to thin film coated surfaces at a much smaller scale, however, the first signs of failure are much less perceptible or may even be invisible to the naked eye.

1.2 Problematic and objectives

In the context we just introduced, many questions arise: (1) How can we access the tribomechanical durability and stability of thin film coatings? (2) What type of coating materials and/or deposition techniques should be used for optimal performance and durability for a specific application, and (3) Is it possible through numerical modeling to gain relevant insight about underlying failures and wear mechanisms as such to propose a film architecture design with improved tribological properties adapted to the operational environment?

(1) The first question about the micro/nano tribomechanical characterization has been the subject of countless studies and is now considered to be a relatively mature field with experimental standards that have been available for a few decades already and used throughout the scientific community. Even in this mature state, the field is still burgeoning with new studies, especially those related to micromechanical characterization.

(2) The second question can partially be answered by investigating the abundant empirical evidences produced in the scientific literature. Copious amount of experimental data is available and can help guide the choice of the appropriate materials combination as it will be discussed in Chapter 2. New players in the field of thin film coatings must often rely on such studies since more often than not, the material designs of commercially available products are protected by patents or are simply too complicated to be reverse engineered. Moreover, as new materials with widely different tribomechanical properties are

introduced, experimental assessments are constantly needed to bring new and improved material solutions to their commercialization which means that an optimal solution may not have been discovered yet and may never be.

(3) Finally, let's talk about the last question, the most fascinating one and the one that is involved at the core of this thesis. To give a brief answer that will be extensively developed throughout this work, as of this day, there are no numerical standards applicable to the modeling of thin films' and coatings' tribomechanical properties. Even though many numerical approaches are proposed in the literature, further investigations and experimental validations are still needed to reach this level of maturity in the field. However, given the current situation of the never-ending cycle of mostly empirical testing as the main research guidance, there is a major imperative from surface and coating researchers and engineers to develop more robust and accessible predictive numerical modeling methodologies that will drive the design process.

Problem statement:

The objective of this work is to develop numerical models to understand and predict the tribomechanical behavior and performances of multifunctional coatings subjected to controlled dry wear conditions. The ultimate objective of these numerical models is to develop tools for surface engineers to assist in the characterization and the design of coated materials with enhanced durability and stability while also cutting the cost and time-consuming process of experimental trials and errors which is currently the typical procedure taken by the industry.

Before getting there, we have a great journey to embark upon, and it is my duty and my pleasure to assist the readers to follow it until the end. This thesis is divided in 7 main chapters as we will present in the next section.

1.3 Thesis outline

To begin our trip, in **Chapter 2.1**, the basic notions of tribomechanical behavior of coated surfaces will be briefly introduced. This chapter is intended to introduce the field to the readers and help

them quickly grasp general context of this work. In this section, a survey of the scientific literature will be presented and exposed in such a way to identify interesting questions that have still to be answered by the tribologists community. From these unanswered questions, the general objectives and questions this work will explore, will emerge and be detailed.

Chapter 2.2 and onward is intended to present the state of the art in the field of tribological coatings. First, the fundamental wear and failure mechanisms of thin film coatings will be introduced. From the material development aspect, tribomechanical properties and architectural design of tribological coatings, we will present the evolution and novel solutions surface engineers have developed to enhance their long-term performances.

Chapter 3 is intended to introduce the basis of the numerical methodologies used in the different projects that this thesis explores. The basics of continuum mechanics, the modeling of fracture mechanics and the numerical accuracy and validation facets will be discussed.

Chapter 4 will present a first peer-reviewed study related to the investigation of coating indentation damages in the context of severe-service ball valves.

- Laberge, M., E. Bousser, J. Schmitt, M. Koshigan, T. Schmitt, F. Khelfaoui, S. Isbitsky, L. Vernhes, and J. E. Klemberg-Sapieha. **"Predicting the Load-Carrying Capacity and Wear Resistance of Duplex-Coated Low-Strength Alloys for Severe Service Ball Valves."** Journal of Thermal Spray Technology 27, no. 7 (2018): 1177-1186.

Chapter 5 consists of a second peer-reviewed paper that investigated the fracturability of optical thin-films deposited on a polymer substrate.

- Michael Laberge, Delphine Poinot Cherroret, Sébastien Châtel, Oleg Zabeida, Ludvik Martinu. **"Assessment of fracturability and of fracture toughness of brittle multilayer optical coatings on polymeric substrates."**, Submitted to Surface and Coatings Technology

Chapter 6 will present a numerical investigation concerning the tribomechanical response of mechanically graded coatings subjected to micro-particle erosion conditions. Parts of this work were presented in the context of three international conferences.

- M. Laberge, J. E. Klemberg-Sapieha, L. Martinu, **Solid Particle Erosion Modeling of Graded Nanocomposite TiSiN Coatings**, 43rd International Conference on Metallurgical Coatings and Thin Films, April 2016, San Diego, CA, USA.
- M. Laberge, J. E. Klemberg-Sapieha, L. Martinu, **Solid particle erosion modeling of stress-controlled functionally graded coatings for aerospace applications**, XIII International Conference on Nanostructured Materials, August 2016, Québec City, Canada.
- M. Laberge, J. E. Klemberg-Sapieha, L. Martinu, **Solid Particle Erosion Modeling of Stress-controlled Mechanically Graded Coatings**, Stress Evolution in Thin Films and Coatings, October 2016, Chicago, IL, USA.

Chapter 7 will summarize the most important and novel results of this work.

Finally, in **Chapter 8,** a few closing remarks about the future of tribology and a discussion of the potential research directions that are of uttermost importance to me will conclude this thesis.

CHAPTER 2 LITERATURE REVIEW

2.1 General context of tribology

Tribology refers to the field of study of contacting and chemically interacting surfaces in motion relative to each other. The term was first coined by the Jost Report published in 1966 [11], and since then has been widely adopted in the scientific and industrial communities. In this report, important examinations about the high maintenance cost of infrastructures maintenance due to friction, corrosion and wear were exposed and combined into the new term “tribology”. Reports exposing similar issues can still be found today, for example in 2007, Holmberg estimated the global energy consumption wasted through tribological contacts for the transportation, manufacturing, residential and power generation sectors [12]. He calculated that 20% of the total energy is lost in overcoming friction which in consequence leads to 3% of the total energy to be spent on the maintenance and replacements of those equipment. Trying to make a modern exhaustive list of every research field where tribology is studied is clearly a complicated task since it has become so widespread. Many reference books that cover the field of thin film coating tribology are available in the scientific literature [13]–[21]. For example, in the second edition of “Coating Tribology” published in 2009 [17], Holmberg and Matthews presented coating tribological studies related to a wide array of applications such as cutting and forming machining tools, biomedical applications (hip prostheses, dental implants, surgical tools), magnetic storage and microelectromechanical systems, scratch and erosion resistant glass, turbine blades and industrial pipelines erosion. It can clearly be appreciated that tribology has become a highly interdisciplinary branch of research interconnecting materials science, physics, chemistry, biology, medicine and engineering.

2.2 Tribomechanical requirements of coated surfaces

This section is targeted at introducing the different types of tribomechanical solicitations that contribute to the wear and failure of thin film coatings. They will be divided in the following three categories: Concentrated contact loads, dynamic impact, and structural loads.

It will become evident that for each category of tribological conditions, many questions about the underlying wear mechanisms are still missing complete answers. Those questions are the ones that new study in the field should aim at to expand our knowledge about tribological coating design. Thereby, from those still unanswered questions will emerge the specific objectives that this thesis wishes to address. Those will be presented in detail subsequently.

2.2.1 Concentrated contact loads

Contact between different surfaces induce mechanical stresses at the surface and inside all components involved. The more the contact area is reduced, or the sharper the counterpart is, the more concentrated and increasingly confined to the surface that the induced stress will be. Using Hertz contact model [22] that behavior can be estimated by calculating the contact stress induced by sphere of varying radius applying a load on a semi-infinite region of a bulk material. The materials are assumed to be homogeneous and their behavior is fully defined by their elastic constants (E, ν), where E is the Young's modulus and ν is the Poisson's ratio. Let's take for example a fused silica sphere ($E = 73.1\ GPa, \nu = 0.17$) applying a normal load of 10 N on a flat surface of AISI 304 stainless steel ($E = 193\ GPa, \nu = 0.29$).

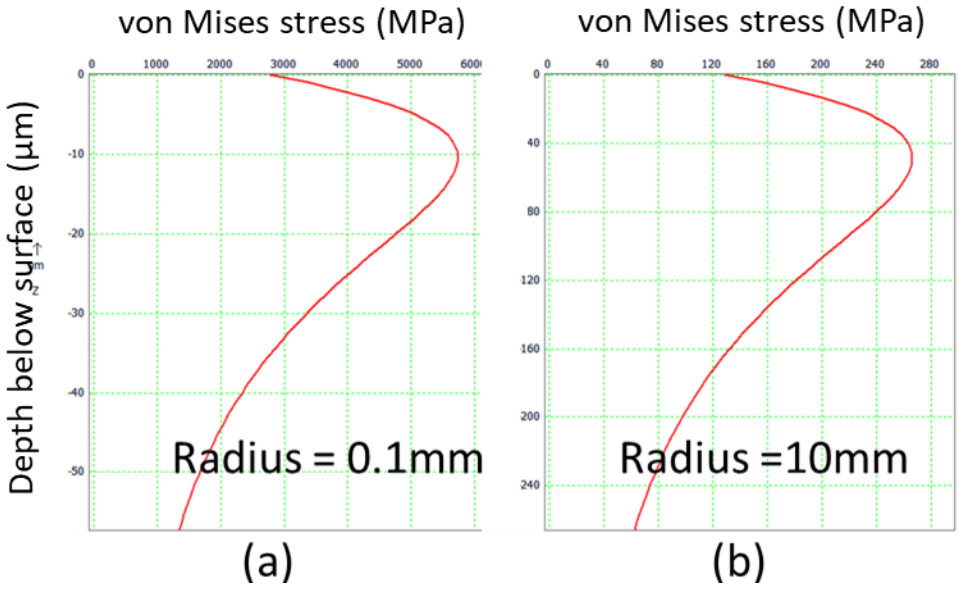

Figure 2.1 Von Mises stress depth profile induced in a stainless steel surface by a 10 N normal load applied by (a) a silica sphere having a radius 10mm and (b) 0.1mm [23].

In the example shown in figure 2.1, by decreasing the sphere radius from $10\ mm$ to $0.1\ mm$ the position of the maximum Von Mises stress relocates from $51\ \mu m$ below the surface to only $11\ \mu m$ respectively. It is easy to imagine that for a very sharp counterpart sliding on a coated surface, the stress field may be so confined that its action is limited inside the coating and the system behaves indiscernibly from a bulk material in these contact conditions. This simple example leads directly to the first non-trivial question related to the tribological coating design, how thick should the coatings be designed so it contributes to the tribomechanical properties of the coated system? To be able to continue on this path, we first need to introduce the relevant tribomechanical properties in action in a tribological contact of coated surfaces as schematically presented in figure 2.2.

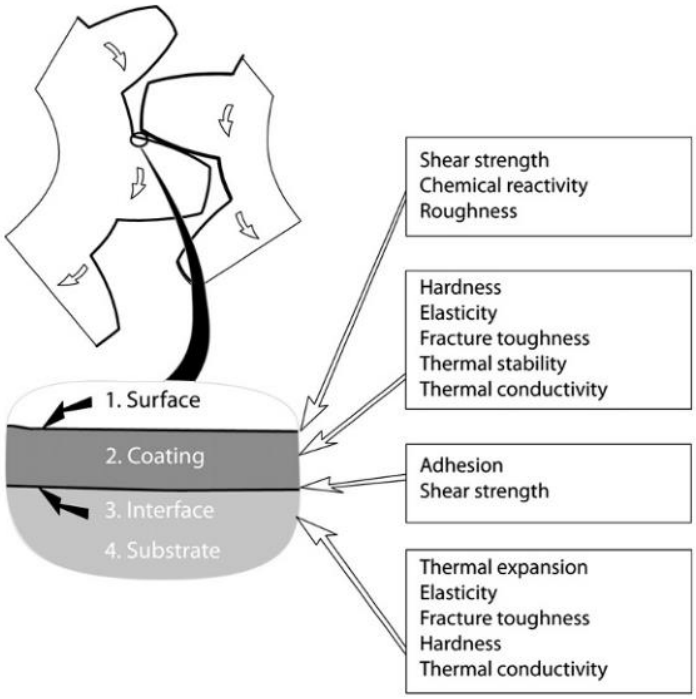

Figure 2.2 Tribomechanical properties involved in coated surface [17].

While the elastic constants still play the main role in defining the contact stresses, the inhomogeneity of the coated surface and other material properties involved (hardness, toughness, thermal expansion coefficient, …) in tribological contacts complexify the behavior beyond the simple capabilities of the Hertz contact model (no layered materials, no plasticity, no non-linearities). The evaluation of realistic stresses inside a coated structure, necessitates the utilization of a numerical approach such as a continuum mechanic model. The more material properties the

model will consider, the more faithful the resulting stresses and deformations results will be. The numerical framework of continuum mechanics modeling will be detailed in Chapter 3.

For now, let's focus on an archetypal situation consisting of a concentrated load induced by a sharp counterpart on a coated surface. In this example we consider a coating that behaves in a brittle manner while the substrate is compliant and ductile. This tribological situation is typical for applications requiring scratch resistance, for example, the protection of soft metallic or polymeric surfaces by a hard ceramic coating. A schematic representation of the induced stresses is presented in figure 2.3.

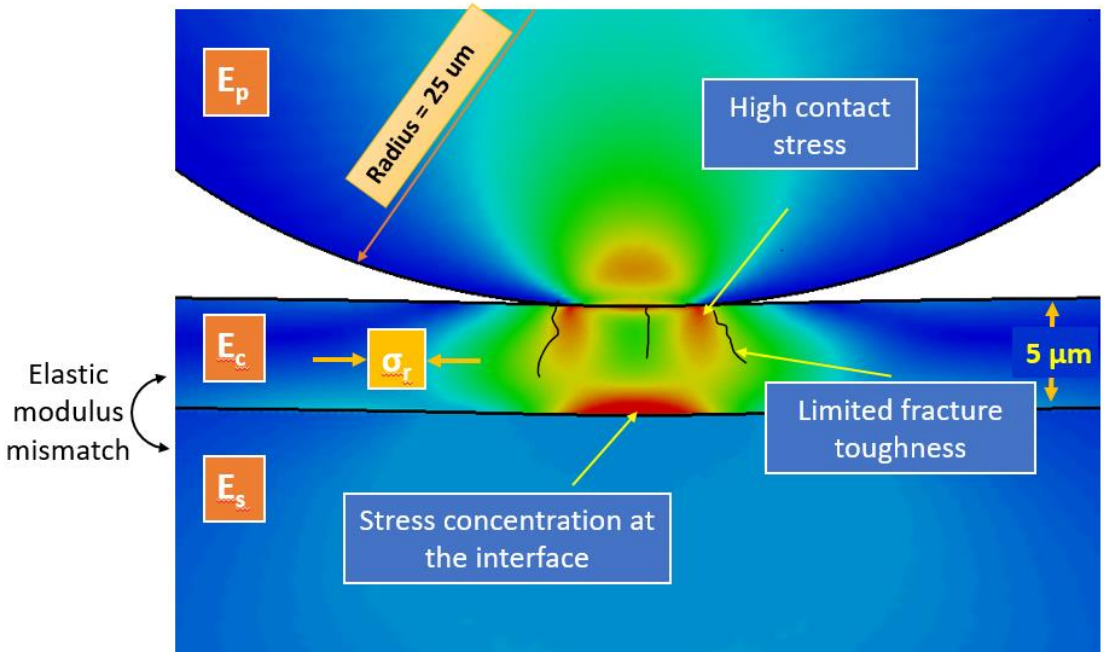

Figure 2.3 Stress concentration induced by a sharp contact on a hard coating.

This simple contact modeling exposes a few interrogations about the mechanical durability of a single layer hard coating solution. High contact stresses may generate cracks and damages directly under the contact area. The mismatch of mechanical properties is also a source of concern since they lead to high interface stresses that may partially delaminate the film from the substrate. Finally, the compliance of the substrate may be the weakest link in the coating design. Highly compliant substrate may suffer permanent deformation (plasticity, densification, cohesive failure)

and generate high stresses around the contact area and at the interface between the coating and the base material. Those regions of high stresses due to excessive substrate deformation may lead to cohesive failure in the coating and adhesion failure at the interface. The obvious solution to this issue is to use a substrate with higher hardness to increase the load carrying capacity of the base material. This is however not always possible due to either the unavailability of a better base material or to design-related constraints related to the chemical and thermal stability in the specific operational environment. In this case, enhancing the coating properties is the only way to improve the tribological performance. One strategy to mitigate the stress concentration zones presented in Figure 2.3 is to design a duplex coating. This solution consists in designing an architecture comprising of a thicker load carrying capacity layer limiting the deformation of the substrate that will be topped by a thinner hard protective coating used for its protection to abrasive wear. This will be the first subject of study in this thesis and presented in Chapter 4. Other coating designs and examples of studies concerning surface protection against concentrated loads will be covered in Chapter 2.

2.2.2 Structural loads

Failure of coatings that originates from a structural load source exhibits different appearances than those discussed previously. Even though no sign of a second body contact may be present, like a scar left by sliding a sharp object, the surface still shows sign of deterioration. Those damages are caused by the in-plane expansion or contraction of the supporting material that leads to tensile or compressive stresses being generated in the coating structure. Under critical conditions, the deformation of the substrate leads to the creation of cohesive and adhesive failure in the thin film coating. The origin of the deformation may be an external mechanical solicitation, for example in flexible electronics, or from thermal expansion cycle such as in microelectronics. This last example was actually the starting point that led to the first efforts in understanding and preventing those specific modes of failure. In the early 90s, both Beuth [24] and Hutchinson [25] published works detailing the different failure mechanisms of a single layer film and modeled their relative relevance in terms of both materials mechanical and fracture properties. The most prominent failure modes are presented in figure 2.4.

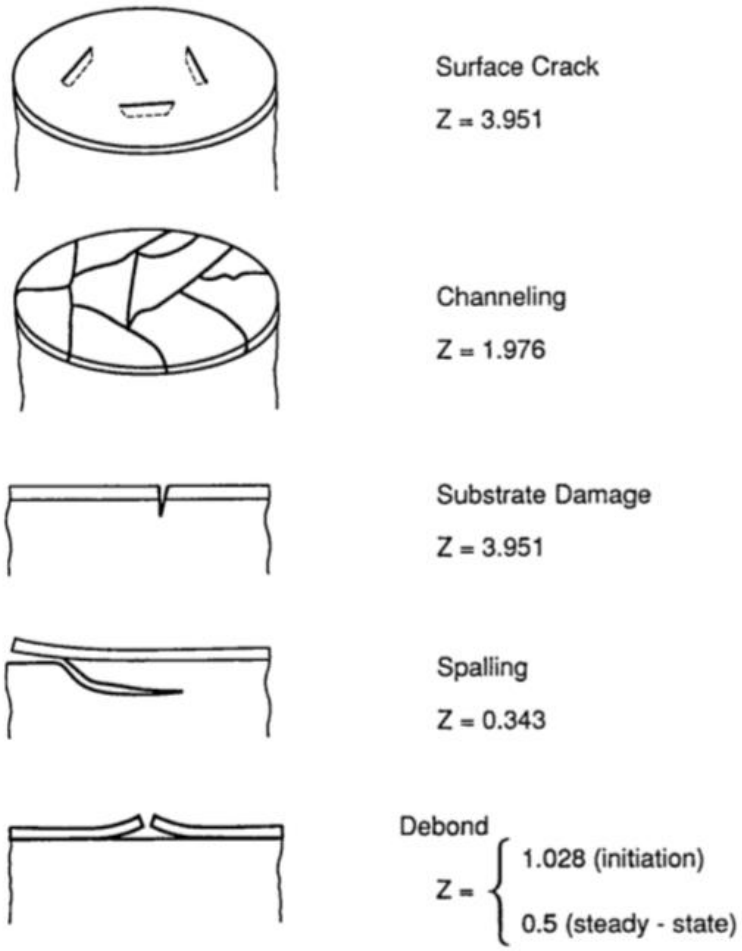

Figure 2.4 Damage patterns of a coated surface under tensile structural load [25].

While these publications still stand today as the most defining works in the field and are widely used as design guides, they lack the capability to be expanded to more complex multilayer structures. In multilayer coatings, the modes of failure are decoupled by the presence of multiple materials and interfaces, each characterized by their distinct fracture properties. In these systems, the failures may originate at the surface and be similar to those presented in figure 2.4; alternatively, failures may initiate in buried layers beneath the surface. Literature about modeling such problems can be found [25]–[30], but is often limited to single layers or bilayers, and insufficient for engineers to be used as a concrete guideline in the design process. In this context, the second subject of this thesis will be to develop a predictive model that will be used to characterize the fracture properties of a multilayer coating deposited on a compliant substrate when subjected to tensile structural loads.

2.2.3 Dynamic impact

In this last section, we are interested in surface wear by an impacting micron-scale counterpart such as sand, dust and other foreign particles travelling at high velocity. In these situations, the wear appearances may be very similar to those created by concentrated loads and the actual wear mechanisms are comparable but usually show more signs of damage due to the harsher operational environment. The material removal is attributed to abrasion and erosion from the impeding particles. Depending on the brittle/ductile nature of the surface, different behavior and wear mechanism are expected as presented in figure 2.5.

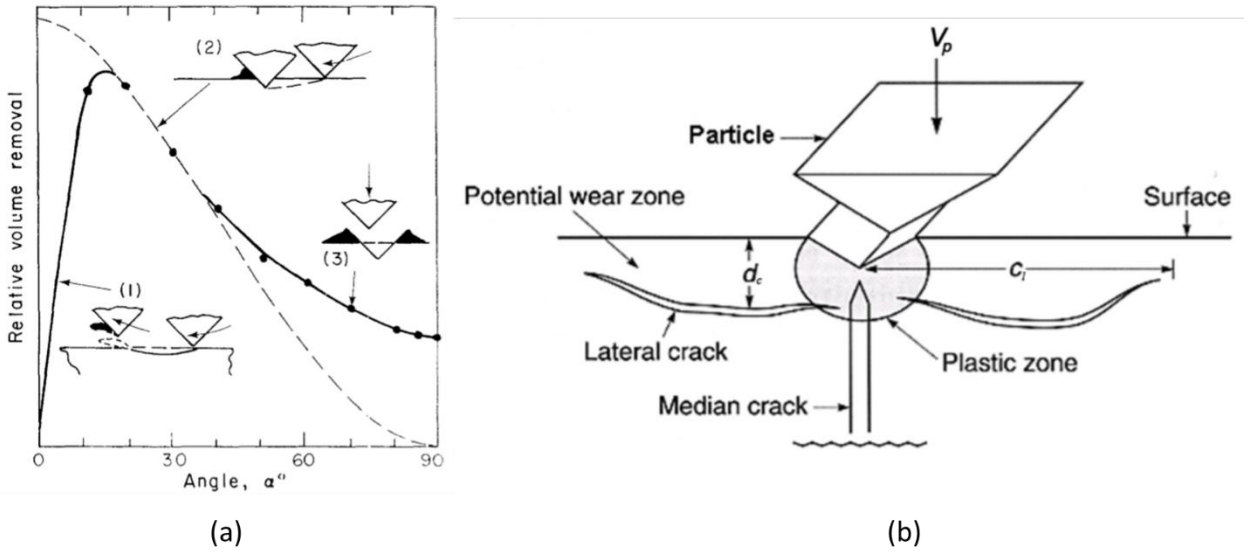

Figure 2.5 Comparison between (a) ductile [31] and (b) brittle [14] micro-particle impact erosion wear mechanisms.

To protect against wear by abrasion and erosion, the most common solution is to use a thick hard ceramic coating, for example, to protect jet engine turbine blade [32] and solar mirror in concentrated solar power plants [33]. The specific wear mechanism will be defined by an intricate relation between the particle, target and operational conditions.

More recently, the metal/ceramic nanolaminates architecture was revealed as a promising solution to enhance the material resistance to dynamic impact from micro-particles [34]. Its superior resistance was attributed to the ability of the multiple interfaces to dissipate energy and deflect incoming cracks from straight propagation thus limiting the damage. This is similar to how nacre

(a naturally formed material found in mollusk shells) is able through this hierarchical geometrical effect to exhibit an emergent higher effective toughness when testing the structure as a whole, than the individual constituents [35]. This capacity of nature to assemble structures in such a way that exceptional tribomechanical properties emerge from a particular substructure has become a field of great interest as depicted in a recent review (2017) by Liu et al. [36]. These studies put in evidence that biomaterials which possess a mechanically graded surface display enhanced fracture resistance. For example, the particular mechanical gradient present in human teeth [37] and shrimp exoskeleton [38] seems to be particularly effective to limit the propagation of cracks in brittle structures. From this perspective, the final subject of this thesis is the development of a dynamic impact continuum mechanics model considering a functionally graded structure. The main objective of the model is to investigate the resistance to fracture propagation inside thin film coatings with different mechanical grading profiles.

In the next sections, we introduce the different concepts related to the description of the tribomechanical behavior of coated materials. First, the fundamental failure mechanisms responsible for the deterioration and wear of material surfaces will be discussed. Subsequently, we will review the different wear categories resulting from those basic failure mechanisms. We will then spend time discussing about multifunctional coating architecture designs considering the tribomechanical requirements. Finally, an introduction to the effect of microstructure on wear behavior and of toughening mechanisms in biomaterials will close this chapter.

2.3 Wear and failure categories

As coated materials are subjected to tribomechanical constraints and solicitations, microstructural scale mechanisms responsible for wearing and degrading the surface are activated (see Figure 2.6). Those solicitations originate either from a tribological or structural load transfer, for example a sharp counterpart sliding on the surface or from the bending of the coated components. For tribological contacts, friction between the parts in relative motion account for a large energy consumption also contributing to wear.

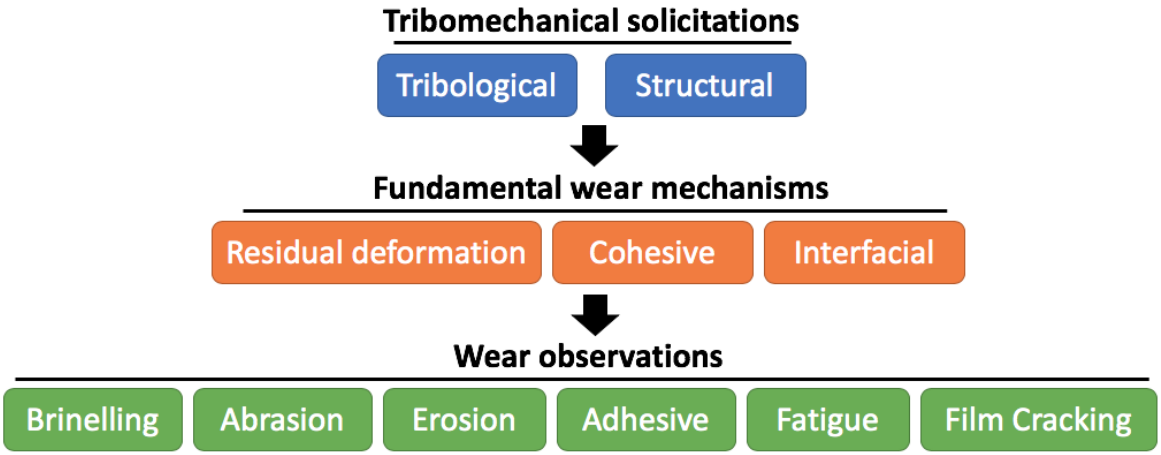

Figure 2.6 Diagram of the wear process from the tribological solicitation to the fundamental wear mechanism leading to surface wear.

The wear rate, as is the coefficient of friction, is not an intrinsic property of the tested materials but a response of the whole system properties and tribological conditions. The holistic tribomechanical response is determined by a vast number of parameters related to both the material properties (Young's modulus, Yield Stress, Hardness, Toughness, Surface roughness, Microstructure, Residual strain, …) and tribomechanical conditions (parts/counterparts geometry, contact load, structural load, temperature, sliding velocity, …).

2.3.1 Tribomechanical solicitations

2.3.1.1 Tribological

The fundamental tribological conditions, occurring at the microstructural asperity scale of contacting materials, are summarized in Figure 2.7. Different fundamental solicitations lead to a unique spreading of the load inside a coated material. In practice, it is the cumulative effect of those different events that leads to the degradation of the surface. The relative weight of each one initiates specific wear mechanisms in distinctive importance.

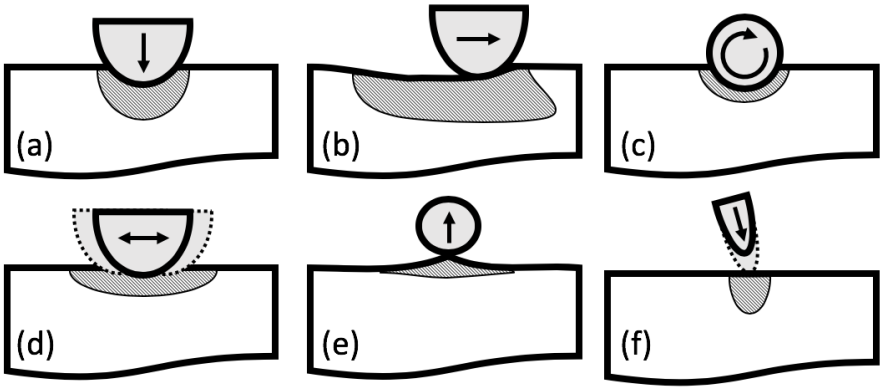

Figure 2.7 Fundamental tribological solicitations: (a) Static contact, (b) sliding contact, (c) rolling contact, (d) fretting, (e) adhesive contact, (f) particle impact. The greyed area schematically represents the plastic strain field associated with the solicitation.

2.3.1.2 Structural

Structural solicitations as opposed to tribological ones, are defined by a homogeneous strain field absent of contact-like stresses generated in the area of interest. The main structural solicitations are schematically presented in Figure 2.8.

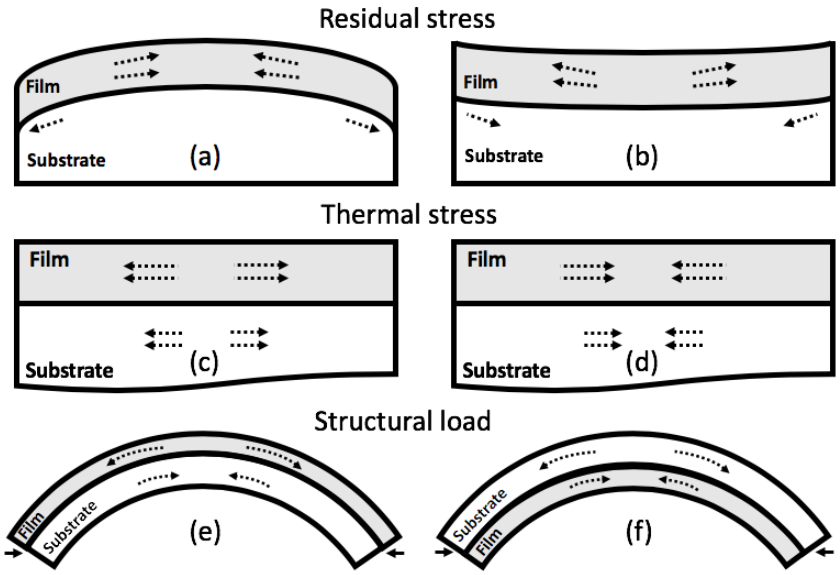

Figure 2.8 Fundamental structural solicitations: Film residual stress in (a) compression and (b) tension. Thermal expansion stress in (c) tension and (d) compression. Structural load with film in (e) tension and (f) compression.

Residual stresses in a coated system occur though three main phenomena: Epitaxial stress, thermal stress and intrinsic stress [39]. Epitaxial stresses originate from the difference in the lattice parameters for interfaces with perfect coherence. Thermal stresses are caused by the difference between the deposition temperature and the operational condition temperature resulting from materials with dissimilar coefficient of thermal expansion. Finally the intrinsic stresses arise from the atomistic processes happening during the grow of the material, the fundamental ones being surface stress effects, grain boundary coalescence and atomic fluxes in the grain boundaries [39]. Since the film is free to expand in the direction perpendicular to the surface, it is assumed for thin films that the final stress state will be biaxial in-plane with the supporting material.

Thermal expansion/contraction stress is equivalent to the thermal residual stresses described previously. As the temperature of the system of the material is varied, under steady state conditions, the mismatch between the coefficient of thermal expansion of the substrate and the coating will induce a homogeneous state of stress through the film. For a film having a lower thermal expansion coefficient than the substrate, the induced stress will be tensile/compressive for an increasing/decreasing temperature while the sign of the stress would be reverse in the opposite case.

Structural load such as bending or tensile/compressive loads will also induce a homogeneous bi-axial stress state in the coating regulated by the angle of curvature or the applied tensile/compressive strain, respectively. As it was the case with the other structural solicitation, this induces a tensile/compressive stress in the coating responsible for particular failure modes that will be presented in the next section.

2.3.1.3 Other solicitations

Other type of solicitations can lead to the degradation of coated material but will not be further presented since they are out of the scope of this study. A non-exhaustive list includes wear by corrosion/oxidation, chemical reactions, ultraviolet radiation, radioactive decay, cavitation, extreme thermal gradient, hydrogen embrittlement, ion impacts, and atomic diffusion/segregation in the coated material.

2.3.2 Wear mechanisms

2.3.2.1 Residual deformation

Residual deformations are caused by any mechanism that lead to permanent deformation of the surface by plasticity and/or densification. For metallic and polymer materials, plasticity is often represented by a yield stress σ_y [Pa] behavior in the stress strain curves and is activated by shear stresses without contribution of the hydrostatic pressure. On the other hand, densification is activated by a combination of shear and hydrostatic pressure which is more common for ceramic materials. In order to relate the three-dimensional stress state to this uniaxial yield stress, the Tresca [40] and von Mises [41] criterion are most commonly applied. Other more refined material constitutive laws (Mohr–Coulomb [42], Drucker–Prager [43]) take into account the difference in compressive versus tensile strength and allow one to model the influence of hydrostatic pressure on the yield surface.

As we introduced in section 1.3, the residual plastic field induced from a contacting counterpart will vary greatly depending on its radius of curvature at the contacting point compared to the thickness of the film. Two typical cases are schematically represented in Figure 2.9. For a very sharp counterpart, the stress field will be mostly confined in the film and we can expect important plastic deformations directly under the contact area. In contrast, if the counterpart is blunt in comparison to the film thickness, then the maximum shear stresses will be located closer to the interface and the imprint will be predominantly a consequence of the substrate residual deformation. Permanent deformation can also result from structural load when the induced stress in the films exceeds their uniaxial tensile/compressive strength.

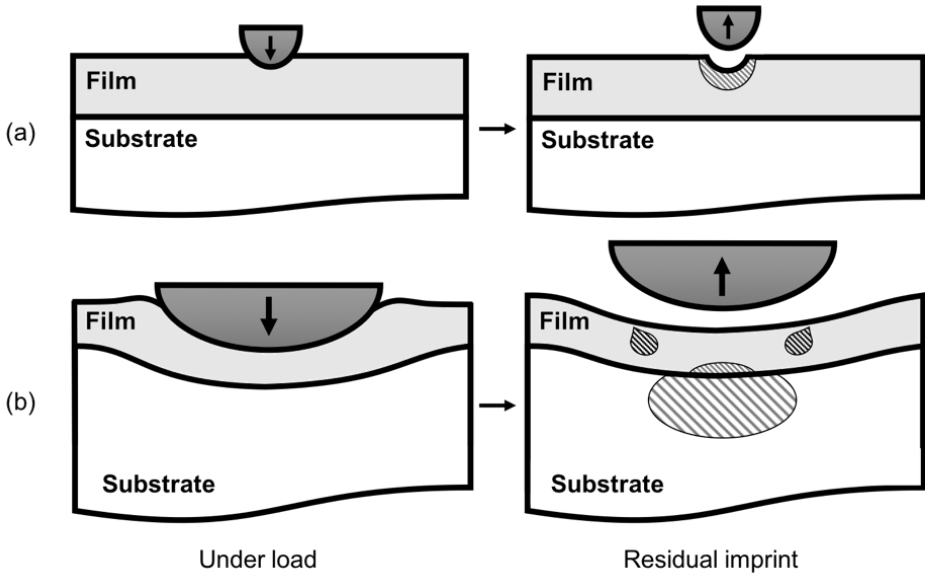

Figure 2.9 Schematic representation of the residual imprint left in a coated system for (a) sharp contact and (b) blunt contact. The greyed area schematically represents the residual plastic strain field.

2.3.2.2 Cohesive

Cohesive failure is related to the breaking of bonds inside a material and is visible by the initiation and propagation of fracture surfaces. The main material parameter controlling the cracks formation is the toughness of the coating Γ which is expressed in unit of energy by unit surface area [J/m^2]. In the linear elastic fracture mechanics framework, the fracture toughness K_C is expressed in terms of the critical stress intensity factor [MPa.m$^{1/2}$] governing the propagation of a material defect [44]. Depending on the origin of the tribomechanical solicitation, distinct fracture networks appearances will develop. Under tribological solicitations (see Figure 2.10), the typical damages are the creation of cracks in the coating having characteristic morphologies which depend on the sharpness of the contact similarly to the deformation damages. For a sharp contact, median and lateral cracks developing directly under the contact area are expected, while ring cracks surrounding the contact area are typically observed for a blunt contact (see Figure 2.10).

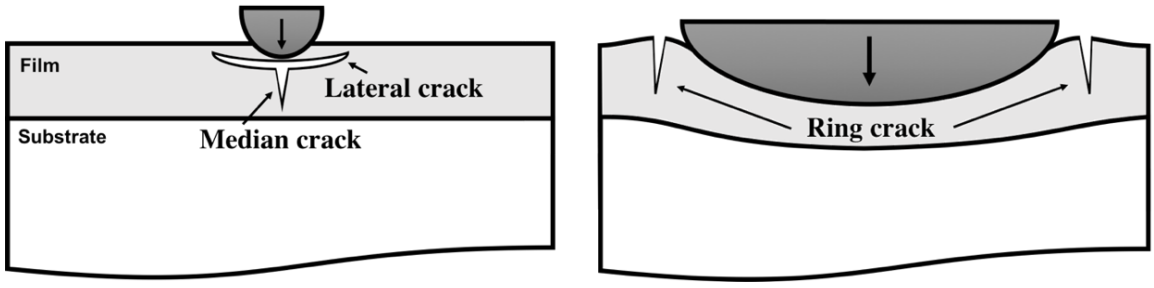

Figure 2.10 Schematic representation of cohesive failures generated in a thin film coating by a (a) sharp counterpart and (b) blunt counterpart.

Cohesive failure can also be initiated and propagated from tensile or compressive structural loads. A typical situation is the propagation of an isolated crack or a channel crack in the film under tensile loads [28]. In the case of channeling, the crack may also penetrate in the supporting material if the stress concentration induced by the cracked coating exceeds the substrate fracture toughness. These three different failure types are presented in figure 2.11.

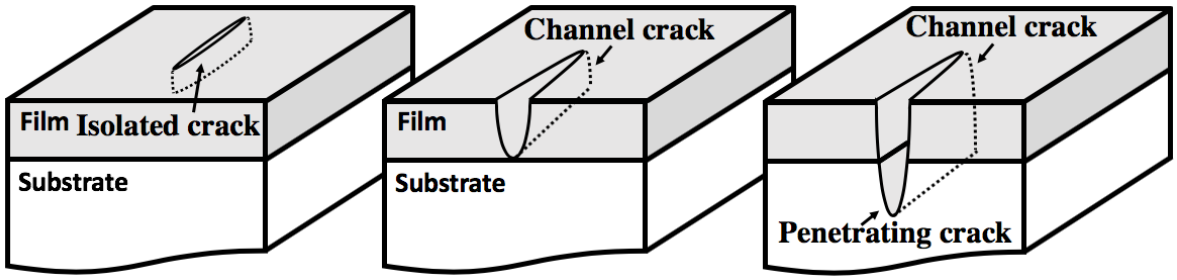

Figure 2.11 Schematic representation of the different failure modes associated with structural tensile stress.

Typically, brittle materials such as ceramics have a low toughness around (~1-~10 J/m^2), ductile metals have high toughness (~10-~100 J/m^2) and polymers may exhibit one or the other extreme behaviors depending on their chemical composition [45].

2.3.2.3 Interfacial

Interfacial failure is defined by the propagation of a crack at the interface between two different materials. In the current context and for ease of presenting the concepts, we will assume a single layer film and its supporting substrate. Under harsh tribological conditions, the difference in elastic properties between both materials induces significant shear stresses at the interfaces responsible

for delamination of the film [46]. Likewise, as in the cohesive failures, the fundamental mechanism in action here is the breaking of the bonds forming the interface between the materials and, it is thus driven by an interfacial toughness expressed in terms of surface energy [J/m^2]. Presented in figure 2.12 are the typical failure modes associated with a tribological contact inducing stress concentration exceeding the critical value of interfacial toughness.

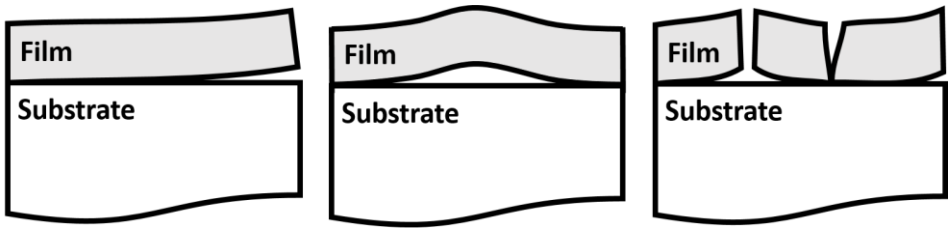

Figure 2.12 Schematic representation of interfacial failure modes induced by tribological contact. (a) Edge delamination, (b) buckling, and (c) combination of both mechanisms.

Comparable situations arise under structural load conditions; in such cases, the typical post-mortem observations are partial delamination accompanying the propagation of a channel crack under tensile loads, and buckling of the film under compressive loads as schematically presented in Figure 2.13.

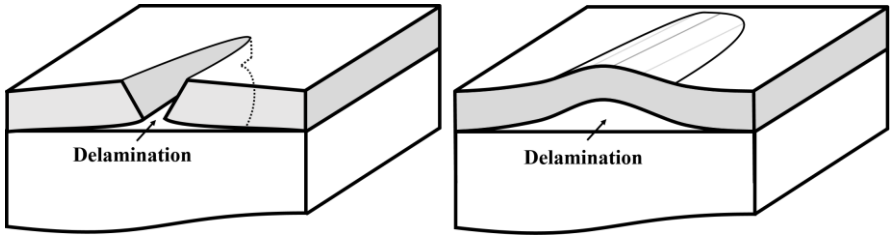

(a) (b)

Figure 2.13 Schematic representation of interfacial failure modes induced by structural (a) tensile and (b) compressive loads.

2.3.3 Wear categories

2.3.3.1 Brinelling

Brinelling appearance is recognizable from the permanent indents left in the surface, which may be or not accompanied by cohesive and/or adhesive failure of the film in the contact area (see

Figure 2.14). The yield stress (or hardness) of the surface define its resistance to permanent deformation. For bulk materials, as the hardness is increase, so is the resistance to brinelling damages. In the case of coated material, the resistance to brinelling depends on the load carrying capacity of the system for the specific tribological conditions the surface is subjected to. For very thin films, or blunt counterpart the load that the coating can sustain is limited and important plasticity may develop in the substrate. Depending on the brittleness of the coating, radial or ring cracks are created due to the excessive tensile stresses engendered around the contact area. In those cases, there are different solutions to increase the load carrying capacity of the whole system; increase the surface coating thickness, use a hardening treatment on the substrate prior to deposition or deposit a thicker intermediate coating which function is to limit plastic deformation from reaching the substrate.

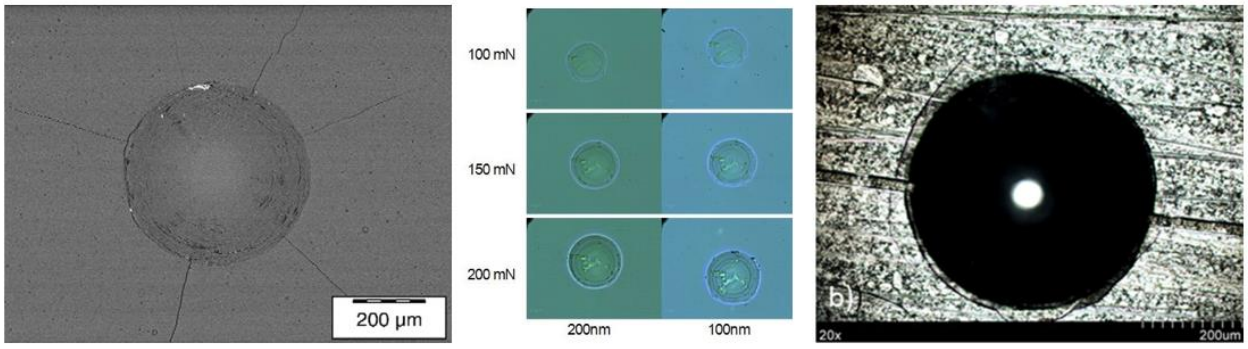

Figure 2.14 Brinelling wear in a coated material with (a) radial and ring cracking [47], ring cracking in the contact area only [48] and (c) ring cracks around the contact area [49].

2.3.3.2 Abrasion

Abrasion wear is a result of the asperity scale contact conditions caused by the inherent roughness of material surfaces (A visual representation is shown in figure 2.15). The resulting abrasive wear is the outcome of the cumulative effect of such contact, often resulting in the formation of parallel wear grooves. The resistance to permanent deformation of the asperities depends on the hardness of the surface and their subsequent failure, and the removal is governed by its toughness. The incorporation of wear debris in the abrasion area also often contributes to increasing the wear rate.

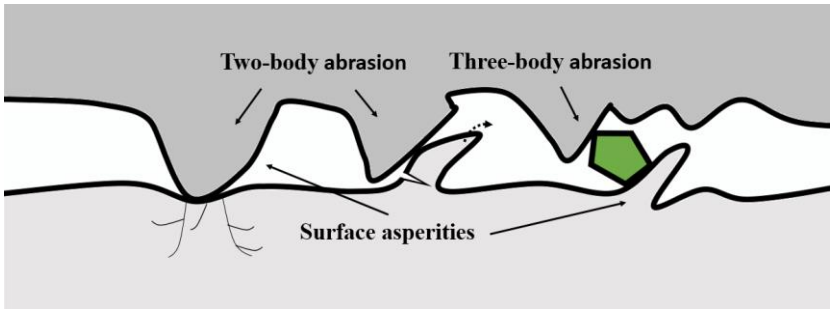

Figure 2.15 Schematic representation of abrasive wear at the surface asperity scale.

Surface hardness is traditionally the most important parameter predicting the resistance to abrasion for bulk materials (see Figure 2.16 (a)). In coated systems, the relation is more complex. and it involves roughness, thickness, hardness and toughness as the main parameters governing the abrasion resistance (see Figure 2.16 (b)).

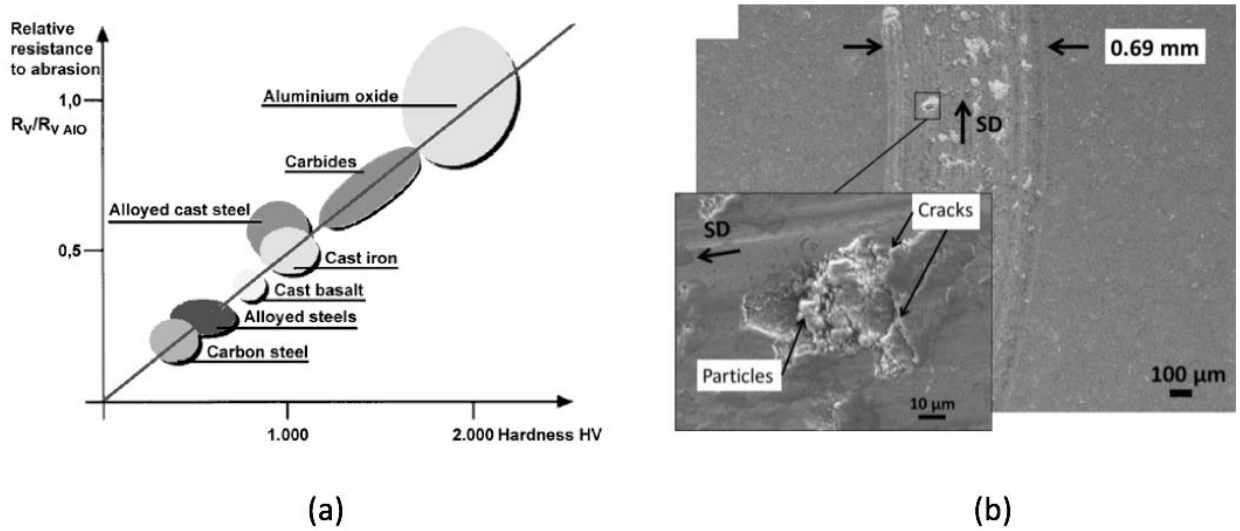

Figure 2.16 Linear dependence of the resistance to abrasion as a function of the surface hardness for different bulk materials. Surface showing sign of two bodies and three bodies abrasive wear [50].

2.3.3.3 Erosion

Erosion wear occurs from the repeated impact of micro particles on the surface. In many ways, the cumulative impacts of those particles reproduce a wear condition similar to abrasion (see Figure 2.17). One noticeable difference is the absence of sliding grooves and the surface which produces

a more evenly worn surface (see Figure 2.18 (a)). Another subtility is that in erosion conditions, the impacting particles are often described by a typical size distribution which is narrower than the asperity size distribution in abrasive wear, meaning that it is easier to predict the wear rate. Typical solution to protect surfaces against erosion is to deposit a hard-protective coating with sufficient thickness to confine the deformation field inside the film. Using this design criterion, it was observed that for similar erosion wear conditions, the hardness of the protective coating is the main parameter predicting its erosion resistance (see Figure 2.18 (b)).

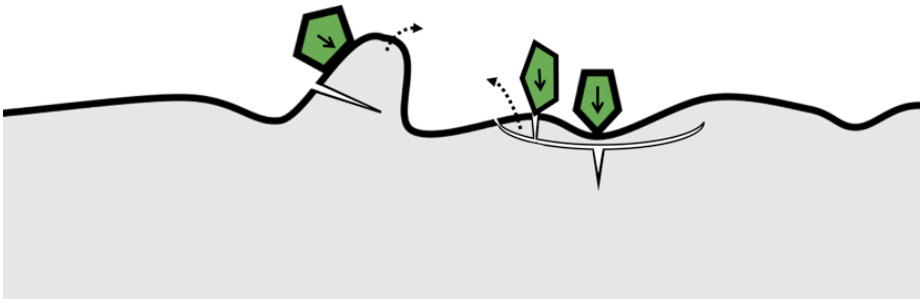

Figure 2.17 Schematic representation of the erosion mechanisms leading to material removal.

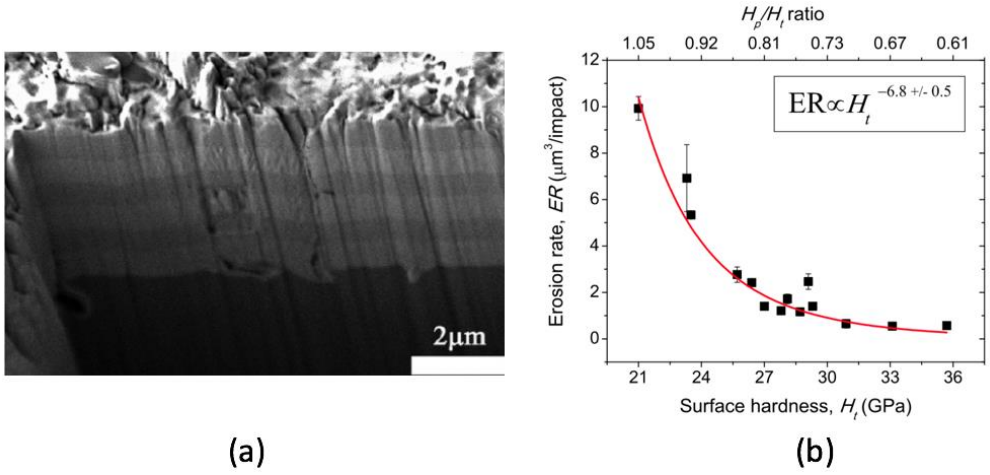

Figure 2.18 (a) Surface micrograph of a multilayer coating subjected to solid particle erosion, and (b) influence of a hard coating surface hardness on the erosion rate [32].

2.3.3.4 Adhesive

Adhesive wear is a consequence to the tribological condition shown in figure 2.7 (e). It is activated by the adhesive friction caused by the molecular bond formed at the junction of contacting materials (see Figure 2.19). The stronger that bond is, the more difficult it will be to shear such that

the failure may not occur at the contacting point but by cohesive failure of the contacted surface. The most typical case of adhesive wear happens when a hard counterpart contacts a softer metallic surface or when there is a metal-metal contact [51].

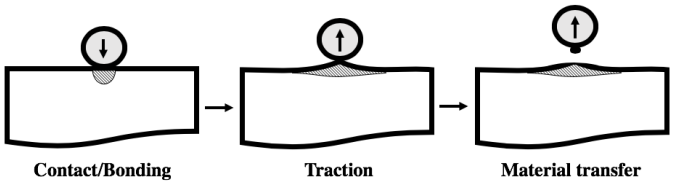

Figure 2.19 Schematic representation of adhesive wear process.

2.3.3.5 Fatigue

The use of thin film coatings is often related to a decrease of performance for structural components subjected to failure by fatigue. This subject is a vast area of study and all the intricacies have yet to be understood; however it is believed that the main factor leading to the decrease of fatigue life is the stress concentration generated by the premature failure of the surface coating [52]. On the other hand, in the case of fretting fatigue, a hard protective coating has been shown to enhance fatigue resistance since it will limit surface damages responsible for the initiation of a fatigue crack (see figure 2.20).

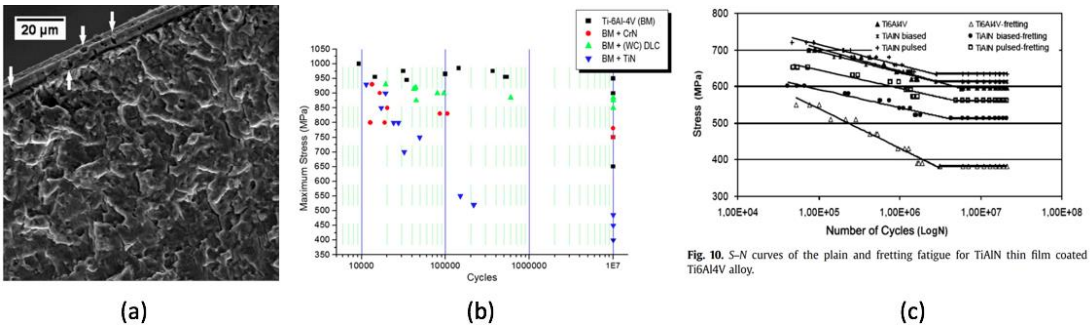

Figure 2.20 (a) Fatigue fracture surface showing sign of initiation in the coating [52]. (b) Example of axial fatigue strength decrease with different coatings [52], and (c) increase in fretting fatigue life [53].

2.3.3.6 Film fracture pattern

Film fracture patterns result from severe mechanical loads, thermal stresses or residual tensile/compressive stresses and can exhibit numerous visual appearances. For films under tensile

stress, the formation of parallel channel cracks is the most common observation as shown in Figure 2.21 (a). Due to the Poisson's ratio effect, the stress in the direction transverse to the load will be compressive and bucking failure may follow for extreme loads (see Figure 2.21 (b)). These types of failure are greatly influenced by the microstructure and intrinsic defects present in the films that leads to peculiar crack patterns as shown in figure 2.22.

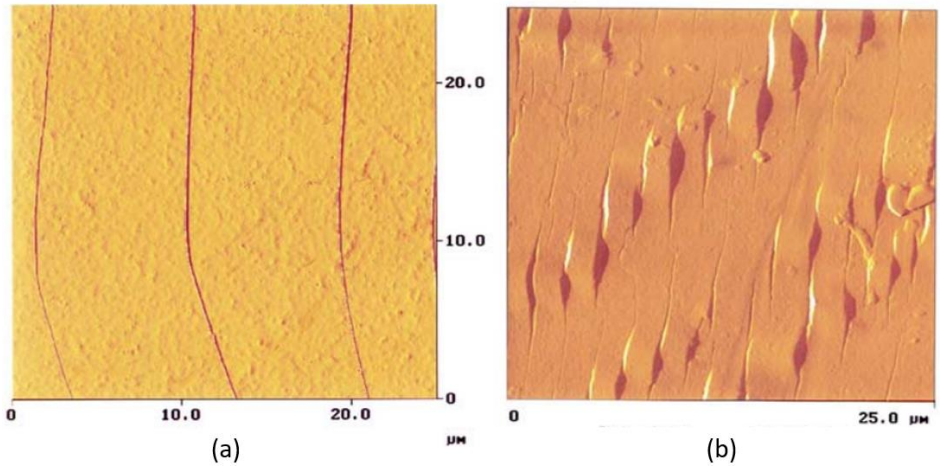

Figure 2.21 Film under uniaxial tension showing sign of (a) channel cracking, and (b) transverse buckling [54].

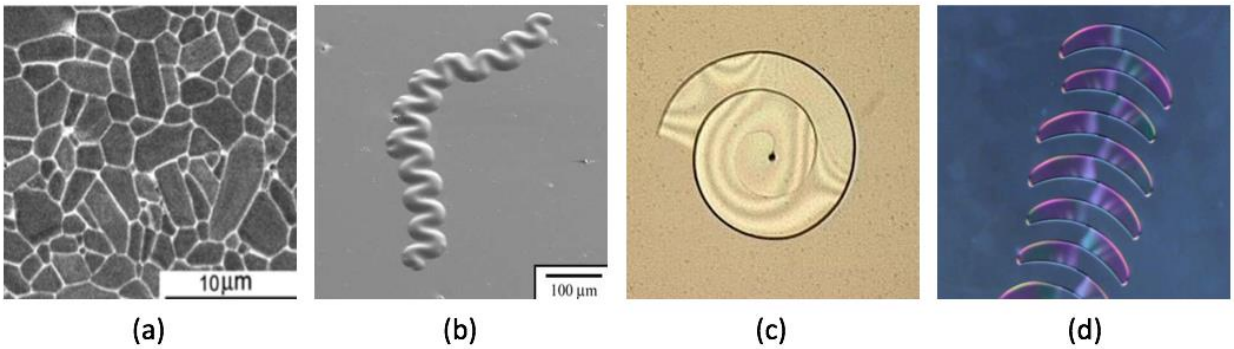

Figure 2.22 Crack patterns in thin films under structural tensile/compressive stress. (a) Crazing [55], (b) Telephone cord buckling [56], (c) Archimedean spirals [57], and (d) Long oscillating alleys [57].

2.4 Design of coating architectures

Throughout the past decades, with the advancement of thin film coating deposition processes, the design of protective coating architecture has become a subject of prime interest. Traditionally, single layer films were deposited to fulfill all the functional requirements for the targeted tribomechanical conditions. However, in the majority of the cases, without a strong predictive model, it is more appropriate to design multilayer films in which every single layer serves a specific tribomechanical function. This multifunctional multilayer representation is schematically presented in Figure 2.23. It is important to note that even though they are represented as single layers in the figure, each of those sublayers may be composed of a more complex substructure (multilayer, laminate, nanocomposite, mechanical gradient).

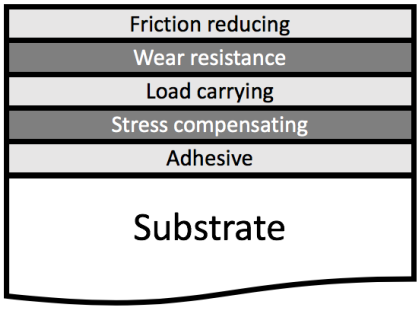

Figure 2.23 Multifunctional architecture representation of tribological coatings.

2.4.1 Adhesive

Adhesion (or bonding) of the coating to the substrate may often be the limiting performance factor, since adhesion failure can lead to delamination and catastrophic failure of the coated system. For this reason, an adhesion layer is often used to increase the bonding of the film to the base material. The choice of this base layer depends on the application requirement and substrate material. Metallic material with good wetting ability and oxidation/metallization (alloying) affinity with the base material are chosen since they will form strong chemical bonds. For this reason, Cr and Ti thin layers are commonly used as bonding layers to improve the adhesion of hard coating on metallic surfaces [17].

2.4.2 Stress compensating

The role of a stress compensating layer is to tune the global stress state in a multilayer film. It is most often used in applications for which the performance target necessitates to control the curvature of the final device. It is used, for example, in Fabry-Perot interference filter for which the parallelism of the optical path enhanced finesse of the filter [58] and its utilization in high precision mirror for astronomical telescopes is indispensable [59]. The stress compensating layer can also have a purely mechanical role to reduce the tensile stress and channel crack formation, or alleviate the compressive stress in weakly adhering films which are prone to failure by buckling [39].

2.4.3 Load carrying

To shield the base material against plastic deformation, the stress field reaching the substrate originating from a tribological contact must be diminished to a level below its yield point. Depending on the requirement of the application, using a hard-protective coating may not fulfill this condition, and a thicker load carrying layer has to be introduced in the design. The function of this layer is twofold, first to protect the base material from permanent deformation and secondly to support the top hard coating against excessive deformation and bending that can induce ring cracking. The required thickness depends on the sharpness of the tribological contact. The sharper the contact, the more confined to the surface the stress field will be, and thus thinner the load carrying layer is needed. For a blunt counterpart, the thickness of this load carrying layer must be increased since the maximum shear stress location will move deeper under the surface toward the base material. Since the load carrying capacity is condition dependent it is not possible to quantify in a general way. In some cases, a hard coating such as TiN can achieve the requirement [60], while in other cases thick HVOF coating [61] or substrate surface hardening treatment has to be used [62] to create a thicker hardened interlayer.

2.4.4 Wear resistance

The wear resistance is often the most desired aspect of a tribological coating. For a coating to be wear resistant, it means that it is resilient to plastic deformation and crack formation, which indicates that hardness and toughness are the prime parameters required for high wear resistance.

As a matter of fact, the highest performing solutions are hard coatings that exhibit ultra-high hardness, which limit the asperities and global contact deformation, while having sufficient toughness to not be overly brittle [63]. Over the years, it was shown that this anticipated combination of properties is reflected by the readily assessable H/E ratio [64]. The most successful materials to date have been ternary and quaternary TiN-based (TiSiN [65], TiAlN [51], TiSiCN [66], TiAlSiN [67]) and CrN-based materials (CrSiN [68], CrAlN [51], CrAlCN [69]) . For applications necessitating transparent materials, Si_3N_4 [70], SiO_xN_y [71], AlSiN [72] and DLC [73] are recognized as having high wear resistance.

2.4.5 Friction reducing

Friction is not a fundamental property of materials, it is in fact a response of the system to the tribological conditions in relation with the material properties and surface morphologies of both bodies in contact. Friction forces originate from three fundamental contributions; shear resistance, ploughing/deformation, and adhesion forces. Taking an holistic view on friction of coated materials, studies indicate that roughness, hardness, ductility, shear strength, tribofilm layer formation and material transfer are the main driving forces involved in the measured coefficient of friction [74]. In the search for low friction coating, limiting the shear resistance in the contact area was shown to be the most effective way to reduce friction forces. For example, DLC low friction originates from the graphitization in the contact area that creates planes with low interfacial strength such that they may glide on top of each other with very low shear resistance [75]. MoS_2 is another widely used material; in this case, the lamellar structure having low shear strength between the atomic layers is responsible for the very low shear resistance contribution to the coefficient of friction [76].

2.5 Influence of microstructure on the wear behavior

The microstructure of coatings directly reflects on their ability to protect against specific kinds of damage. Consequently, to design a wear resistant coating, it is also important to consider the microstructure of each layer and the manner how this microstructure interacts with a propagating crack. For example, when modeling multiphase materials with vastly different mechanical properties, regions of high stress may be induced and be responsible for particular wear

mechanisms such as interphase delamination or localized plasticity. In figure 2.24 we present a contact model of a multiphase surface with mismatching elastic properties. We can see that the stress field is heterogeneous with zones of high stress forming around the interfaces. Once we understand the wear mechanisms, we may be able to adapt the deposition process to grow a material with an enhanced microstructure to protect against those types of damage.

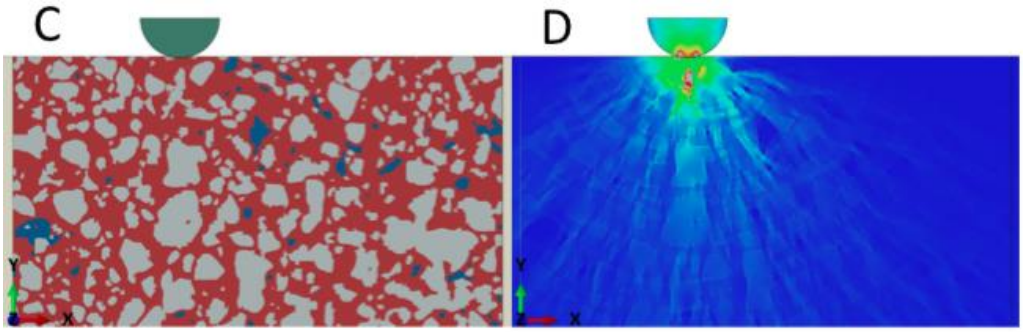

Figure 2.24 Indentation stress distribution by a finite element indentation model taking into account the microstructure of a multiphase thermal spray coating [77].

Porosities, lamellar or columnar structures, multiphase materials and polycrystalline materials are all examples of microstructural features that have a direct effect on fracture initiation and propagation in the material. Presence of porosities and void in a material creates stress risers which may be responsible for the initiation and propagation of the defect. It can be seen that materials with high porosities also suffer in terms of fracture toughness which is reduced as the amount and size of porosities increase in the material [78]. Columnar thin film coatings have a tendency to fail along the columns interface due to high stress concentration [79]. Lamellar structures, such as thick coatings deposited by thermal spray process, has similar weaknesses. In this case, the interfaces between splats can contain oxide inclusions and voids which act as damage initiation areas leading to wear by splat delamination and removal [80] (see Figure 2.25). Another notable example is the effect of hard and tough particles embedded in a ductile matrix. In these materials, the crack direction will be deflected around those particles, which may increase the apparent toughness of the material by increasing the effective length of the crack path [81]. This effect is central to understand the high wear resistance of ceramics/metals nanolaminates under contact loads in which the cracks are deflected into the ductile phase, and their propagation toward the substrate is

impeded. A general review of how the cracks interact with the microstructure and how it modifies it as it propagates can be found in the literature [82].

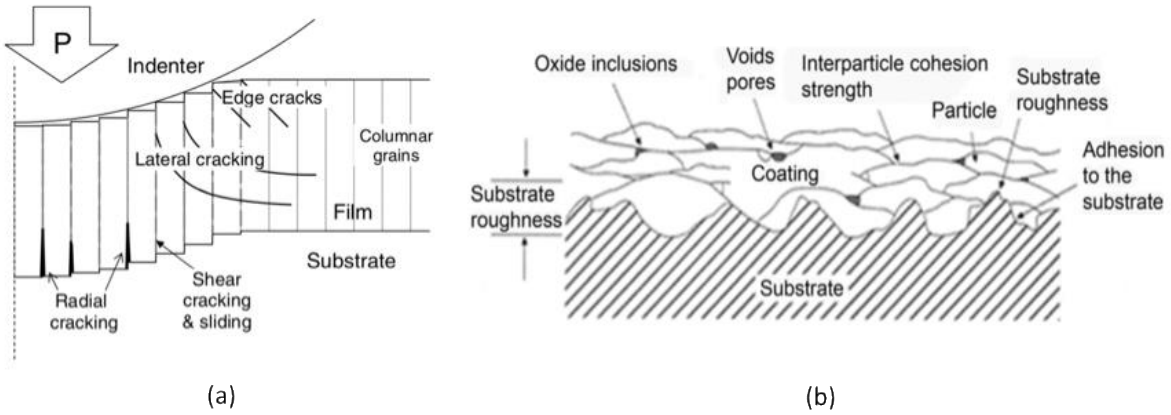

Figure 2.25 Schematic representation of (a) failure modes in a film with columnar structure under indentation loads [79], and (b) the microstructure of a thermal spray coating [80].

In the next section, we will introduce the field of bio-inspired materials and mention specific microstructures that can be mimicked to further increase the toughness of engineered materials.

2.6 Bio-inspired coating design

From a design standpoint, it is often advantageous to start from an established solution and from this starting point iterating modifications can be introduced to optimize the component performances. In this context, we are traditionally looking at the engineered materials as the starting point; however, in the past decades, bioinspired designs, which use naturally occurring materials as the design foundation, have become an extremely active field of study. The main reason for this ever-increasing interest are the exceptional mechanical properties of biomaterials whose behavior cannot be explained using simple macro-scale observations. Those properties emerge from the synergistic interaction of a complex sub-structure that we are only recently able to observe with the evolution of nano-scale imaging tools. Mimicking this hierarchical structural architecture allows one to develop materials with properties far greater than those of the individual components. In particular, the toughness enhancing mechanisms demonstrated by such materials have been shown to be very efficient to limit the crack propagation for tribological applications.

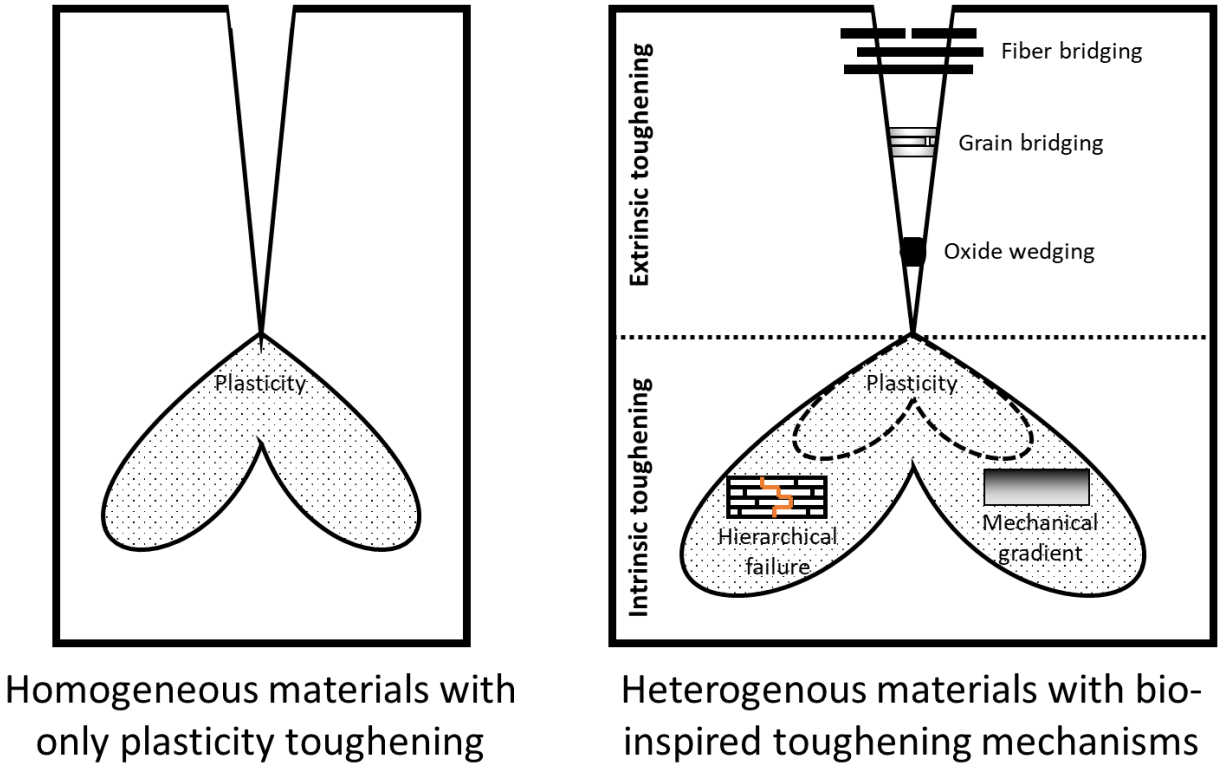

Figure 2.26 Comparison between the classical fracture mechanics viewpoint and fracture mechanics toughening mechanisms for advanced materials.

In the traditional fracture mechanics view, material homogeneity and crack faces free of traction are part of the basic assumptions (see Figure 2.26). In reality, for materials with complex microstructures other mechanisms may come into action; the main ones are illustrated in figure 2.19. They are divided into two categories, intrinsic ones occurring inside the material behind the crack front, and extrinsic mechanisms occurring in the fracture area [83]. Bones and wood are great examples for which extrinsic mechanisms through fibers and ligaments bridging across the crack are the origin of their high toughness [83]. That mechanism is exploited in metal-ceramic composites where the metal phase, having higher ductility, acts to shield the crack opening by an extrinsic bridging mechanism [84]. Intrinsic toughening by hierarchical failure has been vastly studied for nacre; in this case, friction between the platelets and crack deflections increase energy dissipation and are responsible for the enhanced toughness [85]. Teeth and bamboo (see Figure

2.20) are two typical materials displaying mechanical gradients associated with the reduction of the stress intensity factor for surface defects thus making them highly resistant to crack propagation [86]. Functionally graded coatings have demonstrated this same ability and display high resistance to damage from contact loads [87], [88]. However, the resistance to micro particle impact have yet to be sufficiently studied to become exploitable and this is the main reason why it was investigated as part of this work in Chapter 6.

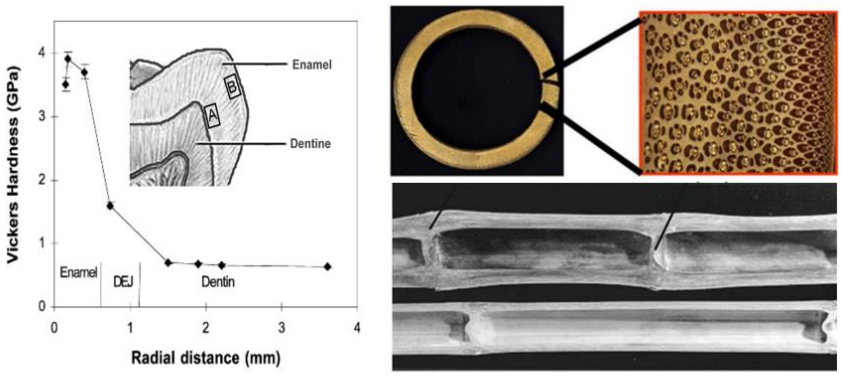

(a) (b)

Figure 2.27 Functionally graded structure of (a) Human teeth [86] and (b) Bamboo [88].

CHAPTER 3 NUMERICAL METHODOLOGY

The development of solid mechanics theory and numerical modeling have allowed a tremendous technological jump in many branches of engineering. For example, civil, mechanical and aerospace engineering all benefit from numerical analysis in such a way that it has now become a fundamental component of the design. While the pyramids may have been built without the help of a numerical model, it is nowadays impossible to imagine realizing such a feat for modern skyscrapers like the Burj Khalifa. Lately, the same can be said about nanotechnology engineering, for example, in the field of microelectronics, microelectromechanical systems, microfluidic devices, and the subject of this thesis, the study and predictive modeling of the tribomechanical response of thin film coatings.

To define what is solid mechanics we first need to define what is a solid. It can be defined as a material that can support normal and shear forces. A solid will then be able to support its own weight if suspended from its upper surface over a large time scale, while on the contrary, a fluid low shear resistance will only offer short time stability governed by its viscosity. To better grasp this time scale view difference between solid and fluid, we can think about the earth crust. On a short time-scale, its behavior is clearly one of a solid, but over a few million years the mantle and tectonic plate behavior are much more representative of a fluid. Most evidently, the constitutive laws governing the material response to loads and deformation is only one of the fundamental components required to model structural and mechanical behavior. Accordingly, we will introduce the numerical approaches that were exploited in this work to model the tribomechanical properties of the different case studies.

3.1 Continuum mechanics

Continuum mechanics is a theoretical framework which assumes that the physical and mechanical properties inside a deformable material vary in a continuous way. Its development was sparked by the formulation of the laws of motion by Newton, and its modern mathematical representation was first put into place by Cauchy in the early nineteenth century [89]. Nevertheless, the bases of continuum theory are still appropriate for modeling modern structural and tribomechanical problems. The most famous and widely used numerical approach to solve its governing equations, the finite element method, was initially developed by the aerospace industry in the 1950s [90].

While Cauchy may not have known about the atomistic nature of materials, we may ask ourselves why would engineers still to this day universally use the continuum approach instead of numerical methods calculating forces between atoms and molecules to predict stresses and deformations. For example, molecular dynamic has been used previously for the study of nanotribology phenomenon [91], and ab-initio calculations are commonly used for the theoretical assessment of the elastic constants for crystalline materials [92], [93]. The answer is undeniably related to the prohibiting computational cost associated with using atomistic models over the time frame and spatial dimension involved in the tribomechanical conditions related to this study and engineering design in general. Other non-continuum methods, including smoothed particle hydrodynamics [94], discrete element method [95], peridynamics [96] have been shown to be applicable to study deformable materials at a time scale similar to those achievable with the finite element method. Even though these methods prime motive for existence is to transcend continuum mechanics limitations, they have yet to mature sufficiently to be applied in an industrial context. Over the last decades, constant developments were introduced to fix finite element inherent limitations associated with the continuum mechanics assumptions. Contact modeling [97], numerical fracture mechanics [98], cohesive zone model [99], extended finite element method [100], strain-gradient plasticity [101], non-local damage theory [102], and crystal plasticity [103] are all examples of modern use of continuum mechanics that enable realistic microstructure-based modeling.

3.2 Finite element method

The finite element method is a numerical procedure developed to solve systems of partial differential equations across an arbitrarily shaped discretized domain. Its primary application by a large margin is its utilization in the context of solving continuum mechanics problems. Over the years the community adopted the denomination finite element modeling (or finite element analysis) as a shortcut to designate this application of the finite element method. Even though a complete presentation of the method is well beyond the scope of this work, we will nonetheless introduce the theoretical framework in such a way that an uninitiated reader may follow this document without great difficulty.

3.2.1 General principles

The fundamental principle of the finite element method is to substitute the infinite dimensional problem of continuum mechanics, for which we can only get analytical solutions for simple geometries and linear conditions, by a discretized domain (mesh) with interconnected elements approximating the solution. This subdivision into elements serves as the basis to the global solution, and obtaining the resulting deformation for those is a much simpler problem than trying to obtain the exact solution for the whole system at once. Depending on the type of analysis, each element is characterized by different parameters (elastic modulus, yield stress, coefficient of thermal expansion, electric conductivity, …). The final solution is then obtained by assembling the results from those sub-elements. The elements deformation is governed by an interpolating shape function, which can be of linear forms or higher order depending on the formulation. Following the deformation of those elements compared to their initial shape allows one to calculate engineering results such as stress, strain, and plastic deformation. If inertial effects are taken into account, the nodes of those elements will also contain a velocity and acceleration components which are required to follow stress wave propagation and estimate derivatives of the engineering results such as the strain rate.

3.2.2 Governing equations

In solid mechanics problems, we generally wish to solve the momentum equation, which may be expressed by the following relation under static equilibrium conditions.

$$\sigma_{ij,j} + \rho F_i = 0 \tag{3.1}$$

σ_{ij} is the Cauchy stress tensor representing the internal forces acting on a unit volume, ρ is the density of the body and F is the external force acting on the volume. This equation represents the force equilibrium for a discrete volume element. The solution is obtained by solving this equation with respect to the geometry and traction boundary conditions. In contrast, for dynamic problems, the right-hand side doesn't cancel and contains an inertial term, which leads to the following relation.

$$\sigma_{ij,j} + \rho F_i = \rho \ddot{u}_i \tag{3.2}$$

In this relation, $\ddot{u}$ is the discrete volume acceleration. Similar to the static equilibrium situation, the solution emerges from the imposed boundary conditions, and in this case also from the initial inertial conditions.

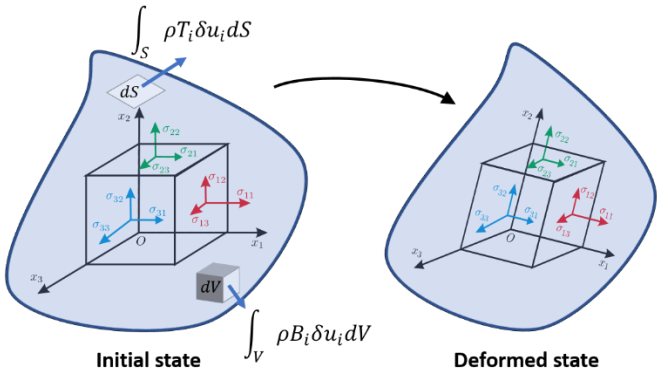

Figure 3.1 Schematic representation of the virtual work principle acting on a unit volume element.

Equation 3.1 and 3.2 are not, as they are represented here, suitable to be solved numerically and need to be discretized to apply the finite element method to a whole component. The virtual work approach is usually applied to realize this discretization. It is based on the principle of least action, which states that among all the virtual displacement possible δu_i that a material point may take in reaction to an infinitesimal strain variation $\delta \epsilon_{ij}$, there is one that will minimize the action and thus the trajectory that it will follow. The conservation of energy implies that the external virtual work has to be equal to the internal virtual work. In other words, it imposes that the energy transferred to the body by external forces to be equal to the internal strain energy stored in the material (see figure 3.1). This leads to the following equation for static equilibrium problems.

$$\underbrace{\int_V \sigma_{ij} \delta \epsilon_{ij} dV}_{Internal\ virtual\ work} - \underbrace{\int_V \rho B_i \delta u_i dV - \int_S \rho T_i \delta u_i dS}_{External\ virtual\ work} = 0 \tag{3.3}$$

In this relation, B_i is the body force, and T_i is the traction force. From this integral form of the problem, a discretization is applied such that the integrals become sums and consequently the problem is converted to a system of linear equations of the following form;

$$\{F\} = [K(u)]\{u\} \tag{3.4}$$

In this equation $\{F\}$ is the force vector, $[K(u)]$ is the stiffness matrix, and $\{u\}$ is the displacement vector. This equation is equivalent to applying Hooke's law to every individual degree of freedom of the system. The stiffness matrix as the name implied is related to the material mechanical properties, and the dependence on the displacement (u) represents the nonlinearities of the problem. Those nonlinearities originate either from geometric nonlinearity, material nonlinearity or contact nonlinearity. To solve this nonlinear implicit equation and obtain the nodal displacements $\{u\}$, $K(u)$ must be inverted. More details about the solving step will be presented in the next section.

A similar approach can be applied to dynamic problems using the virtual work approach; this leads to the following integral form,

$$\underbrace{\int_V \rho \ddot{u}_i \delta u_i dV + \int_V \sigma_{ij} \delta \epsilon_{ij} dV}_{Internal\ virtual\ work} - \underbrace{\int_V \rho B_i \delta u_i dV - \int_S \rho T_i \delta u_i dS}_{External\ virtual\ work} = 0 \tag{3.5}$$

After discretization, by transformation of the integral form to a summation over every degree of freedom, we obtain the following relation.

$$[M]\{\ddot{x}\} + [C]\{\dot{x}\} + [K]\{x\} = \{F\}, \tag{3.6}$$

where $[M]$ is the nodal mass matrix, and $[C]$ is the damping matrix. For both formulations, an important aspect to note is that when a node of an element is displaced, it will pull the other nodes of the element and those other nodes resulting displacements are interpolated accordingly to the specific element formulation and material constitutive relation. The development of different element formulations, with respect to their degrees of freedom and shape function polynomial order, is a significant field of study in itself. For more information about this subject and details about the static and dynamic finite element formulation, we refer the reader to the available literature [104], [105].

3.2.3 Finite element solvers

Many algorithms are available to solve the set of matrix equations and the most suitable ones always depend on the characteristics of the model. Solvers are divided into two categories, implicit solver and explicit solvers. Implicit solvers are generally used to solve for the displacement and as such are more suitable for static problems. For nonlinear static problems, iterative implicit solvers are required since the stiffness matrix $K(u)$ may be quickly evolving throughout the loading phase, and solving for the displacement with the initial stiffness matrix $K(u(t=0))$ would not capture the nonlinearities of the evolving stiffness matrix. The general approach of those solvers is to rewrite equation 3.4 in the following way for the iteration *t*,

$$\{R\}_t = [K(u)]_t\{u\}_t - \{F\}_t, \tag{3.7}$$

where $\{R\}_t$ is the residual force vector at step *t*. A guess solution is trialed for the displacement $\{u\}_t$, and iterative optimizations are applied until the solution converges to a residual force below the tolerance required by the model. The Newton-Raphson algorithm is generally used since it's a low computational approach with quadratic convergence.

An explicit solver is preferred when dynamic effects are to be considered such as ballistic impacts events or when strain rate effects are non-negligible. The explicit solver is always iterative, and using the initial conditions at step *n* will solve for the acceleration at step *n+1*. Using this acceleration, the velocity at n+1/2 is calculated and using a leapfrog integration the new position at *n+1* is obtained. To adequately model the dynamic effects, the fastest transient phenomenon needs to be resolved, which imposes a maximum value on the integration time step. This time condition is known as the Courant time step and is related to the time taken by a mechanical wave to travel across the smallest element of the model [106]. This often leads to very small time steps which limit the time-scale over which dynamic finite element models might be performed. The choice of the adequate solver and its parameters is an essential step to ensure the numerical accuracies of the solution. Section 3.5 will detail the specific considerations, and cares that are required to verify and validate the different finite element models that are part of this work.

3.2.4 Contact modeling

The basic contact modeling approach consists of two steps, first, contact detection and second, applying the contact force. The contact detection algorithm tracks the positions of nodes and elements edge that may potentially be contacting. Once contact is detected, a counteracting force is applied to push back the penetrating bodies resulting in a contact force. The governing equations presented in the previous section need to be corrected since they do not inherently treat contacting bodies problems. In those problems, the contacting bodies may be treated as an external contact force F_c such that the systems of linear equations become,

$$\text{Static: } \{F\} - F_c(u) = [K(u) + K_c(u)]\{u\}, \tag{3.8}$$

$$\text{Dynamic: } [M]\{\ddot{x}\} + [C]\{\dot{x}\} + [K + K_c]\{x\} = \{F\} - F_c \tag{3.9}$$

where $K_c(u)$ represent the nonlinear contact stiffness. In practice, the contact model is equivalent to adding stiff springs in between contacting surfaces (see figure 3.2). The stiffness k_c of those springs is the most important parameter; ideally the contact stiffness would be infinite to eliminate the interpenetration δ_p, but contact stability and solution convergence are compromised as the stiffness becomes too high. In the penalty-based contact approach, the normal contact force is of the following form.

$$F_N = k_c \delta_p \tag{3.10}$$

The appropriate choice of k_c depends on the extent of load increment between integration steps, on both material properties, and the interpenetration tolerance requirement of the problem.

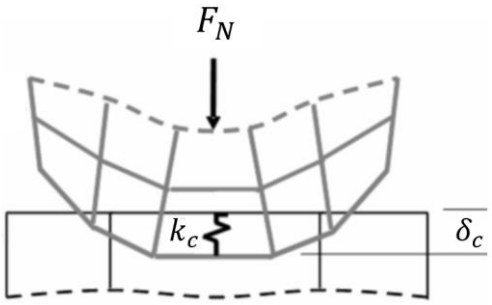

Figure 3.2 Penalty based contact model.

Another approach to contact modeling is the penalty multiplier method (also known as the augmented Lagrange method). It consists in adding a Lagrange multiplier term λ_c to the normal force; in this formulation the normal force is given by

$$F_N = k_c \delta_p + \lambda_c \tag{3.11}$$

The augmented Lagrange method iteratively adjusts the term λ_c such that contact force F_N results in an interpenetration lower than the specified tolerance. This method often results in much lower interpenetration δ_p than the penalty-based method. However, the farther the initial stiffness k_c and λ_c are from generating the correct force, the more iterations the method will take to converge. Thus, the computational cost of this method is generally higher than the penalty-based contact model.

3.3 Fracture mechanics

This section will introduce the mathematical frameworks of computational fracture mechanics with a focus on the methodology that was employed in our current investigation. Mainly we ask to answer the following question: How can we use a finite element model to estimate the critical loads leading to the propagation of a pre-existing defect. The critical loads always depend on the specific tribomechanical solicitation since different solicitations will dictate the level of stress concentration induced at the crack tip.

3.3.1 Fracture modes

The propagation of cracks is divided into three independent modes, which are more or less solicited depending on the loading conditions. Those crack opening modes are presented in figure 3.3.

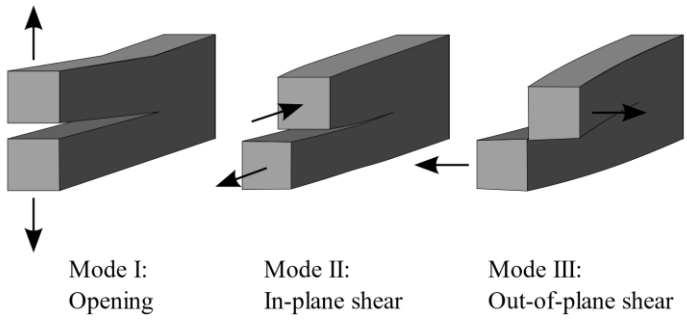

Figure 3.3 Basic modes of fracture.

The propagation of a crack in a body can be interpreted by the weighted superposition of those three basic modes. **Mode I** is the opening mode (also known as the tensile mode), and the crack faces opening is perpendicular to the crack plane. **Mode II** is the in-plane shear mode (or the sliding mode) and is characterized by crack faces displacement normal to the crack front and is solicited by in-plane shearing loads. **Mode III** fracture, often named the tearing mode since it is similar to how we are used to tear paper, is solicited by out-of plane-shear loading.

3.3.2 Stress intensity factor

The most widespread method to characterize the magnitude of stress concentration at a crack front is through the concept of the stress intensity factors $K_m (m = I, II, II)$ introduced by Irwin in 1957 [107]. These stress intensity factors arise from the near-crack tip approximation of Westergaard's stress field solution [108] around a central crack in an infinite plate. The near crack tip singular stress field is scaled by this factor K_m, which leads to the following relation expressed in polar coordinates (see figure 3.4):

$$\sigma_{ij}(r, \theta) = \frac{K_m}{\sqrt{2\pi r}} f_{ij}(\theta), \tag{3.12}$$

where f_{ij} is a dimensionless factor that is dependent on sample geometry, and r is the distance from the crack tip. The $1\backslash\sqrt{r}$ factor represents the singular behavior of the stress field at the crack tip; the stress intensity factor K_m has units $[Pa.m^{\frac{1}{2}}]$ and encompasses the load and crack length dependence for a specific geometry and mode solicitation. For the central crack example shown in figure 3.4, the loading excites mode I exclusively such that $K_I = \sigma\sqrt{\pi a},\ K_{II} = K_{III} = 0$.

A fundamental hypothesis of fracture mechanics is that materials can sustain an increase in load without defect propagation as long as the maximum stress intensity factor stay below a critical value K_c. This K_c value is known as the fracture toughness and is commonly accessed using plane strain geometries testing. The fracture toughness for plane strain mode loading is obtained when

$$K_I = K_{Ic}. \tag{3.13}$$

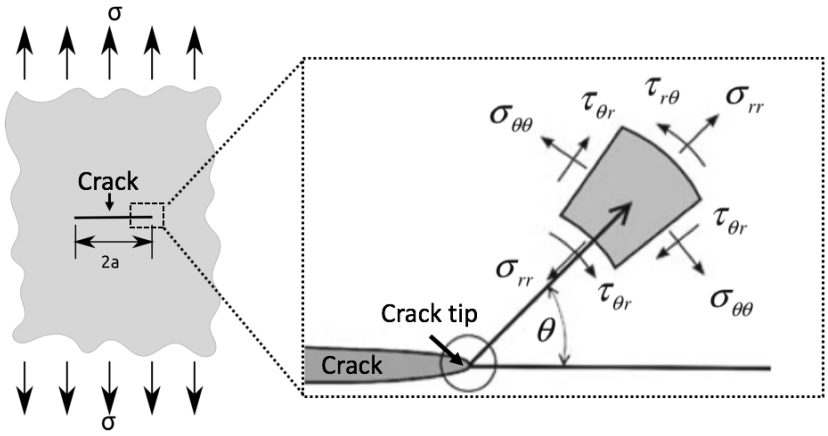

Figure 3.4 Center crack in a semi-infinite plate under uniaxial tensile load and the polar coordinate system used to describe the near crack field [98].

Griffith classic interpretation of fracture is that fracture will occur when the energy release rate, G, of exceeds a critical value G_c. The energy fracture criterion simply reads as follows;

$$G = G_c. \tag{3.14}$$

G has units of surface energy [J/m^2], Griffith derived that for brittle materials this value is equal to the total surface energy of the newly created crack surfaces. In the context of linear elastic materials and for mode I loading, this surface energy is related to the stress intensity factors by the following relation:

$$G_I = \frac{K_{Ic}^2}{E}. \tag{3.15}$$

For mixed mode loading, i.e., when more than one component of K_m is non-zero, propagation criteria have been proposed which take into account the mutual effect of the different stress intensity factor modes contributions. The most common ones are for the case where $K_I, K_{II} \neq 0, K_{III} = 0$, namely the criterion of maximum circumferential stress [109], the criterion of maximum energy release rate [110], and the criterion of strain energy density [111].

3.3.3 J-Integral

The J-Integral is another fracture parameter that has been established and widely recognized to evaluate the crack driving forces responsible for the propagation of a flaw in a material. Its derivation is based on the conservation of the energy-momentum tensor. The total potential energy Π is equal to the sum of the elastic strain energy, and the work of the external forces acting on the material. The energy release rate G is defined by the infinitesimal energy variation $d\Pi$ release by an infinitesimal propagation of a crack da.

$$G = -\frac{d\Pi}{da} \tag{3.16}$$

From this equation, Rice [112] and Cherepanov [113] derived a path integral that converge to G in the framework of linear elastic fracture mechanics. This path integral $\oint J$, named J-integral, is defined by the following relation for an infinitesimal increase of the crack in the x_1 direction (see figure 3.5 for the system geometry):

$$\oint J = G = \int_{\Gamma} \left(W n_1 - T_i \frac{\partial u_i}{\partial x_1} \right) ds, \tag{3.17}$$

where W is the strain energy density, T_i is the traction on the contour boundary, and ds is an infinitesimal arc along the contour.

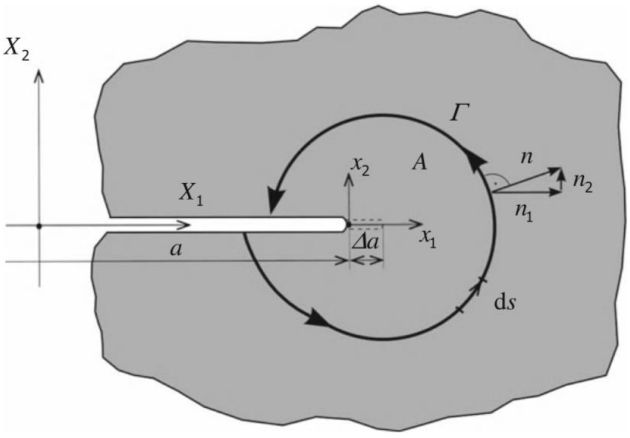

Figure 3.5 Definition of the area and contour in the application of the J-integral around a crack tip [98].

A compelling feature of this integral is that under linear elasticity it was shown to be independent of the area and of the contour path. This property allows the evaluation of G, therefore K, using the far-field solution which doesn't require the high computational cost associated with the calculation of the near crack tip singular field. Path independence has to be verified to validate the model. The virtual crack extension technique is extensively used for the numerical evaluation of the J-Integral for discretized domains [114]. Under mixed mode loading, the different mode contributions can be decoupled using the generalized vectorial form of the J-integral [98].

3.3.4 Introduction to elastic-plastic fracture mechanics

In a ductile material, energy dissipation by plastic deformation has to be accounted for to appropriately characterize the material toughness. The singular field at the crack tip vanishes in the presence of plastic deformation since the maximum stress attainable is limited by the yield stress of the material (see figure 3.6). In this case, it is apparent that the singular field solution does not represent the actual field in the vicinity of the crack tip.

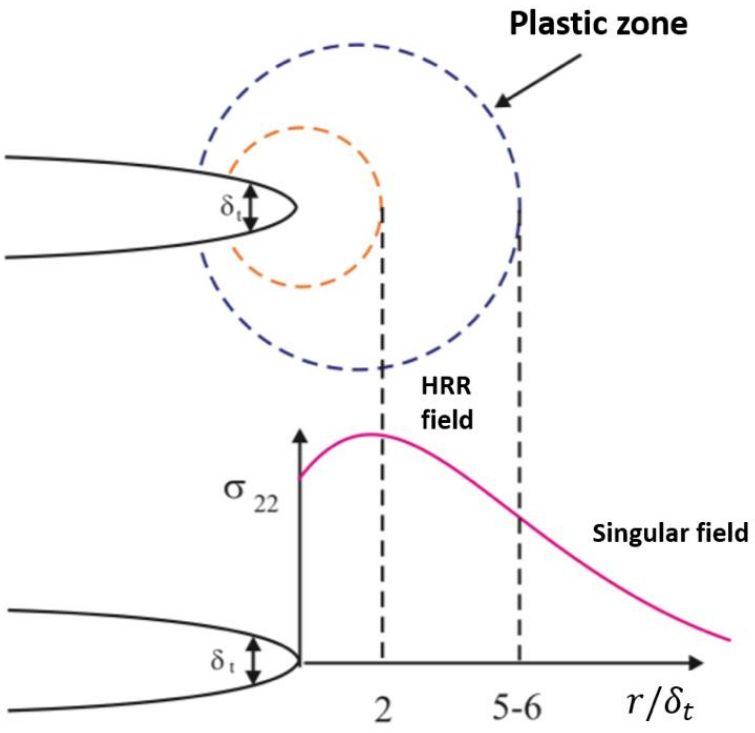

Figure 3.6 Near crack tip stress field in an elastic plastic material [115]

The more important is the extent of the plastic zone compared to the sample size, the more critical will be the deviation of the actual stress field from the singular field solution characterized by the stress intensity factors. This implies that to accurately access ductile material toughness using the linear elastic fracture mechanics theory, the size of the tested sample has to be increased in relation with the ductility level, which may be a limiting factor in some case. Assuming an elastic-plastic power law material behavior, Hutchinson, Rice, and Rosengreen derived a relation for the near crack tip field solution [116], [117]. This solution, named the HRR field, links the plastic HRR field to the singular field. In this HRR region, the J-integral was shown to have an analogous role as the stress intensity factors in the singular K field zone. Using the total strain energy density, including both the elastic and plastic contributions, the value of $\oint J$ constitutes a scaling factor of the HRR field as K was to the singular field. For elastic-plastic materials, under mode I loading, the proper fracture criterion is obtained in terms of J from the following relation:

$$\oint J = J_{Ic}, \tag{3.18}$$

where J_{Ic} represents the fracture toughness expressed in units of $[J.m^{-2}]$.

3.3.5 T-stress

For finite body problems under uniaxial tensile stress (same geometry as in figure 3.4), the Irwin approximation of the singular field requires a modification to take into account the boundary effect. This modification comes in the form of the superposition of a non-singular constant stress term acting parallel to the crack (transverse to the uniaxial load). This term is named T-stress, T_{ij}, and for Mode 1 loading, the near field solution is given by the following relation:

$$\sigma_{ij}(r,\theta) = \frac{K_m}{\sqrt{2\pi r}} f_{ij}(\theta) + T_{11}. \tag{3.19}$$

The constant term T_{11} is parallel to the crack and it modifies the near crack tip field. For an elastic-plastic material, this term results in a modification of the stress triaxiality at the crack tip. If the term is positive, resulting in an additional tensile load, the triaxiality and the plastic zone are enlarged, while the opposite situation occurs for a negative T-stress term. The level of triaxiality

in an elastic-plastic material affects its brittleness. For example, if the triaxiality near the crack tip is increased, a smaller plastic zone will develop, and thus less energy is dissipated by plastic deformation which leads to an increased brittleness behavior of the material.

The finite element and fracture mechanics concepts introduced in this chapter serves as a basic overview of the concepts required to model the tribomechanical behaviors of interest in this study. For more information, in-depth presentation and details about continuum mechanics, finite element modeling and fracture mechanics theory can be found in the literature [16], [98], [118], [119].

3.4 Models verification and validation

Before comparing modeling results with experimental measurements, we need to confirm that they are free of numerical errors due to inadequate parameters. Many parameters such as time step, element formulation, solver parameters, element distortion, material constitutive relations, hourglassing parameters and control of element locking with artificial viscosities need to be considered and accounted for to ensure numerical accuracy of finite element models. Presenting all of those parameters effect is out of the scope of this document; however, we will present specific considerations that relate to the models presented in this study that are often overlooked by finite element analysts.

3.4.1 Domain discretization

The mesh discretization of the domain is one of the crucial aspects that need special attention. To verify that the mesh is sufficiently refined, we can observe that some values of the results converge to a single value as the mesh refinement is improved. As we presented in section 3.4, the singular field around a crack is proportional to $1\backslash\sqrt{r}$, which implies that as the mesh is refined around a defect singularity, the field will increase without upper boundary. The singular field is then evidently not appropriate for this verification. The global strain energy density and the maximum non-singular stress are more suitable as their values will converge toward the exact solution as the element characteristic length is reduced (see figure 3.7). To reach the non-singular field exact solution, local refinement of the mesh has to be made in areas where stress gradients are more important.

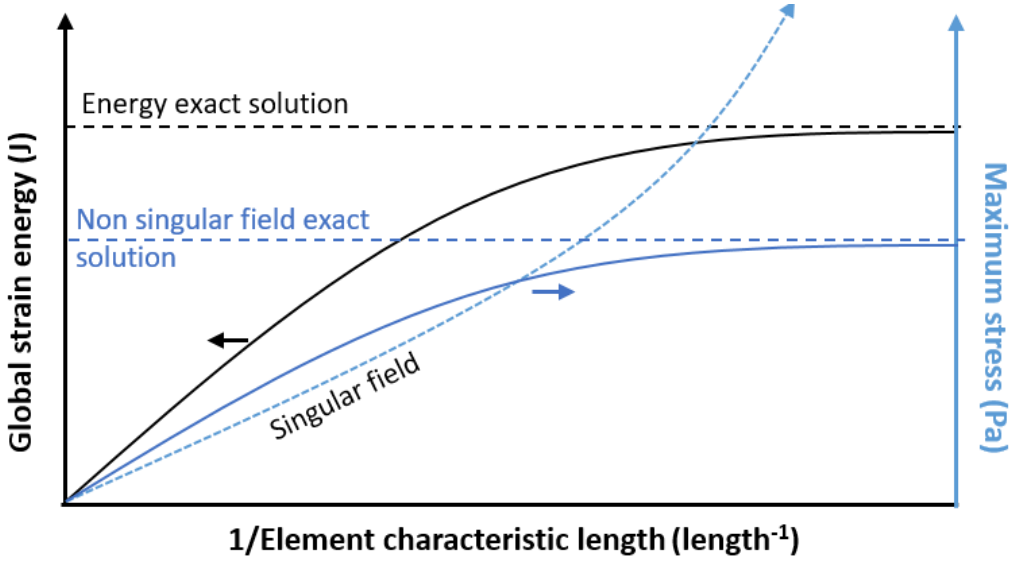

Figure 3.7 Schematic evolution of the strain energy, non-singular field maximum stress, and singular field maximum stress as a function of mesh refinement.

3.4.2 Boundary conditions

Boundary conditions are of two main types: first, the constraints conditions which represent physical boundaries that prohibit displacement in one or multiple axis directions representing a rigid wall or support. For example, in the model presented in the first article (Chapter 4), we modeled the indentation of a bilayer coating deposited on a steel base material. To support the material, the bottom nodes were fixed such that rigid body motion of the tested material was suppressed. The modeling domain was also reduced compared to the laboratory sample that the tests were actually performed on. By reducing the dimension of the system, the computational cost has been lowered to an acceptable level; however, we risk contaminating the stress field with boundary effect. To confirm that it is not the case, we must verify that all the stress components asymptotically converge to 0 far from the contact area. To achieve this verification, we can study the value of the maximum non-singular stress as a function of the model domain size. As the domain size is increased, this value will decrease since the bottom support adds stiffness to the system, and by moving it further, we make the system more compliant. Eventually, this value will converge when boundary effects have vanished. Both conditions are illustrated in figure 3.8.

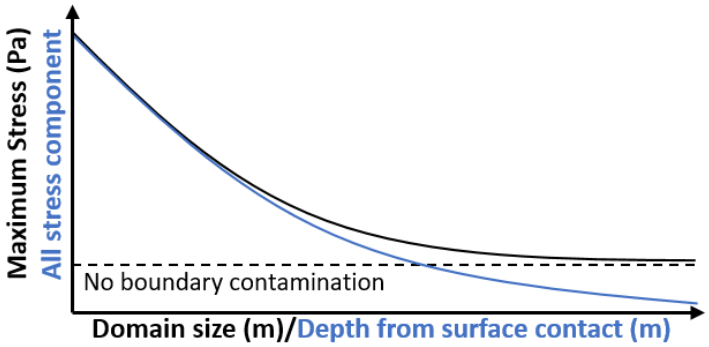

Figure 3.8 Evolution of maximum non-singular stress and far-field stress components induced from a contact load.

For dynamic problems the propagation of the stress wave can be reflected by support constraints and a similar analysis has to be performed. For example, we can verify that the reflected mechanical waves do not have a considerable effect on the deformation stresses in the area of interest. This analysis was performed for the third investigation of this thesis that studied the behavior of a mechanically graded coating subject to micro-particle impacts.

The other type of boundary conditions is the application of a load or displacement to the outer boundary of the model. For example, we used this type of constraint in the second article to strain the tensile specimen. In this model, the deformation is applied to the substrate, and the strain is transferred to the coatings through the interfacial shear force from the base material. Since the axial size of the model was reduced to cut the calculation time, we had to verify that far from the displacement boundary the strain in the coatings was equal to the base material strain and thus free of the stress relaxing effect at the free boundary.

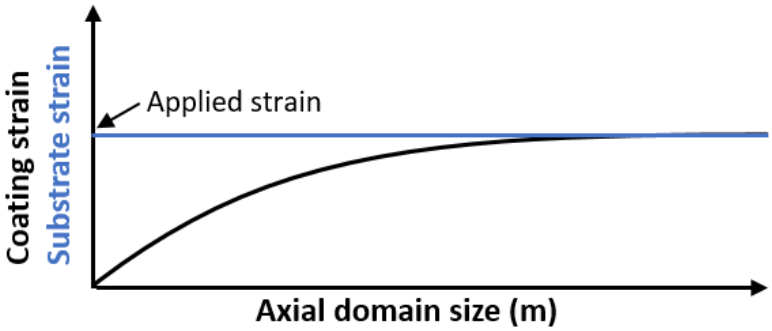

Figure 3.9 Difference between the applied strain on the substrate and coating strain as the axial domain size is increased in a uniaxial tensile model.

3.5 Modeling approach justification

The choice of a particular numerical methodology defines the framework and ultimately affects the scope of the research. Some inherent limitations of the continuum mechanics theory are pushing researchers to develop new numerical models to circumvent the limitations of the finite element framework. However, since the finite element methodology is deeply established and privileged by engineers in the industry, another branch of research is devoted to the development of ad hoc models that enhance the capabilities of the classical finite element methods. We have summarized in table 3.1 the pros and cons, the major alternatives numerical approaches, and the ad hoc methods.

We have identified that for the studies presented in this work the finite element method was the most appropriate choice for many reasons. First, we needed a readily available methodology that was well understood to be able to communicate with ease and share our results with our industrial partners. We also needed an approach that could deal with larger scale differences without being prohibiting on the computational resources required. This can easily be achieved with implicit finite element and adequate meshing, since with this method the computational requirement is proportional to the total number of elements independently of the length scale. For example, in our study presented in Chapters 4, 5 and 6, we investigated the response of nanometer or micrometer scale stress gradients subject to millimeter scale counterparts that required large simulation domains that were not an issue for a finite element implicit solver. Another major limitation that we observed in most of the alternative approaches is the handling of contact mechanics which is severely lacking or non-existent. The finite element method limitation concerning the microstructural features can be avoided by introducing realistic defects in the mesh, or by using more advanced methods such as cohesive zone modeling and crystal plasticity which allows one to simulate different phases and/or grain orientations. Finally, the mesh influence only becomes problematic when it is not appropriately defined or when dealing with material removal methods and arbitrary crack propagation direction, both of which we did not explore in the different investigations we performed. Note that the complete overview of tribomechanical numerical methods is out the of scope of the present work and more details about the specific fields and the available modeling literature will be presented as a preamble in Chapters 4, 5 and 6.

Table 3.1 Pros and cons of the finite element method

<table>
<tr><th>Pros</th><th>Cons</th><th>Alternative approach</th><th>Finite element ad hoc</th></tr>
<tr><td rowspan="4">- Handle complex geometry
- Strong contact modeling
- Low computational requirement
- Readily available methodology
- Engineering oriented results
- Adapted to large length scale differences</td><td>No microstructural features</td><td>Molecular dynamic [120]</td><td>Cohesive zone modeling [121], [122], Crystal plasticity[123]</td></tr>
<tr><td>Complex constitutive relations</td><td>Ab initio [124], Molecular dynamic</td><td>-</td></tr>
<tr><td>Mesh influence
Crack tip singularity
No crack propagation</td><td>Peridynamic [125]
Discrete element method [126]
Phase-Field Mechanics [127]</td><td>Remeshing techniques [128]
Cohesive zone modeling
XFEM [129]
Continuum damage mechanics [130]</td></tr>
<tr><td>Continuum mechanics invalid at the atomistic scale</td><td>Molecular dynamic, Ab-initio</td><td>Multiscale coupled models [131]</td></tr>
</table>

CHAPTER 4 ARTICLE 1: PREDICTING THE LOAD-CARRYING CAPACITY AND WEAR RESISTANCE OF DUPLEX-COATED LOW-STRENGTH ALLOYS FOR SEVERE-SERVICE BALL VALVES

M. Laberge,[1] E. Bousser,[1] J. Schmitt,[1] M. Koshigan,[1] T. Schmitt,[1] F. Khelfaoui,[2] S. Isbitsky,[2] L. Vernhes, [2] J.E. Klemberg-Sapieha[1]

[1]Engineering Physics Dept., Polytechnique Montréal, Montréal, QC, Canada, H3C 3A7

[2]Velan, 550 Rue McArthur, Saint-Laurent, QC, Canada, H4T 1X8

Journal of Thermal Spray Technology

4.1 Preamble - Methodology details and novelty of the study

In this first study we applied the previously presented numerical methodology to investigate the load carrying capacity of a duplex coated steel which consists of a top wear resistant WC-C coating on a thick Co-Cr load carrying interlayer. The materials elastic moduli were accessed using depth sensing nanoindentation, and the Oliver and Pharr analysis was used. This analysis was originally developed for single phase materials, but applying it to multiphase materials allows one to probe the average mechanical properties of the material. We have verified this by indenting at different positions on the surface and observed low variation in the results which indicated that we were probing a collection of several phases present in the material and thus extracting an average effect of the microstructural characteristics. One issue that may arise with materials deposited using thermal spray and laser cladding techniques is the presence of porosities and voids in the material's microstructure. An increase in porosity is usually associated with a decrease in the measured mechanical properties in terms of the Young's modulus, hardness and fracture toughness [132]. In the numerical model, we varied the mechanical properties of the materials to take into account this influence of the porosity on the mechanical response. Furthermore, during all mechanical loading experimental tests we have not observed any sign of material removal or particular features on the indentation load-displacement curves such as pop-in event that would indicate the significance of the material heterogeneity and its effect on the mechanical response in the load conditions we considered. We also did not observe any sign of weak interface that would result in delamination

between the different layers. As a consequence, we assumed in the model that all materials were homogeneous and isotropic as well as perfectly bonded together at their interfaces.

Using the properties extracted from the indentation analysis we have developed a finite element contact model to predict the brinelling resistance of the different coating architectures. Brinelling resistance is the capacity of a surface to sustain a contact load without the formation of permanent deformation upon unloading. As we showed before, the induced stress at the surface strongly depends on the counterpart radius of curvature in the contact area. When testing bulk materials, brinelling resistance is directly associated with the hardness of the surface which dictates its resistance to plastic deformation. We should also mention that there is usually no material or volume loss associated with brinelling. In fact, for materials that permanently deform through plasticity, there is no material or volume loss due to the incompressibility of the plastic deformation. In this case, the brinelling indent volume is what we call a plastically displaced volume, and not a volume loss. By measuring the hardness (or the yield stress of the material), we perform a direct assessment of a surface brinelling resistance. However, in a multilayer coated system, the hardness varies through the coating profile such that the base material can be shielded from plastic deformation while some layers may undergo permanent deformation. In this case, the resistance to brinelling is a function of the global tribological response of the surface. The prediction of this tribological response requires the characterization of the elastic-plastic properties of each constituent of the coated material and a numerical model to evaluate the induced stresses. For example, using an extended Hertz theory approach, Schwarzer developed a numerical model to evaluate the elastic response of a multilayer film on a semi-infinite substrate ([133]). Using this approach, Bemporad et al. studied the influence of the coating architecture on the load bearing capacity and stress spreading inside a duplex coated system [61]. A noticeable shortcoming of this approach is that while it can identify the location where permanent deformation is initiated, it cannot model the response of the system post yielding which strongly limits its application. To model the post yielding response, continuum mechanics models are necessary. For instance, Kot et al. presented a study exploiting a finite element model to predict the brinelling resistance of a TiN coated steel substrate under spherical indentation and the ensuing evolution of the plasticity as a function of the applied load [134]. As we will present in the following article, many experimental studies concerning duplex-coated steel have been published; however relevant

numerical modeling literature touching this subject is still lacking. During our literature review process, we have not identified any publication that developed an approach to assess and predict the failure of the top coating in a duplex coated steel under different loading conditions. As a consequence, there is an important need concerning the development of numerical modeling allowing one to study the influence of coating architecture on the initiation of brinelling and coating fracture. We believe that the article presented in this chapter proposes a novel modeling approach that fills this gap in the scientific literature.

4.2 Abstract

The load-carrying capacity and wear resistance of a duplex-coated 316 stainless steel was determined, and a finite element numerical approach was developed to predict and corroborate experimental observations. Low-strength alloys are generally used for highly demanding valve applications due to their superior chemical stability, galvanic corrosion resistance, and lower susceptibility to stress corrosion cracking failure. Hardfacing (using thermal spraying, laser cladding, or plasma transferred arc welding) is currently the most common solution to protect valve components. Hardfacing provides a thick, hardened case that significantly improves tribological performance. However, hardfaced layers provide lower wear resistance compared to vacuum-deposited hard coatings. One solution to further improve hardfacing performance is a duplex approach, which combines the two processes. This study investigates the following materials: a 316 stainless steel base hardfaced with laser cladded Co-Cr superalloy and topped with a CVD nanostructured W-WC coating. Tribological properties of three configurations were assessed for their ability to delay initiation of plastic deformation and surface cracking under quasistatic loading and for their resistance to dry reciprocal sliding wear. The results demonstrate that finite element modeling allows numerical prediction and comparison of the load-carrying capacity and wear resistance of duplex-coated AISI 316 stainless steel.

4.3 Introduction

Valves regulate the flow of raw natural materials such as coal, oil, and gas from extraction sites to the plants where they are processed. Flow and processing operations are continuously optimized

to maximize production rates, increase pressure capacities, and meet temperature and/or corrosion resistance requirements. Severe-service applications with grueling operating conditions that are exacerbated by solids present in the flow require tailored materials. Whereas almost any valve type can be optimized for these applications, severe-service ball valves (SSBVs) are the preferred choice. A ball valve contains a spherical closure unit that provides on–off flow control by rotating 90 degrees. The open position allows flow. In the closed position, a tight seal is provided by the contact between two sealing surfaces: the outer surface of the ball and the convex inner surface of two radial seats in the valve chamber which are conformal with the ball.

For severe-service applications, the process designer generally specifies a short list of acceptable substrates based on applicable standards and past experience to ensure chemical compatibility with the product flowing through the valve[135]. Low-strength substrates such as AISI 316 austenitic stainless steel are typically used for their superior galvanic corrosion protection and lower susceptibility to stress corrosion cracking.[136], [137] Under certain conditions, ball valves are susceptible to localized corrosion, such as crevice and pitting corrosion of austenitic stainless steel, requiring the use of other low-strength alloys. Although AISI 316 austenitic stainless steel is widely used in the oil and gas industry to handle sour fluids, two NACE standards, MR0175/ISO[138] for oil field applications and MR0103[139] for refining, recommend selecting materials that are specifically tailored for very sour environments and with low hardness to mitigate the cracking risk (e.g., Incoloy 800 or Inconel 718). Other standards such as NORSOK M-001[140] for offshore installations and ASTM G63[141] for high-pressure oxygen specify low-strength substrates such as commercially pure titanium and Inconel 600 or Monel 400, respectively.

Degradation of the sealing surfaces is a major cause of SSBV failure, resulting in two different failure modes. In the first, when high-contact stress is required to seal the pressurized fluid, the valve fails to cycle on demand due to excessive friction between the sealing surfaces. In the second, the valve performs a cycle on demand but fails to seal due to imperfections in the sealing surfaces. Both failure modes can be caused by degradation of the sealing surfaces resulting from one of the wear mechanisms (e.g., indentation, abrasion, erosion, galling, or spallation) combined with

corrosion. To improve wear performance and extend the in-service valve life, valve manufacturers have applied various wear-resistant coatings onto sealing surfaces using techniques such as thermal spraying, laser cladding, or plasma transfer arc welding.[142]

Wear-resistant thin film coatings have demonstrated superior tribological performance to industry-standard hardfacing for valve sealing surfaces.[143] However, despite the widespread application for carbide tools and high-strength engine valves, thin film coatings can only be applied to industrial valves in clean, low-pressure environments. In addition, the abrupt transition between the relative mechanical property gradients of the thin film and of the low-strength base material combined with the low thickness of the film induce high stresses at the interface and within the substrate material when subjected to localized contact pressure [144]. These stresses lead to two failure modes: 1) brinelling (surface indentation due to plastic deformation of the substrate); and 2) eggshell effect (coating fracture and/or spallation) [145]. High contact pressure on the sealing surfaces is generally caused by valve design choices that induce stress concentration or by particles in the flow. The ability of a surface to distribute stresses generated by a high concentrated load to the substrate without surface plastic deformation is called the load-carrying capacity. This capacity can be improved by tailoring the substrate and adding an intermediate layer to provide gradual changes in mechanical properties. A widely used method to produce these coatings is duplex treatment, in which nitrided steel alloys are used as a substrate for the thin film coating.[146]–[148] However, because nitriding can degrade the corrosion resistance of alloys,[149], [150] it is rarely acceptable by end users. Moreover, the hardened case thickness is limited to a few tens of microns, which is insufficient to protect against brinelling. Figure 4.1 shows indentation damage caused by large hard particles (estimated size ~0.5 mm) that became trapped between the ball and seat, generating high contact pressure. Figure 4.2 shows a valve failure caused by a sealing surface design that induced localized contact pressures exceeding the capacity of the coating system combined by abrasive damage due to valve operation.

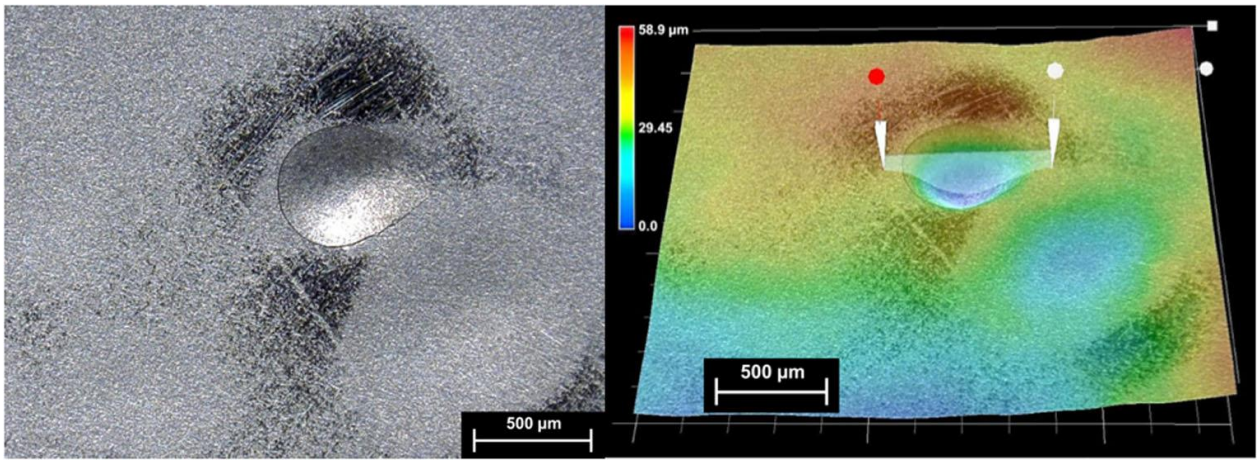

Figure 4.1 Micrograph and depth profile of indentation damage on a W-WC-coated AISI 316 stainless steel ball after valve operations

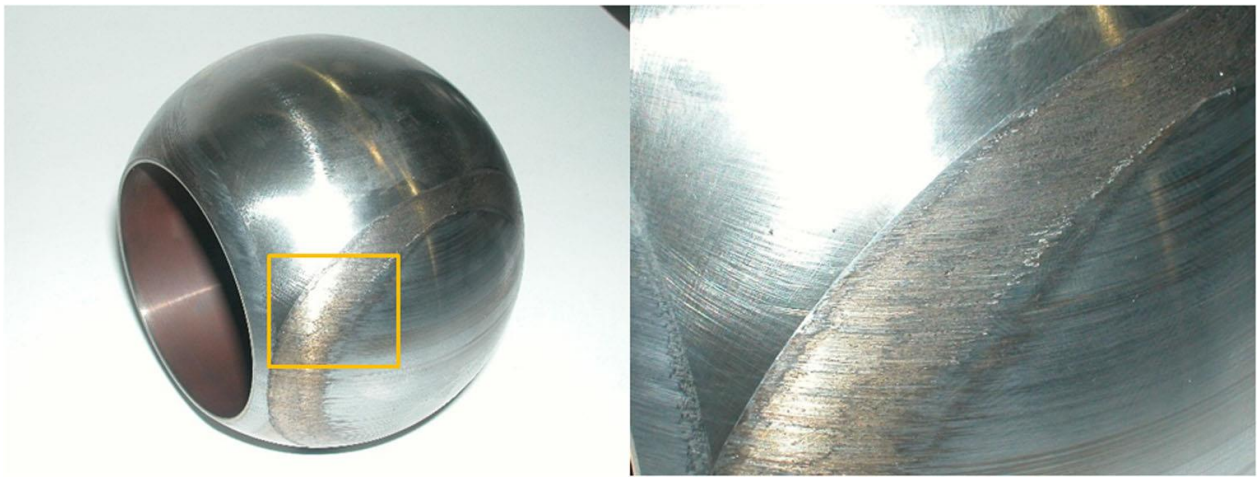

Figure 4.2 After 2000 on–off cycles under steam at 6.9 MPa (1000 psi) and 315 C (600 F), the full bore NPS 3 Cl. 600 valve (Coated by a 50 -µm-thick W-WC layer deposited by CVD) failure has been caused by a sealing surface design that induced contact pressures exceeding the capacity of the coating system. The bond line coating is plastically deformed at the interface with the stainless-steel ball

To protect against this kind of damages, a thin film coating can be deposited onto an industry-standard hardfacing, providing higher load-carrying capacity.[61], [151], [152] Such solutions have been shown to enhance wear and corrosion resistance as well as coating adhesion [143], [151]–[154]. Although it is widely agreed that this gradual change in mechanical properties is responsible for improved tribological properties, the duplex (two-layer) structure design is based on empirical

knowledge. Few studies addressed these issues through a modeling approach, most notably, Bemporad et al. demonstrated improved coating adhesion by optimising the coating architecture using finite element model such that the interfacial shear stress minimization is achieved [47]. Still, there is no standardized tools available to support material selection in terms of the optimal mechanical properties and thickness to protect surfaces under specific wear conditions. Therefore, the aim of this study was to develop a numerical analysis method to predict the load-carrying capacity of valve sealing surfaces that could be used to design effective duplex coating architecture.

4.4 Experimental

4.4.1 Materials

An AISI 316 stainless steel base material and three coating configurations were investigated as shown in Figure. 4.3. Prior to thin film deposition, bare AISI 316 and hardfaced samples were mechanically polished with 200, 600, and 1,200 grit SiC papers. Using a 4 kW direct diode laser system (Coherent Inc.), a 2.5 mm thick Co-Cr hardfacing was deposited onto 20mm x 20mm x 5mm square blocks of AISI 316 plates by FW Gartner (Houston, TX, USA). After polishing, a 50 ± 5 μm thick nanostructured W-WC coating was deposited on all coupons. At Hardide (Oxfordshire, United Kingdom), half the samples were exposed to a hot carbon-containing gas combined with a pressurized tungsten hexafluoride (WF_6) gas to produce a nanostructured W-WC coating according to the standard thermal CVD process developed by Zhuk et al.[155]. To ensure measurement repeatability during tribological testing, all samples were finally mechanically polished using 1,200 grit SiC papers to obtain a smooth surface finish similar to valve sealing surfaces 0.1-0.15 μm R_a. The studied architectures are summarized in Figure 4.3, and more information on the film deposition process is provided in [143].

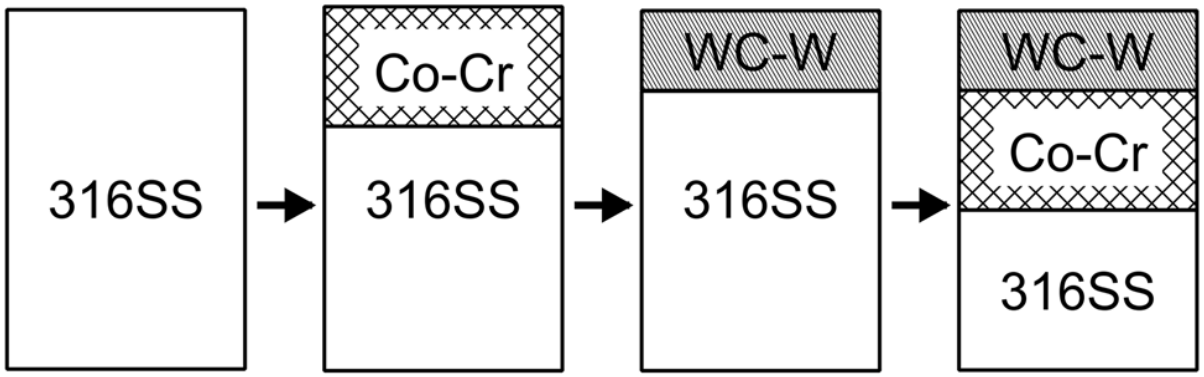

Figure 4.3 Schematic representation of the coating architectures investigated in this paper

4.4.2 Microstructural analysis

Coating system configurations, layers thicknesses, interlayer bonding and high load indentation scars were analyzed by scanning electron microscopy (SEM) using a JEOL JSM-840 scanning electron microscope. Complementary microstructural analysis results are provided in [143].

4.4.3 Mechanical and tribological properties

The microhardness of the constituent layers was measured along the cross-sections using a Micro Combi Tester (Anton Paar, USA) with a Vickers indenter at 5 N load, a dwell time of 10 s, and loading and unloading times of 30 s. Indentation elastic modulus was estimated with a depth-sensing indenter (Hysitron Tribo indenter) equipped with a Berkovich diamond tip using the Olivier–Pharr method [156].

Coating adhesion was assessed by optical microscopy from Rockwell indentation following ISO CEN/TS 1071-8 standard.[157, p. 26433] The load-carrying capacity of the coating architectures in terms of indentation yield strength and fracture resistance was assessed using a high-load tribometer (HLT 500, Tricomat, Montreal, Canada) with normal load varying from 0 to 5 kN. Two counterparts were used: a 750 μm radius Rockwell diamond stylus and a 2.385 mm radius Al_2O_3 ball to simulate the typical indentation damages observed in operation and typical leading edge radius of the valve seat respectively. Indentations were performed at various loads using an alumina ball (radius = 2.385mm) to estimate the normal load required to initiate plastic deformation, thus leaving residual imprint on the surface. Residual depth after indentation was measured by confocal

microscopy (Anton Paar, USA) and surface damage was observed post-mortem by scanning electron microscopy.

A ball-on-flat linear reciprocating tribometer (Tricomat, Montreal, Canada) was used to assess the sliding wear behavior of the coatings according to ASTM G133 standard.[158] Normal load from 10 to 30 N was applied to a 3.175 mm radius alumina ball used as counterpart material. Alumina was selected for its high stiffness and for it's inertness with the investigated materials. A new ball was used for each test. Stroke length was 10 mm with 2 Hz frequency. Normal and tangential force were recorded every second during the test. The wear rate K was assessed using the formula $K = V/(F \times S)$, where V is the worn volume, F is the normal load, and S is the sliding distance.

Total volume loss is obtained by integrating the wear scar area over the total wear scar profile and then multiplying by the length of the track. All wear tests were halted before piercing the top surface coating to ensure that the measured wear rates were specific to the tested coating.

4.4.4 Finite element modeling

A load-controlled axisymmetric finite element model was developed to predict the mechanical response of the duplex-coated systems under quasistatic indentation. Models were executed on LS-Dyna using a frontal implicit solver with fixed timestep[159]. Materials were assumed to be homogeneous and isotropic, and four-node elements with reduced integration were used to mesh the indenter and coated system. The model geometry and boundary conditions are shown in Figure 4.4. The characteristic mesh length was reduced to 2 μm in the vicinity of the contact area to accurately represent the curved geometry of the counterpart and to capture the proper stress gradients across the coatings. The contact detection algorithm used is the surface to surface type and the contact model is penalty based considering Coulombic friction.

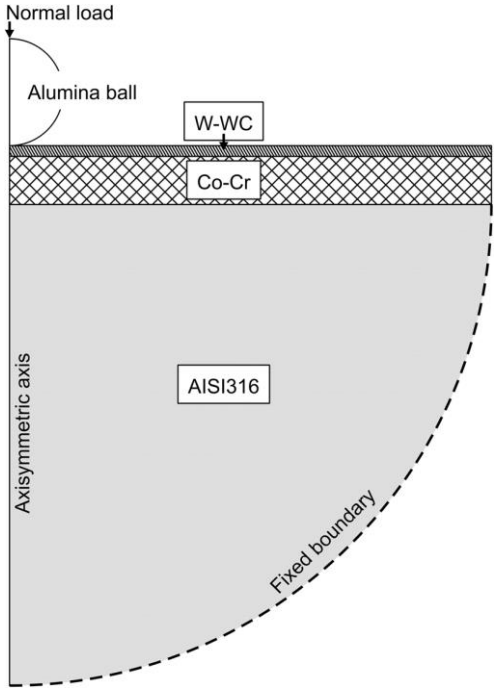

Figure 4.4 Finite element model geometry and boundary conditions.

4.5 Results and discussion

Table 1 presents the Vickers hardness and elastic modulus for the materials measured by depth-sensing indention. As expected, the Young's modulus and hardness for Co-Cr are situated between those for the AISI 316 substrate and W-WC coating. The high hardness for Co-Cr agrees with previous studies showing that laser-cladded Co-Cr had a more refined and denser microstructure compared to Co-Cr deposited by plasma transfer arc welding.[138] Moreover, the W-WC hardness is consistent with the manufacturer's specifications.

Table 4.1 Young's modulus and Vickers hardness for the different materials

Materials	Vickers Hardness (GPa)	Young's Modulus (GPa)
AISI 316	2.5 ± 0.2	200 ± 10
Co-Cr	5.4 ± 0.2	250 ± 20
W-WC	10.8 ± 0.2	450 ± 25

From the CEN/TS 1071-8 adhesion tests, all coated systems show Class 1 adhesion with no visible delamination as presented in a previous study[143]. However, it can be observed that indentation testing without the Co-Cr hardfacing (architecture (b)) generated more cracking around the contact area compared to when the interlayer was present (architecture (c)). This is a first indication of the limited load-carrying capacity of the AISI 316 substrate and an early observation that the increased support of the interlayer limits the generation of tensile stress at the surface under the same loading conditions.

The constitutive behavior of the Co-Cr hardfacing and AISI 316 substrate were simulated as bilinear elastoplastic and the behavior of the W-WC top coating and indenter counterpart were simulated as perfectly elastic due to their significantly higher strengths compared to the other materials. Another indication of the highly elastic behavior of the W-WC layer comes from the brinelling type damages observed after operation as shown on fig. 4.1. While those scars show sign of circular cracking around the contact area, the measured residual depth of the scars were unaltered after stripping off the top W-WC layer which indicates that it behaved elastically in the conditions that we aim to reproduce using the high-load indentation testing.

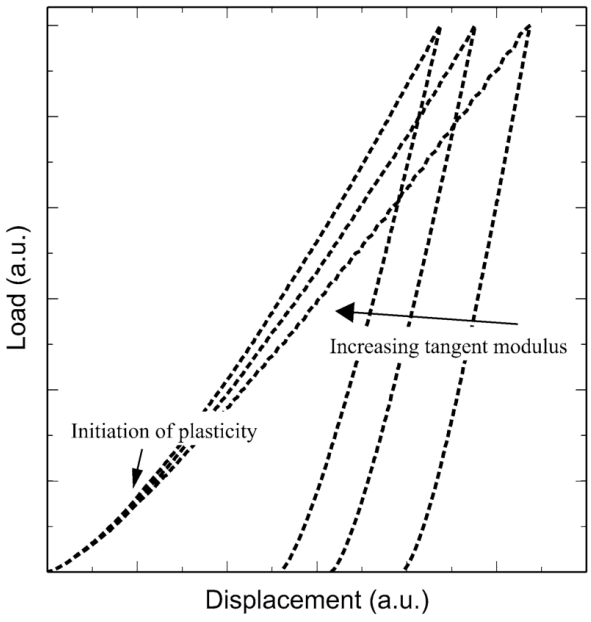

Figure 4.5 Finite element model load displacement curves: influence of increasing the tangent modulus.

The elastic moduli were obtained from depth-sensing indentation measurements. The yield stress for the Co-Cr hardfacing was obtained from uniaxial tensile tests using digital image correlation to evaluate the strain. The tangent moduli for the materials were estimated by iteratively comparing the simulated indentation load-displacement curves to the corresponding high load indentation experiments. The tangent moduli were fit to minimize the difference between the simulated and experimental curves in terms of maximum displacement and residual depth. As shown on Figure 4.5, for equal yield stresses, the influence of increasing the tangent moduli will stiffen and harden the surface by lowering both the maximum penetration depth and residual depth. After obtaining the tangent modulus for the AISI 316 substrate, the tangent modulus for the Co-Cr hardfacing was estimated using the same method. The final elastoplastic properties used in the model are summarized in Table 2.

Table 4.2 Finite element modeling results for the constitutive behavior of the different materials.

Material	E (GPa)	σ_y (MPa)	$E_t/E*100\%$	Poisson's ratio
AISI 316	200	300	2.5	0.27
Co-Cr	250	650	10	0.25
W-WC	450	-	-	0.26
Diamond	1140	-	-	0.07
Alumina	300	-	-	0.21

Figure 4.6 presents the critical load to plastic deformation initiation (L_y) for the different architectures. It can be seen that L_y is slightly improved with the Co-Cr hardfacing, increasing from 10N for the base AISI 316 substrate to 15N for the architecture (a). For the top-coated W-WC configurations, L_y shows a significant improvement from 30N (architecture (b)) to 80N when the substrate is pretreated with Co-Cr hardfacing (architecture (c)). The same indentations were simulated numerically with the finite element model by reproducing the indentation at incrementally increasing loads until the modeled residual depth of indentation reached 200 nm. Considering the surface roughness and the limitations of confocal microscopy, the 200 nm depth

was estimated as the resolution limit of detectable residual depth, and was therefore used as the metric to estimate L_y in the model. Comparison between experimentally measured L_y and simulated L_y shows close agreement within the 5N tolerance for all coating architectures.

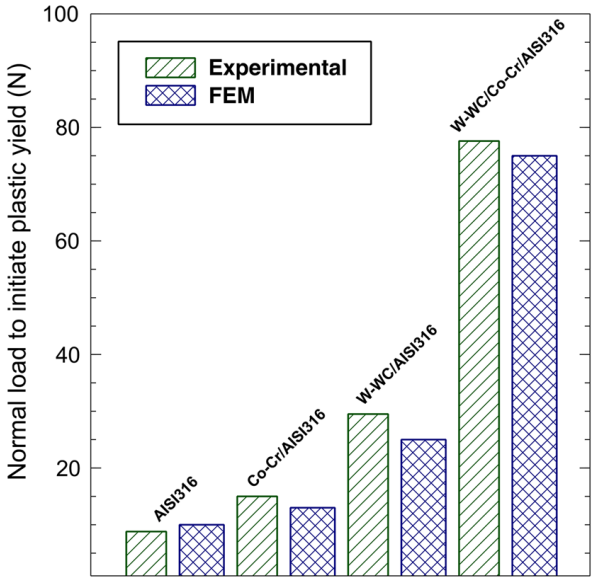

Figure 4.6 Comparison between experimental load and FEM normal load to initiate plastic deformation (L_y) under indentation by an alumina ball (radius = 2.385 mm).

In both configurations with the top W-WC coating, there is already a substantial improvement against brinelling damage initiation. Furthermore, there is an apparent synergy between the W-WC coating and the hardfaced layer that results in increased L_y which is much higher than the sum of their individual load carrying capacity. This can be explained by the fact that the first material to yield is located in the area just below the WC-C coating, close to the interface. Since the relatively high thickness of the W-WC coating is sufficient to contain the zone of maximum von Mises stress, its value at depth below this maximum increase slowly in function of the normal load applied. Therefore, the higher hardness of the hardfacing compared to the substrate delay the initiation of plastic deformation compared the single coating configuration, thereby improving significantly the load-carrying capacity.

To assess the critical load (L_f) required to fracture the coating under point loads, indentations were performed with a Rockwell diamond stylus (radius = 750 µm) and an alumina ball (radius = 2.385mm)until circular cracks around the contact area were visible by SEM (Figure 4.7). Figure 7

shows that hardfacing rise to higher loads the eggshell failure type of the coating. It can be observed that L_f increases from 90N to 200N with the addition of the hardfacing when being indented by the Rockwell stylus, and from 250N to 950N under the alumina ball tests configuration.

These cracks are induced by high level of tensile stress at the surface just outside the contact area, as shown in Figure 4.7. Using the finite element model, the indentations were numerically simulated and the maximum surface tensile stress was tracked throughout the indentations. The modeled tensile stress at normal load L_f for the different architectures then define a range of critical tensile stress required to initiate those circular fractures. For both counterparts and architectures with or without hardfacing, the model-calculated critical tensile stresses fall into a similar range. Those values statistically define the critical surface tensile stress of the W-WC coating as 5 ± 0.5 GPa (Figure 4.8, solid lines). For both indenting counterparts, the L_f value for the hardfaced sample is more than twice the value for the non-hardfaced sample, indicating that the load-carrying layer provides support that limits the penetration depth and thus the generation of high tensile stress at the surface.

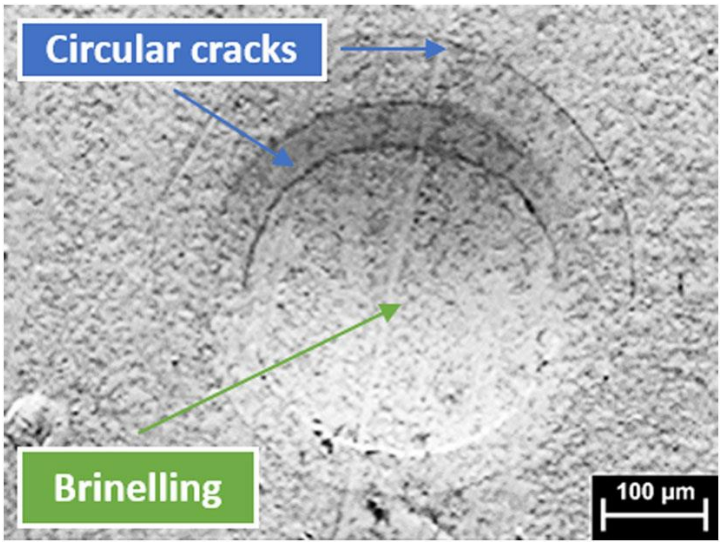

Figure 4.7 SEM micrograph of the surface after indentation of the W-WC/Co-Cr/AISI 316 sample by an alumina ball at 200 N.

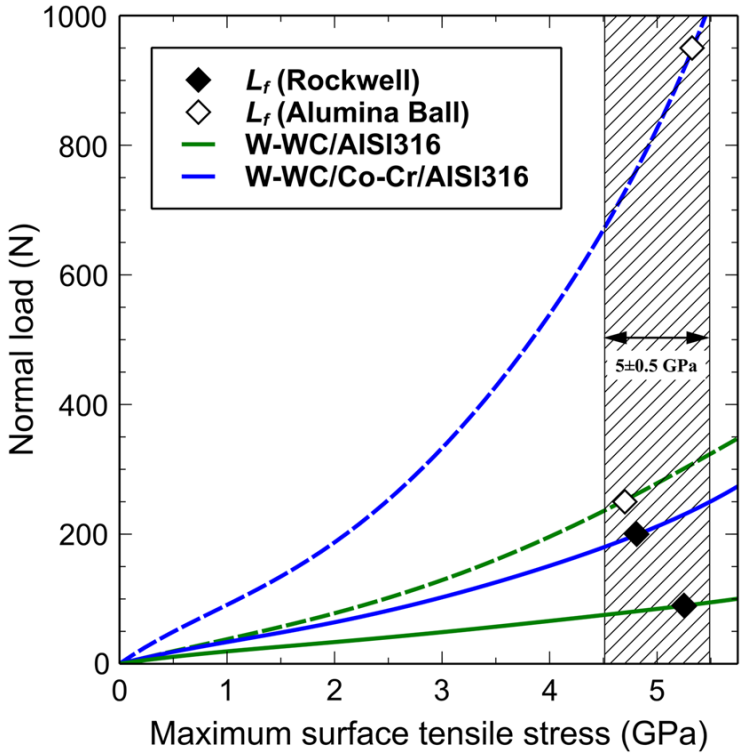

Figure 4.8 Identification of the fracture load and simulated maximum tensile stress for two indenter geometries as a function of normal load. Solid line: Rockwell diamond stylus (radius = 750 μm); dashed line: alumina ball (radius = 2.285 mm).

To predict and assess the wear performance of a specific coating architecture, three components of the stress-strain field were identified as representative of the different wear mechanisms. The contact pressure is related to abrasive wear, in which the rough hard alumina ball counterpart removes material from the surface by cutting and ploughing the micro asperities present at the surface. Since the top W-WC layer demonstrated brittle fracture behavior, the second component of interest is the surface tensile stress, which is the principal element responsible for crack formation under localised contact. Finally, interfacial damage generated by shear stress combined with coating cracks can be responsible for premature spallation of the coating. In a first step, the model was used to reproduce the wear contact condition to help us understand the different wear behaviors. In a second step, the model was used to examine the influence of the load-bearing layer thickness. This paves the way for the development of a predictive tool to optimize coating architecture without compromising sliding wear performance.

Figure 4.9 presents the changes in the coefficient of friction (COF) measurements for the W-WC/Co-Cr/AISI 316 system (architecture (c)) at different loads during the reciprocal sliding wear tests with an alumina ball (radius = 3.175 mm). In all conditions, after a running in period of around 150 m, the COF starts to stabilize, showing the influence of the normal load on the stable COF. Also shown on Figure 4.9 is the evolution of the COF for different test lengths at a 10N normal load. The stable COF are estimated as the average value of the COF following the running in period until the end of the test. The stable COF increases from 0.55 to 0.72 as the normal load increases from 10N to 30N, demonstrating that larger ploughing force plays a role in the overall tangential force at higher loads.

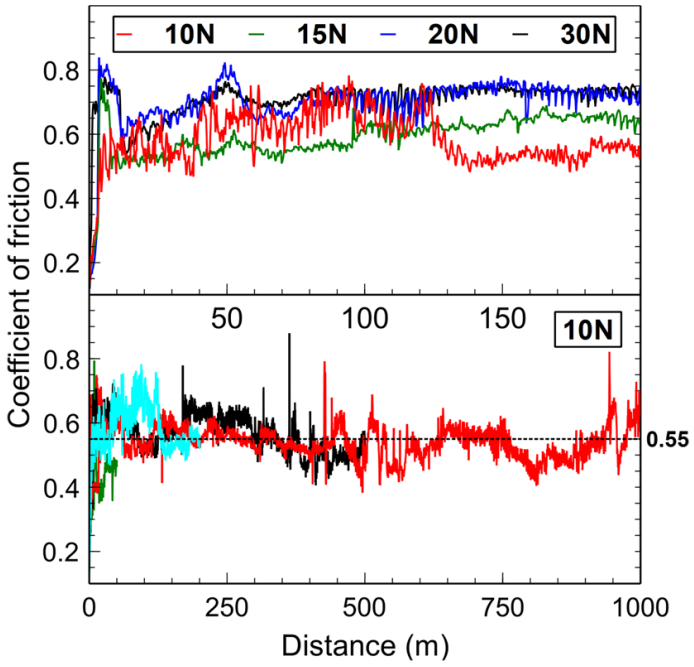

Figure 4.9 Changes in the coefficient of friction (COF) during the reciprocal sliding wear test for the W-WC/Co-Cr/AISI 316 sample at different loads after 200 m (top) and at a normal load of 10N for different total lengths up to 1000 m (bottom).

Figure 4.10 shows the wear volume loss at 10 N for the different surfaces. The dissipated energy in the contact area is estimated by calculating the total work done by the friction force which consists of summing over all cycles the product of the tangential force by the stroke length. For all configurations, the cumulative volume loss is proportional to the total amount of dissipated

energy by the sliding contact as reported previously [160]. In these conditions, the bare substrate showed poor sliding wear resistance. Although the Co-Cr hardfacing alone (architecture (a)) substantially increased the wear resistance, both the W-WC/Co-Cr/AISI 316 (architecture (c)) and W-WC/AISI 316 (architecture (b)) systems showed an increase of one order of magnitude over the industry-standard hardfacing. The similar behavior of the two W-WC top-coated surfaces can be attributed to the minimal effect of underlayer stiffness, as the stress field is predominantly confined to the W-WC at such low wear loads.

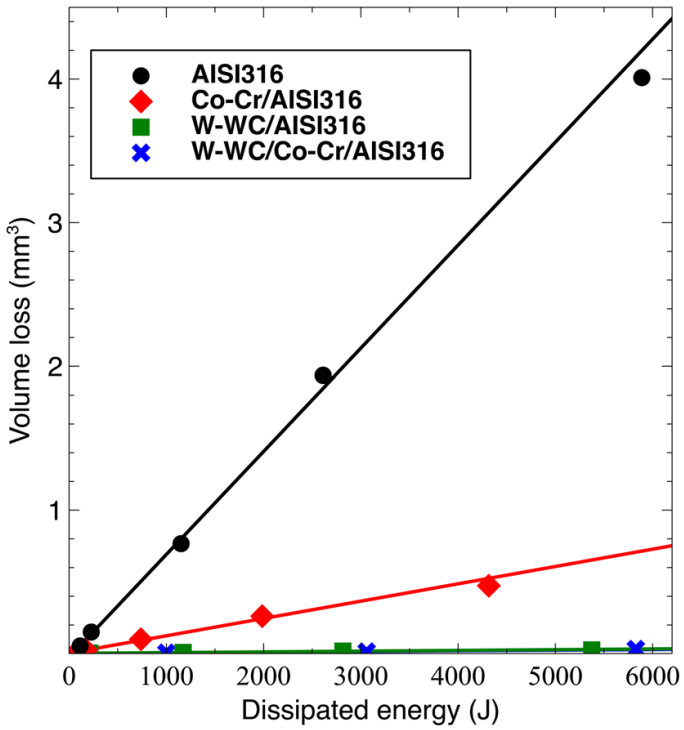

Figure 4.10 Volume loss as a function of dissipated energy for the different coating architectures.

Figure 4.11 shows the influence of the normal load on the volume loss during the sliding wear tests for W-WC coating with and without the LCC underlayer. Because the normal loads are lower than, or at the limit of the load required to initiate plastic deformation, it can be deduced that the measured volume loss is primarily the product of abrasive wear, with only a negligible portion due to plastically displaced material. At a normal load of 10N, the volume losses for the two systems are consistently identical. When the normal load is increased from 10N to 30N, the volume loss for the W-WC/Co-Cr/AISI 316 system shows higher load dependence compared to

the W-WC/AISI 316 system. In these mostly elastic wear conditions, the wear rate scales with the contact pressure generated by the counterpart. To assess this behavior, the contact pressure was simulated as presented in Figure 4.11. The modeled results confirmed that the increase in volume loss is correlated to an increase in contact pressure over this normal load range. Even though the initial contact area is smaller for the stiffer surface (architecture (c)), the increased abrasion rate due to the higher contact pressure quickly wears the surface and leads to significantly higher volume loss as shown by the final wear profile after 200m presented on Figure 4.12.

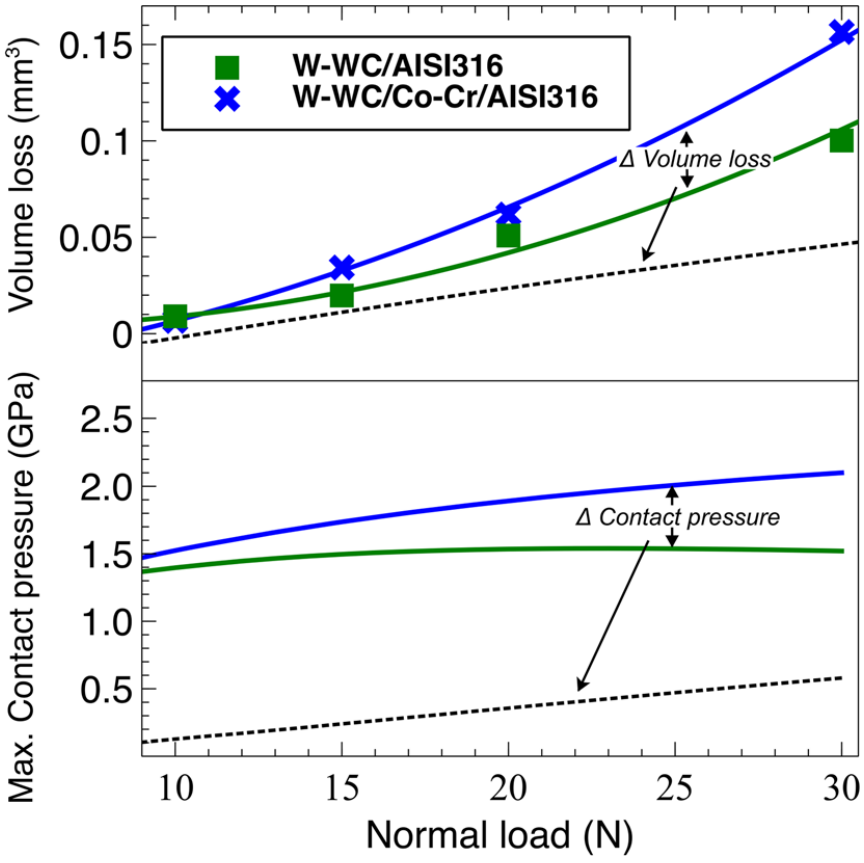

Figure 4.11 Influence of normal load on volume loss under sliding wear by an alumina ball (radius = 3.175 mm) after a sliding distance of 200 m.

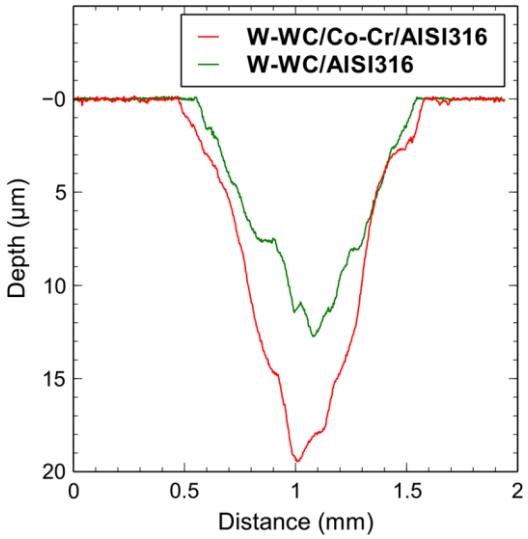

Figure 4.12 Line profiles of the final wear track after a total length of 200 m at a normal load of 30 N.

One of the critical functions of the hardfacing layer is to protect the base material against plastic deformation. The simulated equivalent plastic strain fields for hardfaced and non-hardfaced surfaces under high load indentation are shown in Figure 4.13. Even in these extreme loading conditions, the Co-Cr layer is adequate to confine all plasticity, protecting the base material from any permanent deformation. This indicates that the thickness of the hardfacing layer could be reduced while still providing similar performance in terms of delaying the load to initiate yield and tensile cracking and potentially reducing the load dependence of the sliding wear by decreasing the equivalent stiffness of the surface.

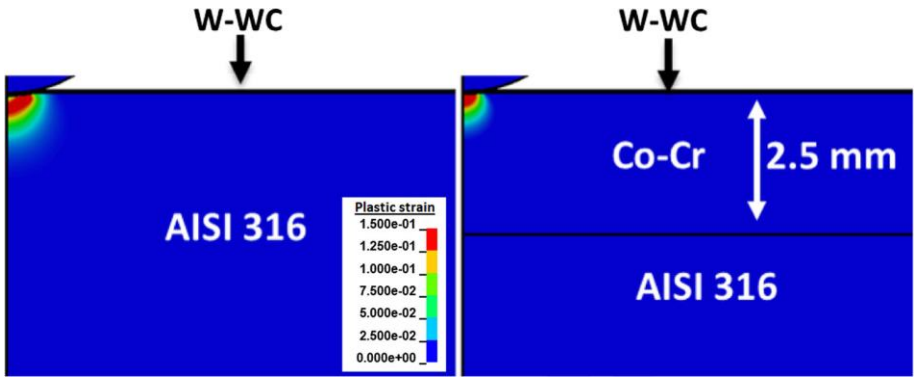

Figure 4.13 Effective plastic strain field induced at the surface under indentation by an alumina ball (radius = 3.175 mm) at a 1000 N normal load.

To estimate the effect of hardfacing thickness, we simulated an increasing normal load indentation up to 100N with decreasing Co-Cr thickness and monitored the changes in contact pressure, as presented in Figure 4.14. The influence of thickness on contact pressure is minimal until a critical minimum value is reached (< 250 µm). At this point, the AISI 316 substrate starts to yield considerably, which limits the contact pressure compared to systems with a thicker interlayer.

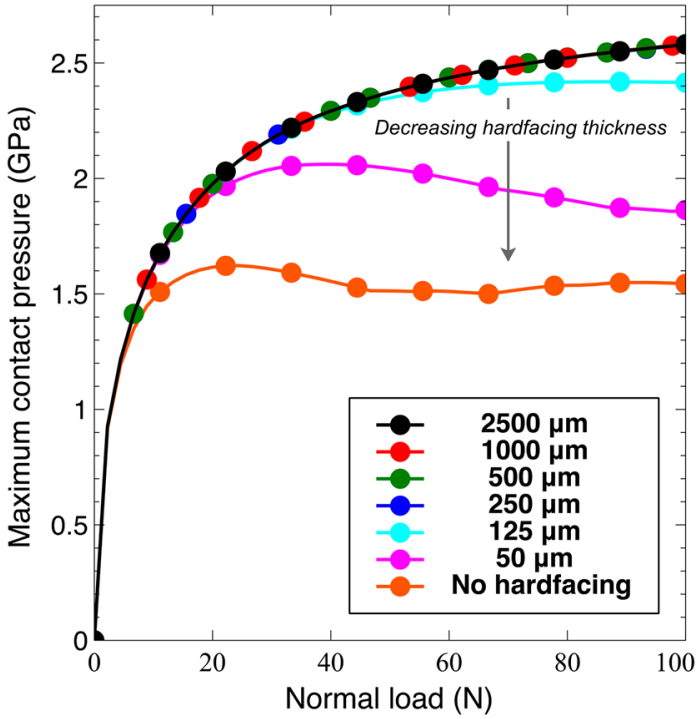

Figure 4.14 Influence of the hardfacing layer thickness on the maximum tensile stress and maximum contact pressure by an alumina ball (radius = 3.175 mm).

Figure 4.15 presents the maximum equivalent plastic deformation in the base AISI 316 material at the interface with the hardfacing. Similarly to the contact pressure behavior, it can be seen that the hardfacing thickness can be reduced by a factor of at least 10 without significantly affecting the overall tribological properties in the previously reported wear conditions. A hardfacing layer thickness of 250 µm achieved complete protection against plastic deformation up to a normal load of 70N while decreasing this thickness sharply reduce the load required for brinelling damage in the base material. Using this methodology, it is possible to optimise the architecture for the local tribological requirement in terms of materials elastoplastic properties and layers thicknesses.

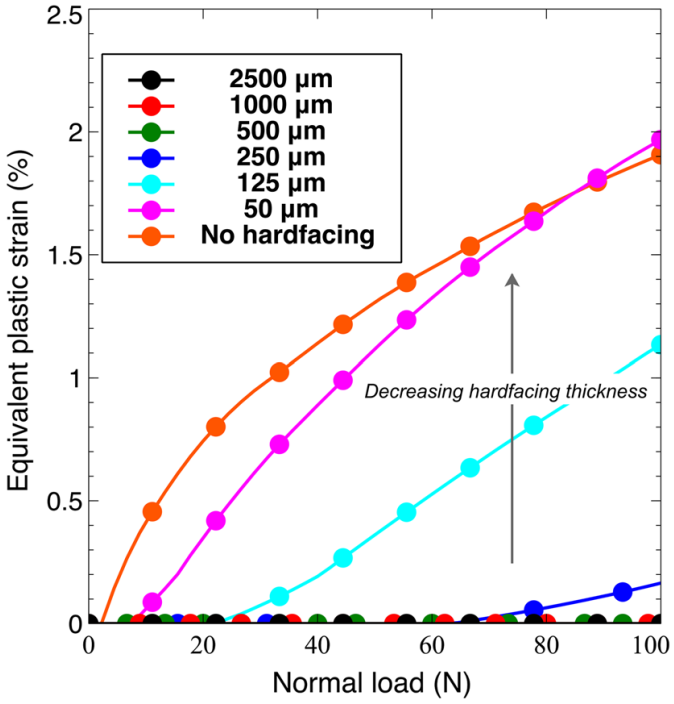

Figure 4.15 Influence of the hardfacing layer thickness on the equivalent plastic strain in the AISI 316 substrate close to the interface with the Co-Cr hardfacing.

4.6 Conclusion

In this study, we investigated the resistance to yielding and fracture and the wear performance of duplex-coated AISI 316 stainless steel. As a first step, the load to initiate permanent deformation was measured experimentally, with results in close agreement with finite element modeling predictions. The critical normal load to fracture for the W-WC coating was related to a critical surface tensile stress of around 5.0±0.5 GPa. The wear tests revealed a higher wear rate at higher load when the hardfaced interlayer was used. The finite element modeling results revealed that the higher wear rate was caused by the increased contact pressure due to the higher stiffness of the Co-Cr interlayer compared to the AISI 316 substrate. Using Co-Cr hardfacing as a support layer for W-WC has been demonstrated to be beneficial by delaying both indentation and fracture damage: the higher hardness of the interlayer delays the initiation of plastic deformation, and its load-carrying capacity limits the generation of tensile stress at the surface. Therefore, finite element modeling has been demonstrated as a valid approach to predict the load-carrying capacity of a coated system. In the near future, this component-scale surface contact modeling approach will be

applied to the system-scale (whole valve) to predict the behavior of coated surfaces under different valve design configurations and operating pressures. Finally, we believe that this novel predictive modeling approach will become an essential tool to address current and future challenges faced by the valve manufacturing industry.

CHAPTER 5 ARTICLE 2: ASSESSMENT OF FRACTURABILITY AND FRACTURE TOUGHNESS OF BRITTLE MULTILAYER OPTICAL COATINGS ON POLYMERIC SUBSTRATES

Michael Laberge[1], Delphine Poinot Cherroret[2], Sébastien Châtel[2], Oleg Zabeida[1], Ludvik Martinu[1]

[1]Engineering Physics Department., Polytechnique Montréal, Montréal, QC, Canada, H3C 3A7

[2]Essilor International, R&D, 81 boulevard Jean-Baptiste Oudry 9400 Créteil, France

Surface and Coatings Technology

5.1 Preamble - Methodology details and novelty of the study

In this study we investigated the propagation of cracks under *in-situ* tensile testing in a brittle oxide optical coating deposited on a polymer substrate. In a sense, the problematic is similar to the one presented in Chapter 4 since the high compliance (or equivalently, the low load carrying capacity) of the substrate is responsible for inducing large deformation in the coating leading to its subsequent failure. However, contrarily to the Chapter 4 study, in this case the solution to this problem cannot be through the increase of the load carrying capacity of the system, since high compliance of the substrate is required by the application. To attack this problem, we have investigated the influence of the coating design on its fracture properties to extract relevant insights to enhance the coating resilience. When subjected to uniaxial tensile loads, we have identified that the main fracture mechanism was the propagation of channelling cracks across the surface. The use of *in-situ* testing to assess the fracturability of single layer coating is commonly applied to evaluate the shear strength of the coating-substrate interface using the Agrawal and Raj model [161]. With this approach, the coating crack density is followed as a function of the increasing applied strain (see Figure 5.1). The crack density curve is used to extract two principal information: first, the crack onset strain which is the critical tensile strain that initiates the propagation of channel cracks in the coating, and second, the crack density at the saturated crack spacing, which is directly proportional to the interface shear strength in the Agrawal and Raj model. Beuth derived a relation for the steady-state energy release rate of a channeling crack as a function of the critical tensile strain in the coating [24]. He developed a general solution and exposed the importance of the elastic

properties mismatch. Agrawal and Beuth pioneer contributions are highly regarded by the scientific community and are still commonly used to characterize single layer brittle films on compliant substrates.

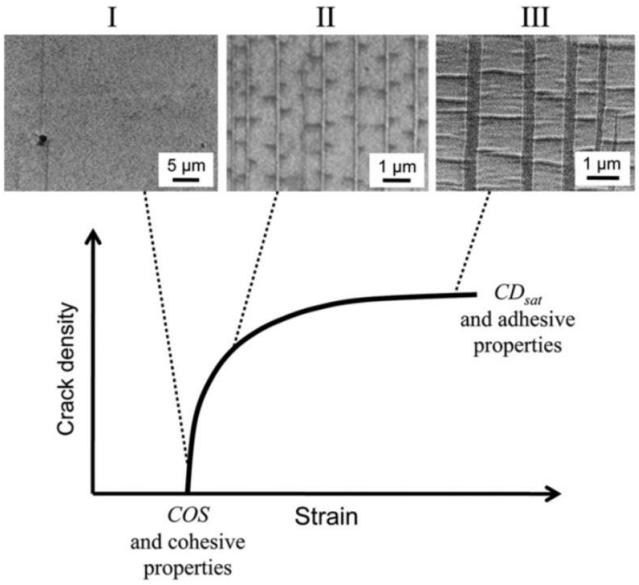

Figure 5.1 Typical curve of a *in-situ* tensile experiment showing the crack density evolution as a function of the applied strain. [162]

Characterization of multilayer coatings requires the development of numerical models. Two principal approaches are found in the literature; one is using finite fracture mechanics, and the other is using cohesive zone modeling. Finite fracture mechanics models estimate the energy release rate of channel or tunnel cracks by calculating the difference in internal energy between an intact coating and a completely propagated crack. For example, this methodology was used to estimate the influence of substrate plasticity [163], estimate the influence of temperature on the crack onset strain [164], and to compare the crack onset strain of a three layer configuration by inserting a compliant hybrid film in the architecture [165] (see Figure 5.2). The finite fracture mechanics approach was also used to evaluate the effect of partial film delamination and in their study the authors have shown that there is an interaction between channeling and delamination where they both facilitate each other's propagation [166]. The cohesive zone modeling approach was developed to simulate the formation and multiplication of cracks in the coating by inserting cohesive zones with finite toughness in the coating and at the interface. This approach was used to

study the stress distribution inside cracked segments, and how those interact as the crack spacing reduces with crack multiplication [122]. The approach was also used to study the influence of plastic deformation and stress transfer to the cracked segment on the delamination mechanisms [167].

In the paper presented in this chapter we developed a fracture mechanics approach based on the evaluation of the energy release rate using the J-Integral. Two main original ideas were proposed. The first innovation, depositing a top coating of different thicknesses that will always fail at lower strain than the bottom layer, allows one to calculate the energy release rate of a penetrating crack, and thus obtain a precise evaluation of the fracture toughness of the bottom layer. The second innovation was to apply the same approach to a multilayer configuration; in this case we characterized the failure sequence in a four layer optical stack, and we were able to propose a design criterion that would inhibit the formation of a visible crack pattern at the surface. We believe that the novel approaches presented in this article can have potential impact for the community, both for the practical evaluation of thin film fracture toughness, and to assist the design of highly resilient films on flexible substrates.

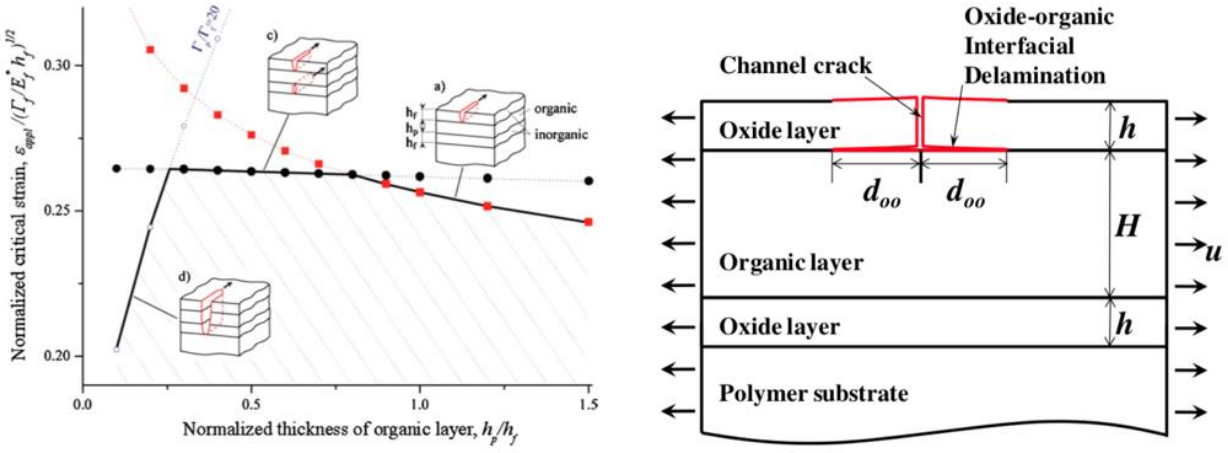

Figure 5.2 (a) Influence of a three layer coating architecture on the critical strain showing an optimal region in terms of the thickness ratio between the organic and inorganic materials [165], (b) Schematic representation of a model taking into account a partial delamination of the film to evaluate the energy release rate of a channeling crack [166].

5.2 Abstract

SiO_2 and ZrO_2 thin oxide films used as low and high index optical coatings were deposited on polymeric substrates precoated by an organosilicon hardcoat. The samples were subsequently subjected to *in situ* uniaxial tensile testing and, using optical microscopy, the failure of the films was followed as a function of the externally applied strain. From the sudden jumps in the visibility of the cracks opening we were able to discriminate between channel cracking limited to the oxide film and more sever failures that propagated deeper inside the hardcoat. The crack onset strain (COS) for both oxides was determined for single layer depositions as a function of thickness. Exploiting those values, a finite fracture mechanics model was developed which allowed us to evaluate the corresponding fracture toughness. For both films, results using this methodology correlated well with values reported in the literature. In addition, we proposed a novel approach to determine the fracture toughness of brittle films by using a bilayer coating taking advantage of a low strain to fracture material harnessed to create an initial notch of controlled length. This approach allowed us to assess the energy release rate using the J-Integral method with defined notch geometry, and thus to get rid of the uncertainty related to the intrinsic defect size present in the studied materials. Finally, this method was extended to study multilayer stacks to estimate failure pathways.

5.3 Introduction

The design of numerous advanced technological devices frequently combine the use of brittle functional thin films deposited on low elastic modulus and highly compliant substrate materials, such as in the case of optical coatings on plastics [168]. When such devices are subjected to mechanical or thermal solicitations, the important mismatch of the thermo-mechanical properties between the films and the base material generates high stress concentration, which in turn limits the durability and lifetime of the whole component [169]. Mechanical failure of the coatings themselves is due to their brittle nature and the complex interaction between the coating toughness, adhesion to the substrate, and the origin and nature of mechanical deformation [27], [29], [170], [171].

The most common types of failure related to thin films are the growth of cracks in the film and/or debonding of the film from the substrate [28]. Propagation of the cracks is activated when the energy release rate at the crack's front exceeds the critical energy release rate of the film, namely its toughness. In the context of highly adhering stiff brittle films supported by a flexible substrate, the most common cracking processes are the propagation of defects by channeling and/or tunnelling (illustrated in Figure 5.3). Channel cracks are through-coating failures originating from a surface defect that subsequently propagates in the direction parallel to the surface, until it crosses another channel or the edge of the surface [25]. Tunnel cracking occurs when a buried layer fails prematurely, and it consequently initiates a region of stress concentration which can then be propagated to the contiguous layers. For weakly adhering coatings, debonding of the films may occur more frequently, and it is observed as adhesive failure such as delamination and buckling [26], [172]. These mechanical issues are present in diverse applications where functional coatings are used in conjunction with a compliant polymer substrate, for instance diffusion barriers [173]–[176] and optical filters [177]–[179].

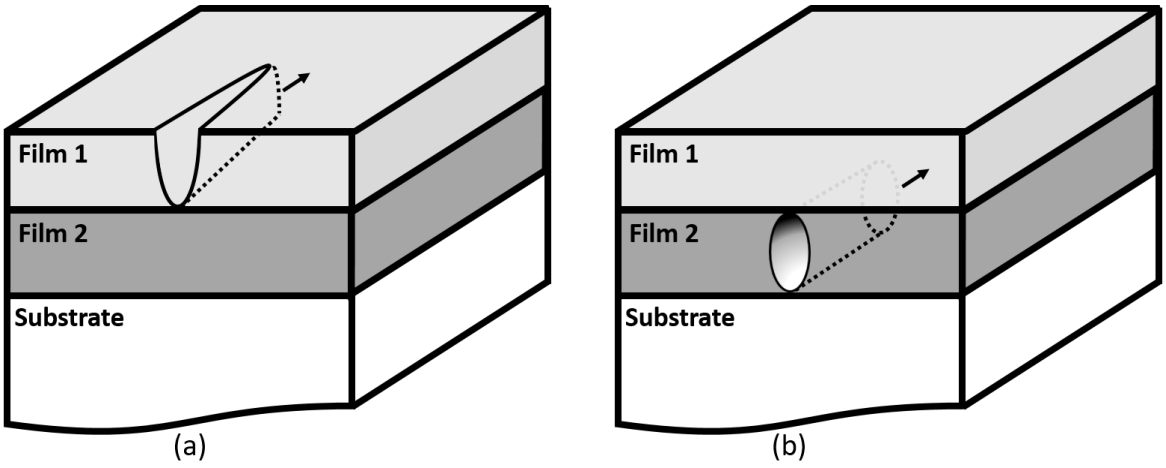

Figure 5.3 Schematic illustration of (a) channelling and b) tunnelling failure types in a bilayer system. The arrows indicate the crack propagation direction

The present study is motivated by a need to better understand the failure mechanisms related to the surface wear and subsequent device deterioration in optical coatings and plastic substrates as illustrated in Figure 5.4. The crazing patterns are a consequence of extreme mechanical/thermal

loads, and they exhibit a typical visible wear associated with the mismatch of the mechanical properties between the transparent metal-oxide materials used in optical coatings and the polymeric substrate. Similar issues occur in the quest for durable flexible electronics designs; this stimulates present efforts to enhance the device properties by introducing compliant organic films in the stack design. This hybrid approach, combining organic and inorganic films, has also been successfully applied to improve mechanical stability of optical filters [177], [178], [180]. While this new approach undeniably improved the mechanical resilience and flexibility, there is still a lack of understanding about the fundamental failure mechanisms from which more general design rules could emerge. The absence of a reliable design pathway still poses many challenges to surface engineers who have the hard task to optimize coating architectures in such a way to satisfy both the functional properties and the tribomechanical requirements of the specific application under its operational conditions.

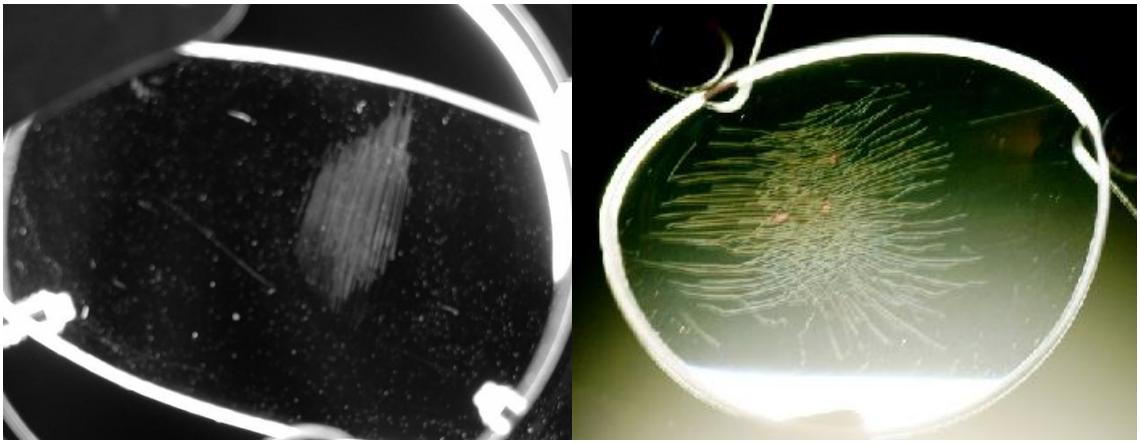

Figure 5.4 Crazing patterns formed on a plastic lens provided with an optical coating stack after the system has been subjected to extreme mechanical and thermal loads.

Uniaxial tensile testing is frequently used to evaluate the elastoplastic behavior of bulk materials from the measurement of strain in the gauge region. With the addition of an *in situ* optical microscope, its applicability can be extended to the study of layered media. Evaluation of the shear strength of the film-substrate interface using the crack density saturation has been developed by Agrawal and Raj in the late 1980's [161]. In fact, *in situ* tensile testing has recently been demonstrated as a powerful tool allowing one to follow the initiation and propagation of cracks

induced in the surface coating as a function of an externally applied tensile strain in relation to the cohesive and adhesive properties within the film system [161], [181], [182].

In the present work, we studied the failure of evaporated thin metal oxide films (between 20 nm and 200 nm thick) deposited on polymeric substrates, provided with a hardcoat, subjected to uniaxial tensile testing, allowing us to evaluate the resistance of the different oxides to tensile cracks. Combining those experimental observations with a continuum mechanics model, we studied the underlying mechanisms responsible for the different failure modes. First, a finite fracture mechanics methodology [183] was applied for the evaluation of the toughness of the single layer and bilayer metal oxide film systems. The results were then compared to a proposed novel methodology using a bilayer coating consisting of at least one material with a significantly lower strain-to-fracture than the other layer. The initial failure of the former layer is exploited to generate defects with controlled length and orientation such that they facilitate numerical assessment of the stress intensity factor at the critical strain without ambiguity about the initial defect size distribution present in the film. Finally, from the numerical evaluation of the energy release rate for different defect morphologies and location in the stack, we were able to formulate general design rules applicable for enhancing the mechanical resistance of multilayer structures deposited on polymeric substrates.

5.4 Experimental procedure

5.4.1 Substrate preparation

The substrates used in this study were dog bone specimens made of polymer (polycarbonate) covered by a ~4.5 μm thick organosilicon hardcoat. Samples were precision machined on a CNC milling machine (Charly Robot, Mecanumeric), with a 2 mm diameter milling cutter. The final dimensions of the dog bone samples are presented in Figure 5.5.

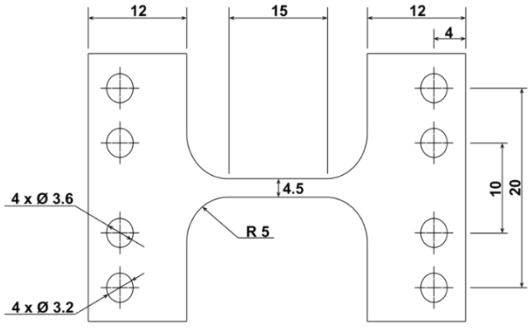

Figure 5.5 Schematic illustration and dimensions of dog bone specimens. Dimensions indicated are in mm.

5.4.2 Film deposition process and conditions

The films were deposited in a box coater system (Boxer Pro, Leybold Optics). The chamber was pumped to a base pressure (<10^{-5} Torr) using a turbomolecular pump. ZrO_2 and SiO_2 layers were produced by evaporation using an electron beam (e-beam) gun mounted in the centre of the bottom plate. During the deposition of some of the layers, the ion assistance (IAD) was provided by an end-Hall ion source (EH-1000, Kaufman & Robinson, Inc. [16]) fed with pure oxygen (99.98%) at a fixed flow. Single layers of both materials with thicknesses varying from 20 to 200 nm were deposited, as well as different bilayer systems with a fixed SiO_2 and variable ZrO_2 thickness (Figure 5.6). Both materials were also deposited on crystalline silicon substrates for complementary mechanical and optical characterizations. Finally, an optical multilayer stack was also studied with its four-layer architecture presented in Figure 5.6 (d).

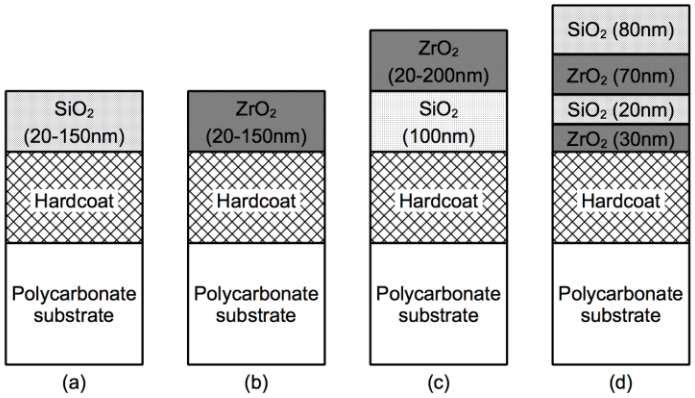

Figure 5.6 Schematic diagram of the different oxide stacks under investigation: a) and b) Monolithic coatings, c) Bilayer coatings, d) Multilayer coatings.

5.4.3 Mechanical characterization

Nanoindentation measurements were performed on 100 nm single-layer oxide films deposited on silicon wafers using an MTS XP system equipped with a Berkovich diamond tip. Silicon wafers were used to limit the influence of the substrate effect which is otherwise very significant when characterizing films deposited on polymeric substrates. The Young's modulus was determined from the continuous stiffness measurements and using the Oliver and Pharr methodology [184]. For each sample, 3 sets of 25 indentations were performed and the average moduli are reported. The hardcoat and polymer substrate were also characterized independently. The Poisson's ratios were determined from a coupled technique using picosecond ultrasonic and Brillouin light scattering measurements to estimate mechanical wave velocity propagating in the coating. Assuming mechanical isotropy and using density obtained from X-Ray reflectivity, the Poisson's ratio can be calculated from the thin film elastic constants. Finally, the coatings residual stress was estimated from the substrate curvature method: A thin glass strip (60mm x 50mm x 0.15mm) was placed in the deposition chamber next to other substrates, and its radius of curvature was measured before and after deposition using a Tencor P-16+ surface profilometer. The in plane residual stress of the thin films was calculated using the difference in the radii and the Stoney equation [185].

5.4.4 Micro-tensile test

The micro-tensile tests were performed on a Deben's micro-tensile stage (5 kN tensile, compression and horizontal bending stage), and optical microscopy was used to assess the crack density and visibility as a function of applied tensile strain ϵ_a. Digital image correlation (DIC) was used to estimate the strain in the gauge region from a reference speckle pattern and VIC2D [186] used for the post-processing of the images. In this *in situ* configuration, the strain was applied at an elongation rate of 0,2 mm/min). The COS was estimated by identifying the first micrograph showing signs of channeling failure.

5.5 Numerical modeling

5.5.1 Monolithic coating channelling energy release rate

In brittle monolithic coatings, the main failure mode under tensile load is the initiation and propagation of channel cracks leading to the creation of a crazing pattern. Experimentally, using traditional fracture mechanics approaches to characterize the fracture toughness of submicron films has been shown to be very challenging. One of the alternative methods to access the fracture properties of coatings is the measurement of the COS using a thin film deposited on an elastic substrate which is subjected to tensile loads. The COS characterizes the critical tensile strain required to fully propagate the first channeling crack(s) for a particular coating-substrate combination. For monolithic films, the critical stress σ_c in the coating at that event is determined from the COS measurements using the Hooke's law:

$$\sigma_c = \bar{E} \cdot COS \tag{5.1}$$

where $\bar{E}$ is the plane strain Young's modulus of the film. It was previously shown that the energy release rate of a channel crack monotonically increases with the crack length until reaching a maximum value when the length is a few times the thickness of the film [25]. This maximum value is associated with the steady state energy release rate G_{ss}. In the linear elasticity fracture mechanics framework, and assuming a semi-infinite substrate, Beuth [24] obtained the following relation for G_{ss}:

$$G_{ss} = \frac{\sigma_c^2 h}{\bar{E}} Z(\alpha, \beta) \tag{5.2}$$

where h is the coating thickness, and $Z(\alpha, \beta)$ is a dimensionless factor that depends on the Dundurs parameters α, β that characterize the elastic properties mismatch between the coating and the substrate [26]. The analysis is based on mode I steady state propagation of a through-coating channel crack. Mode I is defined by an opening mode dominated by the tensile stress perpendicular to the crack path. The $Z(\alpha, \beta)$ function has to be numerically evaluated using a plane strain continuum model, while tabulated values for $Z(\alpha, \beta)$ can be found in [24].

In brittle materials, a crack will spontaneously propagate when the energy release rate reaches or exceeds a critical value G_c. For mode I propagation, the relation between the energy release rate and the mode I stress intensity factor K_I is:

$$G = \frac{K_I^2}{\bar{E}} \tag{5.3}$$

Using this relation, the following failure criterion expressed in terms of critical stress intensity factors is obtained:

$$K_I > K_{IC} \tag{5.4}$$

where K_{IC} is the classical fracture toughness. For a single layer film material, combining (1), (2) and (3) leads to a simple design criterion. For an applied strain ϵ_a, the following condition inhibits the formation of channel type cracking:

$$K_I = \sqrt{h}\bar{E}Z(\alpha,\beta)\epsilon_a \quad < \quad K_{IC} \tag{5.5}$$

When K_I value reaches K_{IC}, failure will initiate. At this point, we can estimate the fracture toughness using the measurement of the critical strain.

$$K_I = K_{IC} = \sqrt{h}\bar{E}Z(\alpha,\beta)COS \tag{5.6}$$

This relation gives a direct path to evaluate the fracture toughness assuming steady state propagation of channel cracks. Rearranging equation 6, the COS dependence versus the coating thickness is given by:

$$COS = \frac{1}{\sqrt{h}}\frac{K_{IC}}{\bar{E}}Z(\alpha,\beta)^{-1} \tag{5.7}$$

The critical strain scales linearly with K_{IC} and with the factor $1/\sqrt{h}$. That clearly corroborates experimental observations that thin films exhibit much higher strain-to-failure than their bulk form.

While this solution deals with single layer films failing by channeling, it still gives a first practical guideline for more complex structures. Having a readily available analytical solution for G_{ss} and knowing that the factor $Z(\alpha, \beta)$ is easily estimated from the literature for a wide range of elastic properties mismatch, enables the use of this methodology with relative ease.

5.5.2 Multilayer coating failure energy release rate

In this section we will extend the previous analysis by investigating the crack propagation from a failed layer in a multilayer system to the adjacent materials. In the case of channelling, the tip of the channel crack induces a high level of stress concentration which promotes the propagation toward the substrate by plane strain cracking. For comparison, a tunnel type failure creates two zones of stress concentration with different propagation directions, one toward the substrate and the other one rising toward the surface. In this case, each direction is characterized by a distinct energy release rate available, and one of them is energetically more favorable compared to the other ones.

Unfortunately, the analysis presented in section 4.1 cannot be directly applied to this situation as no general analytical solutions exist for multilayered materials. In this case, we propose to evaluate the energy release rate by determining the stress intensity factor (K_I) using the J-integral $\oint J_I$ [112] at the crack tip of the failed layers. In the linear elastic approximation, the J-integral is directly analogous to G which allows one to calculate K_I [98] using :

$$\oint J = G = \frac{K_I^2}{\bar{E}} \tag{5.8}$$

The main advantage of using this particular contour integral to estimate K_I is its low requirement on local mesh refinement compared to other approaches.

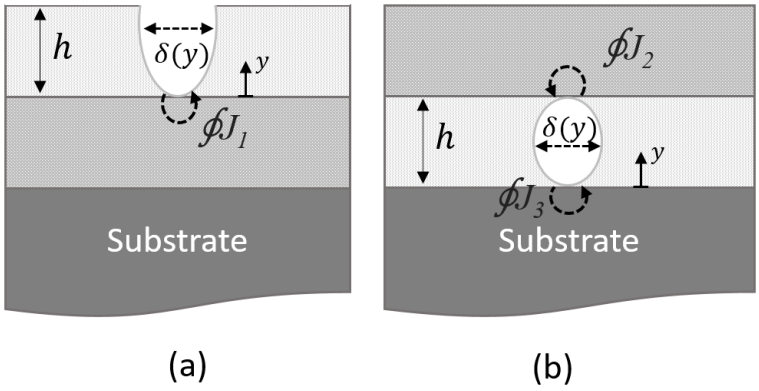

Figure 5.7 Schematic illustration of the J-integral methodology for mode I plane strain cracking propagating from a previously failed layer.

In the present work, the J-integral was evaluated using the virtual crack extension method described in [187]. A schematic representation of this approach is shown in Figure 5.7 for different initial defect conditions. Case a) presents the evaluation of G at the tip of a fully propagated channel crack, and b) presents two different locations where the J-integral is applied for a fully propagated tunnelling failure. Since G is a function of the crack/notch length, and the adjacent layer is assumed to be initially uncracked before plane strain crack propagation occurs, to calculate the J-integral we need to virtually extend the crack by a length a_p. The G value for an initially undamaged layer is then obtained by extrapolating it to $a_p = 0$ as illustrated in Figure 5.8.

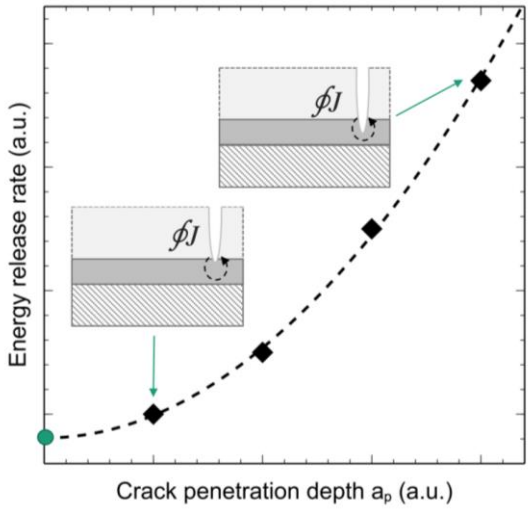

Figure 5.8 Energy release rate as a function of crack penetration a_p used to evaluate the initially uncracked energy release rate.

5.5.3 Additional finite element model details

The plane strain models discussed above were implemented using the Ls-Dyna commercial software [159]. A half symmetry plane was exploited such that the cracks are free surfaces located at the origin of the system (Figure 5.9 (a)), while the uncracked material is fixed at x=0. The strain is applied using translation displacements in the x direction on the right substrate edge, and the stress is transferred to the coating through interfacial shear stress from the base material deformation. The thickness of the modeled system is the same as the total thickness of the samples tested experimentally, while the x dimension was sufficient to generate results free of potential boundary effects. Materials are considered as elastic, and their properties (E, ν) are those obtained from the mechanical characterization as described in section 3. All materials were assumed to be perfectly bonded together, and no interfacial failure was considered. Residual stresses were applied to the different materials from the values measured by the substrate curvature method. Static equilibrium was solved before applying the tensile strain increments. Finally, a mesh sensitivity analysis was performed to select the adequate mesh refinement at the crack tip for which the J-Integral path independence is obtained.

The final computational mesh used for this study is shown in Figure 5.9 (b) with a characteristic mesh length of 0.25 nm in the densest area used for the calculation of the contour integral. In Figure 5.10 (a) we show a typical example of the principal stress field around a plane strain crack that propagated across the topmost film (Figure 5.10 (a)), and G available for further propagation in the second film calculated using the J-integral (Figure 5.10 (b)). It can be seen that the first contours lead to a lower value due to the model inability to precisely reproduce the stress field singularity very close to the crack tip. Consequently, the average value of contour 3 to 7 will be considered for the estimation of the energy release rate.

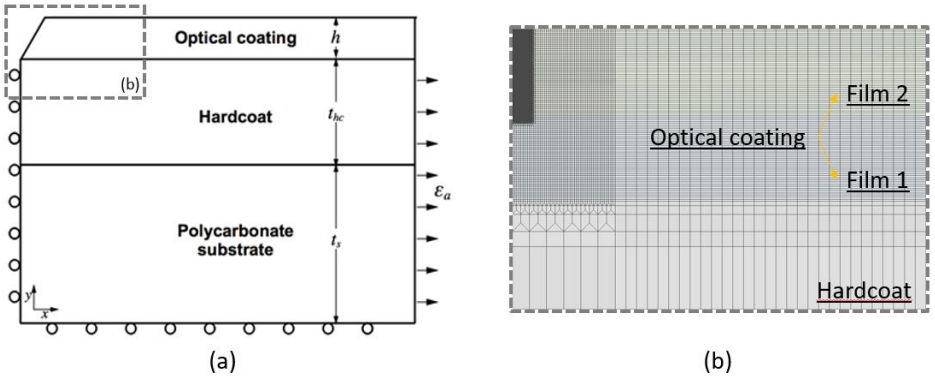

Figure 5.9 (a) Schematic illustration of the finite element plane strain model used in this study. (b) Close up of the computational mesh density close to the surface, and the refinement used in the J-integral approach.

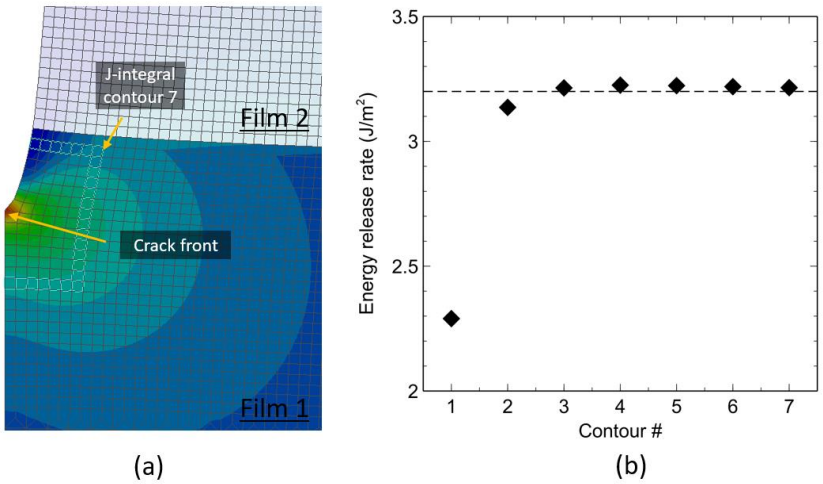

Figure 5.10 (a) First principal stress field around a crack tip and associated domain contour for the J-integral. (b) Calculation of the J-integral for different increasing contours.

5.6 Results and and discussions

5.6.1 Mechanical characterization

The starting point of this study consisted of the mechanical characterization of the different materials of the coated systems; specifically, the accuracy of the measurements is crucial since the results are also required as input in the continuum model to perform the subsequent fracture analyses (see Section 3.3). The results for the different materials under study are summarized in Table 1.

The measured elastic modulus values of both optical films, the SiO_2 and ZrO_2 evaporated layers, are slightly lower than their bulk values (SiO_2 ~ 70 GPa [188], ZrO_2 ~ 200 GPa [189]). This is in accordance with earlier investigations that attributed the differences to the higher porosity of evaporated oxides [190], [191]. The moduli for the supporting materials (Hardcoat and Polycarbonate substrate) are also in agreement with the results from previous studies [192].

Table 5.1 Summary of the materials' mechanical characteristics.

Materials	$E_r(GPa)$	ν	$\sigma_r(MPa)$	$\bar{E}\ (GPa)$	α	$Z(\alpha,\beta)$
Polycarbonate substrate	4.3	0.4		5	-	
Hardcoat	5.3	0.35		6.0	-	
SiO_2	50	0.18	-150	52.3	0.79	3.5
ZrO_2	140	0.27	+50	159.5	0.93	6.4

The importance of the mismatch of elastic properties between the oxides and the underlying material is represented by the first Dundurs' parameter α. Preliminary modeling results revealed that the rather significant thickness of the hardcoat (4.5 μm) compared to that of the coatings (200 nm) supresses the constraining effect of the substrate on the singular field around a crack limited to the coating. In other words, under mechanical tensile solicitations, the stress fields in the coatings are unaffected by the presence of the polycarbonate substrate; in such case, the values of α in Table 1 are calculated assuming the hardcoat as the supporting material. The values obtained for both

coatings/hardcoat ($\alpha(SiO_2) = 0.79$, $\alpha(ZrO_2) = 0.93$) combinations classify them in the stiff film on a compliant substrate category [24]. The particularity of this mismatch condition is the monotonous increase of the energy release rate as a function of the crack length penetration in the coating. This defines an unstable mode of crack propagation for which through-coating channeling is expected.

Such channeling was demonstrated using a partially-cracked-film analysis in which *G* was estimated as a function of α. The higher this parameter is, the steeper is the increase of *G* as the crack propagates.

In summary, the increase of the mechanical mismatch stimulates the unstable character of the crack propagating toward the underlying material. The measurements suggest that both films display a low level of internal stress. The zirconia films were in a state of low tensile stress, while the silica films were under compressive stress after deposition. Such compressive/tensile residual stress behavior of silica and zirconia grown by evaporation is consistent with previous investigations [193], [194].

5.6.2 Crack onset strain measurements

The first step of COS characterization was to establish a discrimination factor between cracks that were confined to the surface coating and cracks that have propagated deeper in the underlying structure. Figure 5.11 presents a typical example of what is observed with the optical microscope while the tensile test is running. The first thing to notice is the formation of parallel cracks that were observed for all coatings tested. These cracks are perpendicular to the applied strain, and they propagate across the whole sample, an effect associated with channelling failure.

The visibility of surface flaws depends on the crack opening displacement which is predominantly controlled by the stiffness of the area surrounding the crack tip. The restraining effect of the stiff coating materials restricts the crack opening displacement until the crack tip reaches the hardcoat. Once the oxide film fails, it basically acts as a crack (notch) for the hardcoat. In this situation, high deformation and large crack opening displacement will develop at the crack tip due to the hardcoat's high compliance. From the difference in crack opening displacements visible by microscopy, it was possible to differentiate between cracks limited to the coating and other defects

that propagated deeper in the hardcoat. This was also confirmed by performing surface profilometry scanning of different samples.

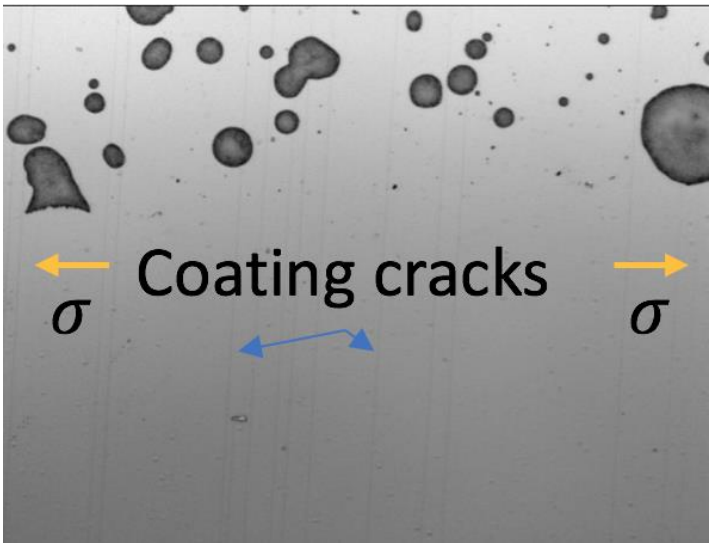

Figure 5.11 Tensile cracks generated at the surface observed *in situ* by optical microscopy showing their visual appearance.

While the analysis of deep cracks is not part of this work, it is still related to the previous discussion; for more information, we refer the readers to a recent study investigating the subcritical crack growth properties of a similar material [195].

5.6.3 Single layers

The first set of samples studied here are SiO_2 and ZrO_2 single layers of varying thicknesses (from 20 nm to 150 nm). Employing the methodology presented above, we performed *in-situ* tensile experiments to follow the formation of cracks as a function of applied strain. The strain was incrementally increased until the saturation of crack density was reached, or substrate failure occurred. Results of COS as a function of thickness for both oxides are presented in Figure 5.12.

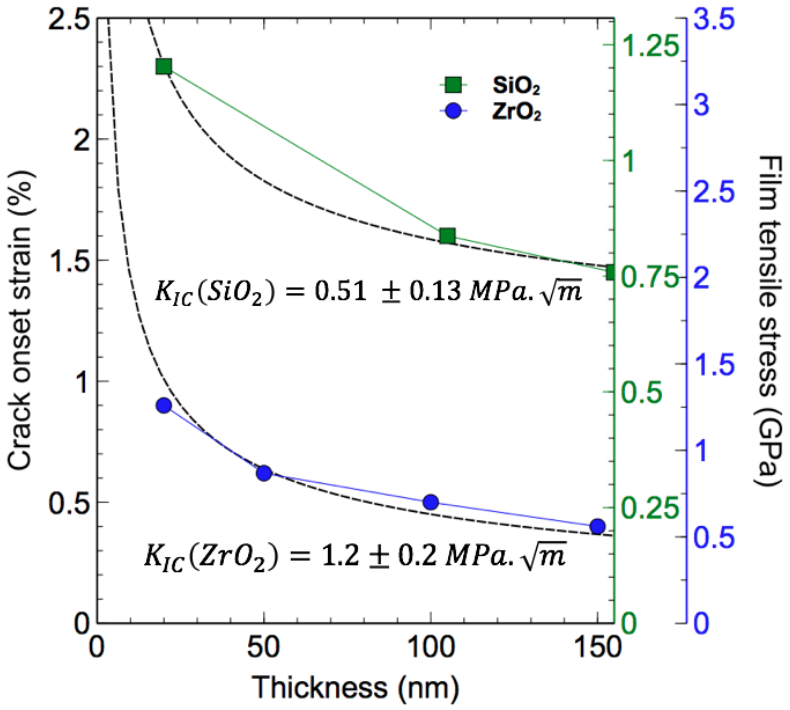

Figure 5.12 Influence of single layer thickness on the COS. The equivalent tensile stress in the films are shown on the right axis.

One can observe a strong influence of thickness on the COS: increasing the coating thickness from 20 nm to 150 nm decreased the COS by ~1% for the SiO_2 single layers and ~0.5% in the case of ZrO_2. It can also be noted that the ZrO_2 systematically fails at a lower strain (1-1.5%) than SiO_2 independently of its thickness.

Using equation (8) and K_{IC} as fitting parameter, we were able to evaluate the mode I fracture toughness for both materials. The results of the analysis are presented in Figure 5.12. The values estimated in this study using the crack channeling approach ($K_{IC}(SiO_2) = 0.51 \pm 0.13\ MPa.\sqrt{m}$), $K_{IC}(ZrO_2) = 1.2 \pm 0.2\ MPa.\sqrt{m}$) are relatively close to the bulk properties reported in the literature (SiO_2 ~ 0.62-0.67 $MPa.\sqrt{m}$, ZrO_2 ~ 1-4.5 $MPa.\sqrt{m}$ [196]). The fact that the values measured in this work are lower may be justified by the intrinsic porosity inside the evaporated silica and zirconia coatings. Increased porosity level in ceramic materials has been shown to cause a drop in fracture toughness [78].

5.6.4 Bilayers crack onset strain

In the second part of this work, we investigated the fracture behavior of ZrO_2/SiO_2 bilayers. In this case, we deposited a series of films consisting of a 100 nm SiO_2 layer topped by a ZrO_2 coating with a thickness ranging from 20 nm to 200 nm. The general objective in this part is to study the influence of a weaker top layer on the stack performance and, at the same time, characterize the SiO_2 fracture properties.

One of the noticeable observations from the previous section was the fact that the COS for $Zr0_2$ is systematically lower than the one for SiO_2 for all thicknesses under investigation. Exploiting this fact, we will assume a similar behavior for bilayers. With this hypothesis, the cracks in the ZrO_2 layers will form a notch that generates stress concentration at the intersection with the SiO_2 layer. Therefore, a higher $Zr0_2$ thickness increases the length of the notch, hence the crack opening and the stress intensity factor for an equivalent strain. Specifically, Figure 5.13 presents the difference in crack opening displacement between a top layer of 20 nm as compared to 200 nm.

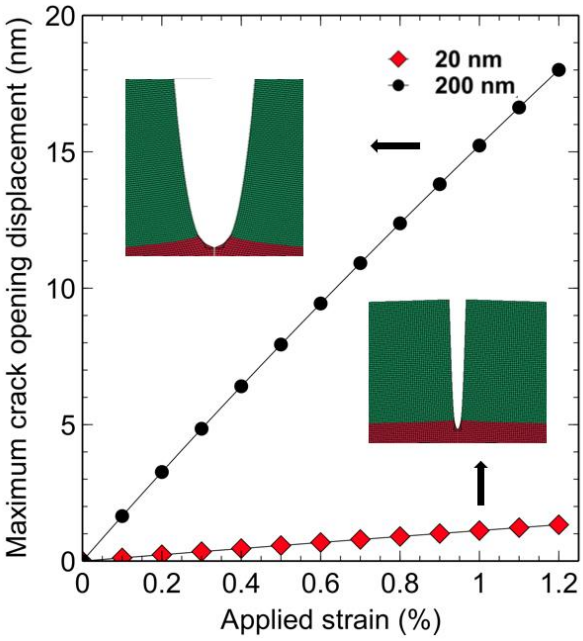

Figure 5.13 Crack opening displacement comparison between a 20 nm and a 200 nm ZrO_2 top coating in the bilayer systems. Also shown is the modeled deformation around the crack tip for an applied strain of 1%.

If the crack propagation is unstable, then the K_I values at COS can be used to estimate the sublayer fracture toughness by calculating the J-integral at the cracked ZrO_2 tip under COS conditions. We verified this by observing that the energy release rate is increasing monotonically with the crack length penetration in the SiO_2 layer. Accordingly, the fracture toughness values using this approach are presented in Figure 5.14.

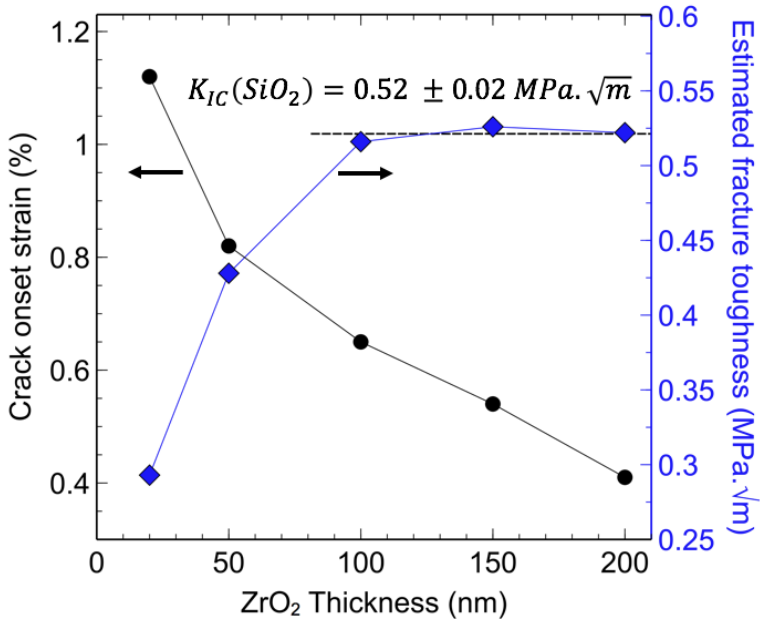

Figure 5.14 Influence of the top ZrO_2 layer thickness on the COS for bilayers.

The estimated SiO_2 fracture toughness for the 20 nm and 50 nm top ZrO_2 are both much lower. This may be explained by geometric and size effects which made the 2D plane strain fracture model hypothesis inapplicable. However, the K_C values estimated using the 100, 150 and 200 nm top layer thicknesses are similar to the results obtained with the single layers. Compared to the single layer channeling analysis, one of the major advantages of this method is that it is not dependent on the intrinsic defects present in the films to initiate the crack propagation.

5.6.5 Multilayer crack onset strain

Finally, the multilayer (4 layers) configuration presented in Figure 5.6 (d) has been subjected to the same tensile tests in order to characterize its COS and to improve our understanding of its overall fracture behavior. In this architecture, the weak ZrO_2 layers are buried, and therefore, they generate tunnel cracks when they fail before the topmost SiO_2 layer. In the first step, we calculate

G for the different possible propagation paths originating from the pre-cracked zirconia (Fig. 5.15). These different paths are characterized by distinct G values represented by the different contour integrals $\oint J_{1,2,3}$. Figure 5.15 presents those different paths as a function of the applied strain.

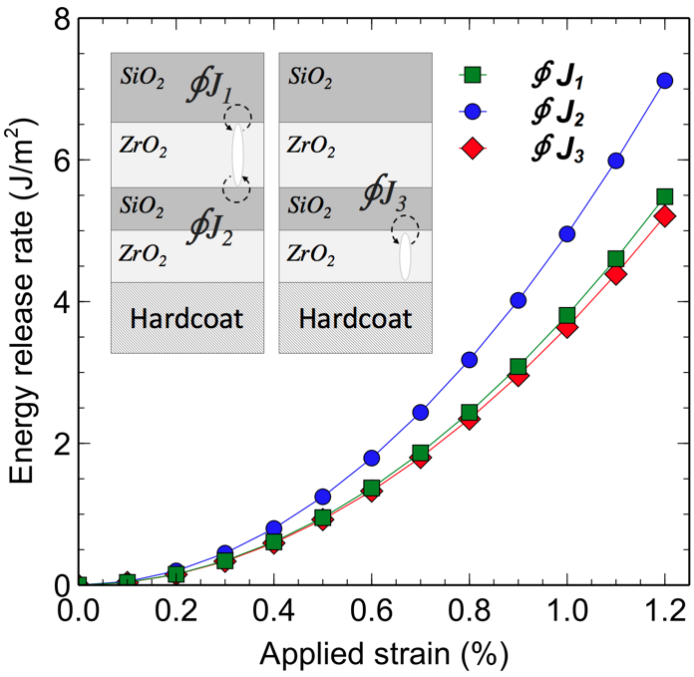

Figure 5.15 Energy release rate as a function of applied strain for the different propagation paths in the multilayer coating.

The $\oint J_2$ crack is the first one to propagate since it possesses the highest G value among all the possible paths. Considering the failure of the buried SiO_2 layer, we then calculated $\oint J_{1^*}$ in this new damaged condition ("post-failure") as presented in Figure 5.16. The G value of the $\oint J_{1^*}$ path is systematically higher than for $\oint J_2$. Consequently, once the buried layer fails, the crack will immediately propagate in an unstable mode across the top SiO_2 layer, hence through the whole stack, and it will become visible. Using the values of K_C estimated earlier, the model predicts that the buried SiO_2 layer (and the whole stack) fails at a strain of 0.95%, which is slightly higher (but very close to) than the experimental observation (0.8%). The complete failure sequence is illustrated Figure 5.17.

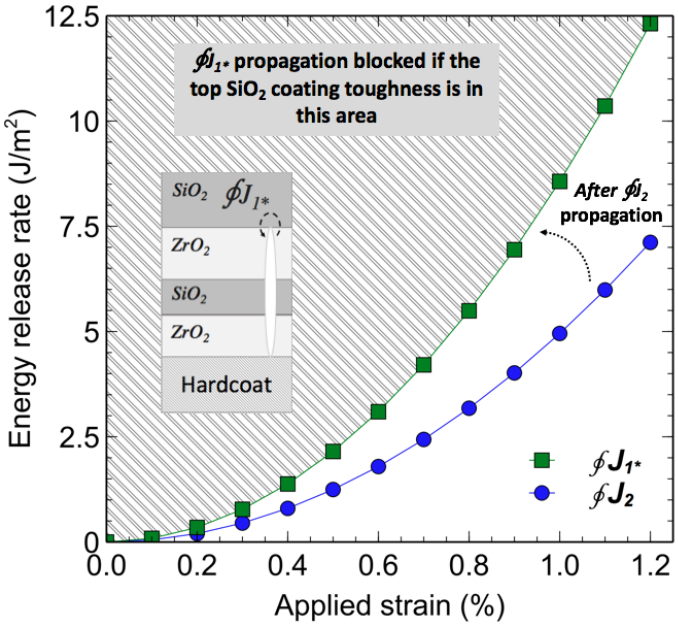

Figure 5.16 Energy release rate as a function of applied strain for the post failure $\oint J_{1*}$ propagation paths in the multilayer coating.

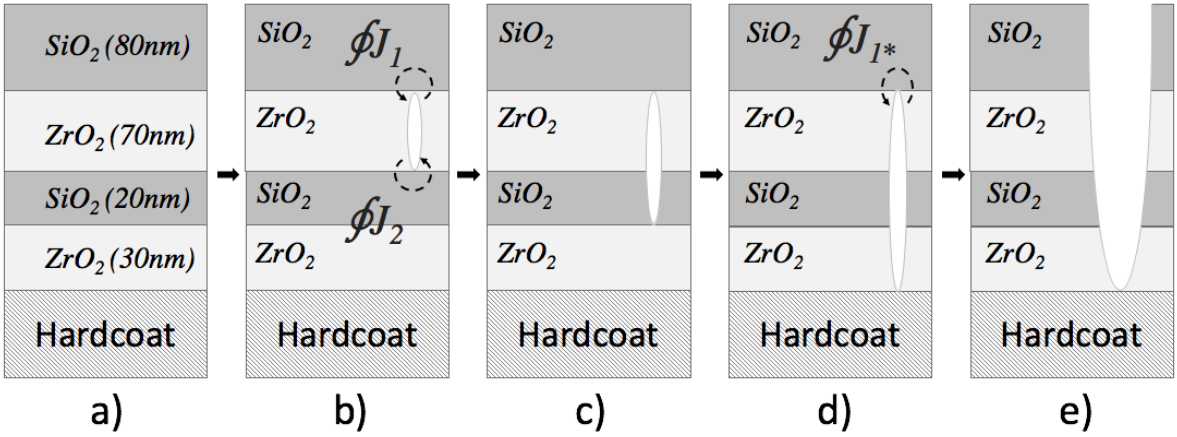

Figure 5.17 Complete failure sequence of the multilayer coating: (a) Intact coating subjected to tensile stress, (b) failure by tunneling of the ZrO_2 layers, (c) propagation in the buried SiO_2 layer, and (d) failure of the top SiO_2 layer and through-coating failure leading to high crack opening displacement and visible damage.

5.7 Conclusion

In this work, we studied the fracturability of transparent oxide optical coatings on polymeric substrates using *in situ* uniaxial tensile test experiments. Single layers, bilayers and multilayer (four layers) stacks were investigated and the crack onset strain of the different configurations was assessed experimentally. The typical failure mode was the formation of parallel cracks perpendicular to the applied deformation which was associated with channelling cracks. Using the steady state channeling crack analysis, we evaluated the fracture toughness of evaporated SiO_2 and ZrO_2 coatings that were found to be consistent with the literature. After noticing that the ZrO_2 layers systematically fail at a lower strain than the SiO_2 layers, we exploited this behavior to evaluate the fracture toughness of SiO_2 considering plane strain crack propagation initiated from the notch generated by the failed ZrO_2. This approach, similar to classic fracture mechanics, led to results that were consistent with the single layers measurements. To the best of our knowledge, this is the first study to exploit this "weak layer" approach to generate a fracture notch at the nanoscale.

Finally, by analyzing the different crack propagation paths in a multilayer coating we have developed a prototypical workflow to perform a fracture analysis of a multilayer film subjected to tensile loads. It started with the identification of the weakest link in the coating structure by characterizing the layers independently. We then applied the J-integral approach to predict the subsequent failure pathway that showed to be consistent with the experimental observations. We maintain that numerical analysis approaches, such as the ones performed in this work, are an essential step toward the design of optical coatings with enhanced tribomechanical performance. As a next step, additional investigation has to be performed to study the limitations of the 2D model applicability for very thin top layers such as ZrO_2 used here. Finally, applying the methodology to estimate the fracture toughness of other optical coating materials would further validate its reliability.

CHAPTER 6 INVESTIGATION OF BIO-INSPIRED FUNCTIONALLY GRADED COATINGS FOR WEAR RESISTANCE

6.1 Preamble - Methodology details and novelty of the study

In this study we were interested in protecting Ti-alloys subjected to high velocity impact from sand erosion. Likewise the studies presented in Chapters 4 and 5, we are confronted with the problematics related to the high mismatch of elastic properties between the film and the base material leading to high stresses at the interface and limited fracture resistance of the coating. Erosion resistance is related to the capacity of a surface to withstand material losses resulting from cohesive and interfacial damage induced by an impacting particle. For different applications, the surface is subjected to distinctive particles with particular size and velocity distributions. To this day, the highest erosion resistance is obtained using hard ceramic coatings [197]. In this type of coating the fundamental material removal mechanism is the initiation and propagation of cracks that intersect. The main methodology to model the erosion wear rate of brittle material is a semi-empirical approach based on brittle elastic-plastic indentation models. These approaches estimate the volume loss V_e caused by a single particle impact using an equation of the following form [198], [199]:

$$V_e = C_1 V_p D_p \rho_p E_s H_s K_s, \tag{6.1}$$

where C_1 is a proportionality factor determined from erosion tests, V_p, D_p, ρ_p are the velocity, diameter and density of the impacting particle and E_s, H_s, K_s are the surface Young's modulus, hardness and fracture toughness, respectively. The significant limitations of this semi-empirical approach are, first, the necessity to experimentally access the constant C_1, and more importantly, its inability to model the behavior of complex coating architectures.

Since the early 2000s, numerous publications regarding numerical modeling of multilayer coatings subjected to sand erosion have been published. A vast majority of these studies are related to the evaluation of stress distribution during particle impact where the brittle coatings are modeled as perfectly elastic materials deposited on elastic-plastic base materials. By varying the coating architecture, the authors have studied the influence of coating thickness [200], base material properties [201], impacting particles shape and size [202], laminated structures [203], multiphase

structures [204] and Young's modulus profile [201] on the stress distribution across the coated system. This continuum mechanics approach, while very helpful to gain insight in the level of stress induced from impacting particles, is lacking since it does not take into account the fracture mechanisms responsible for brittle erosive wear. To simulate the material removal mechanisms, other studies exploited a continuum damage mechanics approach (see Figure 6.1) to model the accumulation of damage and erosion of material [205], [206]. Lately, to avoid the high mesh sensitivity of the continuum damage mechanics method, a lot of effort has been devoted to develop meshless methods (Smoothed-particle hydrodynamics [207], Discrete element methods [208], Peridynamics [125]). These approaches are ultimately limited by the characterization of the continuum damage mechanics parameters which require extensive experimental tests, some of which are difficult, or simply inapplicable, for probing brittle thin film coatings.

In the case study presented in this chapter, we have developed a fracture mechanics methodology to assess the erosion resistance of a functionally graded coating. By introducing flaws in the coating at different locations, the crack driving forces were evaluated during an impact using the J-integral method. Many aspects of this study present unique ideas not yet explored in the literature. To the best of our knowledge, this is the first model simulating dynamic impact on a bio-inspired mechanically graded coating in the context of erosion resistant coating. Another original aspect of this study is the utilization of the J-Integral method to differentiate the influence of the mechanical gradient on the energy release rate for different defect morphologies. We strongly believe that the work presented in this chapter proposes a novel modeling approach with a potentially great impact on the development of erosion resistant functionally graded coating.

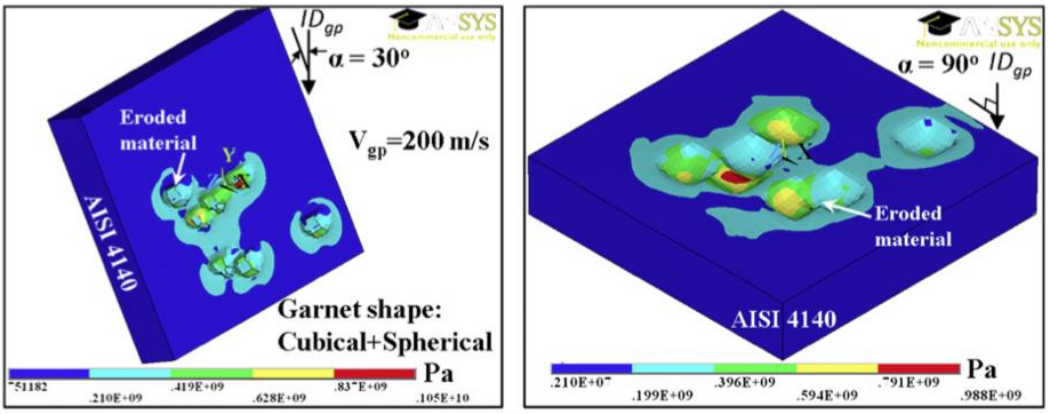

Figure 6.1 Example of a particle impact erosion model of a AISI4140 bulk material using a continuum damage mechanics model to predict the material loss. [204]

6.2 Introduction

Functionally graded materials are an advanced category of engineered materials specifically designed to survive harsh operational environments as a result of their unique properties. A functional gradient is defined by a material volume in which several physicochemical properties (crystalline/amorphous phase, Young's modulus, chemical composition, density, hardness, porosity, ect..) vary spatially in at least one direction. The concept of functionally graded material was first introduced in the late 1980s in Japan with the intention of developing superior thermally resistant material solutions for aerospace applications [209]. Exigent requirements were imposed to create a material that can withstand extreme thermal cycles without adhesion failure while also meeting the tribomechanical behavior (toughness, rigidity, resilience, wear resistance, …) standards required by the application.

In most less demanding applications, depositing a monolithic coating with a specific function (wear resistance, erosion resistance, thermal cycle resistance, …) is sufficient to reach the performance targets. However, single layer coatings are affected by tribomechanical issues that originate from the elastic properties mismatch between the film and the base material [24], [169]. This mismatch is responsible for generating high level of shear stress at the interface when the surface is subjected to extreme tribomechanical solicitations. The interface shear stress level is further increased in the presence of residual stress in the coating that limits the effective bonding capability of single layer coatings [210].

A functionally graded coating can alleviate this concern by allowing one to tailor the mechanical properties profile smoothly across the thickness of the film. The typically exploited mechanical profile consists in varying the elastic modulus from the compliant base material and increasing it to its maximum value achievable by the coating material system at the surface [209]. Mechanical gradients are also associated with a higher energy dissipation, and thus higher fracture resistance under tribomechanical solicitations. This is due to a load spreading effect which increases the effective volume over which the strain energy is dispersed.

Due to the complexity of the problem, analytical solutions for the displacement and stress fields were only developed for monotonically varying elastic constants following a power-law or an exponential function [211], [212]. The investigation of more intricate graded structures necessitates numerical modeling, consequently, only few studies have investigated mechanical gradients in which the maximum Young's modulus is not located at the surface [87]. Lately, this type of structural design was observed in the study and characterization of biomaterials displaying high resistance to fracture propagation [213], [214]. It is now established that biomaterials possess natural hierarchical structures and gradient regions in terms of composition, dimension, arrangement and orientation which are responsible for their exceptional emergent tribomechanical properties [214].

6.3 Bio-inspired materials

The vast number of biomaterials found in nature provide an almost boundless source of inspiration for material engineers. The hierarchical architecture found in those biological tissues are the results of millions of years of structure optimization imposed by the ecological constraints of the environment. The structural design elements can be seen as building blocks used by nature to give emergent properties to hierarchically structured materials [36]. Figure 6.2 presents the eight more common design elements found in biological materials.

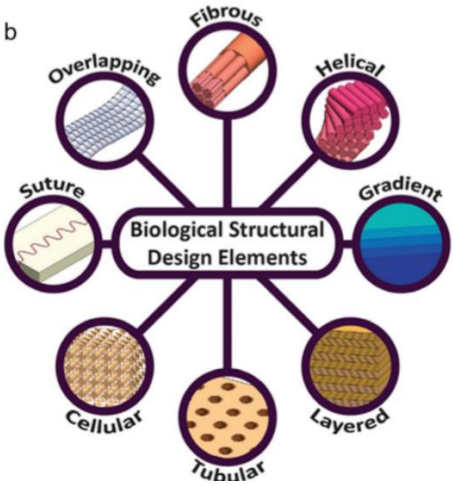

Figure 6.2 Basic structural design elements of biomaterials [214]

As we introduced in chapter 2.3, different mechanisms (pellet interlocking, gradient, …) are responsible for the toughening effects arising from the hierarchical architecture. Of those, the most important design element present in natural material may be the presence of localized gradients between dissimilar materials owing to the smoothly varying properties which supress the appearance of stress concentration in those areas. Figure 6.3 schematically presents the different approaches that nature uses to form the functional property gradients. Engineered materials which exploit and mimic those natural structures are said to be bio-inspired.

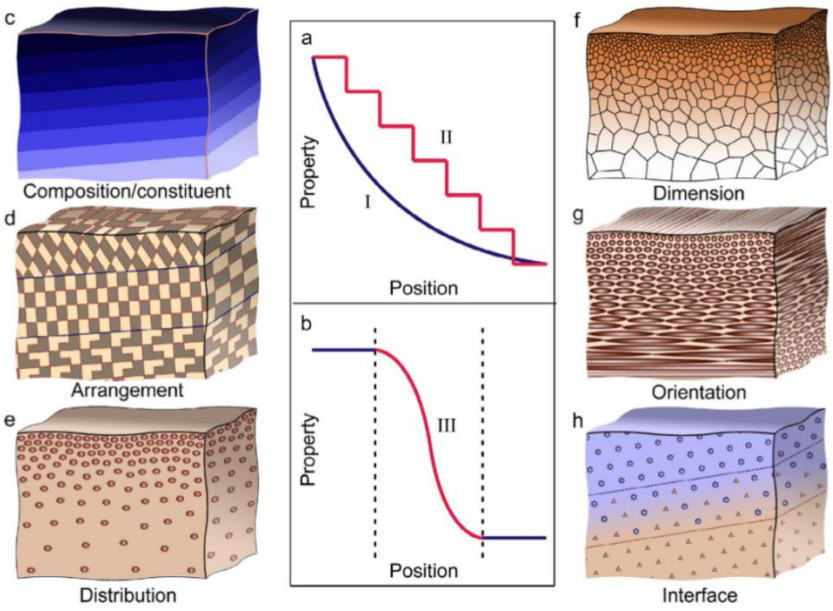

Figure 6.3 Functional gradient categories [36].

For example, lobster and crab exoskeletons are strengthened by a periodic arrangement and varying distribution of fibrils forming a tough Bouligand structure [215], [216]. Biological armors such as mollusk shells and fish scales exhibit higher effective toughness than their individual constitutive components as a consequence of a crack deflection mechanisms emerging from the platelet structure interlocking and localised gradients [35]. Bones, teeth and mantis scrimp club have been widely studied and their high hardness and resistance to fracture propagation were attributed to the functional gradient present across the different layers and interfaces joining them [213], [217], [218]. Figure 6.4 presents the mechanical profile of a human tooth from the enamel region to the dentin core. Many studies and review articles exploring the emergent properties of biological materials can be found in the literature [36], [214], [219]–[221].

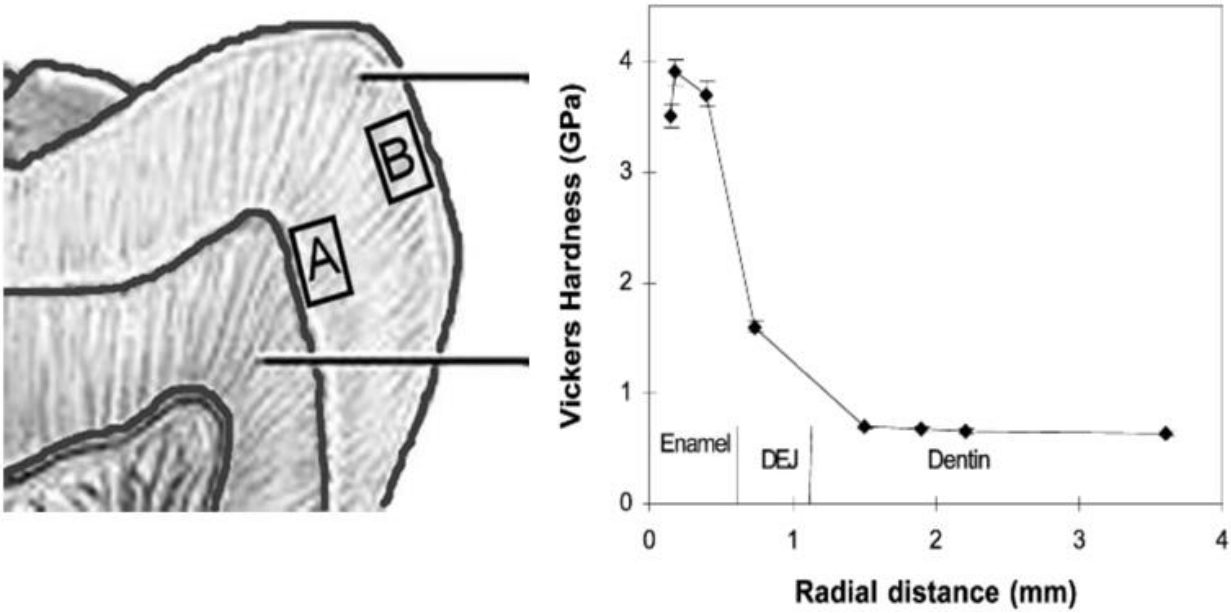

Figure 6.4 Functionally graded properties at the surface of a human tooth [222].

6.4 Functionally graded coatings

While nature had million of years of adaptation and evolution to optimise biological structures though molecular self-assembly, in practice, engineers have adopted additive manufacturing processes to deposit functionally graded layer on top of a base material. Laser metal deposition, electron beam direct deposition, ARC deposition and powder metallurgy sintering are mainly used for depositing thick coatings (> 100 μm) and can even be used as 3-D printing method for

developing structural components with functionally graded properties [223], [224]. Vapour deposition techniques such as PVD and PECVD are generally utilized for thin film coating (<10 μm) allowing the growth of ultra-hard and dense protective coatings. In all of those deposition techniques, the functional gradient is created by varying the deposition parameters, for example by regulating the relative concentration of a specific material flow during deposition or by adjusting the average deposition energy to control the growing microstructure [224].

Thermal barrier coatings for aerospace applications are designed with an increasing porosity gradient toward the surface which grants them low thermal conductivity and high thermomechanical stability [225]. So called sandwich structure consists of mechanically graded interlayer; for example, this approach is commonly used in cutting tools application where a graded $TiSi_xN_y$ interlayer is applied to reduce elastic mismatch and increase adhesion properties [226]. Bio-inspired hierarchical AlSiCN/Ti coatings mimicking the shell structure were demonstrated to have enhanced toughness and resistance to contact damage due to the ability of the structure to efficiently dissipate mechanical strain energy [227]. Orthopaedic alumina components load bearing capacity can be significantly increased by introducing a decreasing elastic gradient which results in the reduction of surface tensile stresses [228]. The influence of different mechanical profiles (increasing, decreasing and maximum modulus in the middle) were studied using graded DLC coatings deposited on aluminum substrate. It was shown that the mechanical profile with the maximum modulus at half thickness of the coating demonstrated enhanced protection against both interfacial and surface damages [87]. Graded zirconia dental implants inspired by the natural bones and teeth architectures were shown to have high resilience to crack propagation and higher biocompatibility with the host tissues [37]. Finally, we have to mention that inhomogeneous optical filters using functionally graded refractive index layers were deposited and characterized previously by members of our research group. For example, single-material rugate filters were deposited by PECVD by adjusting the plasma power levels during the film growth [229]. Silicon oxynitride-based graded filters were also deposited by PECVD by varying the precursors flow [230]. In both studies, it was shown that the tribomechanical performances of the inhomogeneous graded-index filters were superior to their multilayer counterparts.

6.5 Numerical methods

With the increasing interest toward the study of bio-materials and functionally graded materials, there is an essential need to develop new methodologies and modeling approaches for the characterization and design of such materials. Considering the complexity of the problem, only a few analytical approaches have been developed, and those are limited to a simple gradient area with monotonically varying properties. Accordingly, numerical methods based on the continuum mechanics theory have been most successful to study the mechanical response to static and dynamic loads. Those approaches often idealise the heterogenous structure of functionally graded material by a continuum with smoothly varying properties between elements. This can be achieved in two main ways: (i) by using homogeneous elements and assigning different properties compared to the elements in the direction of the gradient, or (ii) by using graded elements that extrapolate the stress gradient from the integration points during calculation.

Both approaches have shown to accurately capture the mechanical gradient response as long as the domain mesh is sufficiently refined for the first one [231]. Researchers have used this continuum mechanics approach to evaluate the stress strain field, particularly the load-spreading and energy dissipation aspect, in response to diverse tribomechanical solicitations [217]. Fracture mechanics of functionally graded coatings have also been widely studied using analytical techniques and numerical calculations using the J-integral and integral interaction methods. The main outcome of those studies is that the nature of the singular field closely follows the one developed for homogeneous materials, being equivalent in the first order approximation. However, contrarily to homogeneous brittle materials, the fracture toughness of the material is not a constant but a function of local properties. Early investigations conducted by Eishen [28], Erdogan [29] and Giannakopoulos [211] can be seen as pioneer studies in the field and are still regarded as the groundwork behind the thermo-mechanical modeling of functionally graded materials. In this regard, in the next section we will investigate the tribomechanical response of functionally graded coatings with different mechanical profiles when subjected to micro-particle impacts.

6.6 Results and discussions

6.6.1 Foreword and scope of this study

In this chapter, we are presenting two studies related to the development of erosive wear resistance of mechanically graded coatings for two different applications: (a) Functionally graded $TiSi_xN_y$ for jet engine turbine blades solid particle erosion protection and (b) Functionally graded SiO_xN_y for solar mirror sand erosion resistance. The modeling aspect of this chapter was first instigated in a general project related to the enhancement of erosion resistance for specific parts of an aircraft gas turbine. In the application that this study was focused on, a titanium alloy is used for as the structural component and TiN-based hard coatings are deposited which grants a massive increase against erosion wear. Aerospace being a highly competitive field, our industrial partner was looking for new ways to increase this protection and lifetime of the components before maintenance is required. Motivated by the rise in interest of biomimetics and bio-inspired materials with emergent exceptional mechanical properties, we had the idea to recreate a particular type of bio-inspired functionally graded surface using the wide range of elastic modulus allowable by a $TiSi_xN_y$-based coating. Many studies present the superior resilience of mechanically graded materials and coatings when subjected to harsh dynamic tribomechanical solicitations. For example, they were shown to inhibit crack propagation and increase effective toughness [214], [232]–[234], improve adhesion under tribomechanical solicitations [234] and high thermal gradients [235], improve protection from ballistic impacts by spreading the energy dissipation [236], [237], and have enhanced biocompatibility in biomedical applications [238], [239]. One noticeable natural hard material with high resistance to dynamic contact damage is the mammal tooth. It was demonstrated that the capacity to absorb more energy before failing is owed to the intrinsic toughening mechanisms originating from the functionally graded properties at the surface [86], [222], [232], [240]. The mechanical gradient in this case relate to the smoothly varying elastic modulus and hardness as a function of depth beneath the surface. This particular functional gradient is build as followed, starting from the base material, the modulus is matched at the interface, then the modulus increases to a maximum value close to the surface and finally there is a small decrease of modulus toward the surface (see Figure 6.4). In the next section (6.5.2) we used a numerical approach to investigate the crack driving forces in a graded $TiSi_xN_y$ coating with different gradient

profiles including this peculiar one found in teeth. Following this section, in 6.5.3 we will examine the deposition of mechanically graded SiO_xN_y for protection of solar mirrors operated in harsh sandy/dusty environments.

6.6.2 Functionally graded $TiSi_xN_y$ for jet engine turbine blades solid particle erosion protection

6.6.2.1 Modeling approach details

To investigate the mechanical response of coated surfaces subjected to micro-particle impacts, a plane strain dynamic finite element was developed. An explicit dynamic formulation was used, and boundary conditions are presented in Figure 6.5.

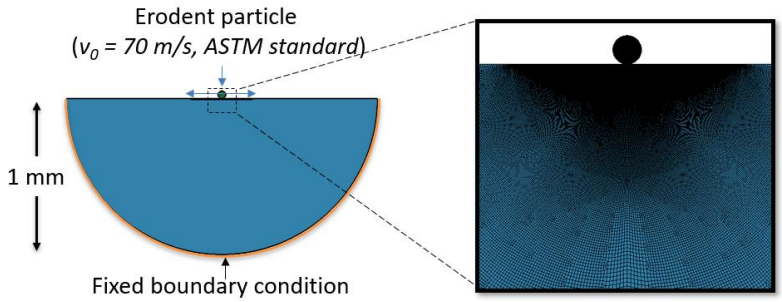

Figure 6.5 Model boundary conditions.

The domain dimensions were verified to be free of boundary effect as all stress components induced from particle impacts vanish before reaching the outer domain fixed boundary. The mesh density in the vicinity of the impact area, both in the coating and in the particle, was refined to accurately capture the stress gradients induced from the particle impact (see Figure 6.6).

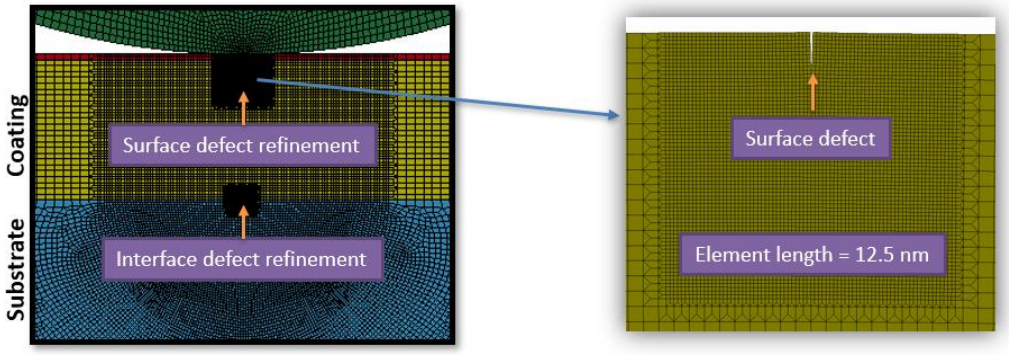

Figure 6.6 Model mesh refinement in the impact area.

The coating was bonded to the substrate material by sharing nodes at the interface. The $TiSi_xN_y$ coating and the alumina particle were assumed to behave elastically, while the Ti6Al4V substrate was modeled by a Johnson-Cook strain rate dependant constitutive relation [241]. The mechanical gradients were modeled by varying the elastic modulus of the coating in the direction normal to the surface. The erosive particles were 25 μm radius spheres with an initial 70 m/s velocity. A surface to surface penalty-based contact model was used between the particle and the surface. Residual stresses were modeled by first solving the equilibrium state of the coating-substrate system using an implicit solver, and than the particle was inserted, and the model switched back to the dynamic explicit solver. In total, 250000 fully integrated quadrilateral elements were used to mesh the domain, which took approximately 2 hours to execute using the SMP explicit solver on 4 cores. To evaluate the potential crack propagations, defects of different morphologies were introduced in the coating and the J-integral method was utilized to dynamically follow the energy release rate during the impact event. The mesh refinement around the defects were more pronouncedly refined in a way to apply the J-integral method and observe path independence. The different coating defects types are presented in Figure 6.7, while the particle impact direction was normal to the surface and centered over the defect.

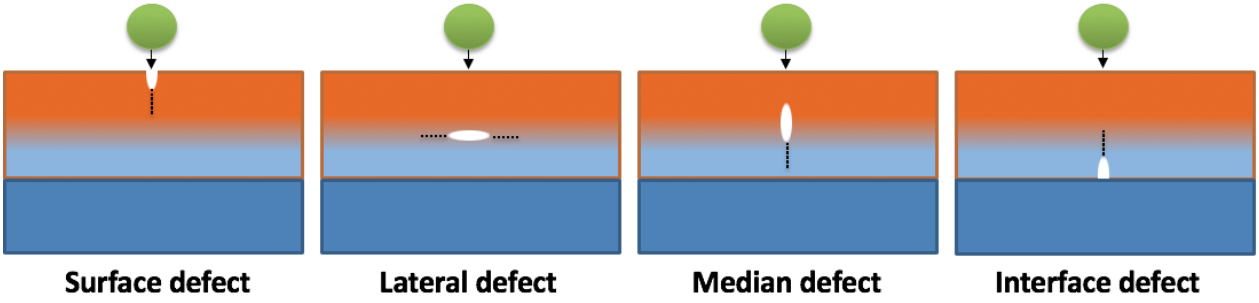

Figure 6.7 Defect morphologies under investigation.

6.6.2.2 Mechanical properties and gradients under investigation

As mentioned in the preamble, the work presented here concerns the protection of a Ti6Al4V substrate subjected to solid particle erosion wear respecting the ASTM G76 standard conditions. The mechanical properties of the different materials are presented in table 6.1. The range of properties accessible by the TiSiN coating (200 GPa – 450 GPa) was based on the reported elastic properties found in the literature [242]. Following preliminary simulation testing of the coating thickness and defect length influence, they were both, respectively, fixed at 5 μm and 250 nm.

Table 6.1 Material mechanical properties of the different materials [243], [244].

Material	Alumina (Erosive particle)	TiSiN (Coating)	Ti6Al4V (Base material)
Constitutive relation	Elastic	Elastic	Johnson-Cook *
Density (kg/m³)	3950	5100-5400	4428
Young's modulus (GPa)	350	200-450	110
Poisson's ratio	0.21	0.25	0.31
Yield stress (MPa)	-	-	1098

For this study four mechanical gradients were investigated as presented in Figure 6.8. We compared a constant modulus, a decreasing modulus, an increasing modulus, and finally the gradient inspired by the functionally graded tooth surface.

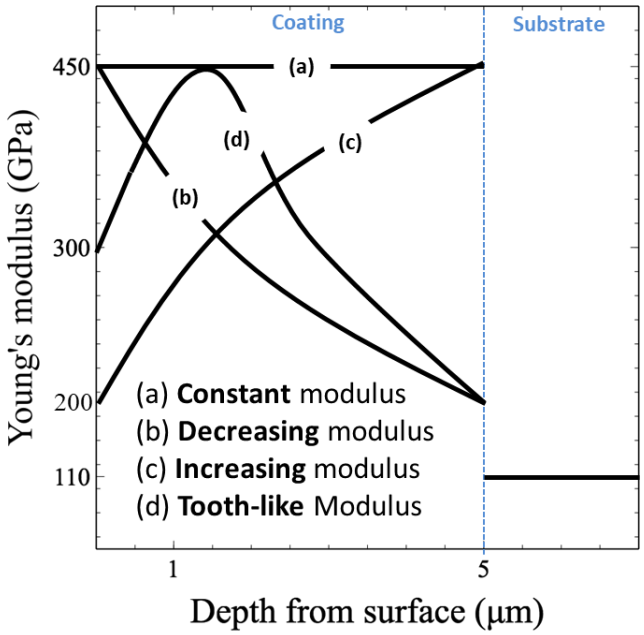

Figure 6.8 Coating mechanical gradient investigated.

The constant modulus, as its name implies, is a monolithic coating with the maximum elastic modulus reachable (450 GPa) throughout the thickness. The decreasing modulus is the traditional gradient often used to improve load carrying capacity and reduce shear stress at the interface by minimising elastic mismatch. It linearly varies from 450 GPa to 200 GPa at the interface with the substrate. The increasing modulus presents an inverse situation, starting from a minimal elastic modulus of 200 GPa at the surface and increasing linearly to 450 GPa at the interface. Finally, the tooth-like gradient is based on the profile shown in figure 6.4. The modulus at the surface is 300 GPa, it increases linearly until reaching 450 GPa at a depth of 1.5 μm, and then it decreases to its minimal value of 200 GPa at the interface. The depth at which the coating reaches its maximum elastic properties was based on preliminary tests done on monolithic coatings. In the erosion conditions we are investigating numerically, we observe two zones of shear stress concentration, one at the interface due to elastic properties mismatch, and one spreading around 1-2 μm beneath the surface due to the Hertzian stress induced by the contacting particle (see Figure 6.9). This explains the reasoning behind the choice of the location of the maximum modulus in the tooth-like profile under study.

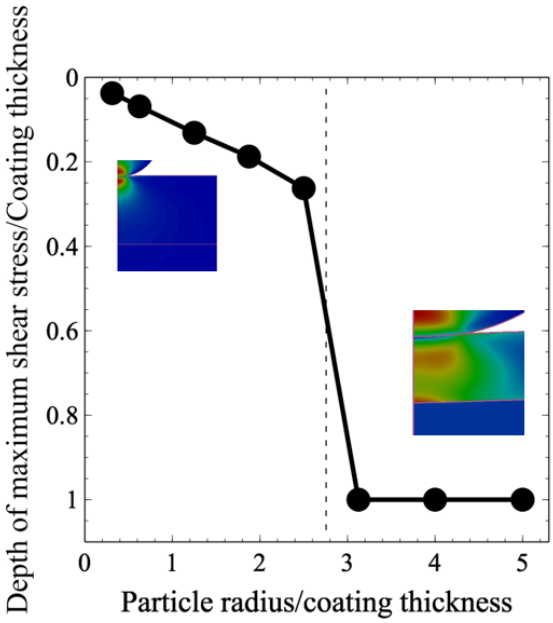

Figure 6.9 Normalised depth of maximum shear stress under impact as a function of particle radius for a 5 μm thick single layer TiSiN coating.

6.6.2.3 Load spreading

We first studied the influence of mechanical gradient on the spatial load distribution throughout the coating profile. We followed the maximum shear stress induced in the coating as a function of time for the different gradient as presented in figure 6.10. The first thing we can note is the short time scale of the microparticle impacts. We can see in Figure 6.10 that the impact event occurs between the 0 ns to 40ns time frame which is consistent with previous literature [245]. After impact, we see in the 40 ns to 50 ns time interval that the system springback to its equilibrium state. After relaxation, the presence of residual stresses is induced from the constraints applied by the permanent deformation of the substrate.

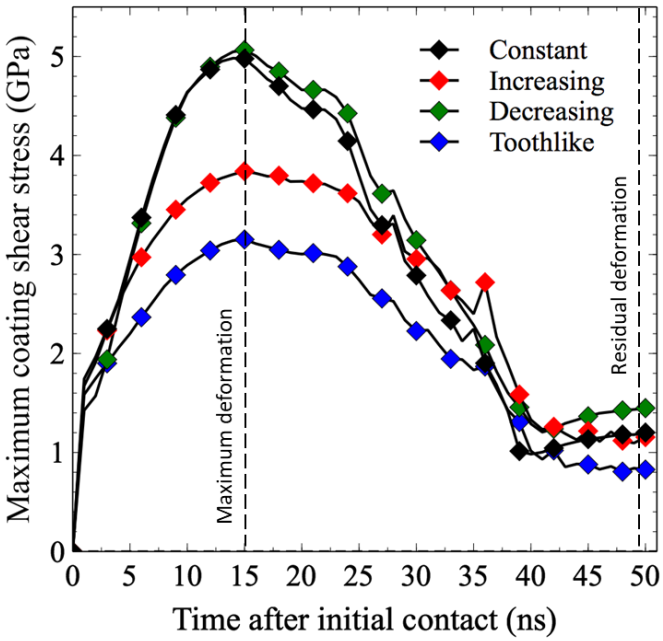

Figure 6.10 Time resolved maximum shear stress during the impact event.

Comparing all gradient with each other, we can see that the constant and decreasing profiles both display the highest induced shear stress, while the increasing and tooth-like gradients decrease significantly the maximum stress induced during the impact. Notably, the stress at maximum deformation between the constant and tooth like solutions decreases from ~5 GPa to ~3GPa. We can also note that the tooth-like gradient level of residual stress is lower than in the constant modulus coatings by 400 MPa which is significant when considering that hard coating wear is accelerated by damage accumulation. To better visualise the previous results, in figure 6.11 we present the stress field profiles of at maximum deformation and at the residual state. Note that the colors in that figure are dynamically scaled to attribute the red color to the maximum shear stress. To compare the relative value between them we must refer to the previously presented results in figure 6.10. Having this spatially resolved field informs us on the location of stress concentration in zones that are susceptible to initiate wear.

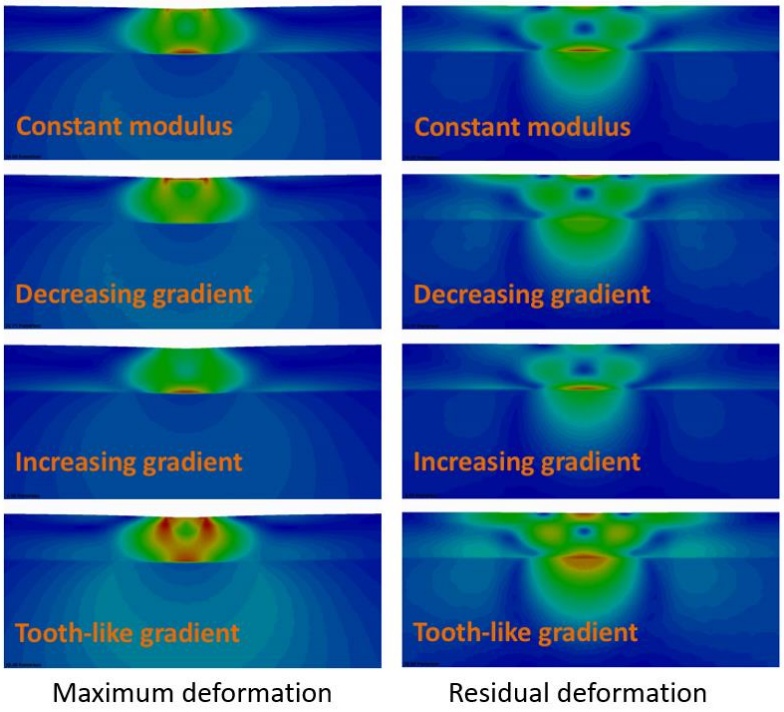

Figure 6.11. Spatially resolved maximum shear stress field during the impact event.

In the traditional constant modulus case, we observe that two zones of important stress concentration are present, one around the contacting area and one at the interface with the base Ti alloy. The stress concentration in the contact area is explained by the high contact pressure induced due to the high stiffness at the surface. The stress concentration located at the interface is caused by the high elastic mismatch between the coating and the substrate. In practice, in the coating close to the interface, since the zone beneath is much more compliant, it is less restrained to deform, and this leads to higher stress and deformation at the interface that may lead to coating adhesion failure. In the decreasing gradient, the stress concentration at the interface is almost suppressed, while we still observe high stress at the surface. The reduction of stress at the interface is attributed to the reduced mismatch in the Young's modulus and thus in the compliance around the interface. The increasing gradient behaves not that surprisingly in a reverse manner, lower contact stress and high interface stress similar to the constant modulus case. The most interesting design emerges as the tooth-like gradient which displays both advantages of the increasing and decreasing modulus, the stresses at the interface and contact area both being significantly reduced compared to the constant modulus coating. In figure 6.11, we can see that to achieve this high reduction in maximum stress,

the tooth-like modulus spread the load over a much larger area resulting in an average lower stress. We also looked at the influence of coating residual stress, since TiSiN based coatings generally have an important level of biaxial compressive residual stress [246]. Accordingly, in figure 6.12 we compared the peak stresses during the impact as a function of coating compressive residual stress.

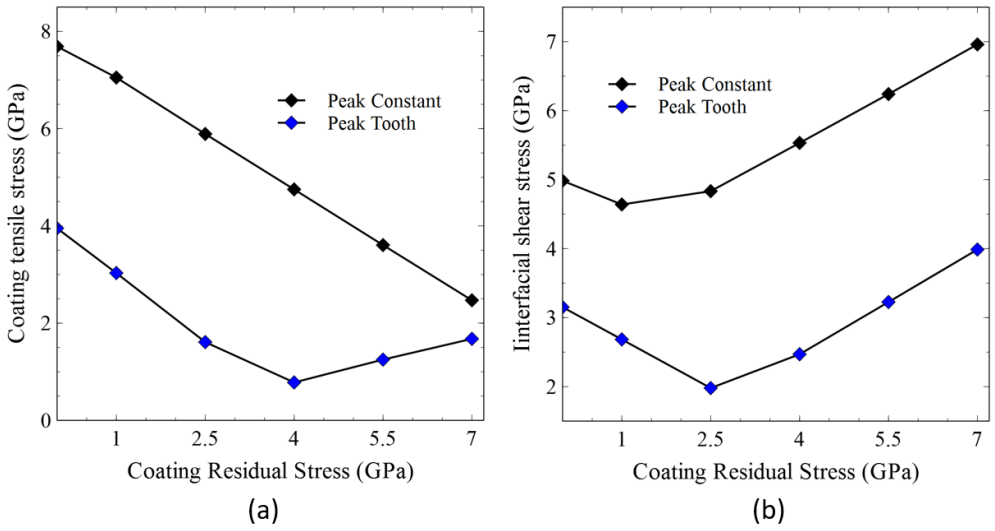

Figure 6.12. (a) Peak coating tensile stress and (b) peak interfacial shear stress during impact event as a function of initial coating residual stress.

First, looking at an initially unstressed coating, we can see that the surface tensile stresses which are responsible for the initiation of cohesive damage in a brittle coating are greatly reduced in the tooth-like gradient. The surface tensile stress is almost halved from 7.7 GPa in the constant modulus coating to 4 GPa in the tooth-like gradient. Increasing the level of initial compressive stress results in lowering the peak tensile stress during the impact that should leads to a higher surface crack resistance. This enhanced crack resistance effect brought by compressive stresses in thin film coatings was also confirmed experimentally [247]. On the other hand, high level of residual stress is also attributed to an increased level of shear stresses at the interface, often leading to delamination damage [248]. As presented above, in the initially unstressed configuration, the tooth-like gradient already decreases the level of stress concentration at the interface, and it is also the case when considering coating residual stress. In fact, the peak interfacial shear stress is lower in the tooth-like coating at all levels of compressive residual stress investigated.

6.6.2.4 Coating defects energy release rate

In the previous section, we have demonstrated several interesting characteristics related to the behavior of mechanically graded surface in terms of stress reduction. However, this continuum vision needs to be refined since TiSiN-based coatings are brittle and thus their main wear mechanism is material removal via intersection of propagated cracks [249]. For this reason, using a numerical fracture mechanics approach, we will examine the relative importance of the crack driving forces around different defects present in the coating (see figure 6.7). As mentioned in 6.5.2.1, defects are introduced simulating a flaw present in the coating microstructure, and the energy release rate at the defect tip is followed throughout the impact event using the J-integral method. Similarly, to the previously presented stress results, we observe the dynamic impact event and the springback to equilibrium which also leads to residual level of energy release rate available to propagate defects. The results for surface and interface defects for the different gradients are presented in Figure 6.13.

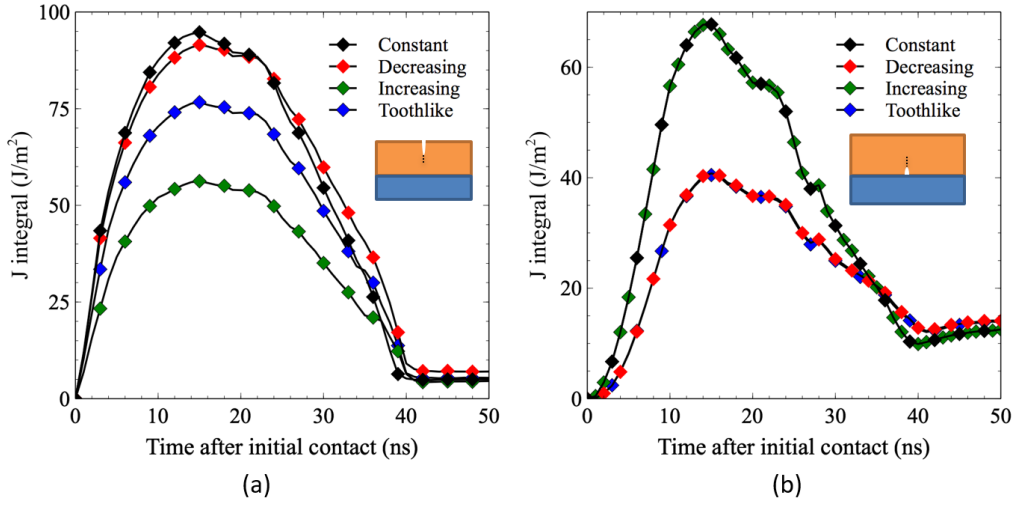

Figure 6.13 Energy release rate during impact event for (a) a surface defect and (b) an interface defect.

For surface defects, we note that both the increasing and tooth-like gradients decrease the energy release rate while the other two gradients behave similarly. This property of an increasing modulus gradient at the surface reducing the stress intensity factor, and thus increasing the effective toughness of the surface, is consistent with previous studies demonstrating this phenomenon [234], [250]. This may be the most significant result of this study, since, as we will see shortly, the surface

flaws are the defect displaying the highest level of crack driving forces, and reducing their propagation directly leads to a decrease in erosion rate. In the case of an interfacial defect, we observe a clear behavior, and the energy release rate is directly related to the local mismatch in elastic properties between the coating and substrate. The decreasing and tooth-like modulus profiles both display similar level of energy release rate while the constant and increasing modulus have a higher level of stress concentration at the defect tip.

We also investigated median and lateral defects introduced in the middle of the coating, and the main results are presented in Figure 6.14. The first aspect we note is that if the defect is confined inside the coating, lateral cracks are much more likely to propagate than median cracks. In both cases, the constant modulus coating displays the lowest energy release rate, closely followed by the tooth-like gradient. It seems that the energy release rate of those kinds of defects is correlated to the effective modulus and the local gradient of mechanical properties.

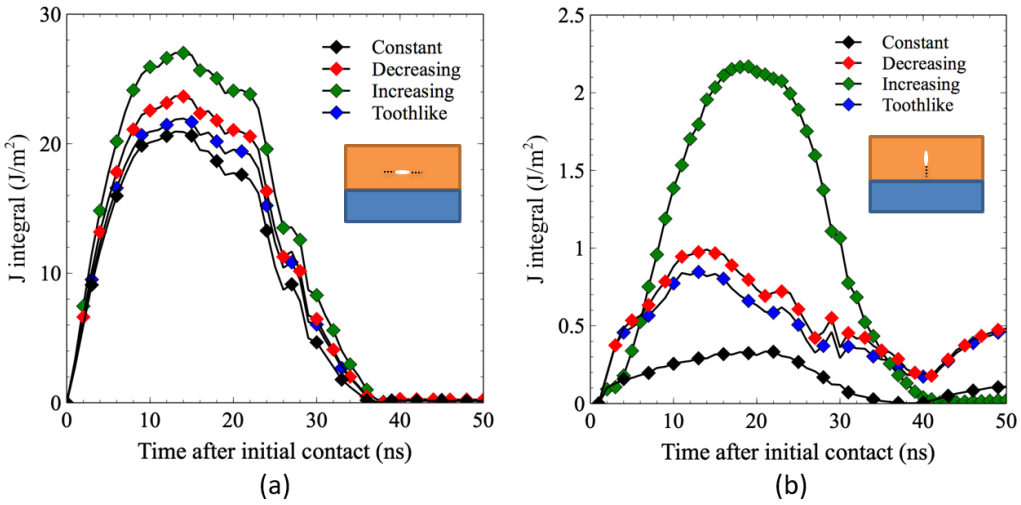

Figure 6.14 Energy release rate during impact event for (a) lateral defect and (b) a median defect.

The tendencies that we observed in this numerical study are great indication that a bio-inspired surface coating based on the functional gradient present in tooth can exhibit superior mechanical and erosion resistance properties by reducing the crack driving forces. This reduction in stress intensity factor at crack tip is due to intrinsic toughening resulting from the bio-inspired mechanical gradient. To validate the modeling approach, we expect to experimentally corroborate the numerical results in the near future.

6.6.3 Investigation of mechanically graded protective films for sand erosion/abrasion protection of solar power components optical surfaces

The growth of efficient solar power plants is closely related to the development of durable materials to guarantee long term operation and low maintenance cost. The most prominent technologies used in those power plants rely on photovoltaic panels (PP) and solar mirrors (SM) for the concentrated solar power (CSP) approach to solar energy conversion. To maximize the productivity of those solar power plants, they should be operated in regions with high sunlight duration. In practice, those areas also often coincide with harsh environments containing high level of dust and sand carried by frequent sandstorms [251]. Over a period of time, sand particles impacts can cause important abrasion damages to any engineered exposed surfaces. To shield the critical component from those hostile conditions, protective glasses are commonly used as they are able to ensure high light transmission and adequate mechanical and chemical resistance to the operating environment. However, the frequently used glass is subject to soiling and non-reversible wear and damage accumulation which reduces its optical performance. While PP and SM expected lifetime is around 25 years, there are major concerns that in some areas, erosion by sand particles may excessively degrade optical performances of the protective glass over this time frame. The loss in optical transmission is caused by the diffusion of light that scatters off the surface defects such as scratches and cracks and thus hinder the specularity of the mirror [252]. Another issue that may arise is damage by corrosion inside the device, for example, when the defects created in the protective glass are significant enough to allow moisture to reach underlying metallic layers [33], [253].

The mechanical resistance to sand abrasion, also named solid particle erosion (SPE), is widely studied in the context of SM durability [252], [254], [255]. Lately, a lot of efforts are put into establishing a reliable test predicting the loss of transmission by using accelerated glass ageing procedures [256]. These tests are performed in environmental simulator with controlled temperature, solar irradiation and humidity. Using those predictive models at the earliest stage of the product development is essential to ensure an adequate design having the required sturdiness for the envisioned operating environment.

While protective glasses do help significantly to delay the transmission losses, protective coatings are now seen as the ultimate solution to limit wear of the surface. This solution is also becoming

predominant for other applications where glasses (or transparent polymers) are exposed to wear from the environmental conditions; this includes, architectural glazing, car windshield, ophthalmic/camera lenses and bendable electronics [257]. In the case of SM and PV modules, silica-based coatings deposited by sol gel are often used; they provide adequate abrasion and corrosion resistance and the deposition processes are readily adaptable to cover large scale surfaces [258]. The second most prominent protective layers used in the field are polymer-based protective top coats [259], [260]. Other materials are also currently under investigation such as silicon nitride [261], silicon oxynitride [262], and silicon carbide-based reflectors [263] as they possess the required combination of optical properties and mechanical resistance.

SPE performance of a surface is governed by an intricate relation which depends on both the properties of the erodent particles (hardness, angularity, mass, velocity, …) and those of the impinged surface (hardness, toughness, Young's modulus, microstructure…) [249], [264]. For brittle coatings, such as metal oxide optical coatings, the wear mechanism is predominantly material removal by flaking from the intersection of lateral cracks induced by single particles impact or through the damage accumulation from consecutive impacts in the plasticized zone [265], [266]. Even though the main parameter responsible for abrasion/erosion resistance is the hardness of the surface [267], many biological tissues containing structural hierarchies [220] were shown to have high resistance to SPE. For instance, desert scorpions [268], mantis shrimps [269] and mammal teeth/bones [37], [270] all exhibit remarkable resistance to crack formation due to the natural gradient of mechanical properties in their biological structures.

In this context, following the previous section results leads us to strongly believe that the same tendencies will be applicable to the less demanding conditions to which SM are exposed. To validate the numerical results, a material system with a wide range of tailorable elastic properties is required. Precise control of those properties during the film growth is also necessary to achieve the desired elastic grading profile. Consequently, we probed the possibility of depositing a mechanically graded silicon oxynitride coating on glass to investigate its stability under sand erosion/abrasion conditions similar to those present in CSP and PV device operations.

6.6.3.1 Deposition methodology

SiO_xN_y coatings were deposited on precleaned B270 glass substrates using an ultra-high vacuum reactive multi-magnetron process chamber (CMS-18, Kurt J. Lesker Co., Ltd.). The magnetron was equipped with a 3 inches target of pure silicon (99.9%). The magnetron was powered by a radiofrequency power supply (13.56 MHz, SEREN). Different flows of N_2 and O_2 were introduced into the process chamber to react with the growing film and produce the SiO_xN_y films. Experimental conditions for the deposition process are summarized in Table 6.2.

A M-2000 spectroscopic ellipsometer (J.A. Woollam Co. Inc.) fixed at an angle of incidence of 70° was used to characterize in real-time the optical properties and thickness of the growing film. A script was written to automatize the alternation between ellipsometer measurements and film deposition and to adjust the deposition time to reach the desired thickness of the film. The film elastic modulus and hardness were estimated with a depth-sensing indenter (Hysitron Triboindenter) equipped with a Berkovich diamond tip using the Oliver–Pharr method [134].

Table 6.2. Deposition parameters for SiO_xN_y films.

Parameters	SiOxNy film
Pressure [mTorr]	2.0
Sputtering gas	Ar
Reactive gas	O_2, N_2
Target power [W]	450
Ar flow ratio [%]	60
$N_2/(N_2+O_2)$ flow ratio [%]	0-100
Film thickness (nm)	~500

6.6.3.2 SiO_xN_y deposition and characterization

Using the in-situ ellipsometer, the refractive index was measured as a function of reactive gas flux ratio (see Figure 6.15). For a N_2 flux ratio up to 50% we obtain a film exhibiting properties similar to pure SiO_2 [210] with an almost constant refractive index of 1.45±0.05. This is due to the much higher reactivity of oxygen which preferably reacts with the sputtered Si. As we increase the N_2

flux ratio we observe at first a slight increase in the refractive index which implies the beginning of the formation of the SiN phase in the material. The most sensible region is located between 90% and 100% N2 flux ratio interval, where the refractive index increases from ~1.5 to 1.99±0.02. This index is comparable to the Si_3N_4 index found in the literature [211]. Also in figure 6.15, we can see that the deposition rate behaves in a similar manner, quickly decreasing in the same flux interval down to a quarter of its initial value. Concerning the optical properties, we have shown that the deposition process can produce films with a continuous variation of refractive index between the values of SiO_2 and Si_3N_4.

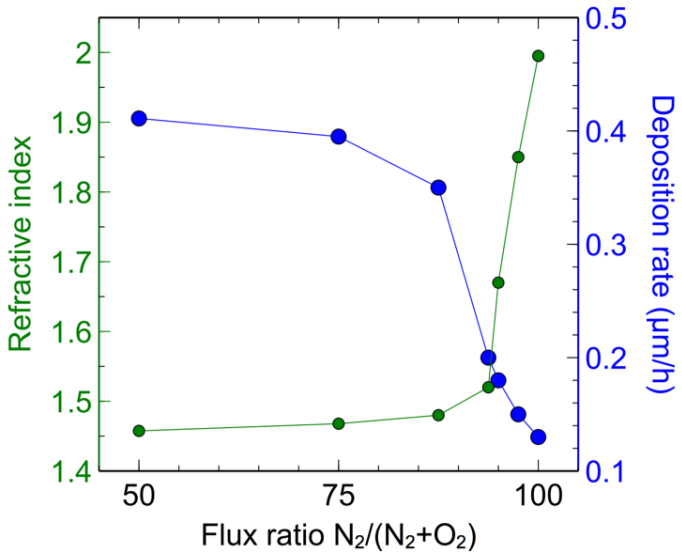

Figure 6.15 SiO_xN_y films refractive index and deposition rate as a function of the N_2 flux ratio.

We then probed the mechanical properties using depth-sensing nanoindentation, and the results are presented in figure 6.16. The elastic modulus varies smoothly with the flux ratio and cover the interval between 70±2 GPa and 185±5 GPa. Those values are comparable to the Young's modulus found in the literature for SiO_2 and Si_3N_4 films. The hardness, which represents the resistance to plastic deformation, increased from 4.7±0.6 GPa to 18.1±1.1 GPa with the variation of the N_2 flux ratio. Using this information allows one to build a deposition recipe which can reproduce any elastic modulus gradient profile in the interval from 70 GPa to 185 GPa.

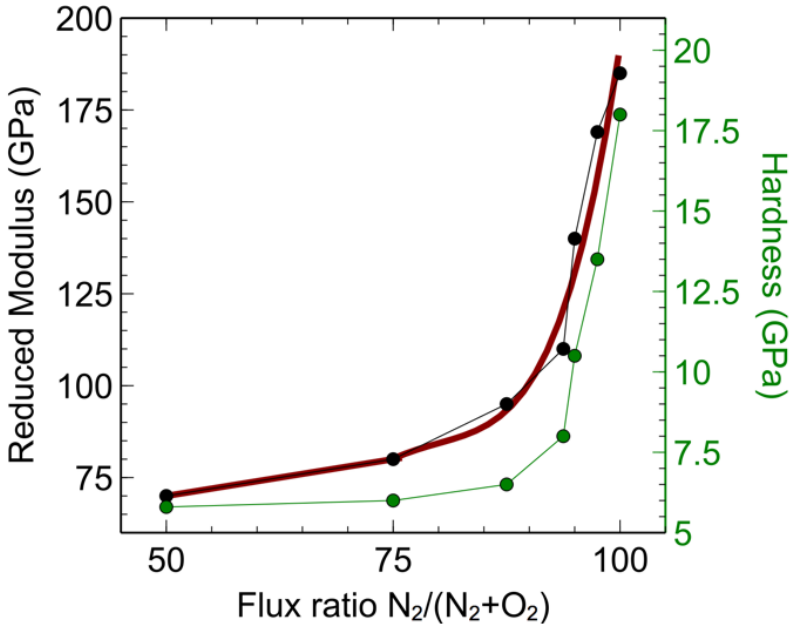

Figure 6.16 SiO_xN_y films reduced modulus and hardness a function of the N_2 flux ratio.

6.7 Summary and discussion

In this study on bio-inspired materials, we developed a fracture mechanics methodology to assess the erosion resistance of functionally graded coatings. We achieved this by introducing realistic microstructural defects in the coating at different locations. We evaluated the crack driving forces during a single particle impact using the J-integral. In the second part of this investigation, we have demonstrated possibility to grow mechanically graded coatings using magnetron sputtering and varying the ratio of the reactive gases. As a continuation of these studies, we foresee to apply the numerical approach presented in 6.6.2 on functionally graded SiO_xN_y deposited on glass substrate, while exploiting the wide range of elastic properties attainable as we characterized in 6.6.3. To evaluate their performance in the context of solar mirror sand erosion, the samples will be subjected to the typical erosion conditions that solar mirrors are exposed too. [254], [271]. A special focus should be put on the tooth-like gradient profile, especially on the optimization of the location of the maximum elastic modulus in the profile. Note that we expect a variation in crack resistance by modifying the Young's modulus due to a variation in the mechanical properties (Hardness, Yield Stress) and microstructure of the film. In this sense, another important aspect that we need to consider if we wish to increase the model predictivity, is the fracture toughness characterization of

single layer SiO_xN_y over complete compositional range. Finally, to experimentally validate the numerical method, we aim at assessing the influence of the gradient on the erosion performance by comparing different mechanical gradients in terms of the erosion mass loss and transmission loss under realistic operation conditions.

CHAPTER 7 GENERAL DISCUSSION

Functional coatings are becoming omnipresent in more and more applications, from everyday appliances to advanced technological components used by the industries. Nonetheless, without predictive modeling, the optimization of coating tribomechanical performance for a specific application is still mainly based on empirical knowledge. Time and cost consuming studies by trial and errors are still the principal means by which research proceeds. Throughout this work, we have shown that predictive tribomechanical modeling is a powerful tool available for tribologists and surface engineers to assist them perform surface damage analyses and coating architectural design. To identify and understand the relevant tribomechanical phenomena we have first presented the fundamental solicitations that can lead to surface damages. A complex amalgam of those basic solicitations is responsible for the wear mechanisms that tribologists observe on a daily basis.

Over the last decades, surface engineers have been able to increase surface coatings tribomechanical performances by exploiting a multilayer multifunctional coating design. This methodology consists in combining coatings with distinct properties to protect the surface against specific wear environments. The success of this approach was to demonstrate that using multifunctional coating solutions, we can obtain a film that exhibits higher performance than each of the individual layers constituting it. However, the classical way to perform tribology analysis, using post-mortem observations, is most often not enough to tell the whole story and thus provide only a limited vision to precisely pinpoint the multifunctional coating tribomechanical weaknesses and avenues for optimization.

In a first instance, using finite element modeling at the coating scale to simulate and recreate the operational conditions should become a standard, since it’s a direct way to obtain an insightful and detailed view of the deformations and stresses induced by the wear environment. With this information, surface engineer can tailor architectures which will confine stresses in specific areas and reduce surface damage caused by permanent deformation. While this type of study, based on contact modeling, is becoming increasingly ubiquitous in the tribology community, it is still not readily available in the industrial context due to the lack of standards. With the constant advancement in computational power and user friendliness of finite element software, we believe that the elaboration of a contact modeling standard could become reality in the near future. To reach this level of maturity, the hypothetical standard should impose extensive verification and

validation to ensure the accuracy of the results, which may be one of the explanations that it has not yet been established.

Using a contact modeling approach in this work, for example in chapter 4, we simulated the wear condition of a coated ball valve and we have been able to characterize the limiting operational conditions which lead to surface brinelling and top coating fracture. After model validation with the controlled experiments, the numerical model was used as a predictive tool to modify the architectural design. In this particular study we have shown that the load carrying interlayer thickness could be significantly reduced without compromising its function, thus lowering the cost and time of production and maintenance. Chapter 6 has also shown the significance of modeling the erosion condition by allowing us to understand the particle radius/coating thickness relation on the area where high stress gradient is induced and consequently adjust the coating thickness and mechanical properties to adequately protect the base material. It also allowed us to understand how different gradients will affect the load spreading throughout the coating profile. We have identified a particular profile based on biomaterials which limits the stress concentration both at the surface and interface with the base material, this strongly suggests that this type of functional gradient may reduce the brittle wear mechanisms generated by an erosive environment.

Development of numerical fracture mechanics and microstructure-based modeling in the context of tribomechanical studies present an even higher potential for improving architectural design. One way to proceed, which is the one we exploited in this work, is by introducing realistic defects in the coating microstructure and evaluating the crack driving forces available to propagate them. Using this methodology, we are able to bring the modeling even closer to the complete simulation of the wear mechanisms. For example, in Chapter 5, we have used this approach in multilayer coatings by introducing cracks in the material showing higher brittleness. We have then evaluated the energy release rate available to propagate that defect across the coating using in-situ tensile experiments. This study allowed us to characterize the fracture properties of an optical film on polymer substrate and predict the failure pathway in a multilayer structure. This allowed us to predict which layer is more subject to initiate failure and thus characterized the tribomechanical conditions that the structure can sustain. In Chapter 6, a similar approach was used to predict the crack resistance of mechanically graded coatings, and we have shown that the peculiar structure

present in bones and teeth could translate to increased crack propagation resistance compared to the currently widely used monolithic hard brittle coatings.

In view of these different results, it is becoming an evidence that finite element modeling and numerical fracture mechanics have an essential role for the future development and advancement of thin film coatings with properties optimized to their operational conditions and environment. The integration of the tribomechanical modeling in the design process is presented in figure 7.1. With this design process, we aim to iteratively refine the model until it corroborates with the post-mortem observations. Once we achieve the desired levels of accuracy and calibration, we can then use the model as a predictive and solution-exploration tool.

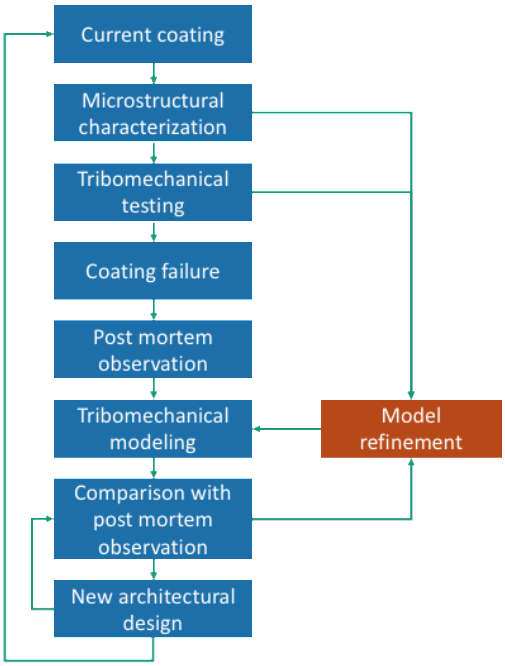

Figure 7.1 Integration of the tribomechanical modeling in the design process of tribologically enhanced material.

CHAPTER 8 CONCLUSION

8.1 Perspectives and future directions

Before concluding this thesis, we will present the principal limitations and aspects that still lack understanding in the study of tribomechanical modeling of coated surfaces. We believe that those points are essential stepping stones for the future progress of the discipline.

8.1.1 Thin film coating mechanical characterization

The first point we must mention is the accessibility to precise and accurate experimental procedures to characterize thin film coating mechanical properties. The most common way to achieve this task to this day is through the Olivier-Pharr indentation method which allows the estimation of the reduced Young's modulus of the indenter tip/coating couple and hardness of the surface [156]. This approach however is affected by the inherent substrate effect and cannot be used to characterize the Poisson's ratio of the surface. To circumvent those limitations, micro-mechanics characterization techniques are being developed that allow one to carry out conventional mechanical tests at the micro/nanoscale. These techniques combine focused ion beam milling and scanning electron microscopy to prepare micro-sized samples [272].

Micro tensile testing is used to evaluate the stress-strain curve and Poisson's ratio of the film [273]. By characterising the full stress-stain curve, we can predict the post-yielding behavior of thin film and thus take into account permanent deformations occurring in the coating. Micropillar indentation is useful for materials that present different tensile/compressive response, most notably this is the case for ceramics and polymers [274]. This technique can be exploited to characterize the pressure dependant plasticity and densification behavior of those materials [275]. For example, it was recently applied to investigate and characterize the densification of silica when subjected to nanoindentation [276].

Micro and nano fracture mechanics testing have significantly matured in the past few years. In particular, the micropillar splitting and the notched cantilever approaches have been widely investigated [247]. By combining continuum mechanics to evaluate the stress intensity factors of

the structure and critical load measurements from nanoindention, the fracture toughness of thin films can be precisely estimated.

Finally, the evaluation of residual stresses across the profile of the film is still a very challenging task. Non-intrusive method such as X-Ray Diffraction Residual Stress Techniques are limited in their resolution and the analysis is a very challenging task with intrinsic substrate effect due to the X-ray beam penetration depth [277]. Again, micro-mechanics approaches using digital image correlation and focused ion beam milling, while intrusive, have been demonstrated as the most accurate manner to characterise coating residual stress. By following the surface relaxation while milling, the residual stress depth profile can be recovered. Recently, there was a major project launched by the European Community Research and Development Information Service that concerned the standardization of such tests [278].

The development of standards and accessibility of the characterization approaches mentioned above are crucial since the results are required as input in continuum mechanics models. The more accurate are the material constitutive relations, the fracture properties and the initial stress states, the more accurate will be the numerical estimation of macro stress field by the models.

8.1.2 Microstructure-based modeling

Another important aspect that continuum mechanics approaches must still advance is its inclusion of microstructural-level behavior and evolution under tribological solicitations. In this work, we have presented models in which discontinuities were introduced in the coating mesh to simulate the presence of defects in the microstructure. For amorphous materials such as ceramics, this approach using homogeneous sections with discontinuities to simulate the presence of pores, void or interface can generate results with high fidelity as long as chemical reactions and phase changes are negligible. However, as introduced in the previous section, there is still a major need to enhance the characterisation and post-yielding behavior of those materials.

Another important aspect not considered in the present study is the characterisation of interfacial constitutive laws to predict the coating-substrate interface damage. While there is a few proposed approached reported in the literature using nanoindentation [279], buckle analysis [191], [280],

super layer method [281] and bulge test [282] the interfacial toughness measurement is still very challenging especially for highly adhering films [46].

The crystal plasticity finite element method can predict the response of polycrystalline materials by considering the grains distribution and orientation and their anisotropic mechanical properties depending on the loading direction [283]. These approaches can also be enhanced to take into account the evolution of the texture and intergranular behavior which allow for a highly accurate evaluation of the micro stresses induced in the film microstructure [123], [284]. Advancement in those numerical methods are essential if we wish to increase the fidelity of thin film tribomechanical modeling especially for the ever increasingly applications of nanostructured coatings.

8.1.3 Fracture mechanics applicability at the nanoscale

Most of the fracture mechanics theory and models used to this day still originate from the pioneer studies of the late 1950s and early 1960s. While this theory is adequate in the long crack regime, there is a critical dimension below which the discreteness of the atomic structure renders the stress intensity factor approach invalid at this scale. From recent theoretical development, it is predicted that for cracks and defects below ~3 nm, the classical theory breakdown and atomistic-based fracture theory must be used to predict crack propagation [285]. These methods exploit the Griffith energy-based theory using atomistic strain energy density calculation at the crack tip. There is still major work required to interconnect the short crack to long crack regime transition, but as we mentioned in the previous section, this will become indispensable in a close future if we wish to study with accuracy the fracture properties of nanostructured materials, in particular for bio-inspired materials with complex nanoscale elements responsible for their emergent properties.

8.1.4 Mechanical and optical design constraints in mechanically graded films

A last point to discuss before the concluding remarks, is the tall order we face when design constraints are required for both the mechanical and optical properties. As we mentioned in 2.2.2, the stress compensating approach has been widely studied and demonstrated to allow precise control of the coated surface curvature and is very useful to ensure mirror flatness and interface parallelism [58]. However, for optical filters requiring a particular index profile to produce the

desired spectral response, taking into account mechanical properties. In 6.5.2 we presented an investigation of the mechanical response of graded coatings and in 6.5.3 we discussed the possibility of exploiting a similar modulus profile for the protection of solar mirror using SiO_xN_y coatings. A fascinating aspect of graded index coating is that they have been shown to be highly performant anti-reflective materials since they eliminate the discontinuous interface reflection owing to the smoothly varying refractive index through the film profile.

Finally, another interesting approach to meet both the mechanical and optical constraints is though the use of hybrid organic materials, the properties of which can be tailored by adjusting the film hybridicity. It was demonstrated that these films Young's modulus is greatly affected by the level of hybridicity while the refractive index can be kept mostly constant such that the optical and mechanical properties can be individually adjusted [180]. We believe that the development of the two approaches presented here will be major milestones for the development of durable optical surfaces.

8.2 Concluding remarks

The holy grail of tribomechanical modeling is to allow one to numerically reproduce with high fidelity the post mortem observations of damaged surfaces and develop new architectural designs that will withstand the same conditions with less or no surface deterioration at all. As of today, using continuum mechanics, we have not been able to reach this high level of accuracy, and we may never have to. In Chapter 3, when we justified the utilization of continuum mechanics, we mentioned that atomistic modeling would intrinsically be able to capture all the phenomena in play in tribomechanical systems. This has not been the path taken by researchers yet, since those methods necessitate extreme computational and memory requirements which limits them to a very short time-scale modeling. If the available computational power keeps increasing at this rate and even more so with the introduction of cloud computing, this situation may soon be a story of the past and atomistic modeling will become predominantly used and thus could render obsolete the continuum mechanics modeling approach. In the past few years, there has been a substantial increase in the number of research papers exploiting molecular dynamics models to study tribomechanical properties of thin film coatings at the nanoscale [131]. Machine learning approaches are also becoming more accessible for the end users and could soon revolutionize the

way we do research. Using these algorithms and existing data, the machine learning method can uncover or even discover new materials configurations and predict their mechanical properties [286]. For example, using an artificial neural network, researchers were able to characterize and predict the stress-strain relation and texture evolution in polycrystalline metals [287].

With this highly plausible scenario in mind, and considering the current situation concerning global warming and climate changes, I wish to finish this thesis on a more environmentally ethical tone. One of the main pretenses, at least the one most openly and publicly stated, is that research in the field of tribology is aimed toward the reduction of environmental impact through the development of coatings that minimize friction and improve wear resistance. However, one of the critical aspects that is often neglected is the environmentally unfriendly and polluting materials and lubricants that are still used in most of the industrial applications. To be considered a green axis of research those two points need to be resolved. One of the most promising answers to those issues is the development of coatings with bio-inspired structures providing enhanced wear resistance and self-lubrication using environmentally-safe and naturally highly abundant materials with low polluting extraction processes. These concepts are part of the green tribology approach that inscribes itself in the broader green engineering initiatives [288]. The principles of green tribology are based on :

- Minimization of heat and energy dissipation
- Minimization of wear
- Self-lubrication
- Bio-degradable lubrication
- Using sustainable engineering principles
- Surface texturing
- Environmental implications of coatings
- Real-time monitoring
- Design for degradation
- Sustainable energy applications
- Bio-mimetic approaches.

Environmental considerations were in fact the main drive behind the investigation presented in chapter 6, i.e., to use abundant materials (Si, O, N) and exploiting a functional gradient based on

nature’s proven optimization skills that is natural evolution. This study did not require high computational power, it was realized on a personal computer in a regular university office by mimicking natural materials using a continuum mechanics approach. I really hope that in the imminent future, tribology researches will concentrate their efforts on the green science view and assume and respect all implications that follow from it.

REFERENCES

[1] M. J. Madou, *Fundamentals of microfabrication: the science of miniaturization*. CRC press, 2002.

[2] B. Baloukas, S. Loquai, and L. Martinu, "VO 2 -based thermally active low emissivity coatings," *Solar Energy Materials and Solar Cells*, vol. 183, pp. 25–33, Aug. 2018.

[3] K. Marsh and B. Bugusu, "Food packaging—roles, materials, and environmental issues," *Journal of food science*, vol. 72, no. 3, pp. R39–R55, 2007.

[4] W. Min, B. Jiang, and P. Jiang, "Bioinspired self-cleaning antireflection coatings," *Advanced Materials*, vol. 20, no. 20, pp. 3914–3918, 2008.

[5] B. Baloukas, J.-M. Lamarre, and L. Martinu, "Active metameric security devices using an electrochromic material," *Applied optics*, vol. 50, no. 9, pp. C41–C49, 2011.

[6] R. Kamada *et al.*, "New world record Cu (In, Ga)(Se, S) 2 thin film solar cell efficiency beyond 22%," presented at the 2016 IEEE 43rd Photovoltaic Specialists Conference (PVSC), 2016, pp. 1287–1291.

[7] W. Kalss, A. Reiter, V. Derflinger, C. Gey, and J. Endrino, "Modern coatings in high performance cutting applications," *International Journal of Refractory Metals and Hard Materials*, vol. 24, no. 5, pp. 399–404, 2006.

[8] Y. Liu *et al.*, "Artificial lotus leaf structures from assembling carbon nanotubes and their applications in hydrophobic textiles," *Journal of Materials chemistry*, vol. 17, no. 11, pp. 1071–1078, 2007.

[9] T. W. Boentoro, B. Szyszka, and L. Martinu, "Chapter 14 - Protective coatings for durability enhancement of optical surfaces," in *Optical Thin Films and Coatings (Second Edition)*, A. Piegari and F. Flory, Eds. Woodhead Publishing, 2018, pp. 539–564.

[10] A. Nathan *et al.*, "Flexible electronics: the next ubiquitous platform," *Proceedings of the IEEE*, vol. 100, no. Special Centennial Issue, pp. 1486–1517, 2012.

[11] H. P. Jost, *Lubrication: Tribology; Education and Research; Report on the Present Position and Industry's Needs (submitted to the Department of Education and Science by the Lubrication Engineering and Research) Working Group*. HM Stationery Office, 1966.

[12] K. Holmberg and A. Erdemir, "Influence of tribology on global energy consumption, costs and emissions," *Friction*, vol. 5, no. 3, pp. 263–284, 2017.

[13] G. Stachowiak and A. W. Batchelor, *Engineering tribology*. Butterworth-Heinemann, 2013.

[14] I. Hutchings and P. Shipway, *Tribology: friction and wear of engineering materials*. Butterworth-Heinemann, 2017.

[15] G. Straffelini, "Friction and wear," *Springer International Publishing, Switzerland. doi*, vol. 10, pp. 978–3, 2015.

[16] L. Dormieux and D. Kondo, *Micromechanics of fracture and damage*. John Wiley & Sons, 2016.

[17] K. Holmberg and A. Matthews, *Coatings Tribology: Properties, Mechanisms, Techniques and Applications in Surface Engineering*. Elsevier Science, 2009.

[18] T. Hoornaert *et al.*, *Advanced Tribology*. Berlin, Heidelberg: Springer Berlin Heidelberg, 2010.

[19] S. Wen and P. Huang, *Principles of tribology*, Second edition. Hoboken, NJ: Wiley, 2018.

[20] P. L. Menezes, M. Nosonovsky, S. P. Ingole, S. V. Kailas, and M. R. Lovell, Eds., *Tribology for Scientists and Engineers*. New York, NY: Springer New York, 2013.

[21] Y.-W. Chung, *Micro-and nanoscale phenomena in tribology*. CRC Press, 2011.

[22] H. Hertz, “On the contact of solid elastic bodies and on hardness,” *Journal of math*, vol. 92, pp. 156–171, 1881.
[23] *Hertzwin 2.8.0, Vink System Design & Analysis, https://www.vinksda.nl/en-2/.* .
[24] J. L. Beuth Jr, “Cracking of thin bonded films in residual tension,” *International Journal of Solids and Structures*, vol. 29, no. 13, pp. 1657–1675, 1992.
[25] J. W. Hutchinson and Z. Suo, “Mixed mode cracking in layered materials,” in *Advances in applied mechanics*, vol. 29, Elsevier, 1991, pp. 63–191.
[26] J. Andersons, S. Tarasovs, and Y. Leterrier, “Evaluation of thin film adhesion to a compliant substrate by the analysis of progressive buckling in the fragmentation test,” *Thin Solid Films*, vol. 517, pp. 2007–2011, Feb. 2009.
[27] H. Chai and D. Josell, “Fracture behavior of nano-layered coatings under tension,” *Thin Solid Films*, vol. 519, no. 1, pp. 331–336, Oct. 2010.
[28] M. R. Begley and J. W. Hutchinson, *The Mechanics and Reliability of Films, Multilayers and Coatings*. Cambridge: Cambridge University Press, 2017.
[29] T. Y. Tsui, A. J. McKerrow, and J. J. Vlassak, “Constraint effects on thin film channel cracking behavior,” *Journal of materials research*, vol. 20, no. 9, pp. 2266–2273, 2005.
[30] S.-H. Choa, B.-H. Ko, and H.-S. Lee, “Fracture analysis of channel cracks in flexible multilayer structure films under bending conditions,” *Engineering Fracture Mechanics*, vol. 200, pp. 283–293, Sep. 2018.
[31] I. Finnie, “Some reflections on the past and future of erosion,” *Wear*, vol. 186, pp. 1–10, 1995.
[32] E. Bousser, L. Martinu, and J. Klemberg-Sapieha, “Solid particle erosion mechanisms of protective coatings for aerospace applications,” *Surface and Coatings Technology*, vol. 257, pp. 165–181, 2014.
[33] A. García-Segura, A. Fernández-García, M. J. Ariza, F. Sutter, and L. Valenzuela, “Durability studies of solar reflectors: A review,” *Renewable and Sustainable Energy Reviews*, vol. 62, pp. 453–467, Sep. 2016.
[34] B. Borawski, J. A. Todd, J. Singh, and D. E. Wolfe, “The influence of ductile interlayer material on the particle erosion resistance of multilayered TiN based coatings,” *Wear*, vol. 271, pp. 2890–2898, Sep. 2011.
[35] K. S. Katti, D. R. Katti, S. M. Pradhan, and A. Bhosle, “Platelet interlocks are the key to toughness and strength in nacre,” *Journal of Materials Research*, vol. 20, no. 5, pp. 1097–1100, 2005.
[36] Z. Liu, M. A. Meyers, Z. Zhang, and R. O. Ritchie, “Functional gradients and heterogeneities in biological materials: Design principles, functions, and bioinspired applications,” *Progress in Materials Science*, vol. 88, pp. 467–498, Jul. 2017.
[37] X. Niu, N. Rahbar, S. Farias, and W. Soboyejo, “Bio-inspired design of dental multilayers: Experiments and model,” *Journal of the Mechanical Behavior of Biomedical Materials*, vol. 2, no. 6, pp. 596–602, Dec. 2009.
[38] D. Verma and V. Tomar, “An investigation into mechanical strength of exoskeleton of hydrothermal vent shrimp (Rimicaris exoculata) and shallow water shrimp (Pandalus platyceros) at elevated temperatures,” *Materials Science and Engineering: C*, vol. 49, pp. 243–250, 2015.

[39] G. Abadias *et al.*, “Stress in thin films and coatings: Current status, challenges, and prospects,” *Journal of Vacuum Science & Technology A: Vacuum, Surfaces, and Films*, vol. 36, no. 2, p. 020801, 2018.
[40] H. E. Tresca, *Sur l’ecoulement des corps solides soumis a de fortes pressions*. Imprimerie de Gauthier-Villars, successeur de Mallet-Bachelier, rue de Seine …, 1864.
[41] R. von Mises, “Mechanik der plastischen Formänderung von Kristallen,” *ZAMM-Journal of Applied Mathematics and Mechanics/Zeitschrift für Angewandte Mathematik und Mechanik*, vol. 8, no. 3, pp. 161–185, 1928.
[42] J. F. Labuz and A. Zang, “Mohr–Coulomb failure criterion,” *Rock mechanics and rock engineering*, vol. 45, no. 6, pp. 975–979, 2012.
[43] L. R. Alejano and A. Bobet, “Drucker–Prager Criterion,” in *The ISRM Suggested Methods for Rock Characterization, Testing and Monitoring: 2007-2014*, Springer, 2012, pp. 247–252.
[44] G. Hahn, M. Kanninen, and A. Rosenfield, “Fracture toughness of materials,” *Annual Review of Materials Science*, vol. 2, no. 1, pp. 381–404, 1972.
[45] S. Zhang, D. Sun, Y. Fu, and H. Du, “Toughness measurement of thin films: a critical review,” *Surface and Coatings Technology*, vol. 198, no. 1–3, pp. 74–84, 2005.
[46] J. Chen and S. J. Bull, “Approaches to investigate delamination and interfacial toughness in coated systems: an overview,” *Journal of Physics D: Applied Physics*, vol. 44, no. 3, p. 034001, Dec. 2010.
[47] E. Bemporad, M. Sebastiani, F. Casadei, and F. Carassiti, “Modelling, production and characterisation of duplex coatings (HVOF and PVD) on Ti–6Al–4V substrate for specific mechanical applications,” *Surface and Coatings Technology*, vol. 201, no. 18, pp. 7652–7662, 2007.
[48] “Nanoscratch and Nanoindentation of Oxide Coatings on Thin Film Polymer Substrates,” *AZoNano.com*, 19-Jun-2017. [Online]. Available: https://www.azonano.com/article.aspx?ArticleID=4529. [Accessed: 05-Feb-2019].
[49] L. Vernhes, M. Azzi, E. Bousser, T. Schmitt, J. M. Lamarre, and J. E. Klemberg-Sapieha, “Hybrid Co-Cr/W-WC and Ni-W-Cr-B/W-WC Coating Systems,” *Journal of Thermal Spray Technology*, vol. 25, no. 1–2, pp. 346–356, Jan. 2016.
[50] F. Pougoum, L. Martinu, J.-E. Klemberg-Sapieha, S. Savoie, and R. Schulz, “Wear properties of Fe3Al-based HVOF coatings strengthened with in-situ precipitated nitride and boride particles,” *Surface and Coatings Technology*, vol. 307, pp. 109–117, Dec. 2016.
[51] L. Aihua, D. Jianxin, C. Haibing, C. Yangyang, and Z. Jun, “Friction and wear properties of TiN, TiAlN, AlTiN and CrAlN PVD nitride coatings,” *International Journal of Refractory Metals and Hard Materials*, vol. 31, pp. 82–88, 2012.
[52] M. Y. P. Costa, M. L. R. Venditti, M. O. H. Cioffi, H. J. C. Voorwald, V. A. Guimarães, and R. Ruas, “Fatigue behavior of PVD coated Ti–6Al–4V alloy,” *International Journal of Fatigue*, vol. 33, no. 6, pp. 759–765, Jun. 2011.
[53] F. Yıldız, A. F. Yetim, A. Alsaran, A. Çelik, I. Kaymaz, and I. Efeoğlu, “Plain and fretting fatigue behavior of Ti6Al4V alloy coated with TiAlN thin film,” *Tribology International*, vol. 66, pp. 307–314, Oct. 2013.
[54] C. Xie and W. Tong, “Cracking and decohesion of a thin Al2O3 film on a ductile Al–5%Mg substrate,” *Acta Materialia*, vol. 53, no. 2, pp. 477–485, Jan. 2005.

[55] H. Chai, “Transverse fracture in thin-film coatings under spherical indentation,” *Acta Materialia*, vol. 53, no. 2, pp. 487–498, Jan. 2005.
[56] M. W. Moon, H. M. Jensen, J. W. Hutchinson, K. H. Oh, and A. G. Evans, “The characterization of telephone cord buckling of compressed thin films on substrates,” *Journal of the Mechanics and Physics of Solids*, vol. 50, no. 11, pp. 2355–2377, Nov. 2002.
[57] J. Marthelot, J. Bico, F. Melo, and B. Roman, “A new failure mechanism in thin film by collaborative fracture and delamination: Interacting duos of cracks,” *Journal of the Mechanics and Physics of Solids*, vol. 84, pp. 214–229, Nov. 2015.
[58] M.-M. de Denus-Baillargeon, T. Schmitt, S. Larouche, and L. Martinu, “Design and fabrication of stress-compensated optical coatings: Fabry–Perot filters for astronomical applications,” *Applied optics*, vol. 53, no. 12, pp. 2616–2624, 2014.
[59] Brandon Chalifoux, Youwei Yao, Heng E. Zuo, Ralf K. Heilmann, and Mark L. Schattenburg, “Compensating film stress in silicon substrates for the Lynx X-ray telescope mission concept using ion implantation,” presented at the Proc.SPIE, 2018, vol. 10699.
[60] M. Kot, W. Rakowski, Ł. Major, and J. Lackner, “Load-bearing capacity of coating–substrate systems obtained from spherical indentation tests,” *Materials & Design*, vol. 46, pp. 751–757, Apr. 2013.
[61] E. Bemporad, M. Sebastiani, M. H. Staia, and E. Puchi Cabrera, “Tribological studies on PVD/HVOF duplex coatings on Ti6Al4V substrate,” *Surface and Coatings Technology*, vol. 203, no. 5–7, pp. 566–571, Dec. 2008.
[62] B. Podgornik *et al.*, “Tribological properties of plasma nitrided and hard coated AISI 4140 steel,” *Wear*, vol. 249, no. 3–4, pp. 254–259, 2001.
[63] J. Musil, “Flexible hard nanocomposite coatings,” *RSC Advances*, vol. 5, no. 74, pp. 60482–60495, 2015.
[64] A. Leyland and A. Matthews, “On the significance of the H/E ratio in wear control: a nanocomposite coating approach to optimised tribological behaviour,” *Wear*, vol. 246, no. 1, pp. 1–11, 2000.
[65] Y. Cheng, T. Browne, B. Heckerman, and E. Meletis, “Mechanical and tribological properties of nanocomposite TiSiN coatings,” *Surface and Coatings Technology*, vol. 204, no. 14, pp. 2123–2129, 2010.
[66] K. Kuptsov, P. V. Kiryukhantsev-Korneev, A. Sheveyko, and D. Shtansky, “Comparative study of electrochemical and impact wear behavior of TiCN, TiSiCN, TiCrSiCN, and TiAlSiCN coatings,” *Surface and Coatings Technology*, vol. 216, pp. 273–281, 2013.
[67] D. Yu, C. Wang, X. Cheng, and F. Zhang, “Microstructure and properties of TiAlSiN coatings prepared by hybrid PVD technology,” *Thin Solid Films*, vol. 517, no. 17, pp. 4950–4955, 2009.
[68] M. Azzi, M. Benkahoul, J. A. Szpunar, J. E. Klemberg-Sapieha, and L. Martinu, “Tribological properties of CrSiN-coated 301 stainless steel under wet and dry conditions,” *Wear*, vol. 267, pp. 882–889, Jul. 2009.
[69] W. Tillmann, D. Stangier, and P. Schröder, “Investigation and optimization of the tribo-mechanical properties of CrAlCN coatings using Design of Experiments,” *Surface and Coatings Technology*, vol. 308, pp. 147–157, 2016.
[70] J. Carrapichano, J. Gomes, and R. Silva, “Tribological behaviour of Si3N4–BN ceramic materials for dry sliding applications,” *Wear*, vol. 253, no. 9–10, pp. 1070–1076, 2002.

[71] V. N. Manikandan, P. R. Kishore Kumar, P. Deepak Raj, and M. Sridharan, “Microstructural and mechanical properties of magnetron sputtered SiOxNy thin films,” *Materials Today: Proceedings*, vol. 3, no. 6, pp. 1531–1535, 2016.
[72] N. Petkov *et al.*, “Study of surface morphology, structure, mechanical and tribological properties of an AlSiN coating obtained by the cathodic arc deposition method,” *Superlattices and Microstructures*, vol. 109, pp. 402–413, 2017.
[73] C. Donnet and A. Erdemir, *Tribology of diamond-like carbon films: fundamentals and applications*. Springer Science & Business Media, 2007.
[74] K. Kato, “Wear in relation to friction — a review,” *Wear*, vol. 241, no. 2, pp. 151–157, Jul. 2000.
[75] H. Ronkainen, S. Varjus, and K. Holmberg, “Friction and wear properties in dry, water-and oil-lubricated DLC against alumina and DLC against steel contacts,” *Wear*, vol. 222, no. 2, pp. 120–128, 1998.
[76] C. Donnet, J. Martin, T. Le Mogne, and M. Belin, “Super-low friction of MoS2 coatings in various environments,” *Tribology International*, vol. 29, no. 2, pp. 123–128, 1996.
[77] G. Bolelli, A. Candeli, H. Koivuluoto, L. Lusvarghi, T. Manfredini, and P. Vuoristo, “Microstructure-based thermo-mechanical modelling of thermal spray coatings,” *Materials & Design*, vol. 73, pp. 20–34, May 2015.
[78] H. Jelitto and G. A. Schneider, “A geometric model for the fracture toughness of porous materials,” *Acta materialia*, vol. 151, pp. 443–453, 2018.
[79] M. T. Tilbrook, D. J. Paton, Z. Xie, and M. Hoffman, “Microstructural effects on indentation failure mechanisms in TiN coatings: Finite element simulations,” *Acta Materialia*, vol. 55, pp. 2489–2501, May 2007.
[80] R. Varavallo, M. Manfrinato, L. Rossino, O. Maluf, and F. Camargo, “Adhesion of Thermally Sprayed Metallic Coating,” in *18th International Federation for Heat Treatment and Surface Engineering*, ASTM International, 2012.
[81] Y. X. Wang and S. Zhang, “Toward hard yet tough ceramic coatings,” *Surface and Coatings Technology*, vol. 258, pp. 1–16, Nov. 2014.
[82] S. Kumar and W. A. Curtin, “Crack interaction with microstructure,” *Materials today*, vol. 10, no. 9, pp. 34–44, 2007.
[83] M. E. Launey and R. O. Ritchie, “On the Fracture Toughness of Advanced Materials,” *Advanced Materials*, vol. 21, no. 20, pp. 2103–2110, May 2009.
[84] H. Cai and G. Bao, “Crack bridging in functionally graded coatings,” *International Journal of Solids and Structures*, vol. 35, no. 7, pp. 701–717, Mar. 1998.
[85] H. Kakisawa and T. Sumitomo, “The toughening mechanism of nacre and structural materials inspired by nacre,” *Sci Technol Adv Mater*, vol. 12, no. 6, Jan. 2012.
[86] L.-H. He, Z.-H. Yin, L. Jansen van Vuuren, E. A. Carter, and X.-W. Liang, “A natural functionally graded biocomposite coating – Human enamel,” *Acta Biomaterialia*, vol. 9, no. 5, pp. 6330–6337, May 2013.
[87] R. K. Singh, Z. Zhou, L. K. Y. Li, P. Munroe, M. Hoffman, and Z. Xie, “Design of functionally graded carbon coatings against contact damage,” *Thin Solid Films*, vol. 518, no. 20, pp. 5769–5776, 2010.
[88] E. C. N. Silva, M. C. Walters, and G. H. Paulino, “Modeling bamboo as a functionally graded material,” presented at the AIP conference proceedings, 2008, vol. 973, pp. 754–759.

[89] A. L. B. Cauchy, *Recherches sur l'équilibre et le mouvement intérieur des corps solides ou fluides, élastiques ou non élastiques*. 1822.
[90] K. Gupta and J. Meek, "A brief history of the beginning of the finite element method," *International journal for numerical methods in engineering*, vol. 39, no. 22, pp. 3761–3774, 1996.
[91] L. Zhang and K. Mylvaganam, "Nano-tribological analysis by molecular dynamics simulation—a review," *Journal of Computational and Theoretical Nanoscience*, vol. 3, no. 2, pp. 167–188, 2006.
[92] M. Bockstedte, A. Kley, J. Neugebauer, and M. Scheffler, "Density-functional theory calculations for poly-atomic systems: electronic structure, static and elastic properties and ab initio molecular dynamics," *Computer physics communications*, vol. 107, pp. 187–222, 1997.
[93] H. Yao, L. Ouyang, and W.-Y. Ching, "Ab Initio Calculation of Elastic Constants of Ceramic Crystals," *Journal of the American Ceramic Society*, vol. 90, no. 10, pp. 3194–3204, Oct. 2007.
[94] M. Liu and G. Liu, "Smoothed particle hydrodynamics (SPH): an overview and recent developments," *Archives of computational methods in engineering*, vol. 17, no. 1, pp. 25–76, 2010.
[95] F. A. Tavarez and M. E. Plesha, "Discrete element method for modelling solid and particulate materials," *International Journal for Numerical Methods in Engineering*, vol. 70, no. 4, pp. 379–404, Apr. 2007.
[96] R. W. Macek and S. A. Silling, "Peridynamics via finite element analysis," *Finite Elements in Analysis and Design*, vol. 43, no. 15, pp. 1169–1178, 2007.
[97] T. A. Laursen, *Computational contact and impact mechanics: fundamentals of modeling interfacial phenomena in nonlinear finite element analysis*. Springer Science & Business Media, 2013.
[98] M. Kuna, *Finite Elements in Fracture Mechanics*, vol. 201. Dordrecht: Springer Netherlands, 2013.
[99] R. De Borst, "Numerical aspects of cohesive-zone models," *Engineering fracture mechanics*, vol. 70, no. 14, pp. 1743–1757, 2003.
[100] N. Moës and T. Belytschko, "Extended finite element method for cohesive crack growth," *Engineering fracture mechanics*, vol. 69, no. 7, pp. 813–833, 2002.
[101] G. Z. Voyiadjis and Y. Song, "Strain gradient continuum plasticity theories: Theoretical, numerical and experimental investigations," *International Journal of Plasticity*, Mar. 2019.
[102] Z. P. Bazant and G. Pijaudier-Cabot, "Nonlocal continuum damage, localization instability and convergence," *Journal of applied mechanics*, vol. 55, no. 2, pp. 287–293, 1988.
[103] L. Evers, W. Brekelmans, and M. Geers, "Non-local crystal plasticity model with intrinsic SSD and GND effects," *Journal of the Mechanics and Physics of Solids*, vol. 52, no. 10, pp. 2379–2401, 2004.
[104] N.-H. Kim, *Introduction to nonlinear finite element analysis*. Springer Science & Business Media, 2014.
[105] J. O. Hallquist, "LS-DYNA theory manual," *Livermore software Technology corporation*, vol. 3, pp. 25–31, 2006.

[106] R. Courant, K. Friedrichs, and H. Lewy, "On the Partial Difference Equations of Mathematical Physics," *IBM Journal of Research and Development*, vol. 11, no. 2, pp. 215–234, Mar. 1967.
[107] G. R. Irwin, "Analysis of stresses and strains near the end of a crack traversing a plate," *J. appl. Mech.*, 1957.
[108] H. M. Westergaard, "Bearing pressures and cracks," *Trans AIME, J. Appl. Mech.*, vol. 6, pp. 49–53, 1939.
[109] F. Erdogan and G. Sih, "On the crack extension in plates under plane loading and transverse shear," *Journal of basic engineering*, vol. 85, no. 4, pp. 519–525, 1963.
[110] M. Hussain, S. Pu, and J. Underwood, "Strain energy release rate for a crack under combined mode I and mode II," presented at the Fracture analysis: Proceedings of the 1973 national symposium on fracture mechanics, part II, 1974.
[111] G. C. Sih, "Strain-energy-density factor applied to mixed mode crack problems," *International Journal of fracture*, vol. 10, no. 3, pp. 305–321, 1974.
[112] J. R. Rice, "A path independent integral and the approximate analysis of strain concentration by notches and cracks," *Journal of applied mechanics*, vol. 35, no. 2, pp. 379–386, 1968.
[113] G. Cherepanov, "The propagation of cracks in a continuous medium," *Journal of Applied Mathematics and Mechanics*, vol. 31, no. 3, pp. 503–512, 1967.
[114] T. Hellen, "On the method of virtual crack extensions," *International journal for numerical methods in engineering*, vol. 9, no. 1, pp. 187–207, 1975.
[115] S. Suresh, "Elastic-Plastic Fracture Mechanics," 2003.
[116] J. W. Hutchinson, "Singular behaviour at the end of a tensile crack in a hardening material," *Journal of the Mechanics and Physics of Solids*, vol. 16, no. 1, pp. 13–31, Jan. 1968.
[117] J. R. Rice and G. F. Rosengren, "Plane strain deformation near a crack tip in a power-law hardening material," *Journal of the Mechanics and Physics of Solids*, vol. 16, no. 1, pp. 1–12, Jan. 1968.
[118] T. L. Anderson, *Fracture mechanics: fundamentals and applications*. CRC press, 2017.
[119] S. K. Maiti, *Fracture mechanics: fundamentals and applications*. Cambridge University Press, 2015.
[120] X. Meng, C. Fang, and K. Niu, "Tribological behavior anisotropy in sliding interaction of asperities on single-crystal α-iron: A quasi-continuum study," *Tribology International*, vol. 118, pp. 347–359, 2018.
[121] T. Slack and F. Sadeghi, "Cohesive zone modeling of intergranular fatigue damage in rolling contacts," *Tribology international*, vol. 44, no. 7–8, pp. 797–804, 2011.
[122] S. Nekkanty, M. Walter, and R. Shivpuri, "A cohesive zone finite element approach to model tensile cracks in thin film coatings," *Journal of Mechanics of Materials and Structures*, vol. 2, no. 7, pp. 1231–1247, 2007.
[123] Z. Li and F. Yang, "Grain rotations during uniaxial deformation of gradient nano-grained metals using crystal plasticity finite element simulations," *Extreme Mechanics Letters*, vol. 16, pp. 41–48, 2017.
[124] G. Sin'Ko and N. Smirnov, "Ab initio calculations of elastic constants and thermodynamic properties of bcc, fcc, and hcp Al crystals under pressure," *Journal of Physics: Condensed Matter*, vol. 14, no. 29, p. 6989, 2002.

[125] F. Han, G. Lubineau, and Y. Azdoud, “Adaptive coupling between damage mechanics and peridynamics: A route for objective simulation of material degradation up to complete failure,” *Journal of the Mechanics and Physics of Solids*, vol. 94, pp. 453–472, 2016.
[126] J. Jerier and J. Molinari, “Normal contact between rough surfaces by the discrete element method,” *Tribology international*, vol. 47, pp. 1–8, 2012.
[127] Hirshikesh, S. Natarajan, R. K. Annabattula, and E. Martínez-Pañeda, “Phase field modelling of crack propagation in functionally graded materials,” *Composites Part B: Engineering*, vol. 169, pp. 239–248, Jul. 2019.
[128] A. Shahani and M. A. Fasakhodi, “Finite element analysis of dynamic crack propagation using remeshing technique,” *Materials & design*, vol. 30, no. 4, pp. 1032–1041, 2009.
[129] K. Holmberg, A. Laukkanen, E. Turunen, and T. Laitinen, “Wear resistance optimisation of composite coatings by computational microstructural modelling,” *Surface and Coatings Technology*, vol. 247, pp. 1–13, May 2014.
[130] P. Woytowitz and R. Richman, “Modeling of damage from multiple impacts by spherical particles,” *Wear*, vol. 233, pp. 120–133, 1999.
[131] A. I. Vakis *et al.*, “Modeling and simulation in tribology across scales: An overview,” *Tribology International*, vol. 125, pp. 169–199, Sep. 2018.
[132] M. Masanta, S. Shariff, and A. R. Choudhury, “Evaluation of modulus of elasticity, nano-hardness and fracture toughness of TiB2–TiC–Al2O3 composite coating developed by SHS and laser cladding,” *Materials Science and Engineering: A*, vol. 528, no. 16–17, pp. 5327–5335, 2011.
[133] N. Schwarzer, “The extended Hertzian theory and its uses in analyzing indentation experiments,” *Philosophical Magazine*, vol. 86, no. 33–35, pp. 5179–5197, Nov. 2006.
[134] M. Kot, W. Rakowski, J. M. Lackner, and Ł. Major, “Analysis of spherical indentations of coating-substrate systems: Experiments and finite element modeling,” *Materials and Design*, vol. 43, pp. 99–111, Feb. 2013.
[135] L. Vernhes *et al.*, “Nanostructured and Conventional Cr2O3, TiO2, and TiO2-Cr2O3 Thermal-Sprayed Coatings for Metal-Seated Ball Valve Applications in Hydrometallurgy,” *Journal of Thermal Spray Technology*, vol. 25, no. 5, pp. 1068–1078, 2016.
[136] H. Chiang, C. Wang, M. Wu, and E. Wolff-Klammer, “Investigation of Stress Corrosion Cracking On Brass Valves With Laboratory Testing And X-ray Computed Tomography,” presented at the CORROSION 2012, 2012.
[137] T. C. Dickenson, *Valves, Piping, and Pipelines Handbook*. Elsevier, 1999.
[138] B. K. Holmes and S. Bond, “Sour Service Limits of Dual-Certified 316/316L Austenitic Stainless Steel and Weldments,” presented at the CORROSION 2010, 2010.
[139] D. Bush, J. Brown, and K. Lewis, “An overview of NACE international standard MR0103 and comparison with MR0175,” *CORROSION 2004*, 2004.
[140] NORSOK Standard M-001, “Materials Selection,” 2014.
[141] “Standard Guide for Evaluating Nonmetallic Materials for Oxygen Service,” ASTM International, 2015.
[142] P. F. Mendez *et al.*, “Welding processes for wear resistant overlays,” *Journal of Manufacturing Processes*, vol. 16, no. 1, pp. 4–25, 2014.
[143] L. Vernhes, M. Azzi, E. Bousser, T. Schmitt, J. M. Lamarre, and J. E. Klemberg-Sapieha, “Hybrid Co-Cr/W-WC and Ni-W-Cr-B/W-WC Coating Systems,” *Journal of Thermal Spray Technology*, vol. 25, no. 1–2, pp. 346–356, Jan. 2016.

[144] K. Holmberg, A. Laukkanen, H. Ronkainen, K. Wallin, and S. Varjus, "A model for stresses, crack generation and fracture toughness calculation in scratched TiN-coated steel surfaces," *Wear*, vol. 254, no. 3, pp. 278–291, 2003.
[145] L. Vernhes, M. Azzi, and J. E. Klemberg-Sapieha, "Alternatives for hard chromium plating: Nanostructured coatings for severe-service valves," *Materials Chemistry and Physics*, vol. 140, pp. 522–528, Jul. 2013.
[146] G. Cassar, S. Banfield, J. C. A.-B. Wilson, J. Housden, A. Matthews, and A. Leyland, "Tribological properties of duplex plasma oxidised, nitrided and PVD coated Ti–6Al–4V," *Surface and Coatings Technology*, vol. 206, no. 2–3, pp. 395–404, Oct. 2011.
[147] Y. Yusuf, Z. Mohd Rosli, J. M. Juoi, O. Nooririnah, and U. A. A. Azlan, "The Influence of the Microwave Plasma Nitrided Ti6Al4V Substrate Properties to the Duplex Coating Performance," *Applied Mechanics and Materials*, vol. 761, pp. 68–72, May 2015.
[148] R. Rodríguez-Baracaldo, J. A. Benito, E. S. Puchi-Cabrera, and M. H. Staia, "High temperature wear resistance of (TiAl)N PVD coating on untreated and gas nitrided AISI H13 steel with different heat treatments," *Wear*, vol. 262, no. 3–4, pp. 380–389, Feb. 2007.
[149] C. X. Li and T. Bell, "Corrosion properties of active screen plasma nitrided 316 austenitic stainless steel," *Corrosion Science*, vol. 46, no. 6, pp. 1527–1547, Jun. 2004.
[150] L. Nosei, S. Farina, M. Ávalos, L. Náchez, B. J. Gómez, and J. Feugeas, "Corrosion behavior of ion nitrided AISI 316L stainless steel," *Thin Solid Films*, vol. 516, no. 6, pp. 1044–1050, Jan. 2008.
[151] J. A. Picas, S. Menargues, E. Martin, C. Colominas, and M. T. Baile, "Characterization of duplex coating system (HVOF+PVD) on light alloy substrates," *Surface and Coatings Technology*, Jun. 2016.
[152] F. Liu, C. Liu, S. Chen, X. Tao, and Y. Zhang, "Laser cladding Ni–Co duplex coating on copper substrate," *Optics and Lasers in Engineering*, vol. 48, no. 7–8, pp. 792–799, Jul. 2010.
[153] F. Casadei and M. Tului, "Combining thermal spraying and PVD technologies: A new approach of duplex surface engineering for Ti alloys," *Surface and Coatings Technology*, vol. 237, pp. 415–420, Dec. 2013.
[154] G. Bolelli *et al.*, "Thermally Sprayed Coatings as Interlayers for DLC-Based Thin Films," *Journal of Thermal Spray Technology*, vol. 18, no. 2, pp. 231–242, Jun. 2009.
[155] Y. N. Zhuk, "Hardide™: advanced nano-structured CVD coating," *International Journal of Microstructure and Materials Properties*, vol. 2, no. 1, pp. 90–98, 2007.
[156] W. C. Oliver and G. M. Pharr, "An improved technique for determining hardness and elastic modulus using load and displacement sensing indentation experiments," *J. Mater. Res.*, vol. 7, pp. 1564–1583, 1992.
[157] "ISO 26443:2016, Fine ceramics (advanced ceramics, advanced technical ceramics). Rockwell indentation test for evaluation of adhesion of ceramic coatings."
[158] "Standard Test Method for Linearly Reciprocating Ball-on-Flat Sliding Wear," ASTM International, 2016.
[159] L.-D. K. U. Manual and I. Volume, "Version 971," *Livermore Software Technology Corporation*, vol. 7374, p. 354, 2007.
[160] M. Z. Huq and J.-P. Celis, "Expressing wear rate in sliding contacts based on dissipated energy," *Wear*, vol. 252, no. 5–6, pp. 375–383, Mar. 2002.

[161] D. C. Agrawal and R. Raj, “Measurement of the ultimate shear strength of a metal-ceramic interface,” *Acta Metallurgica*, vol. 37, no. 4, pp. 1265–1270, 1989.
[162] Y. Leterrier *et al.*, “Mechanical integrity of thin inorganic coatings on polymer substrates under quasi-static, thermal and fatigue loadings,” *Thin Solid Films*, vol. 519, no. 5, pp. 1729–1737, Dec. 2010.
[163] H. Chai, “Channel cracking in inelastic film/substrate systems,” *International Journal of Solids and Structures*, vol. 48, no. 7–8, pp. 1092–1100, Apr. 2011.
[164] J. H. Waller, L. Lalande, Y. Leterrier, and J.-A. E. Månson, “Modelling the effect of temperature on crack onset strain of brittle coatings on polymer substrates,” *Thin Solid Films*, vol. 519, no. 13, pp. 4249–4255, Apr. 2011.
[165] N. Cordero, J. Yoon, and Z. Suo, “Channel cracks in a hermetic coating consisting of organic and inorganic layers,” *Applied Physics Letters*, vol. 90, no. 11, p. 111910, Mar. 2007.
[166] Z. Jia, M. B. Tucker, and T. Li, “Failure mechanics of organic–inorganic multilayer permeation barriers in flexible electronics,” *Composites Science and Technology*, vol. 71, no. 3, pp. 365–372, Feb. 2011.
[167] H. ur Rehman, F. Ahmed, C. Schmid, J. Schaufler, and K. Durst, “Study on the deformation mechanics of hard brittle coatings on ductile substrates using in-situ tensile testing and cohesive zone FEM modeling,” *Surface and Coatings Technology*, vol. 207, pp. 163–169, Aug. 2012.
[168] L. Martinu and J. E. Klemberg-Sapieha, “Optical coatings on plastics,” in *Optical Interference Coatings*, Springer, 2004, pp. 460–489.
[169] H. Chai, B. Lawn, and S. Wuttiphan, “Fracture modes in brittle coatings with large interlayer modulus mismatch,” *Journal of materials research*, vol. 14, no. 9, pp. 3805–3817, 1999.
[170] T. Li, Z. Zhang, and B. Michaux, “Competing failure mechanisms of thin metal films on polymer substrates under tension,” *Theoretical and Applied Mechanics Letters*, vol. 1, no. 4, 2011.
[171] J. M. Ambrico and M. R. Begley, “The role of initial flaw size, elastic compliance and plasticity in channel cracking of thin films,” *Thin Solid Films*, vol. 419, no. 1, pp. 144–153, 2002.
[172] C. Ho *et al.*, “Adhesion characterization of SiO2 thin films evaporated onto a polymeric substrate.”
[173] J.-S. Park, H. Chae, H. K. Chung, and S. I. Lee, “Thin film encapsulation for flexible AM-OLED: a review,” *Semiconductor Science and Technology*, vol. 26, no. 3, p. 034001, Mar. 2011.
[174] A. da Silva Sobrinho, M. Latreche, G. Czeremuszkin, J. Klemberg-Sapieha, and M. Wertheimer, “Transparent barrier coatings on polyethylene terephthalate by single-and dual-frequency plasma-enhanced chemical vapor deposition,” *Journal of Vacuum Science & Technology A: Vacuum, Surfaces, and Films*, vol. 16, no. 6, pp. 3190–3198, 1998.
[175] M. R. Wertheimer, L. Martinu, J. E. Klemberg-Sapieha, and G. Czeremuszkin, “Plasma treatment of polymers to improve adhesion,” *MATERIALS ENGINEERING-NEW YORK-*, vol. 14, pp. 139–174, 1999.
[176] L. Martinu and D. Poitras, “Plasma deposition of optical films and coatings: a review,” *Journal of Vacuum Science & Technology A: Vacuum, Surfaces, and Films*, vol. 18, no. 6, pp. 2619–2645, 2000.

[177] M. Caron, O. Zabeida, J. E. Klemberg-Sapieha, and L. Martinu, “Stability and performance of organic-inorganic thin films on polymer substrates,” *Surface and Coatings Technology*, vol. 314, pp. 131–138, Mar. 2017.
[178] T. Poirié, T. Schmitt, E. Bousser, R. Vernhes, L. Martinu, and J. E. Klemberg-Sapieha, “Hybrid organic/inorganic nanolaminate structures with enhanced tribo-mechanical properties for optical applications,” *Surface and Coatings Technology*, vol. 315, pp. 399–407, Apr. 2017.
[179] M. Mildebrath and K. Klemm, “Ophthalmic optical coatings: the real world can be more aggressive than you think,” 2006, p. 64030W.
[180] O. Zabeida *et al.*, “Hybrid Organic-Inorganic Optical Films Deposited by Ion Beam Assisted CVD,” in *Optical Interference Coatings*, 2013, p. ThA.4.
[181] T. Aoki, H. Hatta, T. Hitomi, H. Fukuda, and I. Shiota, “SiC/C multi-layered coating contributing to the antioxidation of C/C composites and the suppression of through-thickness cracks in the layer,” *Carbon*, vol. 39, no. 10, pp. 1477–1483, 2001.
[182] S. Nekkanty, M. Walter, and R. Shivpuri, “A cohesive zone finite element approach to model tensile cracks in thin film coatings,” *Journal of Mechanics of Materials and Structures*, vol. 2, no. 7, pp. 1231–1247, 2007.
[183] J. Andersons, J. Modniks, Y. Leterrier, G. Tornare, P. Dumont, and J.-A. E. Månson, “Evaluation of toughness by finite fracture mechanics from crack onset strain of brittle coatings on polymers,” *Theoretical and Applied Fracture Mechanics*, vol. 49, no. 2, pp. 151–157, Apr. 2008.
[184] W. C. Oliver and G. M. Pharr, “Measurement of hardness and elastic modulus by instrumented indentation: Advances in understanding and refinements to methodology,” *Journal of Materials Research*, vol. 19, no. 1, pp. 3–20, 2004.
[185] G. G. Stoney, “The tension of metallic films deposited by electrolysis,” *Proc. R. Soc. Lond. A*, vol. 82, no. 553, pp. 172–175, 1909.
[186] R. Cintron and V. Saouma, “Strain measurements with the digital image correlation system Vic-2D,” *System*, vol. 106, p. 2D, 2008.
[187] P. Lindström, A. Jonsson, A. Jernberg, and E. Östby, “Non-linear fracture mechanics in LS-DYNA and LS-PrePost,” presented at the 10th European LS-DYNA conference, 2015.
[188] M. T. Kim, “Influence of substrates on the elastic reaction of films for the microindentation tests,” *Thin Solid Films*, vol. 283, no. 1, pp. 12–16, Sep. 1996.
[189] Z. Gan, G. Yu, Z. Zhao, C. Tan, and B. Tay, “Mechanical properties of zirconia thin films deposited by filtered cathodic vacuum arc,” *Journal of the American Ceramic Society*, vol. 88, no. 8, pp. 2227–2229, 2005.
[190] P. Sarkar, R. Tokas, S. Jena, S. Thakur, and N. Sahoo, “Comparative studies of optical & elastic properties of ZrO 2 thin films prepared under normal and oblique incidence deposition geometries,” presented at the AIP Conference Proceedings, 2014, vol. 1591, pp. 1051–1053.
[191] C. Ho *et al.*, “Adhesion characterization of SiO2 thin films evaporated onto a polymeric substrate,” *International Journal of Engineering Research & Science (IJOER)*, vol. 4, no. 2, pp. 38–46, 2018.
[192] T. Poirié, T. Schmitt, E. Bousser, L. Martinu, and J. E. Klemberg-Sapieha, “In situ real time nanowear testing method of optical functional thin films,” *Tribology International*, vol. 95, pp. 147–155, 2016.

[193] H. Leplan, B. Geenen, J. Robic, and Y. Pauleau, “Residual stresses in evaporated silicon dioxide thin films: correlation with deposition parameters and aging behavior,” *Journal of applied physics*, vol. 78, no. 2, pp. 962–968, 1995.
[194] S. Jena, R. Tokas, S. Thakur, and N. Sahoo, “Optical properties of electron beam evaporated ZrO2: 10% SiO2 thin films: dependence on structure,” *Indian Journal of Physics*, vol. 90, no. 8, pp. 951–957, 2016.
[195] F. Meng, J. L. David, S. Bollin, M. E. Nichols, and M. D. Thouless, “Kinetics of channeling cracks in polymeric coatings,” *International Journal of Solids and Structures*, vol. 132–133, pp. 105–113, Feb. 2018.
[196] V. Karen, “NIST Structural Ceramics, NIST Standard Reference Database 30.” National Institute of Standards and Technology, 1990.
[197] E. Bousser, L. Martinu, and J. E. Klemberg-Sapieha, “Solid particle erosion mechanisms of protective coatings for aerospace applications,” *Surface and Coatings Technology*, vol. 257, pp. 165–181, Oct. 2014.
[198] A. G. Evans, M. Gulden, and M. Rosenblatt, “Impact damage in brittle materials in the elastic-plastic response regime,” *Proceedings of the Royal Society of London. A. Mathematical and Physical Sciences*, vol. 361, no. 1706, pp. 343–365, 1978.
[199] S. Wiederhorn and B. Lawn, “Strength degradation of glass impacted with sharp particles: I, Annealed surfaces,” *Journal of the American Ceramic Society*, vol. 62, no. 1-2, pp. 66–70, 1979.
[200] S. Hassani, M. Bielawski, W. Beres, L. Martinu, M. Balazinski, and J. E. Klemberg-Sapieha, “Predictive tools for the design of erosion resistant coatings,” *Surface and Coatings Technology*, vol. 203, pp. 204–210, Nov. 2008.
[201] S. Hassani, J. E. Klemberg-Sapieha, M. Bielawski, W. Beres, L. Martinu, and M. Balazinski, “Design of hard coating architecture for the optimization of erosion resistance,” *Wear*, vol. 265, pp. 879–887, Aug. 2008.
[202] S. Anwar, D. A. Axinte, and A. A. Becker, “Finite element modelling of abrasive waterjet milled footprints,” *Journal of Materials Processing Technology*, vol. 213, no. 2, pp. 180–193, Feb. 2013.
[203] B. Borawski, J. Singh, J. A. Todd, and D. E. Wolfe, “Multi-layer coating design architecture for optimum particulate erosion resistance,” *Wear*, vol. 271, pp. 2782–2792, Sep. 2011.
[204] P. Balu, F. Kong, S. Hamid, and R. Kovacevic, “Finite element modeling of solid particle erosion in AISI 4140 steeland Nickel-Tungsten carbide composite material produced by the laser-based powder deposition process,” *Tribology International*, Mar. 2013.
[205] D. Aquaro, “Impact of solid particulate on brittle materials,” *Strojniški vestnik-Journal of Mechanical Engineering*, vol. 56, pp. 268–276, 2010.
[206] Y.-F. Wang and Z.-G. Yang, “Finite element model of erosive wear on ductile and brittle materials,” *Wear*, vol. 265, no. 5–6, pp. 871–878, Aug. 2008.
[207] M. Takaffoli and M. Papini, “Numerical simulation of solid particle impacts on Al6061-T6 Part II: Materials removal mechanisms for impact of multiple angular particles,” *Wear*, vol. 296, pp. 648–655, Aug. 2012.
[208] H. Qi, J. Fan, J. Wang, and H. Li, “Impact erosion by high velocity micro-particles on a quartz crystal,” *Tribology International*, vol. 82, pp. 200–210, Feb. 2015.
[209] Y. Miyamoto, Ed., *Functionally graded materials: design, processing, and applications*. Boston: Kluwer Academic Publishers, 1999.

[210] K. Holmberg and A. Matthews, *Coatings Tribology*. Elsevier, 2009.
[211] A. Giannakopoulos and P. Pallot, "Two-dimensional contact analysis of elastic graded materials," *Journal of the Mechanics and Physics of Solids*, vol. 48, no. 8, pp. 1597–1631, 2000.
[212] A. Giannakopoulos and S. Suresh, "Indentation of solids with gradients in elastic properties: Part II. Axisymmetric indentors," *International Journal of Solids and Structures*, vol. 34, no. 19, pp. 2393–2428, 1997.
[213] L.-H. He and M. V. Swain, "Enamel—a functionally graded natural coating," *Journal of dentistry*, vol. 37, no. 8, pp. 596–603, 2009.
[214] Z. Liu, Y. Zhu, D. Jiao, Z. Weng, Z. Zhang, and R. O. Ritchie, "Enhanced protective role in materials with gradient structural orientations: Lessons from Nature," *Acta Biomaterialia*, vol. 44, pp. 31–40, Oct. 2016.
[215] D. Raabe *et al.*, "Microstructure and crystallographic texture of the chitin–protein network in the biological composite material of the exoskeleton of the lobster Homarus americanus," *Materials science and engineering: A*, vol. 421, no. 1–2, pp. 143–153, 2006.
[216] P.-Y. Chen, A. Y.-M. Lin, J. McKittrick, and M. A. Meyers, "Structure and mechanical properties of crab exoskeletons," *Acta biomaterialia*, vol. 4, no. 3, pp. 587–596, 2008.
[217] G. M. Genin *et al.*, "Functional grading of mineral and collagen in the attachment of tendon to bone," *Biophysical journal*, vol. 97, no. 4, pp. 976–985, 2009.
[218] J. C. Weaver *et al.*, "The stomatopod dactyl club: a formidable damage-tolerant biological hammer," *Science*, vol. 336, no. 6086, pp. 1275–1280, 2012.
[219] P. Roach, D. Eglin, K. Rohde, and C. C. Perry, "Modern biomaterials: a review—bulk properties and implications of surface modifications," *Journal of Materials Science: Materials in Medicine*, vol. 18, no. 7, pp. 1263–1277, 2007.
[220] P. Fratzl and R. Weinkamer, "Nature's hierarchical materials," *Progress in Materials Science*, vol. 52, no. 8, pp. 1263–1334, Nov. 2007.
[221] W. Huang *et al.*, "Multiscale Toughening Mechanisms in Biological Materials and Bioinspired Designs," *Adv. Mater.*, p. 1901561, Jul. 2019.
[222] Y. Zhang, H. Chai, and B. R. Lawn, "Graded Structures for All-ceramic Restorations," *Journal of Dental Research*, vol. 89, no. 4, pp. 417–421, Apr. 2010.
[223] M. H. Ghayesh and A. Farajpour, "A review on the mechanics of functionally graded nanoscale and microscale structures," *International Journal of Engineering Science*, vol. 137, pp. 8–36, Apr. 2019.
[224] M. Naebe and K. Shirvanimoghaddam, "Functionally graded materials: A review of fabrication and properties," *Applied Materials Today*, vol. 5, pp. 223–245, Dec. 2016.
[225] A. Portinha *et al.*, "Characterization of thermal barrier coatings with a gradient in porosity," *Surface and Coatings Technology*, vol. 195, no. 2, pp. 245–251, May 2005.
[226] X. C. Zhang, B. S. Xu, H. D. Wang, Y. X. Wu, and Y. Jiang, "Hertzian contact response of single-layer, functionally graded and sandwich coatings," *Materials & Design*, vol. 28, no. 1, pp. 47–54, Jan. 2007.
[227] G. Wu, Q. Chen, Z. Lu, and G. Zhang, "Bio-inspired AlSiCN/Ti hierarchical coatings with high toughness by efficient energy dissipation," *Results in Physics*, p. 102358, 2019.
[228] E. Dorthé and Y. Zhang, "Load-bearing increase in alumina evoked by introduction of a functional glass gradient," *Journal of the European Ceramic Society*, vol. 32, no. 6, pp. 1213–1220, Jun. 2012.

[229] R. Vernhes, O. Zabeida, J. E. Klemberg-Sapieha, and L. Martinu, "Single-material inhomogeneous optical filters based on microstructural gradients in plasma-deposited silicon nitride," *Appl. Opt.*, vol. 43, no. 1, pp. 97–103, Jan. 2004.
[230] D. Rats, L. Martinu, and J. von Stebut, "Mechanical properties of plasma-deposited SiOxNy coatings on polymer substrates using low load carrying capacity techniques," *Surface and Coatings Technology*, vol. 123, no. 1, pp. 36–43, Jan. 2000.
[231] B. E. Abali, C. Völlmecke, B. Woodward, M. Kashtalyan, I. Guz, and W. H. Müller, "Numerical modeling of functionally graded materials using a variational formulation," *Continuum Mech. Thermodyn.*, vol. 24, no. 4–6, pp. 377–390, Nov. 2012.
[232] M. Mehrali, F. S. Shirazi, M. Mehrali, H. S. C. Metselaar, N. A. B. Kadri, and N. A. A. Osman, "Dental implants from functionally graded materials," *Journal of Biomedical Materials Research Part A: An Official Journal of The Society for Biomaterials, The Japanese Society for Biomaterials, and The Australian Society for Biomaterials and the Korean Society for Biomaterials*, vol. 101, no. 10, pp. 3046–3057, 2013.
[233] G. H. Paulino, Z.-H. Jin, and R. H. Dodds, "2.13 - Failure of Functionally Graded Materials," in *Comprehensive Structural Integrity*, I. Milne, R. O. Ritchie, and B. Karihaloo, Eds. Oxford: Pergamon, 2003, pp. 607–644.
[234] S. Suresh, "Graded materials for resistance to contact deformation and damage," *Science*, vol. 292, no. 5526, pp. 2447–2451, 2001.
[235] M. G. Gok and G. Goller, "Production and characterisation of GZ/CYSZ alternative thermal barrier coatings with multilayered and functionally graded designs," *Journal of the European Ceramic Society*, vol. 36, no. 7, pp. 1755–1764, 2016.
[236] E. S. Chin, "Army focused research team on functionally graded armor composites," *Materials Science and Engineering: A*, vol. 259, no. 2, pp. 155–161, 1999.
[237] M. Übeyli *et al.*, "The ballistic performance of SiC–AA7075 functionally graded composite produced by powder metallurgy," *Materials & Design (1980-2015)*, vol. 56, pp. 31–36, 2014.
[238] F. Watari *et al.*, "Biocompatibility of materials and development to functionally graded implant for bio-medical application," *Composites Science and Technology*, vol. 64, no. 6, pp. 893–908, 2004.
[239] M. A. F. Afzal, P. Kesarwani, K. M. Reddy, S. Kalmodia, B. Basu, and K. Balani, "Functionally graded hydroxyapatite-alumina-zirconia biocomposite: synergy of toughness and biocompatibility," *Materials Science and Engineering: C*, vol. 32, no. 5, pp. 1164–1173, 2012.
[240] H. Fong, M. Sarikaya, S. N. White, and M. L. Snead, "Nano-mechanical properties profiles across dentin–enamel junction of human incisor teeth," *Materials Science and Engineering: C*, vol. 7, no. 2, pp. 119–128, 1999.
[241] D. Umbrello, "Finite element simulation of conventional and high speed machining of Ti6Al4V alloy," *Journal of materials processing technology*, vol. 196, no. 1–3, pp. 79–87, 2008.
[242] P. Jedrzejowski, J. Klemberg-Sapieha, and L. Martinu, "Relationship between the mechanical properties and the microstructure of nanocomposite TiN/SiN 1.3 coatings prepared by low temperature plasma enhanced chemical vapor deposition," *Thin Solid Films*, vol. 426, no. 1, pp. 150–159, 2003.

[243] F. Knudsen, “Effect of porosity on Young’s modulus of alumina,” *Journal of the American Ceramic Society*, vol. 45, no. 2, pp. 94–95, 1962.
[244] Y. Zhang, J. C. Outeiro, and T. Mabrouki, “On the Selection of Johnson-cook Constitutive Model Parameters for Ti-6Al-4V Using Three Types of Numerical Models of Orthogonal Cutting,” *Procedia CIRP*, vol. 31, pp. 112–117, Jan. 2015.
[245] M. Bielawski and W. Beres, “FE modelling of surface stresses in erosion-resistant coatings under single particle impact,” *Wear*, vol. 262, pp. 167–175, Feb. 2007.
[246] M. S. Ahmed, Z. Zhou, P. Munroe, L. K. Y. Li, and Z. Xie, “Control of the damage resistance of nanocomposite TiSiN coatings on steels: roles of residual stress,” *Thin Solid Films*, vol. 519, no. 15, pp. 5007–5012, 2011.
[247] S. Zhang and X. Zhang, “Toughness evaluation of hard coatings and thin films,” *Thin Solid Films*, vol. 520, pp. 2375–2389, Feb. 2012.
[248] U. Wiklund, J. Gunnars, and S. Hogmark, “Influence of residual stresses on fracture and delamination of thin hard coatings,” *Wear*, vol. 232, no. 2, pp. 262–269, 1999.
[249] P. Shipway and I. Hutchings, “Measurement of coating durability by solid particle erosion,” *Surface and Coatings Technology*, vol. 71, no. 1, pp. 1–8, 1995.
[250] F. Erdogan, “Fracture mechanics of functionally graded materials,” *Composites Engineering*, vol. 5, no. 7, pp. 753–770, 1995.
[251] F. Wiesinger, F. Sutter, A. Fernández-García, J. Reinhold, and R. Pitz-Paal, “Sand erosion on solar reflectors: Accelerated simulation and comparison with field data,” *Solar Energy Materials and Solar Cells*, vol. 145, pp. 303–313, Feb. 2016.
[252] N. Adjouadi, N. Laouar, C. Bousbaa, N. Bouaouadja, and G. Fantozzi, “Study of light scattering on a soda lime glass eroded by sandblasting,” *Journal of the European Ceramic Society*, vol. 27, no. 10, pp. 3221–3229, Jan. 2007.
[253] C. Kennedy, R. Smilgys, D. Kirkpatrick, and J. Ross, “Optical performance and durability of solar reflectors protected by an alumina coating,” *Thin Solid Films*, vol. 304, no. 1–2, pp. 303–309, 1997.
[254] K. C. Datsiou and M. Overend, “Artificial ageing of glass with sand abrasion,” *Construction and Building Materials*, vol. 142, pp. 536–551, Jul. 2017.
[255] L. Lallemant, V. Garnier, G. Bonnefont, A. Marouani, G. Fantozzi, and N. Bouaouadja, “Effect of solid particle impact on light transmission of transparent ceramics: Role of the microstructure,” *Optical Materials*, vol. 37, pp. 352–357, Nov. 2014.
[256] C. Avenel, O. Raccurt, J.-L. Gardette, and S. Therias, “Review of accelerated ageing test modelling and its application to solar mirrors,” *Solar Energy Materials and Solar Cells*, vol. 186, pp. 29–41, Nov. 2018.
[257] T. W. Boentoro, B. Szyszka, and L. Martinu, “Protective coatings for durability enhancement of optical surfaces,” in *Optical Thin Films and Coatings*, Elsevier, 2018, pp. 539–564.
[258] A. Marouani, N. Bouaouadja, Y. Castro, and A. Durán, “Repair and Restoration of the Optical Properties of Sandblasted Glasses By Silica-Based Sol-Gel Coatings,” *International Journal of Applied Glass Science*, vol. 6, no. 1, pp. 94–102, Mar. 2015.
[259] P. O. Schissel, C. E. Kennedy, G. J. Jorgensen, Y. D. Shinton, and R. M. Goggin, “Durable metallized polymer mirror,” Nov. 1994.
[260] D. Chen, “POLYMERIC MIRROR FILMS: DURABILITY IMPROVEMENT AND IMPLEMENTATION IN NEW COLLECTOR DESIGNS,” p. 41.

[261] C. E. Tracy and D. K. Benson, “Silicon nitride protective coatings for silvered glass mirrors,” Oct. 1988.
[262] N. Sahouane and A. Zerga, “Optimization of Antireflection Multilayer for Industrial Crystalline Silicon Solar Cells,” *Energy Procedia*, vol. 44, pp. 118–125, 2014.
[263] X. Wang, C. Wang, X. Shen, and F. Sun, “Potential material for fabricating optical mirrors: polished diamond coated silicon carbide,” *Applied Optics*, vol. 56, no. 14, p. 4113, May 2017.
[264] E. Bousser, L. Martinu, and J. E. Klemberg-Sapieha, “Effect of erodent properties on the solid particle erosion mechanisms of brittle materials,” *J Mater Sci*, vol. 48, pp. 5543–5558, May 2013.
[265] Y. I. Oka, K. Okamura, and T. Yoshida, “Practical estimation of erosion damage caused by solid particle impact: Part 1: Effects of impact parameters on a predictive equation,” *Wear*, vol. 259, no. 1–6, pp. 95–101, 2005.
[266] Y. Oka and T. Yoshida, “Practical estimation of erosion damage caused by solid particle impact: Part 2: Mechanical properties of materials directly associated with erosion damage,” *Wear*, vol. 259, no. 1–6, pp. 102–109, 2005.
[267] E. Bousser, L. Martinu, and J. E. Klemberg-Sapieha, “Solid particle erosion mechanisms of hard protective coatings,” *Surface and Coatings Technology*, vol. 235, pp. 383–393, Nov. 2013.
[268] J. Zhang, Z. Han, R. Ma, W. Yin, Y. Lü, and L. Ren, “Scorpion back inspiring sand-resistant surfaces,” *J. Cent. South Univ.*, vol. 20, pp. 877–888, May 2013.
[269] M. Tadayon, S. Amini, A. Masic, and A. Miserez, “The mantis shrimp saddle: a biological spring combining stiffness and flexibility,” *Advanced Functional Materials*, vol. 25, no. 41, pp. 6437–6447, 2015.
[270] I.-M. Low, “Depth-Profiling of Crystal Structure, Texture, and Microhardness in a Functionally Graded Tooth Enamel,” *Journal of the American Ceramic Society*, vol. 87, no. 11, pp. 2125–2131, 2004.
[271] M. Karim, S. Naamane, C. Delord, and A. Bennouna, “Study of the Surface Damage of Glass Reflectors Used in Concentrated Solar Power Plants,” *Energy Procedia*, vol. 69, pp. 106–115, May 2015.
[272] J. Cairney, P. Munroe, and M. Hoffman, “The application of focused ion beam technology to the characterization of coatings,” *Surface and Coatings Technology*, vol. 198, no. 1–3, pp. 165–168, 2005.
[273] D. S. Gianola and C. Eberl, “Micro- and nanoscale tensile testing of materials,” *JOM*, vol. 61, no. 3, pp. 24–35, Mar. 2009.
[274] G. Ravichandran and G. Subhash, “A micromechanical model for high strain rate behavior of ceramics,” *International Journal of Solids and structures*, vol. 32, no. 17–18, pp. 2627–2646, 1995.
[275] H. Fei, A. Abraham, N. Chawla, and H. Jiang, “Evaluation of micro-pillar compression tests for accurate determination of elastic-plastic constitutive relations,” *Journal of Applied Mechanics*, vol. 79, no. 6, p. 061011, 2012.
[276] K. R. Gadelrab, F. A. Bonilla, and M. Chiesa, “Densification modeling of fused silica under nanoindentation,” *Journal of Non-Crystalline Solids*, vol. 358, pp. 392–398, Feb. 2012.

[277] M. Klaus, C. Genzel, and H. Holzschuh, “Residual stress depth profiling in complex hard coating systems by X-ray diffraction,” *Thin Solid Films*, vol. 517, no. 3, pp. 1172–1176, 2008.
[278] “Pre-standardisation of incremental FIB micro-milling for intrinsic stress evaluation at the sub-micron scale | Projects | FP7 | CORDIS | European Commission.” [Online]. Available: https://cordis.europa.eu/project/rcn/110690/factsheet/en. [Accessed: 04-Jul-2019].
[279] A. A. Volinsky, J. B. Vella, and W. W. Gerberich, “Fracture toughness, adhesion and mechanical properties of low-K dielectric thin films measured by nanoindentation,” *Thin solid films*, vol. 429, no. 1–2, pp. 201–210, 2003.
[280] J.-Y. Faou, G. Parry, S. Grachev, and E. Barthel, “How Does Adhesion Induce the Formation of Telephone Cord Buckles?,” *Physical Review Letters*, vol. 108, no. 11, Mar. 2012.
[281] J. Zheng and S. K. Sitaraman, “Fixtureless superlayer-driven delamination test for nanoscale thin-film interfaces,” *Thin Solid Films*, vol. 515, no. 11, pp. 4709–4716, 2007.
[282] R. Hohlfelder, H. Luo, J. Vlassak, C. D. Chidsey, and W. Nix, “Measuring interfacial fracture toughness with the blister test,” *MRS Online Proceedings Library Archive*, vol. 436, 1996.
[283] F. Roters, P. Eisenlohr, L. Hantcherli, D. D. Tjahjanto, T. R. Bieler, and D. Raabe, “Overview of constitutive laws, kinematics, homogenization and multiscale methods in crystal plasticity finite-element modeling: Theory, experiments, applications,” *Acta Materialia*, vol. 58, pp. 1152–1211, Mar. 2010.
[284] M. Zecevic, I. J. Beyerlein, and M. Knezevic, “Coupling elasto-plastic self-consistent crystal plasticity and implicit finite elements: applications to compression, cyclic tension-compression, and bending to large strains,” *International Journal of Plasticity*, vol. 93, pp. 187–211, 2017.
[285] T. Shimada, K. Ouchi, Y. Chihara, and T. Kitamura, “Breakdown of Continuum Fracture Mechanics at the Nanoscale,” *Sci Rep*, vol. 5, no. 1, p. 8596, Aug. 2015.
[286] R. Ramprasad, R. Batra, G. Pilania, A. Mannodi-Kanakkithodi, and C. Kim, “Machine learning in materials informatics: recent applications and prospects,” *npj Comput Mater*, vol. 3, no. 1, p. 54, Dec. 2017.
[287] U. Ali, W. Muhammad, A. Brahme, O. Skiba, and K. Inal, “Application of Artificial Neural Networks in Micromechanics for Polycrystalline Metals,” *International Journal of Plasticity*, May 2019.
[288] Nosonovsky Michael and Bhushan Bharat, “Green tribology: principles, research areas and challenges,” *Philosophical Transactions of the Royal Society A: Mathematical, Physical and Engineering Sciences*, vol. 368, no. 1929, pp. 4677–4694, Oct. 2010.
[289] American Society of Mechanical Engineers, Ed., *ASME V&V 10-2006: Guide for verification and validation in computational solid mechanics: an American national standard*. New York: ASME Press, 2006.
[290] K.-J. Bathe, *Finite element procedures*. 1996.
[291] G. Huajian, C. Cheng-Hsin, and L. Jin, “Elastic contact versus indentation modeling of multi-layered materials,” *International journal of Solids and Structures*, vol. 29, no. 20, pp. 2471–2492, 1992.
[292] Q. Ding, L. Wang, and L. Hu, “16 - Tribology optimization by laser surface texturing: from bulk materials to surface coatings,” in *Laser Surface Engineering*, J. Lawrence and D. G. Waugh, Eds. Woodhead Publishing, 2015, pp. 405–422.

[293] D. Bhaduri *et al.*, “On Design and Tribological Behaviour of Laser Textured Surfaces,” *Procedia CIRP*, vol. 60, pp. 20–25, 2017.
[294] Z. Han, W. Yin, J. Zhang, J. Jiang, S. Niu, and L. Ren, “Erosion-Resistant Surfaces Inspired by Tamarisk,” *Journal of Bionic Engineering*, vol. 10, no. 4, pp. 479–487, Oct. 2013.
[295] I. N. Sneddon, “The relation between load and penetration in the axisymmetric Boussinesq problem for a punch of arbitrary profile,” *International journal of engineering science*, vol. 3, no. 1, pp. 47–57, 1965.
[296] G. Abaqus, “Abaqus 6.11,” *Dassault Systemes Simulia Corp Providence, RI, USA*, 2011.
[297] T. Stolarski, Y. Nakasone, and S. Yoshimoto, *Engineering analysis with ANSYS software*. Butterworth-Heinemann, 2018.
[298] Mediaworks, “PRIMER | Oasys LS-DYNA,” *LS-DYNA*. [Online]. Available: https://www.oasys-software.com/dyna/software/primer/. [Accessed: 03-Jul-2019].
[299] “Download/Order LSTC Product Manuals | Livermore Software Technology Corp.” [Online]. Available: https://www.lstc.com/download/manuals. [Accessed: 03-Jul-2019].

.

APPENDIX A CONTACT MODELING GUIDELINE

The American Society of Mechanical Engineers (ASME) Standards committee on Verification and Validation in Computational Solid Mechanics (PTC 60/V&V 10) published their first document in 2006 [289]. The motivation for the document entitled, “Guide for Verification and Validation in Computational Solid Mechanics”, was to lay the foundation for a reference document for finite element analysts. The initial approach was to produce a document in the same vein as the American Institute of Aeronautics and Astronautics (AIAA) Guide for the Verification and Validation of Computational Fluid Dynamics Committee on Standards.

The guidelines are based on the following fundamentals (as stated in document [289]):

- Verification must precede validation.
- The need for validation experiments and the associated accuracy requirements for computational model predictions are based on the intended use of the model and should be established as part of V&V activities.
- Validation of a complex system should be pursued in a hierarchical fashion from the component level to the system level.
- Validation is specific to a computational model for a particular intended use.
- Validation must assess the predictive capability of the model in the physical realm of interest, and it must address uncertainties that arise from both simulation results and experimental data.

However, in its current state, the guide [289] is not intended as a step-by-step procedure and after reading through this document, it became clear that there is an essential need for surface scientists and engineers for a standard on the best practices for tribomechanical numerical modeling. As such, this is intended as a first step toward a comprehensive and systematic methodology and workflow to develop finite element-based contact models to study the tribomechanical behavior of coated alloys.

A.1 Preface

Even though this guide is intended for entry level-users, basics/moderate finite element (FE) knowledge is still required as this guide is not intended as an introduction to continuum mechanics or the finite element method. The methodology presented in this document tries to be as transparent as possible from any specific finite element analysis software and the principles should be applicable to any non-linear implicit finite element solver.

A.2 Introduction

Traditionally, the design of wear-resistant coating solutions is based on empirical knowledge and is mostly driven by a sequence of trials and tests to evaluate the performance of a particular solution in a specific wear condition. While Hertz contact mechanics can be used to estimate the stress field of the elastic solution, it is not adequate to assess the load carrying capacity of a coated/laminated surface.

To accurately evaluate and predict the behavior of a coated system under a specific tribological condition it is then essential to resort to a numerical technique. The finite element method (FEM) is the most commonly used mathematical framework to calculate the stress-strain field solution in the context of continuum mechanics. FEM utilization has quickly spread in the last decade due to the rapid increase in the computational power of desktop computers which are now suitably powerful even for complex problems and systematic parametric optimization.

While the usage of FEM is becoming more and more common practice amongst tribologists, there is still no standardization of the methodology. Consequently, this document is meant to present a brief introduction of the method and more importantly aims to elaborate a set of best practices for finite element contact modeling applied to the tribology of coated alloys.

A.3 Mathematical basis

The finite element method is a mathematical technique developed to solve boundary problems described by partial differential equations. It is so commonly applied to solve continuum mechanics problems that we simply use the name finite element when talking about such utilization. The governing equation of the problem depends on the force equilibrium condition and linearity of the problem. Under static and linear conditions, in which the force equilibrium is enforced, the governing equation is given by,

$$[K]\{u\} = \{F\}. \tag{A.1}$$

Where $[K]$ is the stiffness matrix, $\{u\}$ the nodal vector and $\{F\}$ is the force vector. For linear problem, solving for the displacement requires to invert the stiffness matrix in a single time step. For quasi-static problem with non-linearity, such as any problem with changing contact boundaries or non-linear constitutive laws for materials, the problem must be solved iteratively, and the stiffness matrix has to be updated at each step which increases the computational cost. For a complete presentation of the method, which is out of the scope of this document, the reader may refer to the literature [290].

A.4 Solvers

For static and purely elastics problems, the integration time-step can be arbitrarily large, and the solution will always be stable. However, for non-linear problems, the time-step may have to be reduced due to convergence difficulties if the incremental displacement is too large. The time-step can be adjusted to accommodate for steps where convergence is more difficult. In practice, it is observed that using a very small time-step at the beginning of the simulation is often required to correctly initiate contact between different parts and then the time-step can subsequently be increased to shorten computation time.

Two main types of implicit (static) solvers exist, direct or iterative. Both have their advantages depending on the specific problem. The main factors affecting the solver choice reside in the amount of non-linearity, level of mesh distortion, the number of degrees of freedom (DOF) and computational resources such as, memory, disk space and cores available. The ground rules for the type of solver to use are presented in table 1.

Table A.1. Comparison of computational requirement for direct and iterative implicit solvers.

Solver	**Typical Applications**	**Ideal Model Size**	**Memory Use (approximative)**	**Disk Input/Output uses (approximative)**
Direct	When robustness and solution speed are required (nonlinear analysis); for linear analysis where iterative solvers are slow to converge	10^4 to 10^6 DOFs	1 GB per 10^6 DOFs (out of core) 10 GB per 10^6 DOFs (in core, optimal)	10GB per 10^6 DOFs
Iterative	Reduces disk I/O requirements relative to direct solver. Best for large models with solid elements and fine meshes	10^4 to 10^6 DOFs	0.3 to 1 GB per 10^6 DOFs	0.5GB per 10^6 DOFs

Most solvers also come with a preprocessor to facilitate the assembly of the model, which in the end produces a readable text file with all the necessary instructions to be executed by the solvers (This is the case for Abacus, Ansys and LS-Dyna). The same preprocessor also commonly doubles as a post-processor for visualizing the model results (figure A.1)

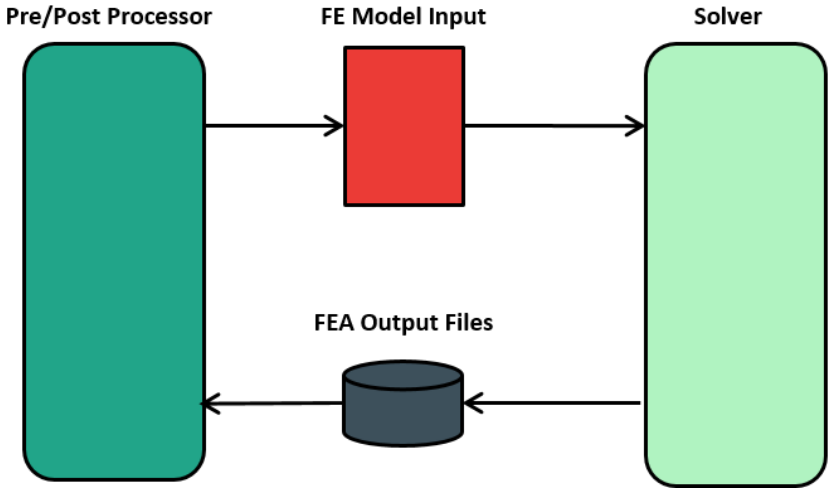

Figure A.1 The typical workflow used in finite element analysis.

A.5 Model dimensionality, symmetry reduction and consistent units

Finite element models can range from 1D (beams and trusses), 2D (shells) to 3D (bricks) formulations. Symmetry reduction should always be exploited to cut the computational cost. For example, a model that applies a normal load to a surface can be reduced under the condition that the counterpart has any axial symmetry. For a spherical contact, the rotation symmetry of the counterpart allows the model to be reduced to a 2D axisymmetric problem which considerably reduces the computational time to execute the model. If any translation is applied to the counterpart, a full 3D model must be used (under certain conditions, a 2D plane-strain model may be appropriate). The number of degrees of freedom can be evaluated by the number of nodes multiplied by their respective degrees of translational and rotation freedom. For instance, a 4 nodes quadrilateral element in a 2D axisymmetric model (x-y translational freedom) has 12 DOFs.

Unit consistency is also something to be aware of since there are no predefined length scales for FEM. The fundamental units are mass, length, time and all other units, such as force, stress and velocity are derived from those basic units. The rules for unit consistency are as follows.

- 1 force unit = 1 mass unit * 1 acceleration unit
- 1 acceleration unit = 1 length unit / (1 time unit)^2
- 1 density unit = 1 mass unit / (1 length unit)^3

In the next table (table 2), examples of consistent units are presented. The value of density and Young's modulus are those of steel *(7830 kg/m^3 and 207 GPa).*

Table A.2. Unit conversion table

MASS	LENGTH	TIME	FORCE	STRESS	ENERGY	DENSITY	YOUNG'S MODULUS	56.33KMPH 35MPH	Gravitational Acceleration
kg	m	s	N	Pa	J	7.83E+03	2.07E+11	15.65	9.806
kg	cm	s	1.0e-02 N			7.83E-03	2.07E+09	1.56E+03	9.81E+02
kg	cm	ms	1.0e+04 N			7.83E-03	2.07E+03	1.56	9.81E-04
kg	cm	us	1.0e+10 N			7.83E-03	2.07E-03	1.56E-03	9.81E-10
kg	mm	ms	kN	GPa	kN-mm	7.83E-06	2.07E+02	15.65	9.81E-03
g	cm	s	dyne	dyne/cm²	erg	7.83E+00	2.07E+12	1.56E+03	9.81E+02
g	cm	us	1.0e+07 N	Mbar	1.0e+07 Ncm	7.83E+00	2.07E+00	1.56E-03	9.81E-10

g	mm	s	1.0e-06 N	Pa		7.83E-03	2.07E+11	1.56E+04	9.81E+03
g	mm	ms	N	MPa	N-mm	7.83E-03	2.07E+05	15.65	9.81E-03
ton	mm	s	N	MPa	N-mm	7.83E-09	2.07E+05	1.56E+04	9.81E+03
lbf-s²/in	in	s	lbf	psi	lbf-in	7.33E-04	3.00E+07	6.16E+02	386

A.6 Type of elements

The elements define the smallest spatial discretization for which the displacements are solved for. Many geometries and integration rules are available (figure A.2). Finite element solvers use a numerical technique called Gaussian quadrature to integrate quantities over each element. Each element has several internal points, known as integration points (Gauss points), where the reactions to the applied conditions are calculated. Fully integrated elements consist of sufficient integration points to exactly solve each of the terms, if the element is undistorted. Reduced integration (or first order elements) uses less integration points, reducing the accuracy, but also reducing computational requirements at the same time. Under bending loads, reduced integration elements can allow deformations to occur that cause no strain at the integration point. As a result, no stresses or strains can be seen to occur at the integration point at the element center. This is known as a zero-energy mode, and in this case, results in a phenomenon called "hourglassing". Hourglassing can be severe in first order quadrilateral elements if element refinement is too coarse and/or displacements are too large between steps. This problem can be lessened by introducing an additional artificial stiffness to the elements. However, it is suggested that caution be used particularly for nonlinear problems as the default hourglass controls are not always effective.

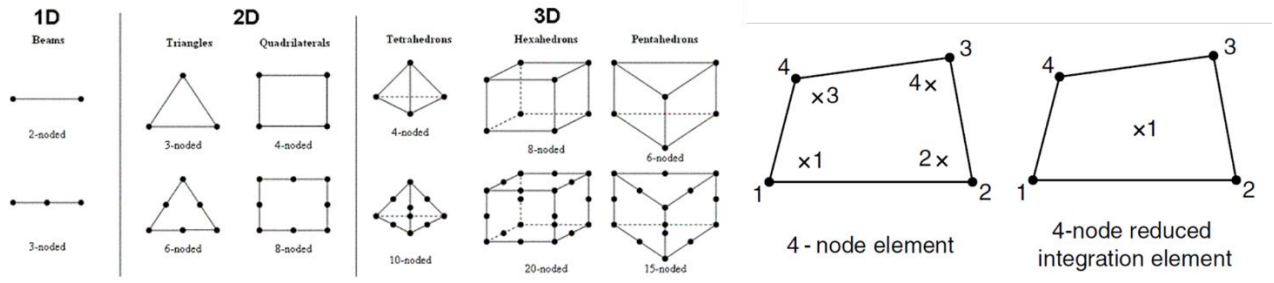

Figure A.2. Most commonly used finite element shape in continuum mechanics.

Reduced elements are not without issues however. In ideal bending, the intersections of the dashed lines remain perpendicular to one another. These angles change in fully integrated elements, resulting in shear strains and stresses observed and evaluated at the integration points. This behavior is known as shear locking and its severity can be reduced by refining the mesh as smaller elements can more closely approximate ideal behavior. Another locking phenomenon associated with fully integrated elements is volumetric locking. This occurs in quasi-incompressible materials, or materials tending towards incompressibility, such as perfectly plastic materials. The values of strain at each integration point cannot combine effectively to conserve the volume of the element, causing the element to lock. This is commonly countered by utilizing reduced integration and it's what is most commonly done. However, this is not always the best approach and strongly depends on the specific situation. Documentation from the software developers about the numerical accuracy versus the computational cost for different element types (2D shells and 3D solids) can be found in their respective manuals.

A.7 Meshing considerations

Throughout the rest of the document, including this section, we will consider that 2D 4-nodes shells elements are exclusively utilized in the models, This is the default type of element recommended to use for 2D contact modeling has they were shown to be the most robust for these types of problem.

A.7.1 Contacting mesh

It is generally favorable to have similar density mesh between different contacting parts surfaces as this leads to more stable contact behavior and local contact pressure accuracy. However, this is not always possible, and some workaround is possible. More information about contact modeling will be presented in section 6.9.

A.7.2 Mesh sensitivity

The first rule of thumb is that, for reduced integrated elements, a minimum of 4 elements must be used through the thickness of bending components to be able to adequately represent the bending and the stress gradients inside coatings. The higher the stress gradients, the more elements must be used if the peak value of stress is of interest. This is critical when modeling very thin coatings against a contact with a large radius. In this case, meshing challenges can arise as the model must

be spatially large enough to suppress boundary condition effects while an adequate meshing refinement is essential to capture stress gradients inside the thin coatings.

One of the most important aspects when modeling contact is the evaluation of mesh sensitivity on the calculated results. Getting incorrect results from using too fine of a mesh seems counterintuitive. However, it is a result of the basic idealized mathematical equations used by FEM, and how they are solved. For example, if there is a sharp interior corner (known as a re-entrant corner) on the surface, the theoretical stress at that point is infinite. The feature would either contain a radius or quickly deform to reduce this stress. However, when analyzed with a linear-elastic simulation, the stresses will continue to increase as the mesh is refined which is known as a stress singularity. This error can be resolved by applying a radius to the original part. However, far from this stress singularity, accordingly to Saint-Vernant's principle, the stresses are unaffected by that local disturbance. If we are not interested in resolving the stress gradients around this singularity then the mesh refinement sensitivity must be based on another component, most commonly the global strain energy (Figure A.3). The most appropriate way to study mesh sensitivity in this case is to reduce the elements characteristic length until the global strain energy of the deformed system asymptomatically converges to a stable value. For contact modeling without surface features, the maximum Von Mises located under the contact point is a valid method to study mesh sensitivity since it behaves as a stress concentration point and not a singularity. Concise and informative documentation about mesh sensitivity dependence on stress singularities and stress concentration can be found in the literature.

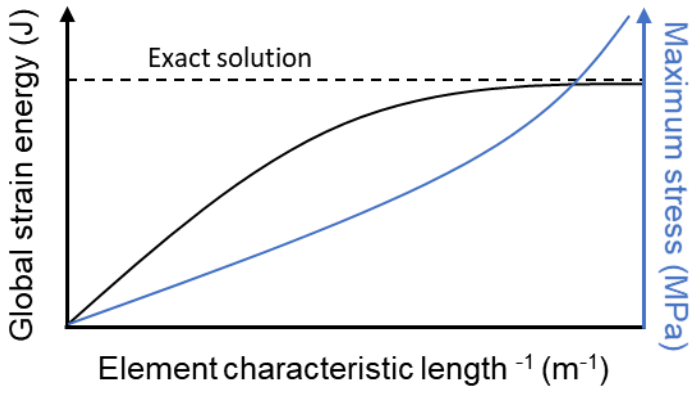

Figure. A.3 Influence of element length on the global strain energy and maximum.

A.8 Material properties

Stress-strain curves for alloys are directly assessable by tensile tests that can be performed in different conditions to characterise the strain-rate and temperature dependence. However, this procedure can rarely be applied to coatings and no standard currently exists to characterise their constitutive behavior. Indentation is the most common method to extract the reduced Young's (E_r) modulus of the surface. Combined with the Poisson's ratio (ν) this value defines the Young's modulus (E) and the complete elastic properties of the coating. The Poisson's ratio can be estimated from material similarities and available literature, but commonly 0.25 is used when no information is available as the influence of Poisson's ratio ranging between 0.15 and 0.35 is negligible. Brittle coatings, showing none or limited signs of plastic deformation, can be modeled by perfectly elastic behavior. When modeling a tribological contact with a diamond or alumina counterparts, these can also be assumed as been perfectly elastic.

For more ductile coatings, such as hardfacing materials deposited by HVOF or laser cladding, the plastic behavior can be evaluated by micro or nanoindentation. From indentation hardness, the yield stress (σ_y) of the coating can be estimated from the Tabor relation which states that for perfectly plastic materials the yield stress is related to hardness through a constraint factor K. That constraint factor is characteristically around 3 for highly ductile (perfectly plastic) alloys but that value varies for different material types. A common starting point to use for those hardfacing interlayer is to utilize a constraint factor of 3 and assume an almost perfectly plastic behavior after yielding (tangent modulus around 1% of the Young's modulus, because perfect plasticity does not converge well with implicit solvers).

A.9 Contact model

The basic contact approach in FEM solvers consists of two steps, contact detection and contact force model. The main contact detection algorithm of interest are node-to-surface and surface-to-surface. After contact has been detected, the most common method to apply the counteracting force is the penalty-based method, which in practice is like adding stiff springs in between contacting surfaces. The stiffness of those springs is the most important parameter of penalty-based contact modeling. Ideally the contact stiffness would be infinite to eliminate interpenetration between contacting surfaces (see on Figure A.4) but contact stability and solution convergence is compromised as the stiffness becomes too high. It is common to have to increase the stiffness by

a factor 2-100. Coulomb friction conditions can also be applied using both static and dynamic coefficients of friction. The augmented Lagrange method is very similar to the penalty method but uses an iterative technique to reduce the sensitivity to the contact stiffness. All things being equal, the augmented Lagrange method should produce less penetration than the pure penalty method, but it might take more iterations to converge. Other contact considerations and details are available in the literature.

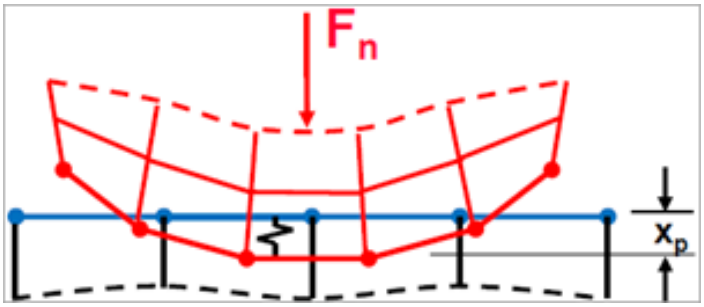

Figure A.4. Schematic of the interpenetration of penalty-based contact models.

A.10 Applying loads and displacements

To induce contact stresses, either load-controlled or displacement-controlled boundary conditions must be applied. For non-linear problems, displacement-controlled models are normally easier to converge, but load-controlled modeling better represents real life tribological conditions. The difficulty with load-controlled conditions is that strain increments between steps are difficult to predict, therefore an appropriate adaptive time-step strategy should be used to increase model convergence and numerical accuracy.

A.11 Case study

In this section, we will present an example of how to develop and validate an axisymmetric spherical contact model applying a normal load on a duplex-coated stainless steel. The example will be built according to the guideline presented in this document and validation of the model will be demonstrated. The model geometry is presented in Figure A.5. The constitutive behaviors of the different materials are presented in table 3. The alumina ball radius is 1mm, the hardfacing layer thickness is 500 μm and the wear resistant coating is 50 μm thick.

Table A.3. Material properties for the model case study.

Material	*Constitutive behavior*	*Young's modulus (E) (GPa)*	*Poisson's ratio (ν)*	*Yield stress (σ_y) (MPa)*	*Tangent modulus (E_t) (GPa)*	*K (MPa)*	*n*
Alumina	Elastic	300	0.21	-	-	-	-
Substrate SS316	Ramberg–Osgood	200	0.27	-	-	1150	0.286
Load carrying interlayer	Bilinear elastoplatic	200	0.25	4000	2	-	-
Wear resistant coating	Elastic	400	0.25	-	-	-	-

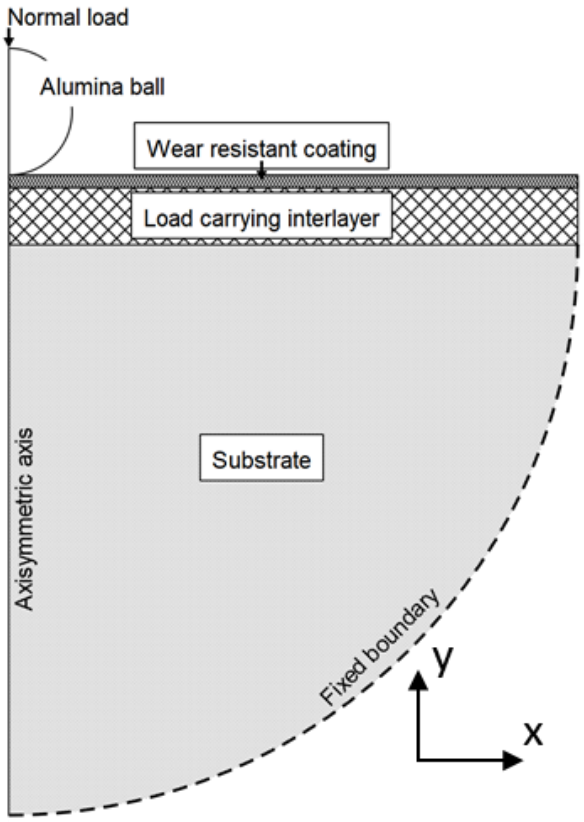

Figure A.5. Schematic of the 2D axisymmetric contact model for duplex coated surfaces.

A.11.1 Assembly

The model assembly was handled through LS-Prepost which is the official preprocessor/postprocessor for LS-DYNA solvers. The first step is to define the geometry and the meshing parameters (Figure A.6). Note that the spatial units are in microns.

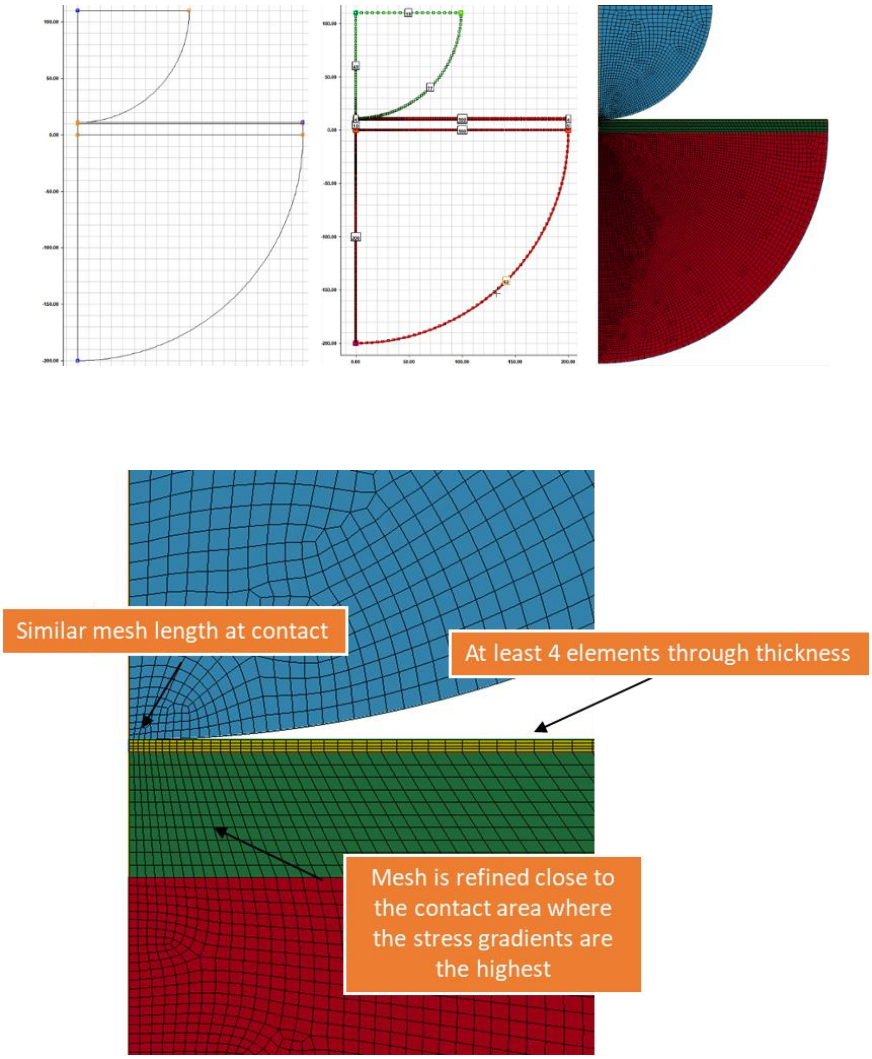

Figure A.6. Example of a 2D mesh obtained through the mesh generator tools of LS-Prepost.

Before continuing further, mesh quality must be verified, a rule of thumb is that the aspect ratio of quadrilateral elements must remain lower than 1:10 to reduce the error due to excessive mesh distortion. This shape factor condition must also remain true throughout the induced deformation

to generate valid results. This can only be verified after trial runs of the model, and meshing must be adapted if needed subsequently.

After the quadrilateral mesh has been generated, we need to apply the different material constitutive laws to different model parts (depicted by the different colors). The next step is to impose the boundary conditions. In the axisymmetric model, all displacement in the azimuthal direction should be constrained and the line passing through x=0 is the symmetry line and consequently no x displacements are allowed. The outer curve boundary of the model is completely restrained from any displacements which clamp the material in place. Finally, a load-controlled boundary is assigned on top of the alumina ball to apply the normal load. To avoid stress concentration on top of the alumina ball where the load is applied, it is recommended to add a rigid body to apply the normal load and let that top surface of the alumina ball be unconstrained (Figure A.7). This rigid body indenter translation is prescribed to y and other translations and rotations around the rigid body center of mass are constrained.

The meshing for each part has now to be assigned to a specific element formulation, which will be the reduced integrated quadrilateral axisymmetric element for this case study. The material properties of each part must be assigned from the parameters given in table 3. The contact model between the alumina ball and the top surface is described as a penalty-based surface-to-surface contact with frictionless conditions. The contact stiffness is initially assigned to the default value calculated by the software, which should be verified later for interpenetration case. The load is applied on the rigid body indenter in the negative y direction. In this problem, the load will linearly increase from 0 to 30N then reduce to 0N, which will allow us to generate a load-displacement curve. The initial time-step is adjusted to have a total of 60 time-steps, 40 steps for the loading and 20 steps for the unloading. The idea behind the reduced number of time-steps for the unloading part comes from the fact that the additional element distortion in this portion of the test is negligible.

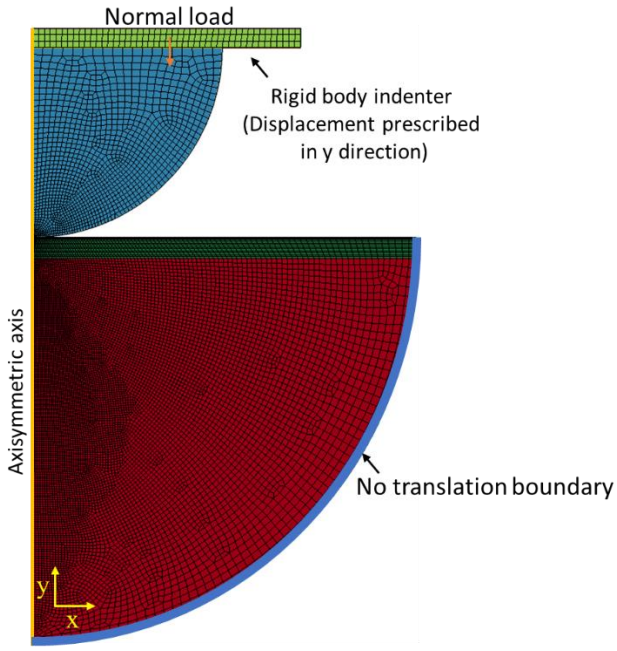

Figure A.7. Final 2D meshed model respecting the best practices guide.

6.11.2 Verification and validation

The first things to check after solving are spurious results, such as convergence problems, hourglassing, element locking, anomalous stress concentration/spike, boundary condition complying, extreme mesh distortion, element inversion and contact instabilities. If any of those problems are visible, then the model parameters should be verified and refined, and the solver time-step settings must be adjusted for improved convergence. Finally, it must be verified that the mesh quality throughout every step follows the quality criteria for the specific element formulation. Once those potential issues are fixed, boundary conditions interference must be verified. To be unaffected by boundary conditions, all the stress components should asymptotically converge to zero far from the contact area.

To estimate the required model size to be unaffected by boundary conditions, the Hertz contact model can be used to obtain the depth dependence of the stress field. Since classic Hertz theory cannot model layered materials, the idea is to estimate the worst-case scenario. To accomplish that, we calculate, using the Hertz theory, the elastic stress field of the counterpart applying the maximum modeled load on a semi-infinite medium having the same elastic properties as the substrate. Since plasticity dissipates more energy close to the surface, the stress field of a purely elastic model will overestimate the elastic field depth under the contact. The depth at which the

elastic stress components are asymptotically converging to zero can be used as a first estimate of the minimum finite element model size to not be affected by the fixed boundary. The software HertzWin (https://www.vinksda.nl/toolkit-mechanical-calculations/hertz-contact-stress-calculations/) was utilized for Hertzian contact calculation (following the restrictions presented on Figure A.9). For this case study, Figure A.8 presents normal stress depth dependence and demonstrate that the model spatial domain is large enough to not be affected by the boundary conditions as the stress asymptotically converge to 0.

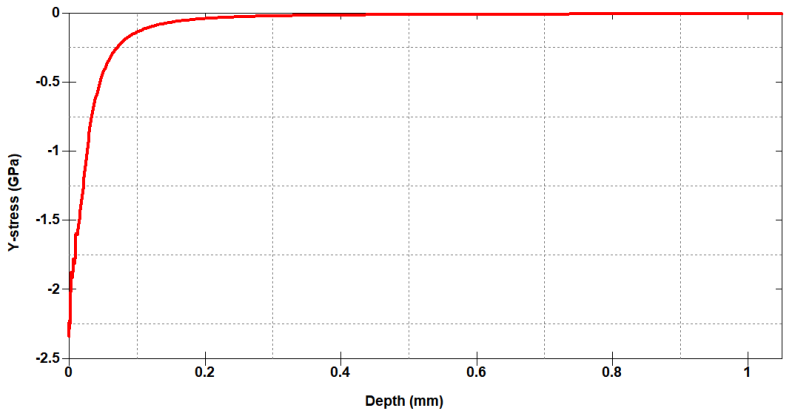

Figure A.8. Normal stress as a function of depth used to verify the effect of fixed boundary conditions.

Calculation Criteria

HertzWin calculation results are only valid when the following criteria have been met:

- both objects' contact areas are small relative to the their radii [1];
- contact areas are completely smooth (no surface roughness);
- materials deform linearly and elastically, and are homogeneous;
- no friction [2].

[1] Errors remain acceptable for ratios of contact surface radius to object radius of 1:3.

[2] In situations where traction forces are exerted, a friction coefficient of 0.3 is still permissible.

Figure A.9. Hertz contact model initial assumptions (from HertzWin documentation).

Contact interpenetration verification is the next step. In this step we observe how important the interpenetration is and we will increase the contact stiffness factor to diminish its importance while also avoiding spurious contact behavior. To do so, it is recommended to verify the load curve to see if the load is applied smoothly. As the stiffness is increased, the load curve smoothness can be affected. To counteract this the time-step must be reduced. As shown on Figure A.10, it can be observed that the default penalty stiffness is too low for sharp contacts such as indentation. The maximum interpenetration between contacting surfaces scales roughly with the stiffness factor.

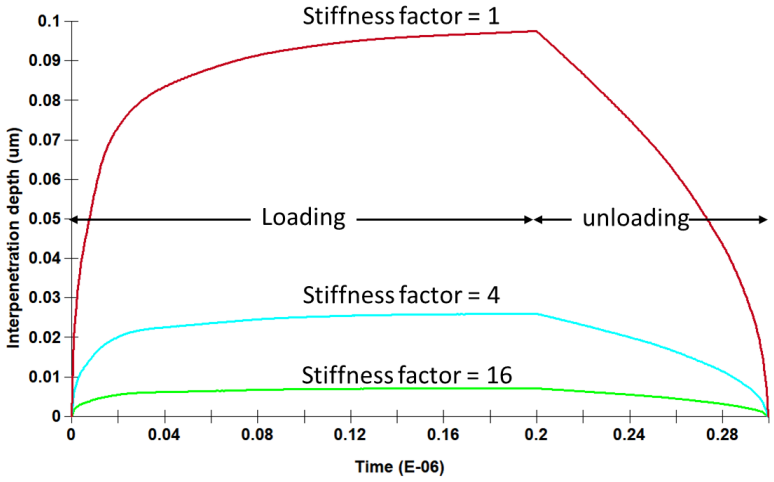

Figure A.10. Contact interpenetration for different contact stiffness factor.

Finally, a comparison of the model in the Hertz theory limits will be performed. For this validation, we can compare different stress field components such as the maximum Von Mises, the maximum surface tensile stress or the area of contact. The comparison of the elastic FEM and Hertz is presented in figure A.11.

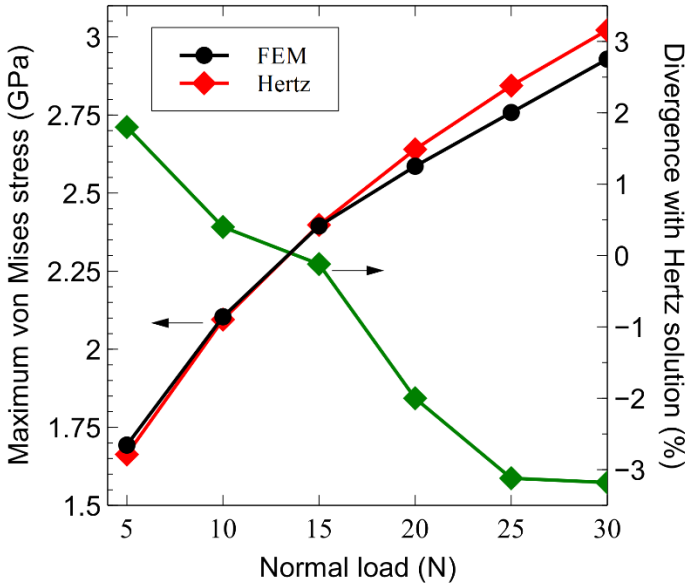

Figure A.11. Comparison between Hertz and finite element contact models. For example, the maximum von Mises stress in the indented surface is shown as the comparison criterion.

6.11.3 Complementary discussion about the mechanical characterisation of protective coatings

Once the elastic model has been validated, plastic properties of the substrate can be restored. The validation of the complete contact plastic model is made by comparing with the load-displacement curve of the equivalent experimental configuration. It is crucial to understand that the accuracy of the plastic model is greatly affected by the complexity and amount of details taken into consideration by the modeled constitutive laws. Elastoplastic constitutive laws are obtained through fitting of experimental data originating from uniaxial tensile tests.

This process is usually used to obtain the full stress-strain laws for base metallic materials. However, the same procedure cannot be directly applied to evaluate protective coating properties. The reduced Young's modulus of coatings is standardly evaluated by nano/micro-indentation with special care to avoid contaminating the results via base material effects (ISO 14577, ASTM E2546, ISO 6507, ASTM E384). To completely define the linear elastic properties of the coatings, its Poisson's ratio needs to be estimated. There is no standard method to measure these values for thin films, but it is often estimated from other similar materials or fixed as 0.25 since the influence of the Poisson's ratio between 0.15 and 0.35 was shown to have limited influence on the calculated stresses for contact modeling [291]. For brittle coatings it is often adequate to approximate their properties as perfectly elastic since we are normally interested in the crack formation processes and not the post failure behavior of the coated system.

The derivation of the plastic properties from indentations is much more complex and still a major subject of research in the field of protective coatings. Using freestanding films and a micro-mechanical uniaxial setup it is possible to apply the same method as used for bulk materials to obtain the stress-stain laws, nevertheless it is still technologically very challenging and not a readily available technique. The simplest evaluation of the plastic properties for coatings is obtained by a linear relation which links the uniaxial flow stress value (σ_y) and hardness (H) through a constraint factor (K) dependant on the indenter geometry. For ductile materials behaving as quasi perfectly plastic, it is well known that the constraint is around 3 (Tabor relation). The apparent increase in resistance to plastic deformation compared to uniaxial flow stress comes from the fact that the plastic zone under the indenter is confined within a large volume of material behaving elastically. For example, in the Johnson cavity model, there is a region under the indenter where the stress state

is purely hydrostatic compressive with the deviatoric part (shear stresses) being null which is the only component responsible for plastic flow. In reality, for materials with strain-hardening, the constraint factor was shown to be dependent not only on the indenter geometry but also on the material properties.

As of today, there is still no standard procedure to evaluate the constraint factor and even less to obtain the full stress-strain behavior of coatings. For intermediate thicknesses hardfacing layers such as the one deposited by HVOF or cladding, it is normally possible to produce classic tensile specimens to evaluate its plastic properties. For example, the yield stress of Stellite 6 was measured using digital image correlation technique used as a local strain measurement on a tensile hardfaced sample.

More information and examples of useful analysis that can be used to guide the design of duplex-coated alloys has been summarised in an article that was submitted to the Journal of Thermal Spray Technology under the following titled: “Predicting the Load-Carrying Capacity and Wear Resistance of Duplex-Coated Low-Strength Alloys for Severe-Service Ball Valves”.

Finally, as famously stated by the statistician George Box: "All models are wrong but some are useful". This quote is a great reminder that we should not accept any values produced by a numerical model before thorough verification and experimental validation are completed. It is the responsibility of the finite element analyst to ensure the validation of the model outputs through a rigorous workflow (Figure A.12) before the results can be exploited for design refinements.

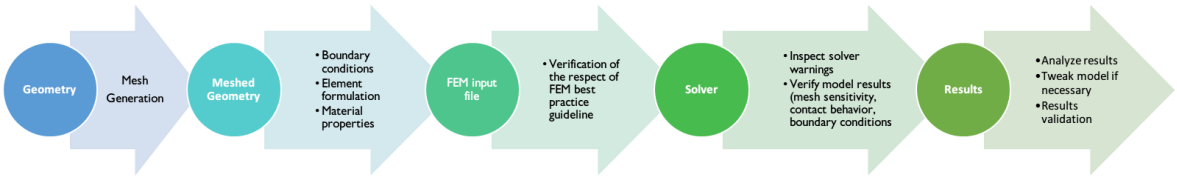

Figure A.12. Finite element verification and validation workflow.

APPENDIX B TRIBOMECHANICAL MODELING OF PATTERNED SURFACES

In this second appendix, we are briefly presenting the main results from different modeling investigations related to the stress analysis of patterned surfaces and patterned coatings.

B.1 Texturing for coefficient of friction reduction

Surface texturing, which consists in generating topographical patterns at the surface of a material, was shown to enhance sliding wear performances by reducing the coefficient of friction [292]. Nowadays, the common approach used to introduce those patterns is by laser ablation techniques producing high energy impulses generated by nanosecond and femtosecond lasers [293]. This approach allows one to introduce a specific array of micro-dimples and grooves at the surface. The beneficial effects of surface texturing are as followed:

- Reduction of the contact area and adhesive part of friction.
- Facilitation of the evacuation of debris or trapped third bodies.
- The grooves act as lubricant reservoir.
- Lower the in-plane residual stresses through structure relaxation.

The main parameter controlling the coefficient of friction was shown to be the surface roughness introduced by the pattern [293]. As the roughness increases, initially, there is a reduction of the contact area and thus a reduction of the friction forces. On the other hand, a surface with high roughness will display higher friction forces caused by an intensification of the ploughing forces contribution caused by the structure deformation and lateral forces exerted on the sliding counterpart. Figure B.1 presents that by varying the surface roughness, we are actually adjusting the trade-off between adhesion forces and ploughing forces. For a specific combination of surface

roughness and tribomechanical conditions there is an optimal motif for which the friction forces will be minimized.

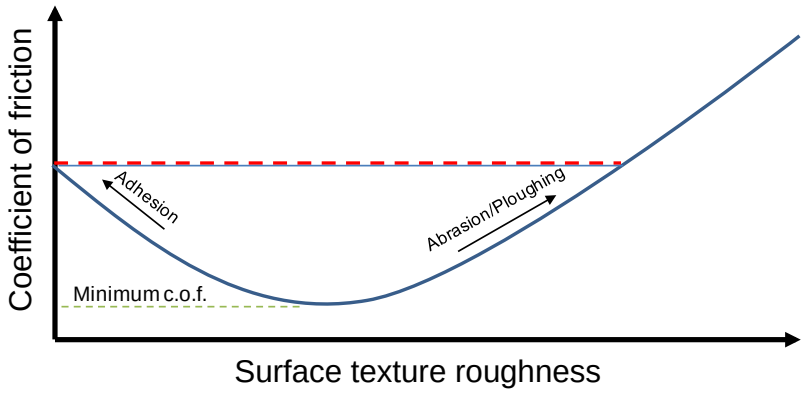

Figure B.1.Influence of surface texture roughness on the coefficient of friction.

We have developed a 2D plane-strain finite element model to study the influence of an array of groove lines introduced by a typical surface texturing laser on a stainless steel coated by a tungsten carbide. The flat counterpart surface was also made of stainless-steel. We followed the Von Mises contact force along the surface, by increasing the load until the contact force at the edge of the grooves reached 483 MPa (70 ksi, by the industrial partner requirement). This value of required minimum contact pressure was established by the sealing valve application aimed at by our industrial partner. Figure B.2 presents the modeled domain and dimensions and the two area (A, B) on which we performed the stress analysis under quasi-static loading.

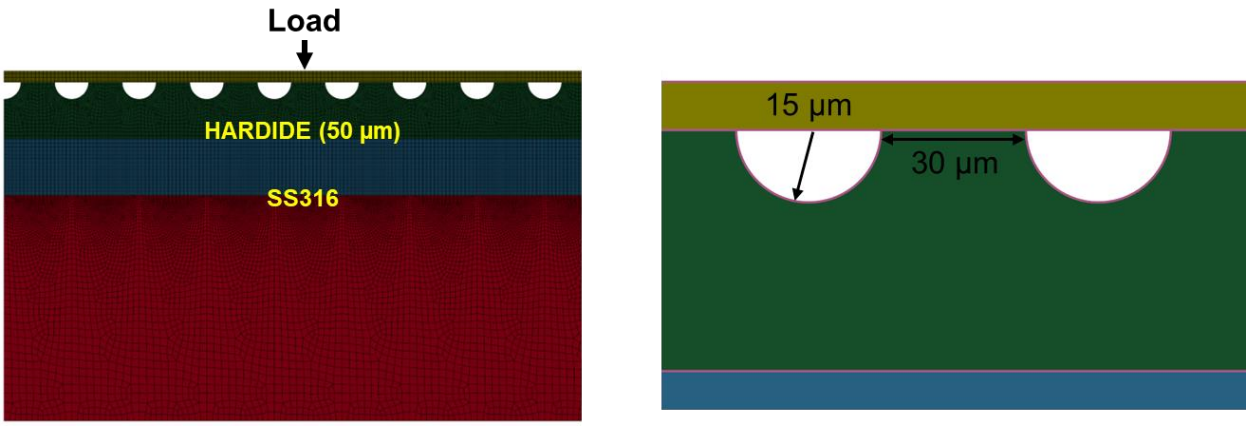

Figure B.2 2D Plane strain modeled domain and grooves dimensions and spacing.

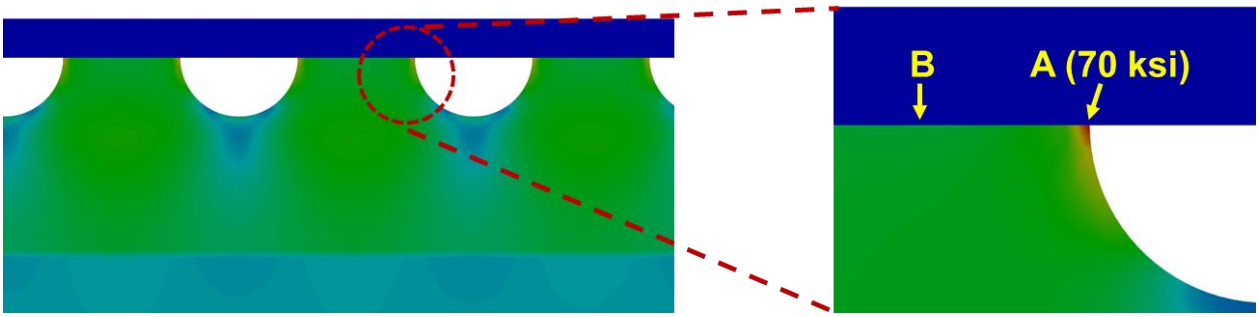

Figure B.3 Von Mises stress field under load inducing 70 ksi at the contacting edge between the flat counterpart and surface.

The evolution of contact Von Mises stresses at location A and B as a function of the applied load are presented in figure B.3. Also presented in this figure is the tensile stress field induced in the coated surface.

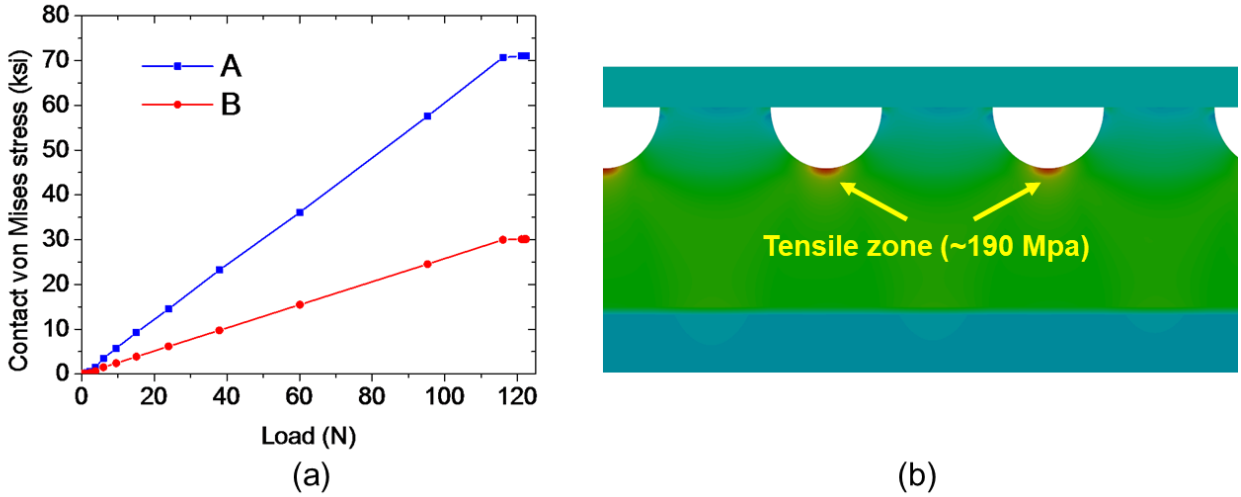

Figure B.4 (a) Contact Von Mises stresses and (b) the maximum principal stress field at maximum load.

The first thing we can note is that both stresses (at location A and B) increase linearly as a function of the applied load by the flat counterpart. The slope of the contact stress at B is slightly less than the half of the one for A. This high border effect stress brings the required sealing capabilities while the lower average surface stress should lead to lower wear rate when the valve is operated. There is also a creation of a tensile stress at the bottom of the grooves caused by the opening of the structure under load. The maximum tensile stress reached a value of 190 MPa which is significantly lower than the tensile elastic limit of the coating which indicates that those tensile zones are at no

risk of generating damage in the surface. This preliminary numerical investigation was useful to demonstrate the potential of patterned surface for valve applications and also displayed the predictive design capability of contact modeling.

B.2 Solid particle erosion of patterned surfaces

As introduced in the previous section, surface texturing was widely reported to reduce friction by lowering the adhesive forces. Besides, cavities in the structure are beneficial to evacuate debris or trapped third bodies which would otherwise contribute to an additional term in the coefficient of friction and wear rate. The cavities also enhance lubricants performance by acting as reservoir and thus keeping more lubricant available. Consequently, we asked ourselves: What is the influence of surface patterning on the solid particle erosion resistance? For one, it was shown that the natural patterning on desert scorpion back and on the body of the tamarisk plant are the origin of their high resistance to sand erosion [268], [294]. Using computational fluid dynamics, those studies showed that the beneficial effects originate from the interaction between the erodent carrier gas and the surface texturing. The turbulent flows induced by the rough surface are responsible for slowing down impinging particles and therefore lowering the energy transferred to the surface and the wear rate.

In this work, we investigated the modeling of textured surface to predict the dynamic mechanical response of the structure under micro particle impacts. Silicon (100) substrates were micro-patterned using an automated diamond dicing saw producing a rectangular microcolumns motif. We will present the results for two patterns, Sample A consisted of (25x25x100) μm^3 microcolumns interspaced by 50 µm and Sample B is made of (50x50x100) μm^3 microcolumns interspaced by 50 µm. When subjected to low velocity solid particle erosion (35 m/s) with alumina particles (radius ~ 50 µm) we observed a very distinct behavior between the two samples. Post mortem observation indicated that Sample A surface texturing was totally removed in the erosion scar, while Sample B still had columns and trace of patterning observable. To gain some insights about the mechanisms in action, we developed a 3D dynamic finite element model using an explicit integration scheme. We modeled the Silicon substrate as a perfectly plastic material ($E_{Si(100)} = 130$ *GPa,* $\upsilon_{Si(100)} = 0.17$, $\sigma_y = 6$ *GPa*) and the alumina particle as an elastic materials ($E_{Si(100)} = 130$ *GPa,* $\upsilon_{Si(100)} = 0.21$). We first studied the energy dissipation mechanisms during normal impact

directly over the geometrical center of the column. Presented in figure B.5 is the plastic strain field at maximum deformation during the impact. First, we can see that the maximum plastic deformation (5.1%) is higher for the wider 50x50 μm^2 columns. In these conditions, the columns acted very similarly to a flat surface and the plastic field was confined close to the surface. On the other hand, the 25x25 μm^2 columns display a lower maximum plastic strain (3.15 %), however, the plastic energy is dissipated more homogeneously and over a considerable larger area of the column about its length. This mechanism could be exploited to enhance the protection of ductile materials allowing them to reduce damages by dissipating energy by plastic deformation over a larger volume than in the bulk form.

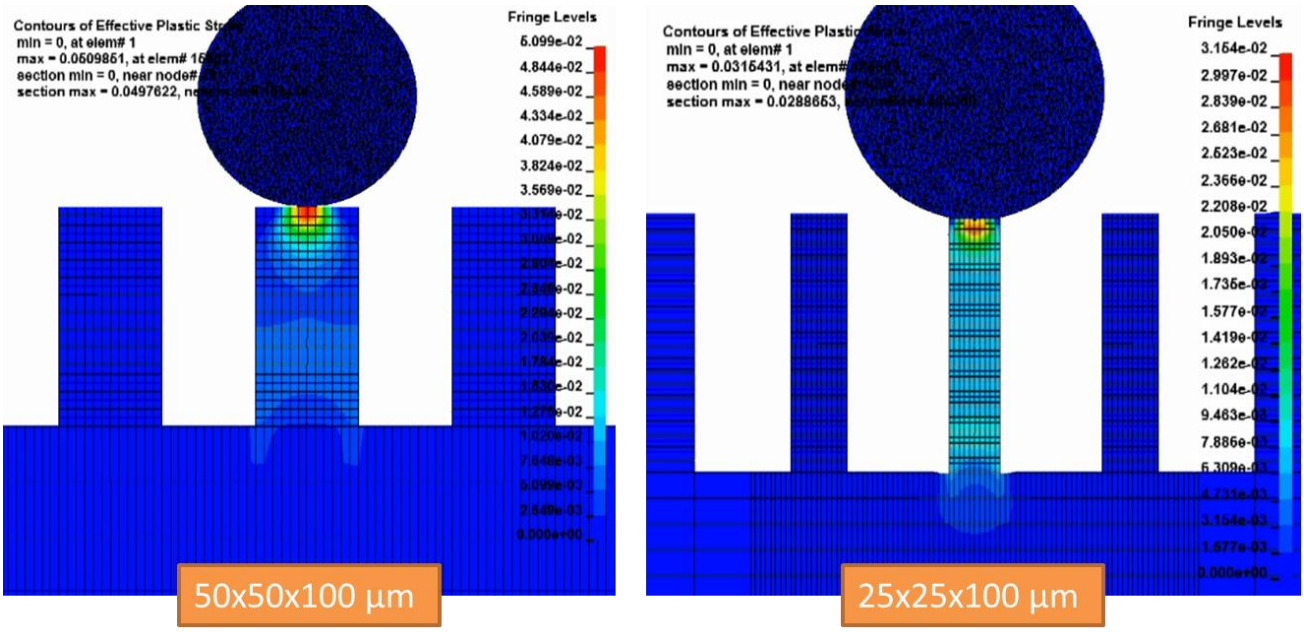

Figure B.5 Plastic strain field at maximum deformation during normal impact in the center of the column.

We also investigated the column response when the micro particles hit the sides of the column at normal incidence by aiming them directly in between the columns. With this angle of impact, the particle also applies a lateral force on the column structure, which induces in a moment of inertia and bending of the columns. We followed the tensile stresses generated in the columns for both sample motifs and identified that the column bending creates a zone of tensile stress at the base of the columns with the sub-material (see figure B.6). We observed a significant bending in the thinner 25x25 μm^2 columns while the effect was much less pronounced for the 50x50 μm^2 columns motif. The maximum tensile stress in Sample A were around five times higher than in the sample B,

reaching a maximum of 5 GPa (see figure B.6 (b)). This high level of stress at the base indicates that any defect located in this area could easily propagate and fracture the whole column from the base. We believe that this is what is responsible for completely removing the Sample A pattern, since the column can be fractured from the base material which would cause the complete vanishing of the pattern that we observed experimentally.

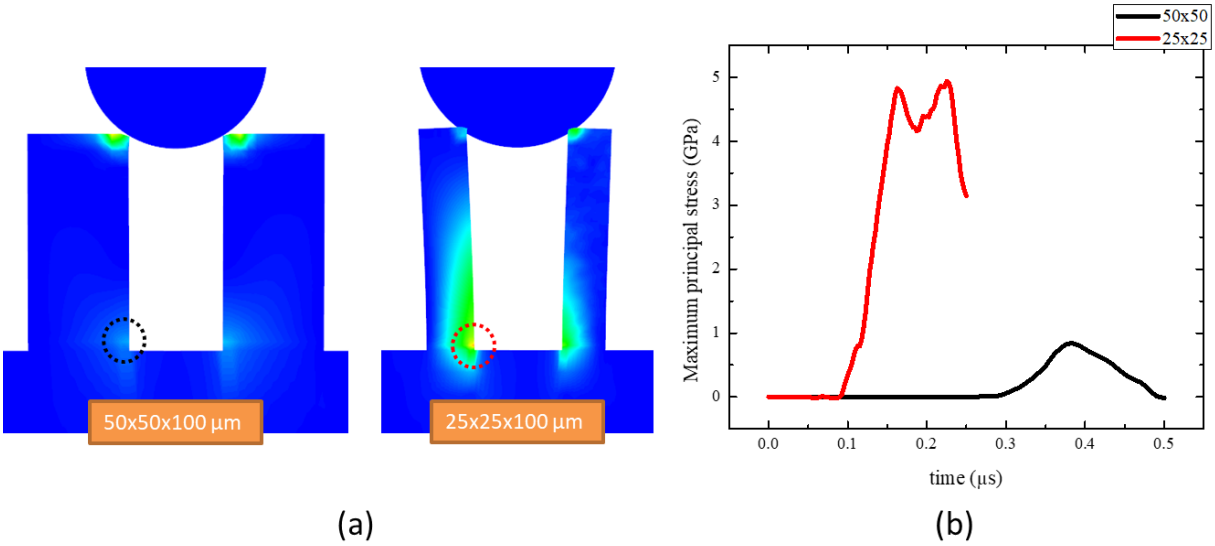

Figure B.6 (a) Maximum principal stress field at maximum deformation and (b) the maximum principal stress at the column base during the impact event.

This numerical investigation elucidated the distinct behaviors as a function of the aspect ratio of the microcolumn pattern. It demonstrated the model predictiveness capabilities and its potential as a design tools to identify the optimal surface motif for the intended tribomechanical conditions.

B.3 Mechanical properties characterization using micropillar indentation.

The main interest of micropillar indentation testing is that it provides a loading condition which comes close to an ideal uniaxial compression test and thus greatly reduced the dimensionality and complexity of the induced stress field compared to standard surface indentation. In these tests there is three contribution to the total compliance, $C_{indenter}$, C_{pillar} and $C_{substrate}$. The total compliance $C_{measured}$ is given by the following relation.

$$C_{measured} = C_{indenter} + C_{pillar} + C_{substrate} \quad \text{(B.1)}$$

The indenter compliance can be calibrated and corrected for using the calibration procedure established by the indenter manufacturer. The compliance of the pillar is simply given by the next relation.

$$C_{pillar} = \left(E_{pillar} \cdot \frac{A}{L}\right)^{-1} \quad \text{(B.2)}$$

where E_{pillar} is the Young's modulus of the pillar, A is the cross-section area of the pillar and L is the length of the pillar. Finally, the compliance of the substrate represents the deformation that the pillar induces in the supporting material. It can be evaluated using the Sneddon relation (B.3) which was developed to evaluate the amount of sinking by a cylindrical punch indent in an elastic half-space [295].

$$C_{substrate} = \frac{\sqrt{\pi}(1-\upsilon^2)}{2E_{substrate}\sqrt{A}} \quad \text{(B.3)}$$

This compliance system is schematically presented in figure B.7. It was previously demonstrated that if the aspect ratio of the pillar is at least 2:1 (length: width) then the stress field is sufficiently uniform and homogeneous in the pillar section to be used to characterize the uniaxial constitutive law of the material. Referring to the previous section, we observed this effect, the level of homogeneity of the stress field was higher for the pillar with the smaller cross section area. Considering the previous results, the micropillar indentation tests were conducted on the same 25x25x100 μm^3 Silicon sample presented in section B.2. We first validated the numerical model by generating load-displacement curves for different constitutive laws. In the model the indenter tip was perfectly rigid, and the pillar and substrate made of Silicon ($E_{Si(100)} = 130$ *GPa,* $\upsilon_{Si(100)} = 0.17$). We then treated those data sets as they were originating from an experimental setup and analyze them using the compliance approach. The results are presented in figure B.8.

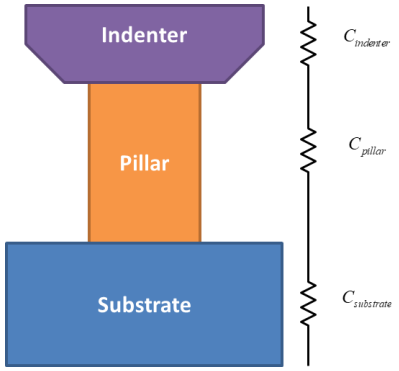

Figure B.7 Compliance system in a micro-pillar indentation test.

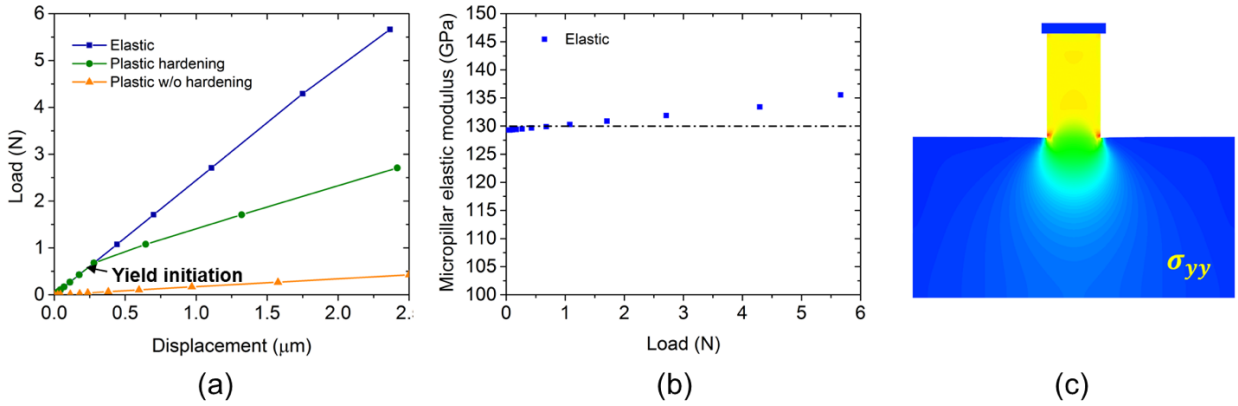

Figure B.8 (a) Load displacement curves for different constitutive laws and (b) the micropillar elastic modulus obtained using the compliance method.

Since the compliance analysis assume elastic materials without plasticity, we will focus on the blue curves in figure B.8. If the system response is linear elastic, a linear load-displacement curve is expected. This is the case for the elastic curve in (a) and only at higher load the curve marginally deviates from the linear relation. This can be explained by the initiation of non-linearity in the pillar sinking behavior due to high border effect between the pillar's base and the substrate which deviates from the Sneddon relation (see figure B.3 (c)). At lower loads (0N → 2N) the extracted elastic modulus agrees well with the value we input in the model. At higher loads (3N → 6N) the modulus is slightly over evaluated due to the overestimation of the sinking-in effect that we mentioned previously.

Finally, we considered the effect of a misalignment between the indenter tip and the column top surface. In the example shown in figure B.9 we present the results for a 2.5° misalignment between the indenter flat and column top surface. In (b) the first principal stress field under load is shown

and we can observe two areas with high level of tensile stress which could prematurely damage brittle micro pillars. The effect can also be detected on the load displacement curves during the tip accommodation with the column top surface at lower loads (see figure B.9 (c))

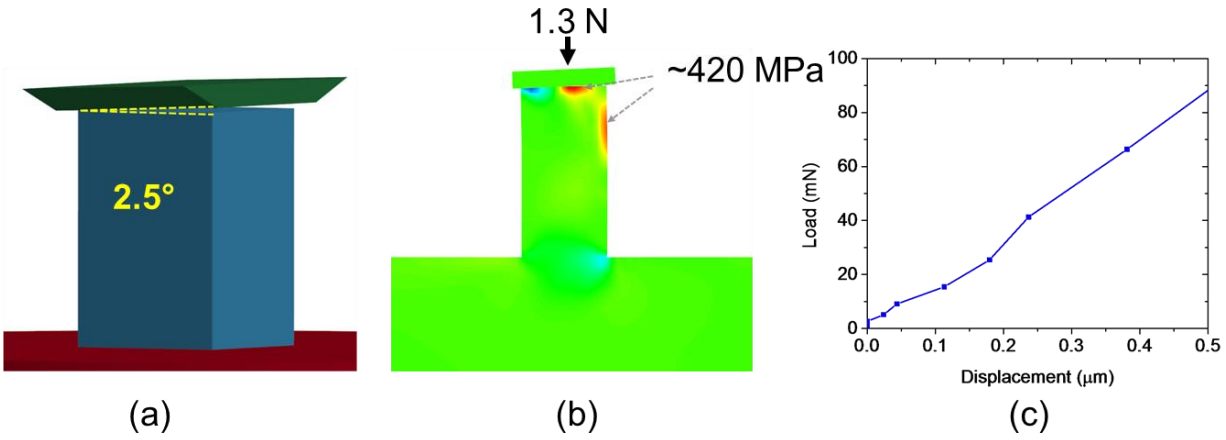

Figure B.9 (a) Schematic of a 2.5° misalignment between the indenter flat and column top surface. (b) First principal stress field under load. (c) Load displacement curves.

In summary, we developed a micro pillar compression tests model to acquire knowledge about the pillar deformation response. The model could be used to calibrate the column sinking correction and correct data due to misalignment issues. These steps are essential to precisely evaluate the compliance of the pillar which is even more crucial for characterizing thin film coatings when the substrate effects are even more apparent.

APPENDIX C FINITE ELEMENT MODELS INPUT FILES PARAMETERS

All modeling results presented in this thesis were executed through LS-Dyna [105]. LS-Dyna is a general-purpose finite element software developed by Livermore Software Technology Corporation capable of nonlinear static and dynamic analysis and fracture mechanics calculations [187]. It is similar in its approach to other well know finite element software such as Abaqus [296] and Ansys Mechanical [297]. Models are executed by the selected solver (linear, nonlinear, static, dynamic, thermomechanical) that parses an input ASCII text file named the input deck. In the input deck, commands are given to the solver using specific keywords each serving a different function. While the input deck can be manually edited and assembled, a preprocessor is generally used to simplify the task. LS-Prepost is the officially distributed preprocessor, but other third party's preprocessors such as Oasys Primer [298] are also officially supported. The official documentation available for LS-Dyna consists in a manual split in three volumes (Keywords, Material models, Multi-physics solvers), a theory manual detailing the continuum mechanics approach and an example manual containing simple introductory input decks for new users [299]. During the accomplishment of my thesis I have used both the manual and LS-Dyna preprocessor methods, and I also wrote scripts to automatize certain tasks and to add missing features to the preprocessor through macro scripts. Attached below is an input deck files containing all the parameters (contact, solver configurations, elements formulation, etc...) that were used to run the models presented in this thesis.

ParametersInputdeck.k

```
$# Created on Dec-02-2019 (15:48:00)
*KEYWORD MEMORY=1008464440 NCPU=2
*TITLE
$#title
Tribomechanical model
*CONTROL_ACCURACY
$#     osu       inn    pidosu      iacc
         1         4         0         1
*CONTROL_BULK_VISCOSITY
```

```
$     Q1_F      Q2_F      TYPE     BTYPE
$#      q1        q2      type     btype
       1.5      0.06        -2         0
*CONTROL_CONTACT
$#  slsfac    rwpnal    islchk    shlthk    penopt    thkchg     orien    enmass
       0.1       0.0         2         0         1         1         1         0
$#  usrstr    usrfrc     nsbcs    interm     xpene     ssthk      ecdt   tiedprj
         0         0         1         0       4.0         0         0         0
$#   sfric     dfric       edc       vfc        th     th_sf    pen_sf
       0.0       0.0       0.0       0.0       0.0       0.0       0.0
$#  ignore    frceng   skiprwg    outseg   spotstp   spotdel   spothin
         2         1         0         0         0         0       0.0
$#    isym    nserod    rwgaps    rwgdth     rwksf      icov    swradf    ithoff
         0         0         1       0.0       1.0         0       0.0         0
$#  shledg    pstiff    ithcnt    tdcnof     ftall    unused    shltrw
         1         0         0         0         0                 0.0
$=========================================================================
$ Implicit LS-DYNA control cards
$=========================================================================
*CONTROL_HOURGLASS
$     Q1_F      Q2_F      TYPE     BTYPE
$#     ihq        qh
         6       0.1

*CONTROL_IMPLICIT_AUTO
$#   iauto    iteopt    itewin     dtmin     dtmax     dtexp     kfail    kcycle
         0       100        20       0.0     700.0       0.0         1         0

*CONTROL_IMPLICIT_DYNAMICS
$#   imass     gamma      beta    tdybir    tdydth    tdybur     irate
         0       0.6      0.38       0.0       0.0       0.0         1

*CONTROL_IMPLICIT_GENERAL
$#  imflag       dt0    imform      nsbs       igs     cnstn      form    zero_v
      -992.5000E-11         2         1         1         0         0         0

*CONTROL_IMPLICIT_SOLUTION
$#  nsolvr    ilimit    maxref     dctol     ectol     rctol     lstol    abstol
        12        11        15     0.001      0.01       0.0       0.9       0.0
$#   dnorm    diverg     istif   nlprint    nlnorm   d3itctl     cpchk
         2         1         1         3         2         1         0
$#  arcctl    arcdir    arclen    arcmth    arcdmp    arcpsi    arcalf    arctim
         0         0       0.0         3         2         0         0        10
$#   lsmtd     lsdir      irad      srad      awgt      sred
         5         2       0.0       0.0       0.0       0.0
```

```
*CONTROL_IMPLICIT_SOLVER
$#  lsolvr    lprint     negev     order      drcm    drcprm   autospc   autotol
         5         2         2         0         4       0.0         1       0.0
$#  lcpack    mtxdmp
         2         0
*CONTROL_OUTPUT
$#   npopt    neecho    nrefup    iaccop     opifs    ipnint    ikedit    iflush
         1         3         0         0       0.0         0       100      5000
$#   iprtf    ierode   tet10s8    msgmax    ipcurv      gmdt   ip1dblt      eocs
         0         0         2        50         0       0.0         0         0
$#   tolev    newleg    frfreq     minfo    solsig    msgflg    cdetol
         2         0         1         0         0         0      10.0
*CONTROL_SHELL
$#  wrpang     esort     irnxx    istupd    theory       bwc     miter      proj
      20.0         1        -1         4         2         1         1         1
$# rotascl    intgrd    lamsht    cstyp6    tshell
       1.0         0         0         1         0
$# psstupd   sidt4tu     cntco    itsflg    irquad
         0         0         0         0         2
$#  nfail1    nfail4   psnfail    keepcs     delfr   drcpsid    drcprm
         0         0         0         0         0         0       1.0

*CONTROL_SOLID
$#   esort   fmatrix   niptets    swlocl    psfail   t10jtol    icohed    tet13k
         1         0         0         2         0       0.0         0         0
$#   pm1     pm2     pm3     pm4     pm5     pm6     pm7     pm8     pm9     pm10
       0       0       0       0       0       0       0       0       0       0

*CONTROL_SOLUTION
$#    soln       nlq     isnan     lcint
         0         0         0      1000

*CONTROL_TERMINATION
$#  endtim    endcyc     dtmin    endeng    endmas
2.00000E-9         01.00000E-6       0.01.000000E8

*CONTROL_TIMESTEP
$#  dtinit    tssfac      isdo    tslimt     dt2ms      lctm     erode     ms1st
       0.0       0.9         0       0.0       0.0         0         0         0
$#  dt2msf   dt2mslc     imscl    unused    unused     rmscl
       0.0         0         0                           0.0

*CONTACT_2D_AUTOMATIC_SINGLE_SURFACE_ID
$#     cid                                                              title
```

```
         1
$#    sids      sidm     sfact      freq        fs        fd        dc     membs
         0         0       2.0         1       0.4       0.4       0.0         6
$#  tbirth    tdeath       sos       som       nds       ndm       cof      init
       0.01.00000E20       1.0       1.0         0         0         0         0
$#      vc       vdc       ipf     slide    istiff   tiedgap
       0.0      10.0         0         0         0       0.0

*PART
$#                                                                         title
Coating
$#     pid     secid       mid     eosid      hgid      grav    adpopt      tmid
         1         1         8         0         0         0         0         0

*SECTION_SHELL_TITLE
Elform 13
$#   secid    elform      shrf       nip     propt   qr/irid     icomp     setyp
         1        13  0.833333         4       1.0         0         0         1
$#      t1        t2        t3        t4      nloc     marea      idof    edgset
       0.0       0.0       0.0       0.0       0.0       0.0       0.0         0

*INITIAL_STRESS_SHELL_SET
$#     sid    nplane    nthick     nhisv    ntensr     large
         1         1         1         0         0         0
$#       t     sigxx     sigyy     sigzz     sigxy     sigyz     sigzx       eps
       0.0       0.0       0.0       0.0       0.0       0.0       0.0       0.0
         2         1         1         0         0         0
       0.0       0.0       0.0       0.0       0.0       0.0       0.0       0.0
```